Ilmar Kleis
Priit Kulu

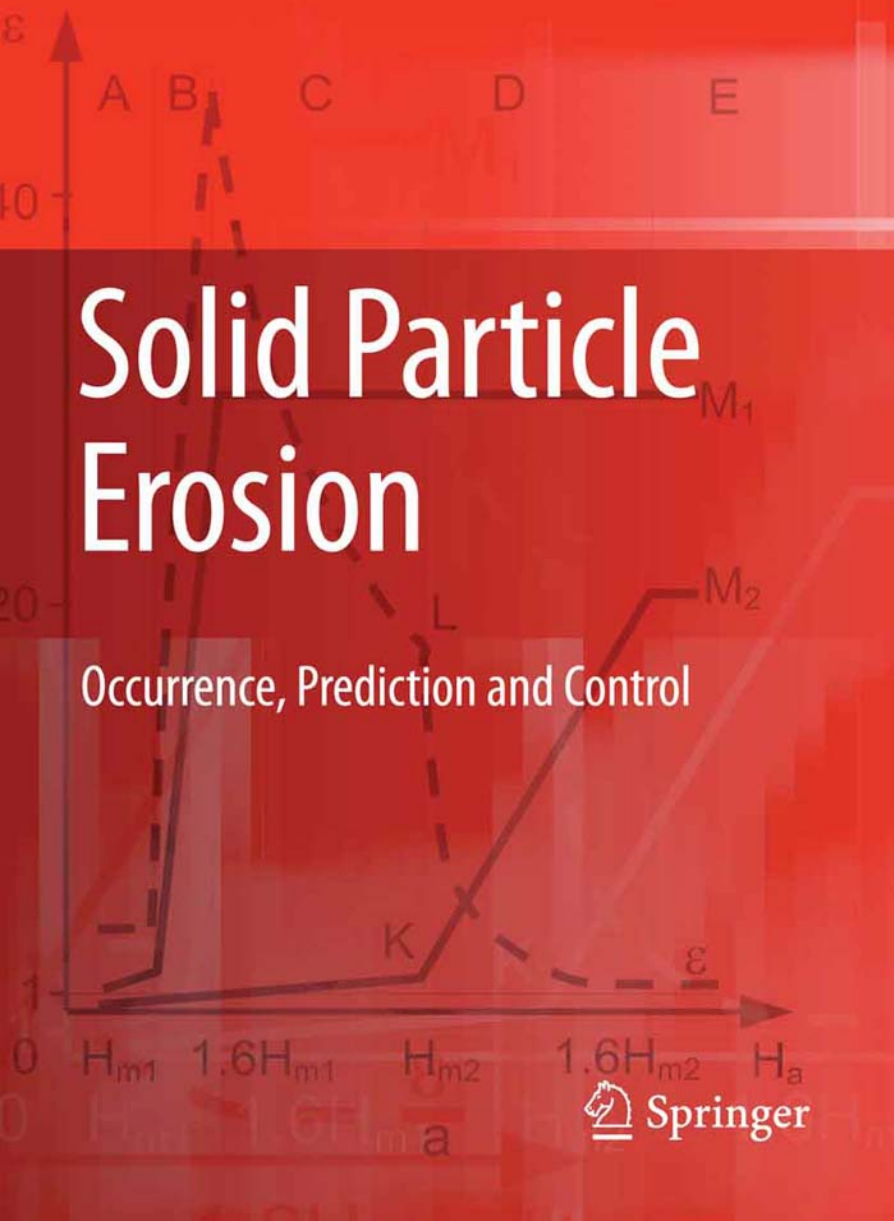

Solid Particle Erosion

Occurrence, Prediction and Control

Springer

Solid Particle Erosion

Ilmar Kleis • Priit Kulu

Solid Particle Erosion

Occurrence, Prediction and Control

Springer

Ilmar Kleis, DSc Eng.
Priit Kulu, DSc Eng.

Department of Mechatronics
Tallinn University of Technology
Ehitajate tee 5
19086 Tallinn
Estonia

ISBN 978-1-84800-028-5 e-ISBN 978-1-84800-029-2

DOI 10.1007/978-1-84800-029-2

British Library Cataloguing in Publication Data
A catalogue record for this book is available from the British Library

Library of Congress Control Number: 2007937988

Cover design: eStudio Calamar S.L., Girona, Spain

Printed on acid-free paper

9 8 7 6 5 4 3 2 1

springer.com

Preface

Depending on the kind of equipment, erosion phenomena may appear in various forms. Though harmful as a rule, erosion sometimes can be used as a method of processing. One of its variations known for a long time is gas erosion that occurs in gun barrels. Erosion caused by cavitation, which appears in pipes, water turbines and pipelines, has also been known for quite a long time. Later, problems of drop erosion were encountered on last stage steam turbine rotor vanes and on the fuselage of high-speed aircraft passing through rain clouds. Cosmic erosion caused by the impacts of micrometeorites on the external surfaces of the objects moving in the universe (spaceships, artificial satellites) is a comparatively new discovery. The variations of erosion used in material processing are electro- and ultrasound erosion.

This monograph covers erosion caused by impacts from solid particles. In terrestrial conditions, impact velocity is generally limited to *ca* 400 m/s. Cosmic erosion that takes place at hypervelocities is touched upon in the section concerning the theory of impact.

Historically speaking, high-velocity erosion first found practical application as a method of cleaning castings, house facades, *etc*. It emerged as a problem first in thermal power engineering when pulverized local ash-rich fuels were taken into use for burning in boilers of thermal power plants (in the former Soviet Union in the mid-1930s) and later in solid fuel operated gas turbines. The components eroded by ash particles were boiler tubes, exhaust fans and turbine blades. In Germany, erosion problems became apparent in pneumatic transport systems used in mining engineering (especially tube elbows), as well as in the components of mills for grinding minerals, working on impact principles. Large-scale investigations of these problems started after World War II.

In Estonia, however, the problem of erosion emerged simultaneously in two fields. Namely, in the 1950s, when the disintegrator was taken into use to grind mixtures of sand and lime for the production of silicate concrete and powdered local ash-rich oil shale was burnt in power station boilers. In the disintegrator, impact elements and rotor rings, as well as economizer tubes, cyclone-catching collectors, draft fans and hammer mills were subject to severe wear. Research into the problem and development of the methods required started in 1955 at Tallinn Technical University (from 2005 Tallinn University of Technology (TUT)). Three departments were involved – machine elements, materials technology, and thermal

engineering. The respective laboratories were founded at each department. Erosion at normal temperature was the area of research in the Laboratory of the Department of Machine Elements, whereas erosion at elevated temperatures was studied in the Laboratory of the Department of Thermal Engineering. The latter area will not be covered below, but its thorough treatment has been published by Prof. Ots in his monograph "Corrosion and Wear of Heating Surfaces", Moscow, 1987. In contrast to erosion behaviour at normal temperatures, the concurrent effect of corrosive processes stimulates erosion at high temperatures, and specific techniques are applied for metal target protection.

As erosion greatly depends on the properties of the material and changes occurring in it during the process, materials researchers and physicists at TUT collaborated in this research programme. TUT became known as a major research centre in the Soviet Union engaged in studies of erosive processes, elaboration of new testers, and materials resistant to erosion. Clear evidence of this fact is that TUT researchers got the proposal to develop the state standard GOST 23.201-78 *Gas abrasive wear testing of materials and coatings with centrifugal accelerator*.
In 1961, another team founded a research laboratory at the Tallinn Institute of Silicate Concrete, performing experimental erosion studies directly under industrial conditions and maintaining close cooperation with TUT.

Founded in 1967 was the TUT Laboratory of Powder Metallurgy aimed at the development of new erosion resistant materials and components.

Until 1980, research was focused on the elucidation of the effect of various parameters on the erosion rate; thereafter emphasis was placed on the development of energetic theory of impact and its verification. At the same time, studies and elaboration of cermets and coatings resistant to erosion proceeded in the Powder Metallurgy Laboratory of the Department of Materials Engineering. These studies are still in progress.

Problems of erosion have been studied at TUT for 50 years. Over 30 theses covering problems of erosion and 100 research projects ordered by industry have been completed. Before the 1990s these reports and publications, mainly written in Estonian and Russian, remained unknown to scientists and engineers in the West. Special attention was paid to the original impact theory, a basis of the energetic theory of erosion, developed in close cooperation with German scientists. This monograph attempts to provide a systematic review accessible to a reader of English. References to widely known works done in the USA, Great Britain and Germany and available in English may be omitted here. But references will be given to express different viewpoints or to supplement the results obtained by us. However, this does not concern the results gained from research projects conducted in co-operation with Stuttgart University, Tampere University of Technology and Zittau Technical University.

Our presentation attempts to follow a chronological and logical order. First, the development of reliable testing equipment is introduced, then the laws related to erosion are verified, followed by the creation of the theory of erosion and verification of its reliability. Finally, measures are described on how to limit and prevent erosion in equipment. Ilmar Kleis is the author of Chapters 1 and 2, Priit Kulu has written Chapter 4, and Chapters 3 and 5 are a joint effort.

Tallinn, September 2007 *Ilmar Kleis*
Priit Kulu

Contents

Notation

a_c – Coriolis acceleration
A – area
A_c – coefficient of abrasivity

CAK – centrifugal accelerator of Kleis
C_m – specific heat capacity
C_r – length of the radial crack

d, D – diameter
d_m – mean diameter

e_0 – specific energy, J/mm^3 or
dynamic hardness, GPa
e_s – specific shear energy density
E – Young's modulus
E_1 – Young's modulus of target material
E_2 – Young's modulus of impacting body material
E' – reduced modulus of elasticity

f – friction coefficient
F – force
F_c – minimal force of crack initiation
F_m – maximum force
F_n – normal force
FS – flame spray
FSF – flame spray fusion

g – free falling acceleration
G – weight loss of the test material
G_e – weight loss of the reference material

h – height
h_e – penetration depth, elastic part
h_l – depth of the cavity caused by the surface-parallel lateral crack
h_m – maximum penetration depth
h_p – depth of impact crater; penetration depth, plastic part
H – hardness
H_a, H_2 – hardness of the abrasive
H_c – contact hardness
H_d – dynamic hardness
H_m, H_1 – hardness of the material
H' – reduced hardness
HB – Brinell hardness
HET – hot erosion tester
HR – Rockwell hardness
HV – Vickers hardness
HVOFS – High Velocity Oxy-Fuel Spray
HVS – High Velocity Spray

I – wear rate
I_c – calculated value of wear rate, mg/kg or
weight wear rate per 1 cm length of rotor channel, mg/kg·cm
I_{exp} – experimental value of wear rate, mg/kg
I_e – wear rate of the reference material
I_g – weight wear rate, mg/kg
I_v – volumetric wear rate, mm^3/kg
I^B – wear rate from brittle fracture
I^P – wear rate from plastic deformation
I_g^B – weight wear rate from brittle fracture
I_g^P – weight wear rate from plastic deformation
I_x – wear rate caused by the dust
I_{cx} – wear rate caused by the dust per 1 cm length of rotor channel, mg/kg·cm

J_{I} – the share of wear from tangential component
J_{II} – the share of wear from normal component

k_α - impact angle coefficient
k_d – particle roundness coefficient
k_H – particle hardness coefficient
k_R – particle shape coefficient
k_v – particle velocity coefficient
k_φ – particle concentration coefficient
k_{60} – impact angle ($\alpha>60^o$) coefficient
K – coefficient of restitution

K_1 – the coefficient that corresponds to the wear rate caused by the unit force
K_{1c} – fracture toughness, $N/mm^2 \cdot m^{0.5}$
K_d – coefficient of additives in abrasive
K_g – weight wear of the material, mg or weight wear in 1 m^2 of new surface, mg/m^2
K_v – volumetric wear of the material, mm^3

L – material latent heat of melting
LDA – Laser Doppler Anemometer

m, M – mass

n – rotation speed, rpm

p – pressure, fracture probability
p_d – dynamic pressure

r, R – contact radius
R, R_2 – radius of the impact body
R_0 – radius of the ring with specimen

S – specific surface, m^2/g
ΔS – change of specific surface, m^2/g
SPQ – particle shape parameter “quadratic fit”

t – time, duration
T – temperature
T_m – melting temperature

v – velocity, m/s
v_0 – impact velocity, m/s
v_R – particle velocity, m/s
v_T – critical impact velocity, m/s
v_{grind} – grinding velocity, m/s
V – volume of the impact crater
VK – vacuum wear tester

W – energy absorbed in impact
W_0 – initial energy of the body before impact
W_e – energy spent on elastic deformation

α – impact angle, ^{o}
α_{max} – maximum impact angle, ^{o}
β – ejection angle, ^{o}

δ – target hit sector angle, ^{o}
ε – relative wear resistance
κ – flatness ratio of the curve
μ – Poisson's ratio
μ_1 – Poisson's ratio of target material
μ_2 – Poisson's ratio of impacting body material
ρ – density
ρ_e – density of reference material
ρ_1 – density of target material
ρ_2 – density of impacting body material
σ – stress
σ_m – maximum stress
σ_{mean} – mean residual stress
σ_y – yield point of the material
τ_0 – shearing stress
τ_0/e_s – shear energy density
φ – particle concentration, g/cm^2·s or
apex angle of the pyramid or cone
ω – angular velocity, rad/s

1

Experimental Study oF Erosion Characteristics

It was found early on that erosion rate depends mainly on the velocity of erodent particles and on the angle between the target surface and particle trajectory (impact angle). Further, it was revealed how other parameters (*i.e.*, particle size and shape, their concentration, abrasive to target hardness ratio and the effect of liquid and solid additives) can change the nature and result of the process of erosion.

Before 1938, the scale of practical tests was limited, although Gary's pneumatical test device equipped with a nozzle already existed in 1904. Intensive studies were stimulated by ash-rich fuels used in power plant boilers and the resultant heavy erosion of boiler tubes and exhauster blades. Later, gas turbine blades also contributed to these studies when an attempt was made to use solid fuels in those turbines [1]. In Germany, erosion problems appeared with pneumatic transport systems (especially concerning bends and elbows of pneumatic lines) [2] used in the mining industry and in impact mills. Laboratory research progressed in these fields after World War II.

In Estonia, problems with erosion emerged with ash-rich fuels used in power plants and in the manufacturing process of silicate concrete, when disintegrator mills were taken into use in 1951 for processing ground sand-lime mixtures [3].

Early studies of erosion problems conducted at Tallinn University of Technology (TUT) and knowledge acquired from previous research proved that attention must be focused on the development of testing equipment and on the determination of the characteristics of this wear type.

1.1 Laboratory Equipment Used in Erosion Research

Schematic representations of the most widespread types of laboratory equipment are as shown in Figure 1.1. The scheme with tubular specimens (Figure 1.1a) simulates the airborne ash erosion process in a boiler. Particles are accelerated into the shaft by a gas (*e.g.* air). This design is only suitable for investigating erosion in boiler tubes.

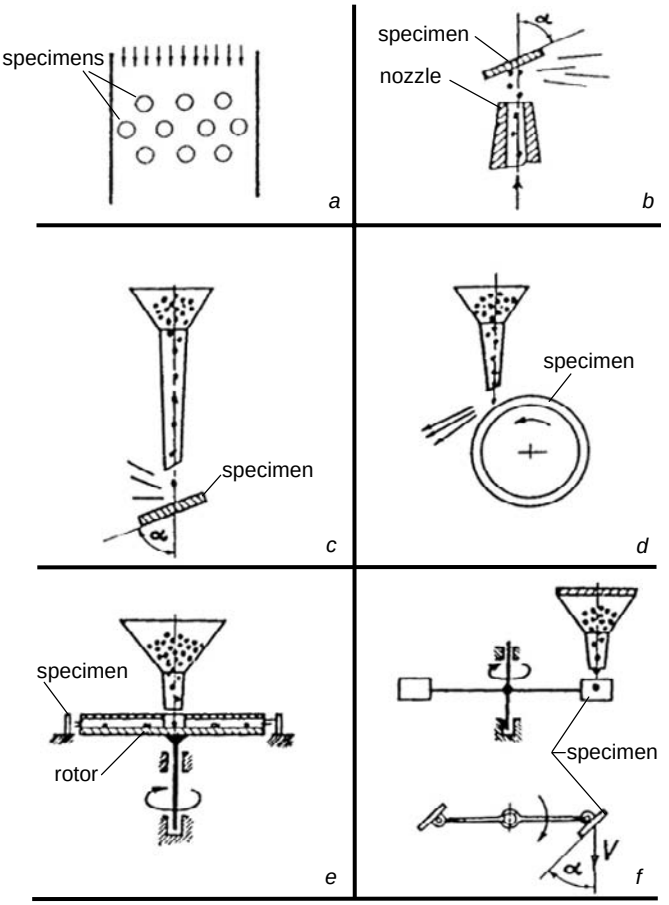

Figure 1.1. Schemes of equipment for erosion testing of materials

One of the most widespread test equipment designs used by many researchers in different countries is shown in Figure 1.1b. This design was taken for the basis of the German standard DIN 50332. It allows testing of specimens one by one, blasting them with erosive particles entrained in a gas stream. Particle velocity is taken to be equal with the velocity of a gas stream because the latter is easy to determine.

However, the actual impact velocity depends on the size and shape of the particles and on the length of the acceleration distance. Moreover, the productivity of testing with such equipment is low and it is impossible to test both the material under study and reference material simultaneously. The design based on the free fall of the particles (see Figure 1.1c) allows only limited particle impact speeds (*ca* 10 m/s) and is therefore used primarily to investigate the erosion of paint layers and enamels. In terms of kinematics, the design shown in Figure 1.1d is simple, for the test specimen is rotating around a horizontal shaft. This design has been used by researchers from Tomsk University, Russia, led by Kaschejev. Such equipment, however, has an essential drawback in that the particle velocity and impact angle

prove to be functionally dependent as pointed out in [4]. In specific terms, at the minimal particle velocity of 13 m/s, the corresponding impact angle α was 13° and at the maximum particle velocity of 126 m/s, the impact angle was only 2°. That design did not allow for the use of larger impact angles.

Figure 1.1e shows a centrifugal accelerator design, where particles are hurled through the radial channels of the rotor against test specimens fixed at any desired angle. CAK-1 (see Figure 1.2); the first device of such design was taken into use by its author Kleis in 1957 [5]. The principal advantage of this device is that it allows simultaneous testing of several specimens and standard test specimen in the same conditions. Therefore, it allows one to determine the relative erosion resistance of different materials in a short time. Parameters of different models of centrifugal accelerators are as shown in Table 1.1.

Table 1.1. Brief data of centrifugal accelerators

Parameters	**Model designation**						
	CAK-1	**CAK-2**	**CAK-3m**	**CAK-4**	**VK-2**	**CAK-HET[b]**	**CAK-5**
Rotor diameter, mm	400	600	200	200	400	225	200
Particle velocity range, m/s	15–90	15–165	15–130	15–130	20–350	20–100	15–125
Motor power, kW	0.6	7	0.5	1.0	2.8	2.2	2.2
Overall dimensions of accelerator, m	1.2×1.6×1.6	2×2×1.2	0.3×0.4	0.3×0.5	1×1×1.2	0.65×1.2	0.3×0.6
Mass of accelerator, kg	210	415	35	50	2500[a]	150	40
Maximum size of abrasive particles, mm	1.6	2.0	1.2	1.2	2.5	1.2	1.2
Number of simultaneously tested specimens	Up to 20	Up to 32	Up to 15	Up to 15	Up to 36	Up to 20	Up to 15
Rotor speed control	Stepped	Stepped	Stepless	Stepless	Stepless	Stepless	Stepless
Year of manufacture	1957	1962	1967	1980	1969	1999	2003

Note: The rotor speed of CAK-3m, CAK-4 and VK-2 is automatically controlled

[a] Mass together with additional evacuation equipment

[b] For hot erosion testing (up to 650 °C)

Initially, large-sized high capacity centrifugal accelerators were designed (CAK-2) later, however, reductions in size and portability were pursued (CAK-3, CAK-3m and CAK-4) in order to spread the use of these devices. For the sake of compactness, the belt drive was eliminated and the motor coupled directly to the rotor. In addition, the erodent was fed directly into the rotor. The accelerator was equipped with a generator and a control panel to determine the rotating speed of the machine. It is possible to change the rotating speed and thus particle velocity with the aid of the control panel by stepless adjustment of electric feed. CAK-3, the first portable device, had a cast light-metal casing and a relatively small motor (only 0.27 kW). That 1964 design was thoroughly tested and the shortcomings found were eliminated. CAK-3m, a modified version of that device, was built in 1967. It then had a welded housing and a more powerful motor. The control panel was enhanced with control electronics to ensure stable rotating speed of the rotor, regardless of the concentration of outgoing particles. In order to regulate the impact angle, as already on CAK-2, the method of specimen set-up by turning around the y-y axis (see Figure 1.2) was altered, because, at low impact angles, this leads to a significant decrease of the target hit sector angle δ (Figure 1.3), which, in turn, brings about an increased consumption of the erodent material and wider scatter of the test results. The latter was caused by the strong influence of any deviation of the setup angle on the target hit sector angle δ.

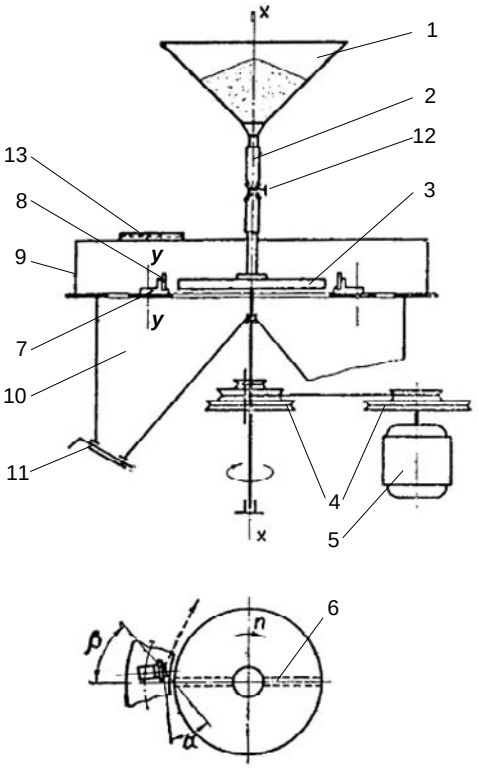

Figure 1.2. Centrifugal accelerator CAK-1: 1 – abradant hopper, 2 – rubber feed tube, 3 – rotor, 4 – belt drive, 5 – electric motor, 6 – channel, 7 – specimen holder, 8 – specimen, 9 – removable cover, 10 – collector bin, 11 – plug, 12 – regulator valve, 13 – window

A new method was used, where the longitudinal axis of specimen holders coincides with the trajectory of the particles hurled out of the rotor (Figure 1.3a) and, to vary the impact angle, the specimen can be inclined around the horizontal axis. As a result, the hit sector angle δ remains constant. The fixing method of the specimen was also changed by replacing the awkward fixing screw with a quick and accurate wedge and a clamp (Figure 1.4b). The clamp also protects specimen edges and back surface from rebounding particles. The latter modification of the accelerator CAK-4 differs from its predecessors only by a more powerful motor and improved control panel, where readout panels with analog indicators has been replaced by digital displays. CAK-5, the latest model of the accelerator, is shown in Figure 1.4a.

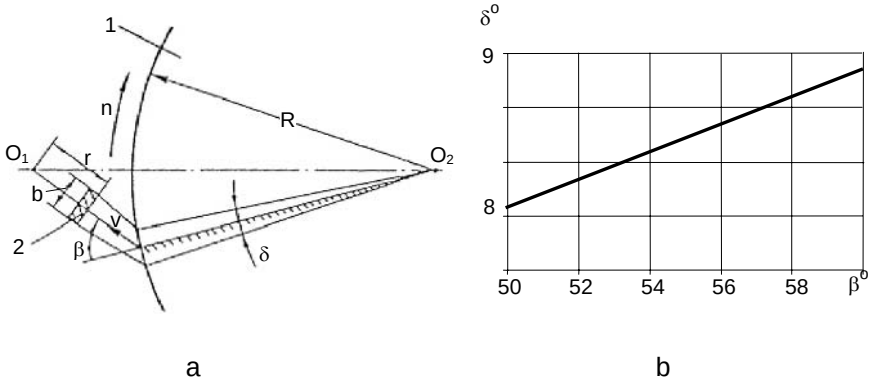

Figure 1.3a, b. Position of the specimen in relation to rotor (**a):** β – particle ejection angle, δ – target hit sector angle; R = 100 mm, r = 22 mm, b = 12 mm, O_1O_2 = 132 mm and dependence of the impact angle δ on the ejection angle β (**b)**

Based on the drawing in Figure 1.3a, mass M_1 of the particles hitting one specimen is expressed as follows:

$$M_1 = M\delta/2\pi \tag{1.1}$$

where M – total mass of the particles in the hopper,
δ – hit sector angle in radian measure.

Accelerators CAK-3m and CAK-4 have been demonstrated in many trade fairs and the latter model received a gold medal at a major USSR trade fair. The mechanical workshop at TUT fulfilled 30 orders by different research institutes from many countries, such as Russia, the Ukraine, Germany, the Czech Republic, Finland and Bulgaria. In addition to the accelerator shown in Figure 1.4, its set of delivery includes a rotor balancing device, needed after the replacement of the worn out rotor channels, and a device to facilitate setting-up of the specimen holders (Figure 1.5). The latter becomes necessary with an erodent other than quartz sand, whose angle of ejection differs from β = 55°.

In 1978, the state standard GOST 23.201-78 *Gas abrasive wear testing of materials and coatings with a centrifugal accelerator* was developed at the

Machine Design Department of TUT under the supervision of Kleis. This standard, based on the equipment described, was put in force in the former Soviet Union from January 1979. Since the tests described in this book were conducted according to the same standard, a brief description will be appropriate here.

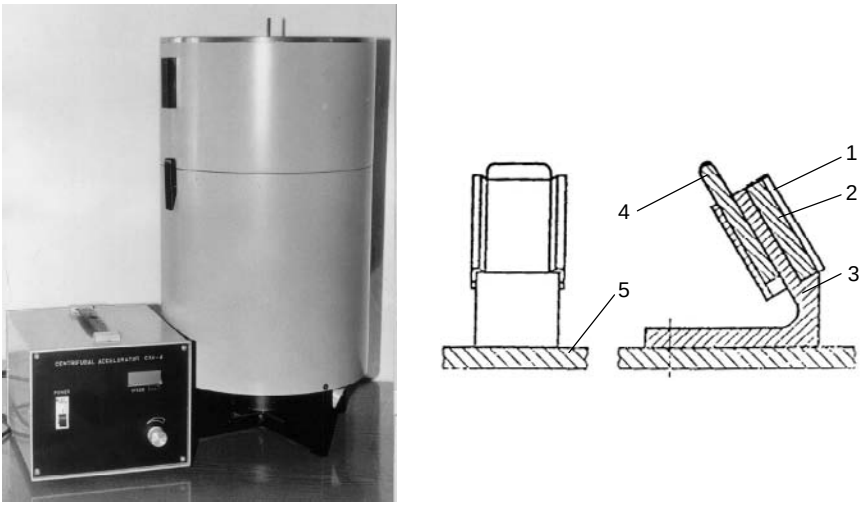

a b

Figure 1.4a,b. Overall view of a CAK-5 accelerator with a control panel (**a**) and fixation of the specimen (**b**): 1 – clamp, 2 – specimen, 3 – specimen holder, 4 – wedge, 5 – bottom ring

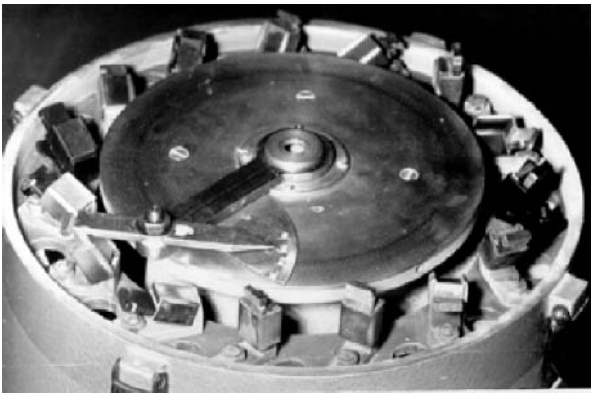

Figure 1.5. Setup of specimen holders depending on the angle β

This standard covers the determination of erosion resistance of metals and coatings whose hardness is at least 20 HV and size of pores does not exceed 0.02 mm. The minimum thickness of coatings shall be 0.3 mm. Specimens sized 20×15×4 mm are fixed in holders as shown in Figure 1.4b that leave a face of b = 12±0.1 mm width exposed to erosion. The reference material against which the

material under study is compared is annealed steel of 0.45% C according to GOST 1050-74 of hardness 185–195 HV. Specimens are cleaned with acetone and weighed with an accuracy of 0.1 mg before and after the tests, while the weight loss of one specimen during the primary test must be at least 5 mg. Before that, specimens are subjected to the wear-in process in the same conditions. A minimum of three specimens are typically required during one test run, while with porous materials, cermets and heterogeneous coatings, five specimens are the case. Quartz sand from the Privolsk area (GOST 6139-70) is used as the standard abrasive material, with its grain size ranging from 0.5 to 0.9 mm and moisture content less than 0.15%. Specimen holders are set up in compliance with the ejection angle β = 55°. The recommended test velocities are particle ejection velocities of 38 and 76 m/s that correspond to rotor speeds of n = 3000 and 6000 rpm, respectively. The recommended amount of quartz sand in the hopper at those speeds is 30 and 5 kg if the hardness of the test material is less than 1000 HV and twice as much if its hardness is higher than 1000 HV. When replacing worn out channels of the rotor, the condition $R = 100 \pm 0.5$ mm shall be observed. Experiments can be carried out at other speeds and with different erodents, but in such cases it is important to determine the particle ejection angle β previously and to reset the specimen holders accordingly.

Relative wear resistance ε of the material is expressed as follows:

$$\varepsilon = G_e \rho / G \rho_e , \tag{1.2}$$

where G_e – weight loss of the reference material,
G – weight loss of the test material,
ρ_e – density of the reference material,
ρ – density of the test material.

In addition to the above rotor design, an accelerator can be equipped with two more rotors for special purposes (see drawings in Figure 1.6). The first (a) is used for testing at low impact angles (3–30°) and for determining of the effect of particle concentration φ on the erosion rate. Design solution (b) enables erosion testing at α = 0°, *i.e.*, when particles are sliding on the surface being subjected to the Coriolis forces (*e.g.*, blades of fan blowers and turbo-machines). Using the notation in Figure 1.6b, we can express the Coriolis acceleration a_c acting on a particle as

$$a_c = 2\omega^2 x \operatorname{ctg}\beta \tag{1.3}$$

The force pressing particles against the surface is proportional to the above acceleration.

There is no doubt that a centrifugal accelerator is perfect for the determination of relative erosion resistance of a material. However, if the purpose is to determine erosion rate I_v (mm^3/kg) it fails to provide test results with a high accuracy because of shortcomings similar to the design solution shown in Figure 1.1a). Namely, it produces a fairly wide scatter of particle outlet velocities and ejection angles β (thereby also impact angles α). The main reason lies in differences in the sliding resistance in the rotor channels because of different particle shape. This distribution was investigated on the accelerator CAK-1 with a SKS1m film camera at a speed of 2500–3500 shots per second (see schematic representation [2] in Figure 1.7).

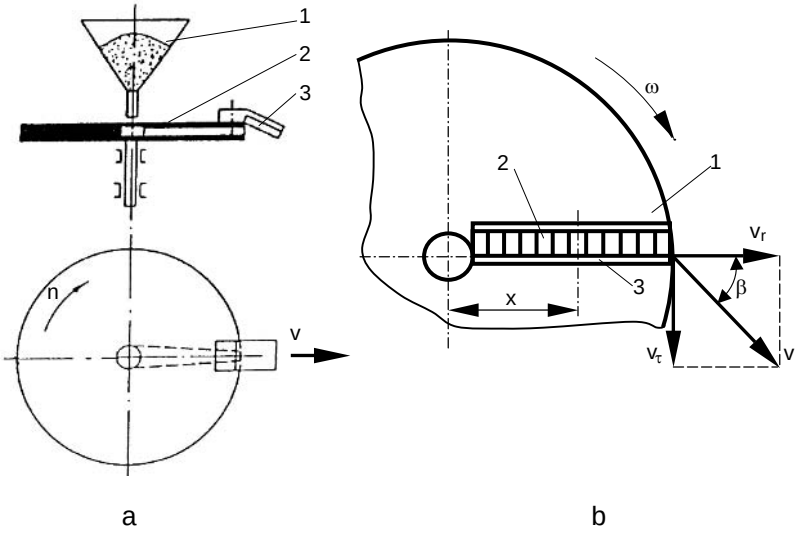

Figure 1.6a,b. Rotors of a centrifugal accelerator for special purposes with rotating specimen (**a**): 1 – abradant hopper, 2 – rotor and 3 – specimen and scheme of rotor where particles slide on the surface of the specimen (**b**): 1 – rotor, 2 – specimen, 3 – rotor channel

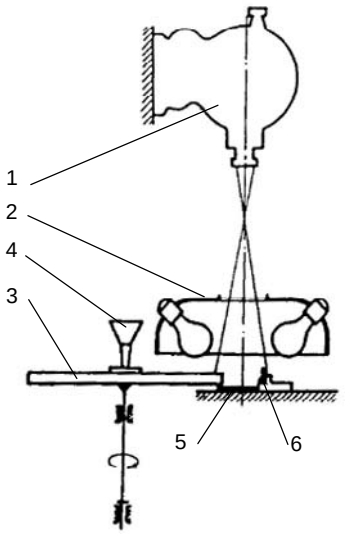

Figure 1.7. Schematic drawing of speed filming equipment: 1 – camera, 2 – lamp with a hole, 3 – rotor, 4 – hopper, 5 – black silk backdrop, 6 – specimen

Quartz particles used for filming were from the Männiku quarry in Estonia, classified into size ranges of 0.3–0.4 and 0.6–1.0 mm. In the tests conducted at different rotation speeds, under different conditions, velocities and ejection angles of at least 150 particles were measured. Typical results of distribution are shown on histograms in Figures 1.8 and 1.9.

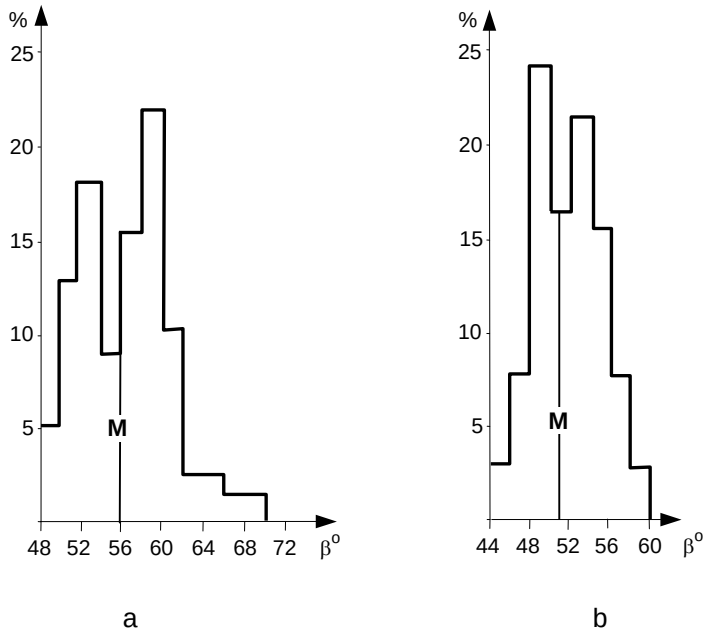

Figure 1.8a,b. Histograms showing the distribution of ejection angle β at rotating speed of 3285 rpm and abrasive particles size range: **a** – 0.3–0.4 mm, **b** – 0.6–1.0 mm. Line M shows the arithmetical average

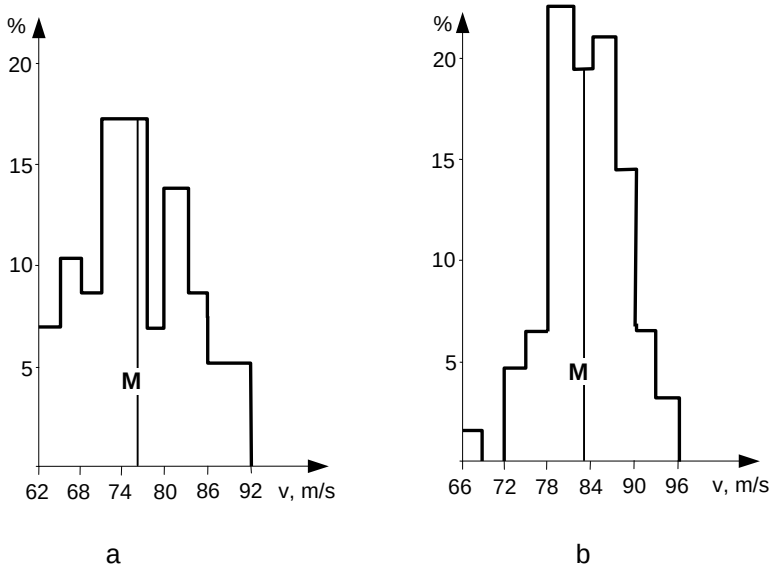

Figure 1.9a,b. Histograms showing the distribution of exit velocity v at the rotating speed of 3285 rpm and abrasive particle size range: **a** – 0.3–0.4 mm, **b** – 0.6–1.0 mm. Line M shows an arithmetic average

On the basis of the analysis of the film, the following conclusions can be drawn:

1. The distribution of particle ejection angle β and exit velocity v values is quite significant; both parameters depend on the particle size. When the particle diameter decreases, the average value of β increases and, accordingly, the value of v decreases.
2. Particle trajectory from rotor to specimen is a straight line and its velocity remains constant.

Further tests with a laser anemometer (see Figure 3.14) conducted on CAK-4 provided analogous results, *i.e.* the deviation of particle velocities from the mean value was ±10–16%. Suur [6] used the filming method to observe the trajectory and velocity of particles exiting from the nozzle of the pneumatic test device. This device, commonly used in testing at high temperatures, is described in detail in Section 1.7.1. Using a nozzle with a diameter of 4.5 mm for specimens fixed at 135 mm from the nozzle, the following conclusions can be drawn:

1. The abrasive stream leaving the nozzle takes the form of an exhaust cone with maximum particle density around its central axis and minimum within its outer surface. The angle between the generatrix and axis of the cone is up to 11°.
2. The increase in particle velocity on their way from nozzle to specimen is on average 5%. A straight line trajectory is maintained.
3. Particle velocity is proportional to the air pressure p depending to some extent also on the air temperature (Figure 1.10). The distribution of velocity values is shown in Figure 1.11.
4. Wearout of the nozzle brings about a change in the trajectory of the particles; therefore, the steel nozzle was abandoned and replaced with a WC-Co hardmetal nozzle of high wear resistance.

Based on the above, both of the methods provide approximately the same deviation of the velocity and impact angle values from the mean value. Since 1960–1970 scientists have been actively discussing the influence of these fundamental parameters (*e.g.*, many believed that velocity must always be of the power of 2; deviations from this value can be explained by test errors), we were seeking an approach that would finally lead to clarity. The design shown in Figure 1.1f was realized in a vacuum to avoid aerodynamical disturbances (mainly air whirls) in the working chamber of the test rig and excessive heating of the rotor at greater speeds. To implement the vacuum chamber, it was required to redesign the tester using additional equipment and take into account extended testing time. However, it ensured minimum deviations of particle velocity and impact angle (±1.5%) from their mean values. Figure 1.12 shows the design of accelerator VK-1, for which Kleis was granted SU patent No. 167660.

The procedure of testing on the VK-1 machine is as follows. When a previously run-in specimen (7) has been set up in the required position (in the case of low impact velocity, two specimens of the same material are weighed together) and a weighed portion of abrasive has been poured into the hopper (12), cover (14) and valve (15) are to be sealed airtight. Next the vacuum pumps are turned on, keeping watch on vacuum gauge readings. When the reading reaches 10^{-2} mm Hg, the tester motor (4) is turned on. When the reading of the frequency meter (10) has stabilized, the vibrofeeder is turned on. At the end of the test, first the valve (15) is opened and then the bolts holding the cover (14) are released. The cover with the feeding device attached to it is lifted by a hydraulic appliance and moved aside (Figure 1.13) to facilitate specimen removal.

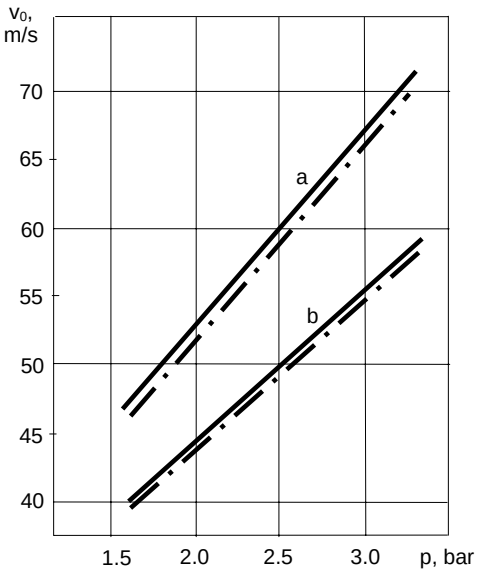

Figure 1.10. Dependence of the velocity v of quartz particles on the air pressure p that accelerates them; the *full line* corresponds to the air temperature of 20 °C, *dashed line* to 700 °C at abrasive particles size range: a – 0.4–0.6 mm and b – 0.6–1.0 mm

To ensure that all particles will hit the specimen and that the wearable area will remain the same for all impact velocities, two conditions must be satisfied (notation from Figure 1.14):

$$h > 2\pi(2gH)^{0.5}/z\omega \tag{1.4}$$

and

$$H = h_1^2 n^2 z^2 / 7200g, \tag{1.5}$$

where g – free falling acceleration,
n – rotating speed of the shaft,
z – number of specimens,
h_1 – height of the wear mark.

The impact velocity v_0 is expressed as follows (Figure 1.14a):

$$v_0 = (v_1^2 + v_2^2)^{0.5} = (\omega^2 R^2 + 2gH)^{0.5} \tag{1.6}$$

In this formula, v_2 means free falling speed that has an effect only at lower impact velocities (*e.g.* at v_1=15 m/s increases the value of v_0 by 2%). Already at the velocity v_1 = 50 m/s, the influence is negligible (less than 0.2%); therefore beginning from this velocity $v_0 = v_1 = \omega R$ was taken.

To achieve higher impact velocities and to study the behaviour of specimen material and reference material simultaneously, a rearrangement of the tester into a centrifugal accelerator VK-2 (see Table 1.1 for specification) is necessary. That would require changing the rotor, moving the hopper into the center of the cover and installing an additional support ring into the work chamber.

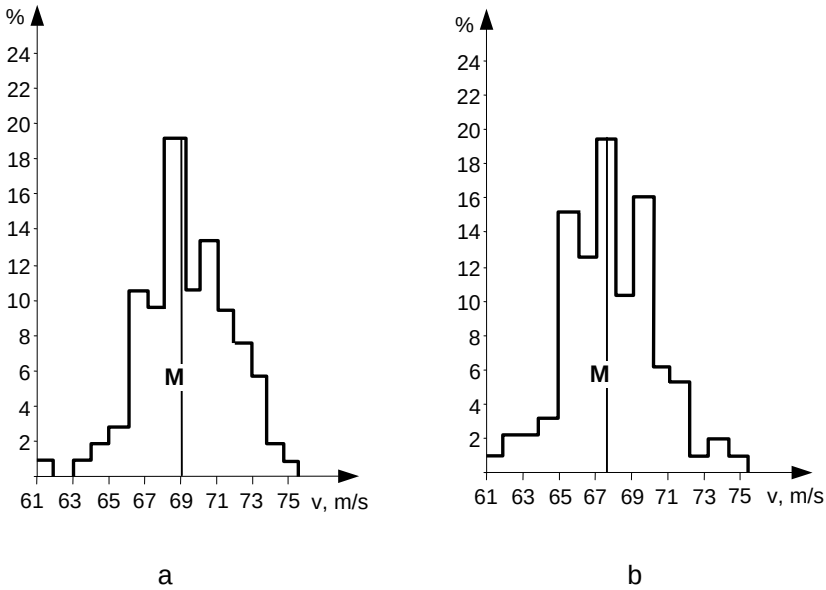

Figure 1.11a,b. Histograms of actual velocity distribution of abrasive particles size range 0.4–0.6 mm at air pressure p = 0.3 MPa: **a** – at temperature 20 °C and **b** – at temperature 700 °C. Line M shows an arithmetic average.

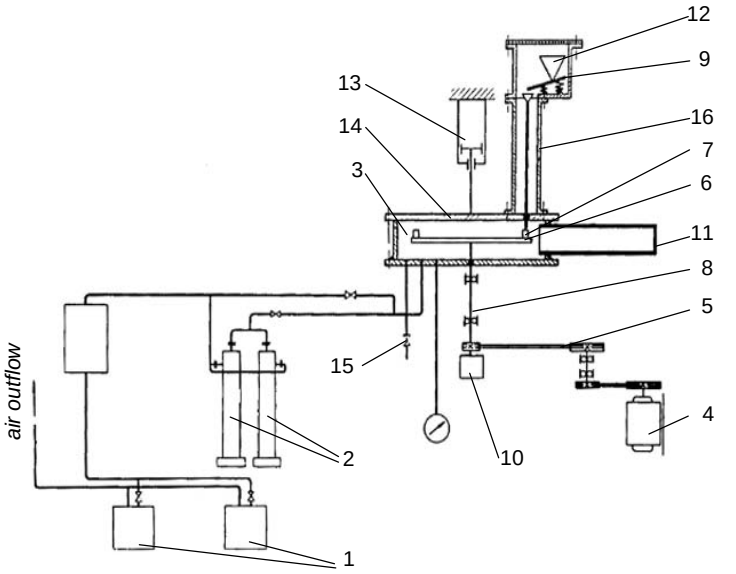

Figure 1.12. Vacuum tester VK-1: 1 and 2 – system of vacuum pumps, 3 – work chamber, 4 – electric motor, 5 – accelerating belt drive, 6 – rotor, 7 – specimen, 8 – main axle, 9 – dosing vibrofeeder, 10 – frequency meter, 11 – capturer of particles, partially filled with cotton, 12 – abradant hopper, 13 – hydraulic cylinder, 14 – removable cover, 15 – valve, 16 – feeder pipe (of interchangeable height H)

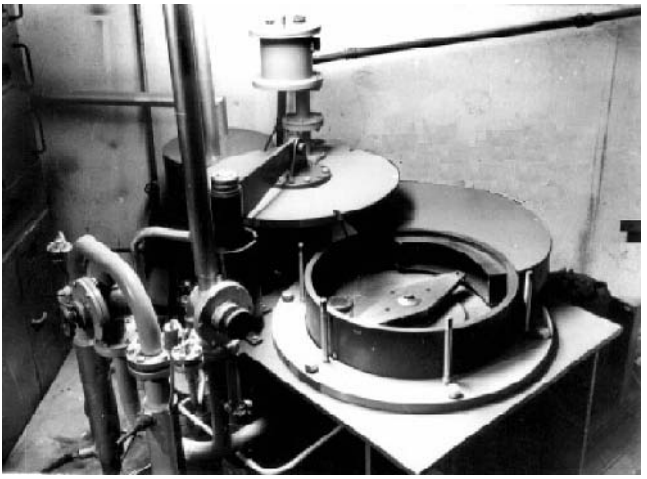

Figure 1.13. View of the tester VK-1 with its cover open

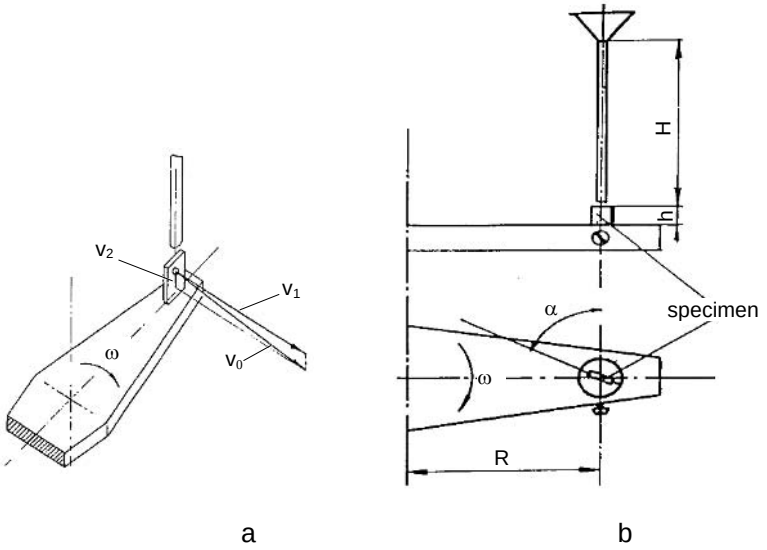

Figure 1.14a,b. Parameters that define particle kinematics and impact accuracy in the VK-1 device: **a** – components of impact velocity v_0, circular velocity v_1 and free falling velocity v_2; **b** – parameters that influence impact accuracy of all particles, H – particle free falling distance, h – height of the specimen, α – impact angle, ω – angular velocity of the rotor, R – distance of the specimen from the axis of rotation

All erosion researchers agree that, for the majority of materials, wear rate is not constant at the beginning of the process. Therefore, specimens need some wear-in before the main test. In our research, the parameters resembled those of the main test.

1.2 Dependence of Erosion on Particle Velocity

Particle velocity v_0 at the moment of hitting the target surface has the highest influence on erosion rate. An early fundamental study on erosion conducted at the University of Stuttgart was published in [7]. Quartz sand from the Neckar River used for testing was, accelerated by the Stotz pneumatic device. Particle velocity was assumed to be equal to the velocity of the air stream that was changed within the range of 35 to 330 m/s.Two types of steels were investigated (steel St37 and hardened steel C60H), together with molten basalt and rubber. At the impact angle of 90°, test points obtained for all the above materials fall in a log graph in straight lines, whose gradient determines the value of exponent *m* in Equation 1.7.:

$$I_v = a \cdot v_0^{\,m} \tag{1.7}$$

where coefficient *a* depends on target material, impact angle and properties of eroding particles. The value of exponent *m* was found to be 1.4 for St 37, 1.6 for C60H, 4.6 for rubber and 2.9 for basalt, respectively.

To evaluate differences in particle velocity and that of air stream, it is reasonable to compare data given in [7] with those obtained on the vacuum device VK-1 [8]. Figure 1.15 shows a comparison for mild steel, plus the data obtained on a centrifugal accelerator. Clearly, if the mean value derived from the filming data serves as a basis for particle velocity in the centrifugal acceleration, the line obtained in the graph is quite similar to the one obtained using the vacuum device and the value of the exponent is in both cases 2.3. In contrast, the experimental data obtained on the pneumatic device and on the centrifugal accelerator still more or less coincide up to the velocity of 35 m/s, whereas the velocity of particles accelerated by air stream of *e.g.* 200 m/s will reach only *ca* 80 m/s on the same device.

Since the results obtained on the vacuum device and on the centrifugal accelerator are in sufficiently close coincidence (in particular, as far as exponent *m* is concerned), results received on the latter shall be considered dependable. With the aid of the tester CAK-1, the effect of impact velocity on pure metals was investigated by Tadolder [9], on plastics by Arumäe [10] and on enamels by Lepikson and Kleis [11]. At low impact angles, the effect of velocity on the erosion of metals was studied by Langeberg [12] who performed experiments on the rotor illustrated in Figure 1.6a.

The values of exponent *m* presented in Tables 1.2 and 1.3 by far exceed those obtained with more defective sands. Namely, sand from the Privolski quarry is distinguished by its round shape and pellets of high fracture resistance of grains.

Proof tests with steel St3 on the vacuum tester VK-1 showed that at normal impact ($\alpha = 90°$), sand from the Männiku quarry yields $m = 2.3$, whereas the result with sand from Privolski quarry was $m = 3.0$ [8], *i.e.* the same value as obtained by Tadolder in testing technically pure Armco iron.

Table 1.4 shows that with each metal tested, exponent *m* tends to decline as the angle of attack approaches 0°.

Results of studies conducted on VK-1, which can guarantee utmost reliability, have been published in articles [8] and [15] and in a monograph [13]. The studies show that over a wide range of impact velocities, exponent *m* in Equation 1.8 does not necessarily have to remain unchanged. In the case of brittle particles, which break up intensively starting from a threshold impact velocity, there occurs a relatively

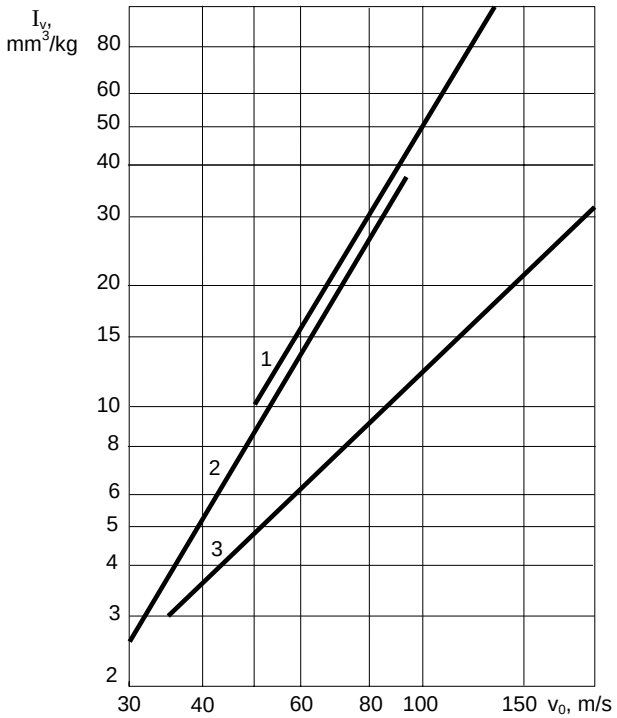

Figure 1.15. Dependence of wear rate I_v of the low-carbon steel on the impact velocity of particles (v_0) at $\alpha = 90°$: 1 – with 0.2% C steel (130 HV), when tested with quartz sand from the Männiku quarry on a vacuum device VK-1; 2 – with 0.2% C steel (130 HV), when tested on a centrifugal accelerator CAK-1; 3 – with steel St37, when tested on Stotz's pneumatic device using sand from the Neckar River

sharp decline in the value of the exponent. The latter may be, on the one hand, explained by the fact that for the fragmentation process considerably more energy is consumed, while on the other hand, by the deconcentration of stresses in the material which will accompany the breakup (see Figure 1.16).

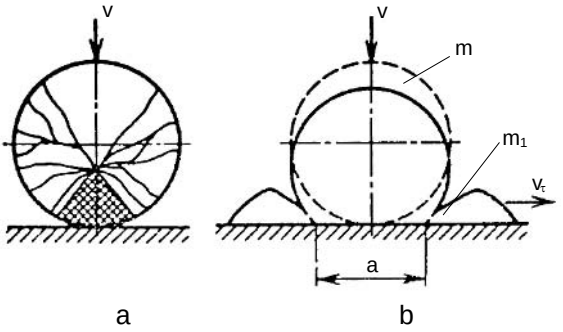

Figure 1.16a,b. Scheme of fracture of a brittle particle according to Reiners [14]: **a** – location of cracks, **b** – division of masses and velocities in the impact process, in which m_1 is the mass of the powdery part and v_τ – the velocity of spread of mass m_1 along the surface

Table 1.2. Values of coefficient a and exponent m within the impact velocity range 30–80 m/s for wear rate I_v (mm³/kg) calculations; sand from the Privolski quarry (0.5–0.8 mm)

Metal	$\alpha = 20^o$		$\alpha = 45^o$		$\alpha = 90^o$	
	a	m	a	m	a	m
Lead	4.8×10^{-3}	2.7	5.5×10^{-3}	2.5	2.5×10^{-2}	2.0
Tin	1.3×10^{-3}	2.7	4.8×10^{-4}	3.1	6.4×10^{-6}	4.0
Zinc	2.4×10^{-4}	2.8	1.6×10^{-5}	3.5	2.2×10^{-5}	3.2
Aluminium	1.7×10^{-4}	3.1	4.1×10^{-4}	2.8		
Cadmium	1.5×10^{-3}	2.6	2.1×10^{-4}	3.1	1.2×10^{-4}	3.0
Copper	2.2×10^{-4}	2.8	1.9×10^{-4}	2.8	6.6×10^{-5}	2.9
Nickel	1.6×10^{-4}	2.7	3.5×10^{-4}	2.6	1.3×10^{-4}	2.7
Pure iron	2.3×10^{-5}	3.2	4.1×10^{-4}	2.6	4.4×10^{-5}	3.0
Cobalt	2.8×10^{-5}	2.9	7.6×10^{-5}	2.9	8.1×10^{-4}	2.4
Titan	4.1×10^{-5}	2.9	1.5×10^{-5}	3.4	7.0×10^{-5}	3.0
Molybdenum	8.4×10^{-5}	2.5	7.4×10^{-5}	2.9	4.3×10^{-5}	2.9
Niobium	5.5×10^{-5}	2.7	9.1×10^{-5}	2.8	2.0×10^{-4}	2.5
Tungsten	5.5×10^{-6}	3.1	1.3×10^{-5}	3.1	3.2×10^{-6}	3.4

Note: In the case of aluminium, the determination of weight loss at 90° impact angle was disturbed by embedding of particles in target surface

Table 1.3. Values of coefficient a and exponent m in the case of plastics at impact velocity ranging from 30–80 m/s, for wear rate I_v (mm³/kg) calculations; sand from the Privolski quarry (0.5–0.8 mm) [10]

Material	α^o	a	m
Organic glass	20	8.5×10^{-4}	2.8
	45	2.9×10^{-3}	2.8
	80	1.5×10^{-2}	2.5
Vinyl plastics	20	9.1×10^{-4}	2.7
	45	1.2×10^{-3}	2.8
Teflon (PTFE)	20	1.2×10^{-5}	4.1
	45	3.0×10^{-4}	3.5
	80	4.0×10^{-6}	4.2
Rolled polyvinylchloride	20	2.3×10^{-3}	2.5
	45	2.6×10^{-2}	2.6
Low-density polyethelene	20	6.2×10^{-4}	3.0
	45	1.2×10^{-3}	2.9
Epoxy-composition ED-5	20	5.5×10^{-2}	2.5
	45	2.8×10^{-2}	2.6
	80	1.7×10^{-3}	2.9

Table 1.4. Values of velocity exponent m obtained in testing with 0.4–0.6 mm sand from the Männiku quarry, v_0 = 37–97 m/s [12]

Material	$\alpha = 3^o$	$\alpha = 9^o$	$\alpha = 15^o$
0.2% C steel, 140 HV	1.9	1.9	2.5
0.8% C steel, 850 HV	2.5	2.6	2.6
White cast iron, 740 HV	2.3	2.8	2.8
Grey cast iron, 230 HV	1.9	2.4	2.8
Hard-facing T620, 760 HV	2.0	2.1	2.3
Hardmetal WC-6Co, 1600 HV	1.2	1.3	1.6

Typical test results in such cases are presented in Figures 1.17 and 1.18. With coarse fractions, the decline of *m* starts at a lower level of velocity than with finer sand (Figure 1.17). The reason lies in the fact that large grains of sand are more defective. As far as hardmetals are concerned, material structure may be an underlying reason – changes in the exponent start to occur at a lower level of velocity with coarse-grained as compared to fine-grained sand (Figure 1.18a). When cermets wear out in the stream of quartz sand (Figure 1.18a), the values of exponent *m* are considerably lower than those of steels, *i.e.*, their sensitivity to the velocity of impact is extremely low (*e.g.*, with WC-3Co m =1.5 if v_0<200 m/s and only 0.3 if v_0>200 m/s).The situation changes radically in the case when the cermet is eroded by a stream of particles harder than itself the target (Figure 1.18b). Then the point of inflection of the straight lines is hardly noticeable, and exponent *m* practically coincides with that of steels (m = 2–2.1). Thus the advantage of higher erosion resistance over that of steels disappears.

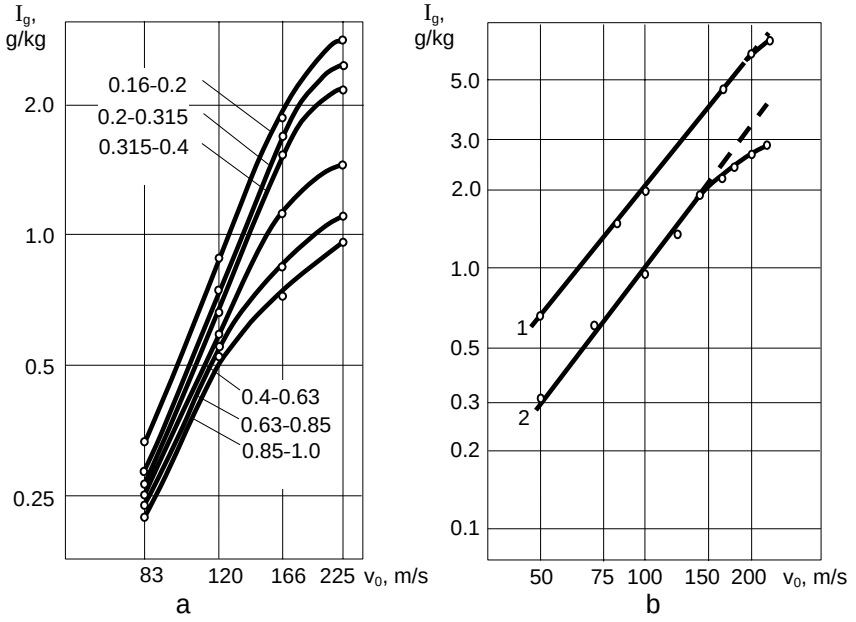

Figure 1.17a,b. Dependence of weight wear rate I_g on the impact velocity v at the impact angle α = 90°: **a** – material of the test specimen 0.8% C steel (850 HV), various fractions of sand from the Männiku quarry; **b** – straight line 1 – hardmetal WC-6Co (1600 HV) in a stream of corundum particles, 2 – 0.8% steel (450 HV) in a stream of glass grit

It is possible, however, that at high impact velocity, exponent *m* does not decline; on the contrary, it rises sharply. This may happen to soft steel, when unbreakable spherical cast iron pellets act as erosive particles (Figure 1.19). Microscopic research has shown that with pellets at high impact velocities the target material surrounding the impact crater area will crack and thin out (Figure 2.2e), which evidently facilitates detachment of wear debris from the surface layer under the action of further impacts. It cannot be excluded that material softening caused by local instantaneous high heating will have an important role to play here.

In his research, Uuemõis [16], working on the VK-1, conducted a detailed analysis of the influence of particle shape on the value of exponent *m*, using particles of various origin. The results are shown in Table 1.5.

Table 1.5. Coefficients a and exponents m to determine the weight wear rate I_g (g/kg) for 0.2% C steel (130 HV) at the impact velocity 50–200 m/s

Particles 0.4–0.6 mm	$\alpha = 30^o$		$\alpha = 60^o$		$\alpha = 90^o$	
	a	***m***	***a***	***m***	***a***	***m***
Corundum	0.38×10^{-4}	2.3	1.7×10^{-4}	1.9	0.80×10^{-4}	2.0
Glass grit	2.10×10^{-4}	1.9	1.7×10^{-4}	1.9	1.6×10^{-4}	1.9
Cast iron splinters	0.61×10^{-4}	2.2	0.81×10^{-4}	2.1	0.37×10^{-4}	2.2
Ground quartz sand	0.35×10^{-4}	2.2			0.20×10^{-4}	2.2

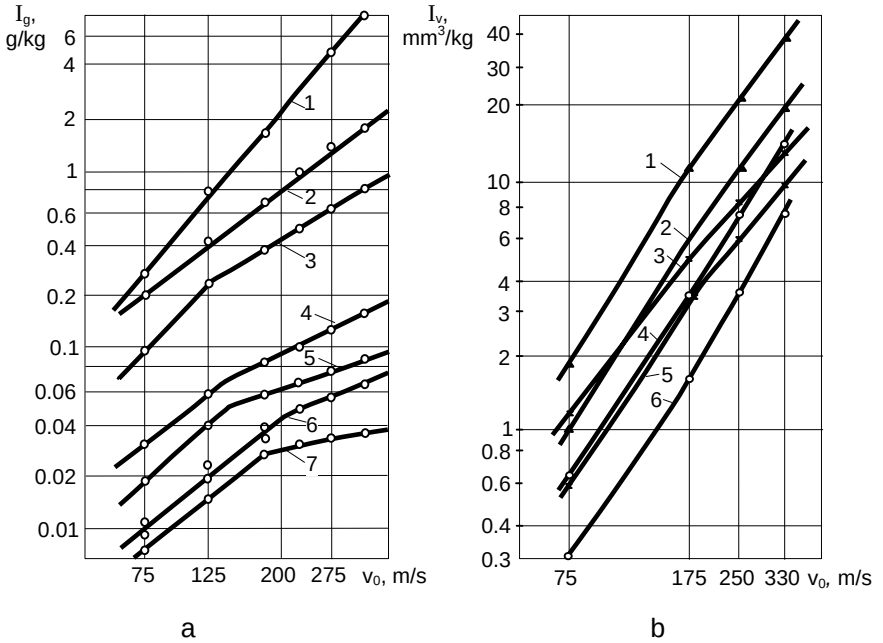

Figure 1.18a,b. Dependence of weight wear rate I_g of hardmetals and steel on impact velocity v_0 in the stream of: **a** – quartz sand from the Männiku quarry (d = 0.4–0.6 mm) at the impact angle $\alpha = 90°$; 1 – 0.2% C steel, 2 – hardmetal WC-20Co, 3 – hardmetal WC-15Co, 4 – coarse grained hardmetal WC-6Co, 5 – hardmetal WC-6Co, 6 – especially fine-grained hardmetal, WC-6Co and 7 – fine-grained hardmetal WC-3Co and **b** – corundum (d = 0.4-0.6 mm); 1 – hardmetal WC-15Co, $\alpha = 90°$, 2 – the same as 1, $\alpha = 30°$, 3 – fine-grained hardmetal WC-3Co, $\alpha = 90°$, 4 – 0.2% C steel, $\alpha = 30°$, 5 – fine-grained hardmetal WC-3Co, $\alpha = 30°$ and 6 – 0.2% C steel, $\alpha = 90°$

Thus, for sharp-edged particles, in most cases, exponent m is smaller than in experiments with natural sands (relatively round in shape). Experiments performed using a centrifugal accelerator on brittle enamel coatings resulted in m ranging from 4–4.5 [11], whereas on a variety of rubbers the latter ranged from 2.7–5.1 [13].

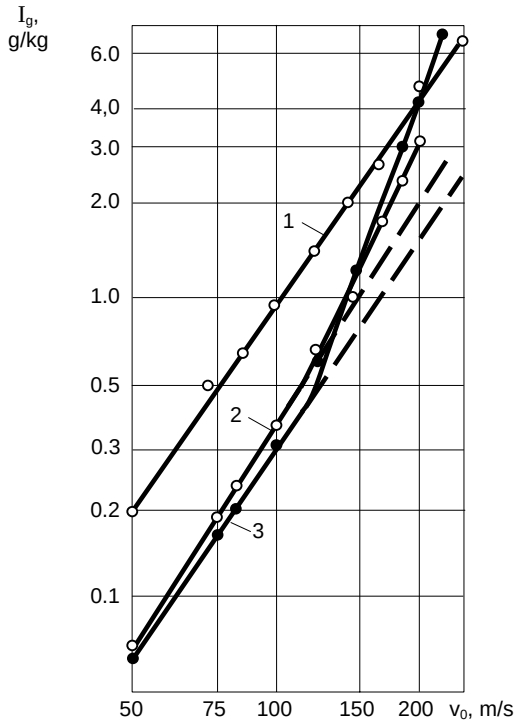

Figure 1.19. Dependence of weight wear rate I_g on impact velocity v_0, 0.2% C steel (130 HV) in a stream of cast iron particles of 0.4–0.6 mm: curve 1 – sharp splinters of cast iron, $\alpha = 90°$; curve 2 – spherical pellets, $\alpha = 30°$; curve 3 – spherical pellets, $\alpha = 90°$

1.3 Dependence of Erosion on Impact Angle

Another parameter influencing the erosion rate is the angle between the velocity vector of particles and the target surface. Although researchers used different types of testing devices, as far as the influence of α is concerned, similar curves with a single maximum were obtained. Curves characterizing steel tested on a vacuum device VK-1 [8] are presented in Figure 1.20.

The graph in Figure 20 shows that wear rate of soft steel reaches its maximum at impact angles ranging from 17° to 45°, that of hardened steels (data from other researchers) from 60°–90°. At a certain impact velocity, the maximum of soft steel is primarily determined by the shape of the particles – the sharper the particles the smaller the impact angle at which the curve reaches its maximum. The shape of the curve is also featured by the ratio between the maximum value of the wear rate and the value at normal impact (α = 90°) – the rounder the particles the flatter the curve. Thus, according to Figure 1.20b, that ratio is 1.9 for sharp cast iron particles, whereas for spherical particles it amounts to 1.4 only. It can be explained, considering the wear, to consist of two components, *i.e.*, resulting from the components of velocity which act across and along the surface. The first to

suggest such an approach were Wellinger and Uetz [7]. It was successfully applied by Bitter [17] and thereafter by Beckmann and Gotzmann in the development of their theory of erosion [18]. Thus, in soft and plastic materials, the role of the cutting component of sharp-edged particles moving along the surface is substantial, whereas for hard and brittle materials, the impact component, which is crosswise to the surface, has the predominant effect. The latter was also proved in the data obtained by Tadolder for pure metals [19]. An extract from the study above is presented in Table 1.6. In addition to the maximum wear rate, the table gives a ratio κ which indicates flatness of the curve and is found as the quotient of maximum wear rate divided by the value of the wear rate at $\alpha = 90°$. Data in the table confirm observations from Figure 1.20 as regards wear rate maximum; however, ratio κ sometimes fails (particularly with Al, Zn, Cd, Cu, and Nb).

The wear rate maximum for brittle non-metallic materials usually occurs at normal impact ($\alpha = 90°$); only in extremely fine-grained abrasive erosion process can it shift toward small angles [20, 21]. A shift in such a maximum was observed for hardened steels as well. Examples of wear curves for brittle materials are shown in Figure 1.21.

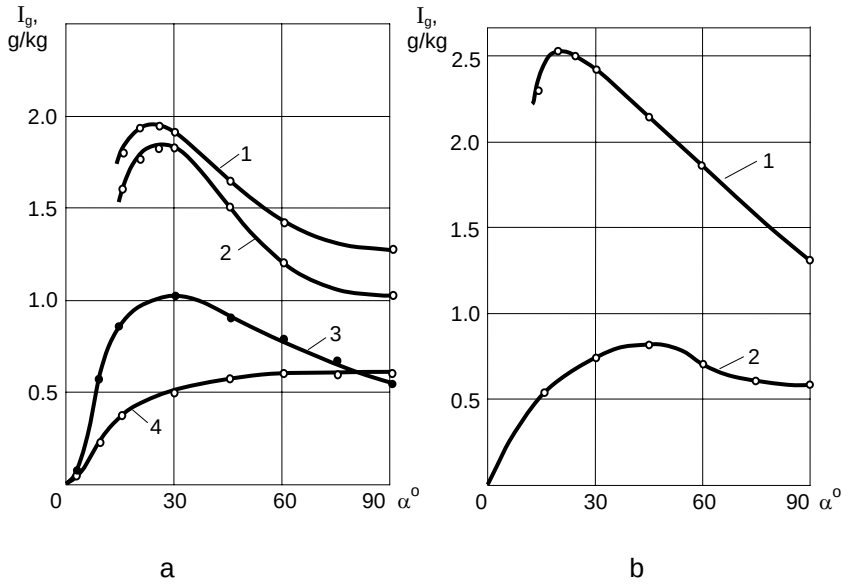

Figure 1.20a,b. Dependence of weight wear rate I_g on impact angle α at the impact velocity of particles v_0 = 120 m/s, the diameter of particles 0.4–0.6 mm: **a** – curve 1 – 0.2% C steel in a stream of glass grit (130 HV), 2 – 0.2% C steel in a stream of corundum (130 HV), 3 – 0.2% C a stream of quartz sand from Männiku quarry , 4 – 0.8% C steel (850 HV) in a stream of quartz sand from the Männiku quarry; **b** – curve 1 – 0.2% C steel in a stream of sharp-edged particles of cast iron, 2 – 0.2% C steel in a stream of cast iron pellets

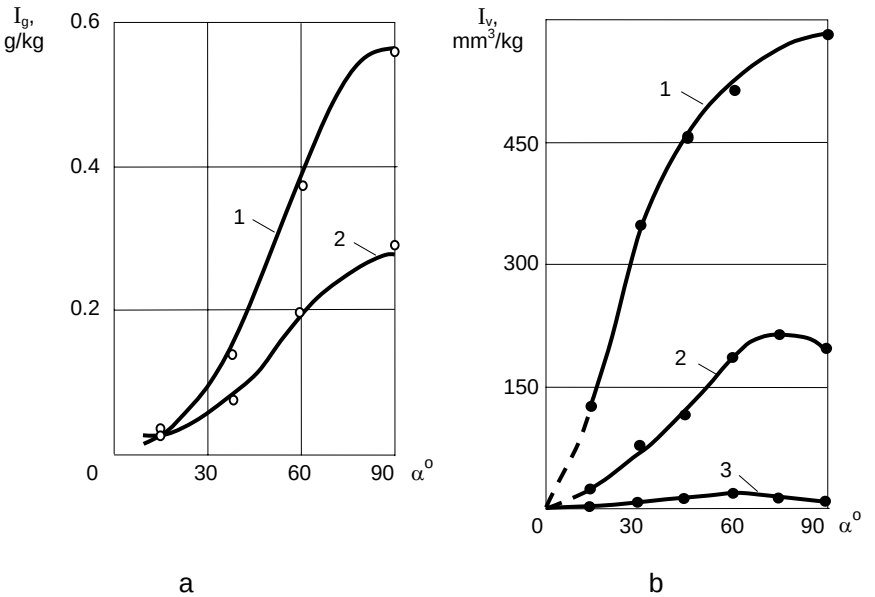

Figure 1.21a,b. Wear curves of brittle materials: **a** – wear of enamel in quartz sand, d = 0.16–0.3 mm, v_0 = 26 m/s [11]; curve 1 – with priming enamel, 2 – enamel R193; **b** – sintered corundum (1750 HV) worn with quartz sand, v_0 = 130 m/s [20]; curve 1 – the mean diameter d_m sand particles 1.0 mm, curve 2 – 0.1 mm and curve 3 – 0.01 mm

Table 1.6. Location of wear rate maximum and ratio κ when using various abrasives at the impact velocity of 80 m/s

Metal	**Pb**	**Sn**	**Cd**	**Al**	**Zn**	**Cu**	**Ni**	**Fe**	**Ti**	**Nb**	**Co**	**Mo**	**W**
HV	4.5	11	20	24	35	86	97	120	160	171	196	248	496
α_{max} quartz sand	20°	50°	20°	20°	45°	30°	40°	40°	60°	45°	75°	50°	75°
Ratio κ	3.5	1.5	3.1	4.1	2.8	2.4	1.8	1.7	1.2	1.7	1.2	1.3	1.04
α_{max} glass grit	20°	40°	15°	20°	20°	20°	30°	30°	40°	40°	60°	30°	75°
Ratio κ	2.3	1.5	2.0	2.7	1.8	1.6	1.5	1.6	1.2	1.4	1.3	1.4	1.4

1.4. Dependence of Erosion on Particle Size

In Sections 1.2 and 1.3, the influence of geometrical shape of particles on erosion rate was reviewed. In addition, however, the size of the particles hitting the target surface has a significant role. To estimate the latter, equal velocity should be granted for the sake of repeatability. The graphs in Figure 1.22a may be lead to erroneous conclusions resulting from the type of the tester [13]. While the results obtained on the vacuum device VK-1 are the most dependable, and those obtained on the accelerator CAK-3m are close to them (and based on the average velocity of particles), the situation is different on a pneumatic device operated at a stable pressure, where higher velocities will be obtained by smaller particles and vice versa. Figure 1.22b demonstrates the initial part of the wear curves, in which their steady rise in the range d_m = 0–0.15 mm [8] can be seen. Analogous results have been reported by other scientists [22]. At the average diameter d_m>0.15 mm, it is difficult to predict the run of the curves without testing. For example, curves of different shape in Figure 1.22c obtained in testing with unbreakable white cast iron

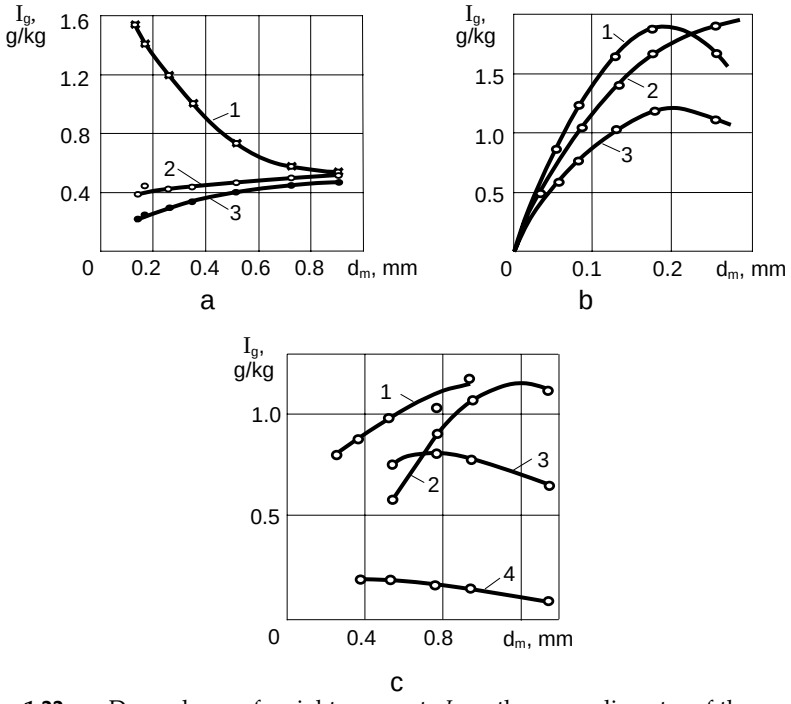

Figure 1.22a–c. Dependence of weight wear rate I_g on the mean diameter of the particles d_m: **a** – experiments with the Männiku sand, 0.2% C steel (130 HV), α = 38°: curve 1 – on a pneumatical test device when the overpressure in front of the nozzle is 0.3 MPa; 2 – on a vacuum tester VK-1, v_0 = 81 m/s, 3 – on a centrifugal accelerator CAK-3m at a mean velocity of particles of 81 m/s; **b** – experiments on vacuum tester VK-1, v_0 = 166 m/s, α = 90°; curve 1 – 0.8% C steel (850 HV) with the Männiku sand, 2 – 0.2% C steel (130 HV) with corundum, 3 – 0.2% C steel with the Männiku sand; **c** – experiments of 0.2% steel (130 HV) test pieces on device VK-1: curve 1 – sharp-edged white cast iron pellets, v_0 = 83 m/s, α = 30°; 2 – spherical white cast iron pellets, v_0 = 120 m/s , α = 90°; 3 – the same as 2, α = 30°; 4 – spherical white cast iron pellets, v_0 = 83 m/s, α = 90°

particles can prove the statements above. On the other hand, the behaviour of experimental curves is quite logical in the case of brittle particles, like sand, glass, and corundum. Namely, starting from a certain threshold velocity, there begins an intensive fragmentation, bringing about a decline in further wear rate by more deficient particles with a larger diameter (Figure 1.22).

In erosion testing of hardened steel with Männiku sand, particles of d_m= 0.16 mm (Figure 1.22b, curve 1) demonstrated the greatest wearing effect. The sharper the decline in the curve the higher the velocity v_0 (Figure 1.23a, curves 1 and 4); at the velocity v_0 = 83 m/s, at which the fracture energy of particles is insignificant, wear rate remains practically the same (curve 6). Wearing an extremely hard metal with corundum (Figure 1.23b), the peak of the curves lies at d_m = 0.35 mm, again with steeper descent of the curve at higher values of v_0. Wearing of 0.2% C steel with glass grit, Uuemõis found the maximum of the curves to be at d_m = 0.4–0.5 mm [16]. Curves 2 and 3 in Figure 1.23a indicate, however, that in case of a relatively soft steel, and after a short decline, a new monotonous rise from d_m = 0.15 mm is possible.

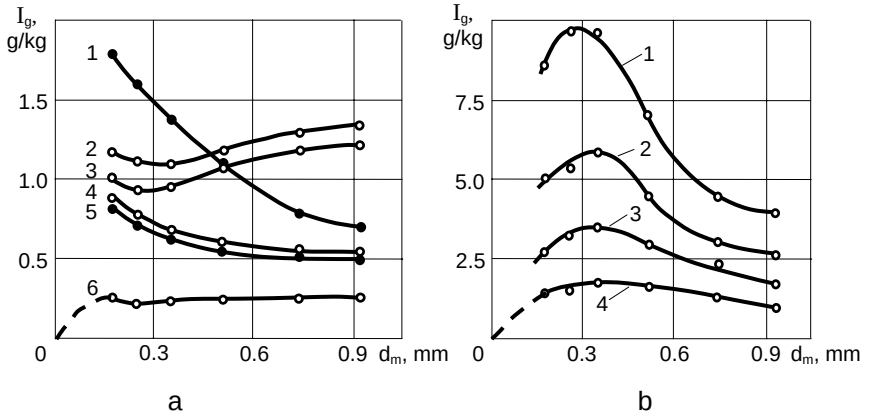

Figure 1.23a,b. Dependence of weight wear rate I_g on the mean diameter of the particles d_m at tests on the vacuum tester VK-1: **a** – tests with the Männiku sand performed on test bodies of various materials; curve 1 – 0.8% C steel (850 HV), v_0 = 166 m/s, α = 90°; 2 – 0.2 % C steel (130 HV), v_0 = 166 m/s , α = 90°; 3 – 0.8% C steel (450 HV), v_0 = 166 m/s, α = 90°; 4 – 0.8% C steel (850 HV), v_0 = 120 m/s, α = 90°; 5 – the same as curve 4, α = 30°; 6 – 0.8% C steel (850 HV), v_0 = 83 m/s, α = 90°; **b** – wear of hardmetal WC-6Co (1600 HV) with particles of corundum, α = 90°; curve 1 – v_0 = 225 m/s, 2 – v_0 = 166 m/s, 3 – v_0 = 120 m/s, 4 – v_0 = 83 m/s

The erosive effect of natural sands is also different owing to their different geometrical shape and defectivity of grains, which also results in curves of various shape in coordinates $I_g = f(d_m)$ [13]. This effect can be established only by experimentally eroding a given material with a certain sand. In terms of the relative wear resistance of the material, the testing conditions should be as similar as possible to those of the component for which the material is to be selected. To illustrate a wrong choice, we provide data in Table 1.7, obtained when testing with Männiku sand of different grain size. It is evident that with d_m<0.5 mm, hardened steel does not have any advantages over soft steel (especially at high impact velocity); the advantage of hardening appears from d_m = 0.7 mm.

Table 1.7. Dependence of relative wear resistance ε of 0.8% C steel (850 HV) on the size of Männiku sand particles d_m and impact velocity v_0; reference material 0.2% C steel (130 HV), $\alpha = 90°$

v_0, m/s	Erosion resistance ε at particle diameters d_m, mm				
	0.2	**0.3**	**0.5**	**0.7**	**0.9**
83	1.0	1.2	1.4	1.4	1.4
166	0.7	0.7	1.0	1.7	1.9

1.5. Influence of Particle Concentration

The term "particle concentration" (also known as "phase density") is very often interpreted as the percentage content by weight or by volume of the particles in a gaseous or fluid medium. Erosion by fluid or gas streams having a small abrasive content is linearly dependent on the abrasive content. With an increasing abrasive content, erosion increases linearly up to a certain point; thereafter a change in the linear dependence is observed. A better and more precise characterization of particle concentration or the surface load due to erosion is the quantity of the abrasive particles hitting a surface unit in a unit of time (g/cm^2·s). Such an evaluation index of particle concentration was adopted by a number of authors [23,24].

An analysis of published approaches shows conflicting opinions concerning the role of particle concentration [23–29]. The fact that a number of authors have observed no influence of particle concentration, or only a negligible influence, may be explained in most cases by the narrow scope of particle concentration studied or by conducting the experiments within the ranges of concentration where the concentration effect is negliglible.

Figure 1.24 shows typical erosion rates *vs* particle concentration and duration of feeding. When experimenting within ranges 1, 3 or 1', 3' even at great variations of particle concentration or duration of feeding (increasing or decreasing), hardly any changes in the erosion rate are experienced. But there are ranges 2, 2' where small variations in particle concentration or, correspondingly, in the duration of feeding, result in relatively great changes of the erosion rate.

In practice, in testing machines and installations, the action of a particle stream on wearing surfaces is either continuous or intermittent. For example, in a centrifugal-type rig (Figure 1.5a), the specimen is subjected to constant action of a particle stream, but with rigs (Figure 1.1c), the action is intermittent. This fact must be taken into account in calculating particle concentration.

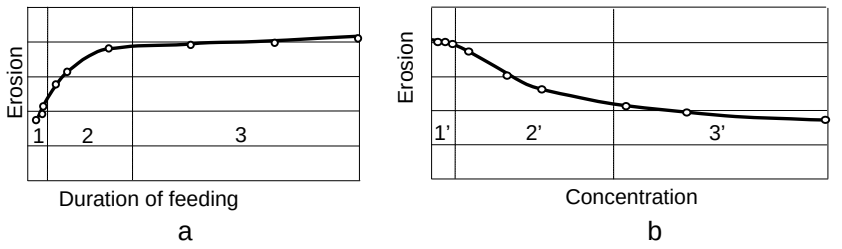

Figure 1.24a,b. Typical erosion rates *vs* duration of feeding (**a**) and particle concentration (**b**)

With constant action, particle concentration can be expressed by the formula

$$\varphi = M/A \cdot t \,, \tag{1.8}$$

where φ – particle concentration, g/cm^2·s,
M – the quantity of abrasive used in the test, g,
A – the area of wear,
t – the duration of feeding, s.

At intermittent action, the calculation of the concentration is most complicated. To compare the results obtained on different testing machines, the value-concentration at one working-cycle, termed as "instant concentration", is used, expressed by the formula

$$\varphi_i = M'/A \cdot t', \tag{1.9}$$

where M' – the quantity of the abrasive hitting the specimen during one cycle, g,
t' – the duration of one working cycle, s.

The effect of particle concentration with particle sizes ranging from 30 to 1000 μm at velocities from 50 to 225 m/s and impact angles 30° to 90° with a great variety of materials have been observed on all the types of testing machines mentioned.

With metals, alloys and ceramics, an increase in concentration leads to a decrease in erosion. The opposite was observed in the behaviour of rubber and some plastics. Rubber specimens showed a rapid increase in wear from a certain critical limit of concentration. Experiments with smaller particle sizes (up to 30 μm), using either a dry abrasive or a mixture of quartz sand and water, have shown that the nature of the erosion of metals, alloys and ceramics remains unchanged, but substantial changes are experienced with rubber specimens. If the erosion rate of rubber specimens at α = 90° and 60° by v_0 = 108 m/s increases rapidly with an increase in particle concentration, then at α = 30° the nature of the erosion of rubber specimens was found to be similar to that of metals, alloys and ceramics. At low velocities (v_0 = 45 m/s), rubber specimens behave similarly to metals and other materials at α = 90° (Figure 1.25c). The effect of particle concentration was also observed in the processes of erosion by abrasive particles in a fluid stream.

On the basis of experimental results it can be concluded that the effect of particle concentration, in general, depends on the following factors [30]:

1. Impact velocity. The effect of particle concentration within the given velocity limits increases. At a velocity of 115 m/s, the influence of concentration is 2.1 times greater than at v_0 = 56 m/s (when varying concentration from 2 to 200 g/cm^{2}s).
2. Impact angle. A certain increase in the concentration effect was observed at greater impact angles.
3. Crushing of the abrasive particles. For example, the effect of particle concentration on the erosion of 0.2% C steel was 1.4 times greater with quartz sand than with cast iron pellets of identical size.
4. Particle size. The effect of changes in particle concentration was greater when smaller particles were used.

Results of the studies have shown (at velocities up to 200 m/s), that erosion is mainly caused by the mechanical action of rebounding particles and their fragments on incident particles. At high particle concentration, before impinging on the specimen, attacking particles have to penetrate a "cloud" of rebounding

particles and fragments, the size and quantities of which may vary within a wide range, depending on the test conditions. The probability of collision between attacking and rebounding particles in such a “cloud” is high, resulting in the retardation of the former. This, in turn, causes not only a loss of velocity, but also changes in the direction of the attacking particles. There is also a probability of the same attacking particles being deviated to such an extent that they cannot impinge on the specimen. During the process of collision between attacking and rebounding particles, disintegration occurs, which can be estimated by changes in granularity.

The dependence of rubber erosion on particle concentration can by explained as follows. The duration of impact and the depth of penetration of the abrasive on rubber surface are much greater than on steel. With high concentrations, a number of particles penetrate deep into the rubber to break down the rubber layer between the embedded particles, before being ejected by the resilience of rubber and further particle penetration.

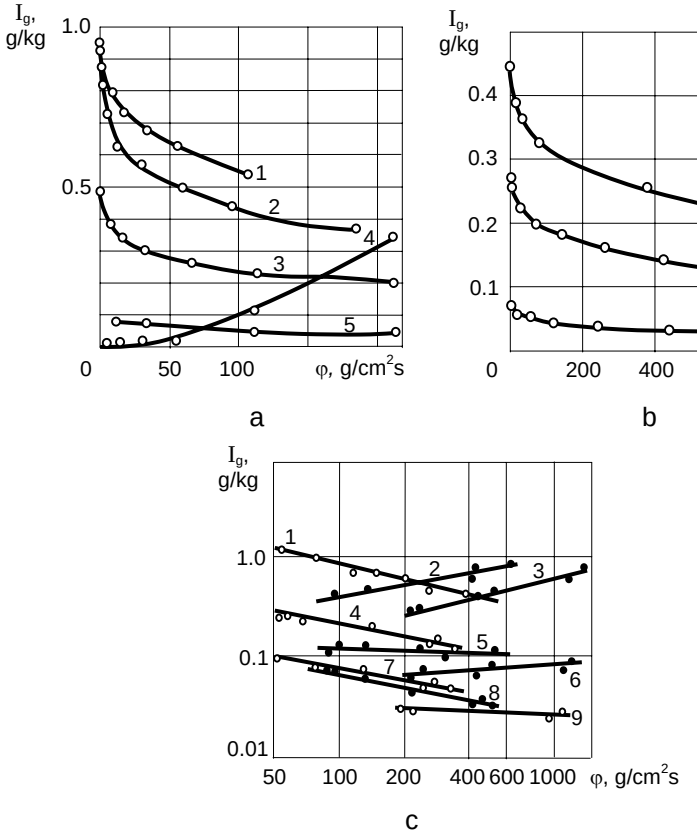

Figure 1.25a–c. Erosion rate I_g *vs* particle concentration φ; graph c – in logarithmic coordinates: **a** – abrasive material – quartz sand 0.4–0.6 mm, v_0 = 115 m/s; 1 – 0.2% C steel, α = 30°; 2 – 0.2% C steel, α = 60°, 3 – 0.2% C steel, α = 90°; 4 – rubber, α = 90°; 5 – hardmetal, α = 90°; **b** – 0.2% C steel, 1 – abrasive material – corundum 0.4–0.6 mm, v_0 = 90 m/s; 2 – abrasive material – quartz sand 0.4–0.6 mm, v_0 = 90 m/s; 3 – abrasive material – quartz sand 0.4–0.6 mm, v_0 = 53 m/s; **c** – rubber, abrasive material – mixture of fine quartz sand <30 μm and water; 1 – α = 30°, v_0 = 108 m/s; 2 – α = 60°, v_0 = 108 m/s; 3 – α = 90°, v_0 = 108 m/s;4 – α = 30°, v_0 = 65 m/s; 5 – α = 60°, v_0 = 65 m/s; 6 – α = 90°, v_0 = 65 m/s; 7 – α = 30°, v_0 = 45 m/s; 8 – α = 60°, v_0 = 45 m/s; 9 – α = 90°, v_0 = 45 m/s

At high particle concentrations and impingement frequencies, the erosion rate of rubber surfaces is high not only because of particle embedding, but also due to the elevated temperature of rubber. The inversion of the relationship $I_g = f(\varphi)$ in the erosion process with fine quartz particles at impact angles approaching 90° may be due to the fact that abrasive particles of small mass (low kinetic energy) will not penetrate into the rubber surface and the wear mechanism is different due to rebounding.

In practice, particle streams of high concentration are formed due to aerodynamic whirling. High concentration of particle stream is attainable, if so desired, for example in grinding machines of appropriate design. In industrial conditions, the positive effect of particle concentration in disintegrators and other impact mills is well studied.

1.6 Effect of Abrasive Mixtures and Liquid Additives on Erosion

1.6.1 Effect of Mixtures of Uniform Granularity

When mixing abrasives of similar granularity, the erosive effect of the separate components of the mixture shall be taken into account, *i.e.* the total wear is determined by the ratio of the particles in the mixture [31]:

$$I_v = I_{v1} \cdot i_1 + I_{v2} \cdot i_2 + \ldots + I_{vn} \cdot i_n, \tag{1.10}$$

where $I_{v1} \ldots I_{vn}$ – wear rates of material in the flow of each component of the mixture (from 1st to n), mm³/kg,

$i_1 \ldots i_n$ – percentage weight of each component in the mixture.

The results of tests with two-component mixtures provide further support for the authentity of Equation 1.10 (Figure 1.26). The mean size of the particles tested on the CAK-3m tester was 0.7 mm. Problems of abrasivity of mixtures have also been dealt with in Section 3.4.4, where Table 3.12 provides data on erosion obtained for a three-component abrasive. It was found that in this case Equation 1.10 also provides real results.

1.6.2 Effect of Fine-grained Solid Additives on Abrasion

Research has proven that Equation 1.10 is not necessarily valid if fine-grained additives [30, 32] softer than the material itself (according to Mohs hardness scale < 3) are added, the hardness of which exceeds that of the target material. Slaked lime has been tested more than other additives (see Table 1.8); however, no plausible theoretical explanation has been found yet. In order to characterize the significance of the effect of the additive, ratio $K_d = I`/I$ was used, where $I`$ is the erosion rate when tested with the additive, and I with a pure abrasive. It follows from Figures 1.27 and 1.28 that the effect of slaked lime content in the abrasive on the erosion rate is most pronounced on ductile low-carbon steel and at greater angles of impact. The ratio K_d also depends on the shape of the abrasive particles. In the case of round particles it is smaller when testing with sharp-edged particles. The effect of additives does not appear in the erosion process of WC-Co type hardmetals. According to research [33], the latter is also true for hardened steels, white cast irons and hard coatings, where Equation 1.10 is valid.

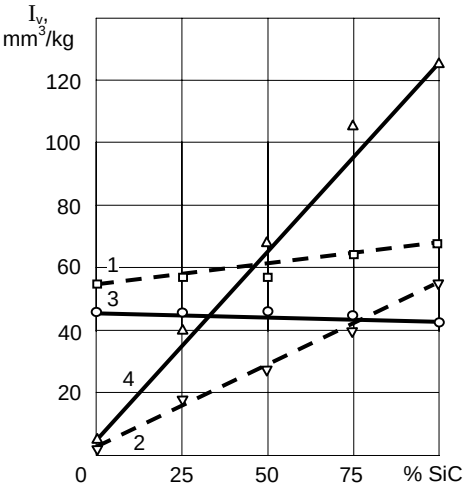

Figure 1.26. Wear rate I_v *vs* SiC content in the mixture of glass grit and SiC at $v_0 = 76$ m/s: 1 – 0.45 % C steel (175 HV) at $\alpha = 15°$, 2 – 0.8 % C steel (910 HV) at $\alpha = 15°$, 3 – 0.45 % C steel (175 HV) at $\alpha = 90°$, 4 – 0.8 % C steel (910 HV) at $\alpha = 90°$

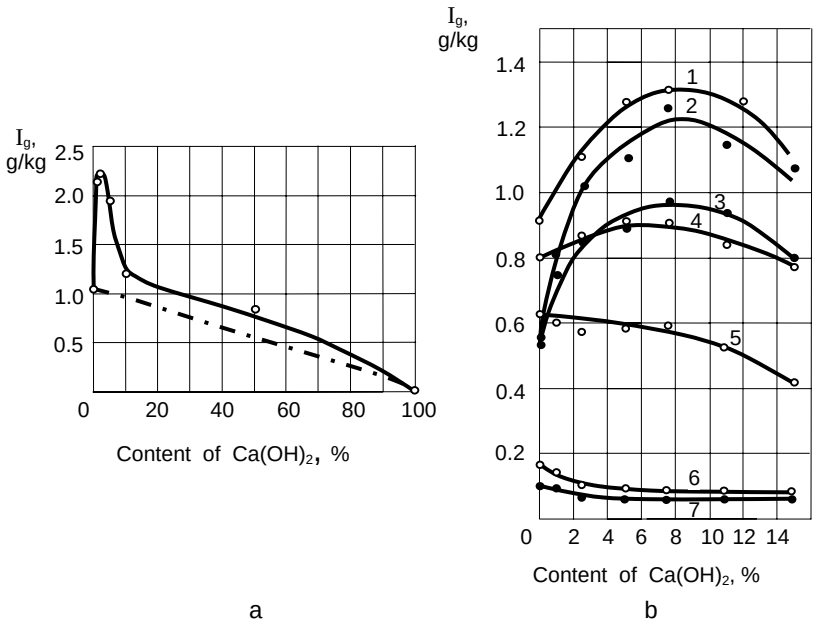

Figure 1.27a,b. Influence of addition of slaked lime on the abrasive qualities of quartz sand from the Männiku quarry: **a** – erosion rate I_g *vs* Ca $(OH)_2$ content in quartz sand 0.3–0.4 mm, testing machine – sandblast rig $p = 0.6$ MPa; **b** – dependence of I_g on the additive when testing on the tester CAK-2, $v_0 = 108$ m/s; 1 – mild steel (130 HV), $\alpha = 30°$; 2 – mild steel, $\alpha = 90°$; 3 – 0.8 % C steel (210 HV), $\alpha = 90°$; 4 – steel (850 HV), $\alpha = 90°$; 5 – 0.8 % C steel (850 HV), $\alpha = 30°$; 6 – hardmetal WC-15Co (1000 HV), $\alpha = 90°$; 7 – hardmetal WC-15Co (1000 HV), $\alpha = 30°$

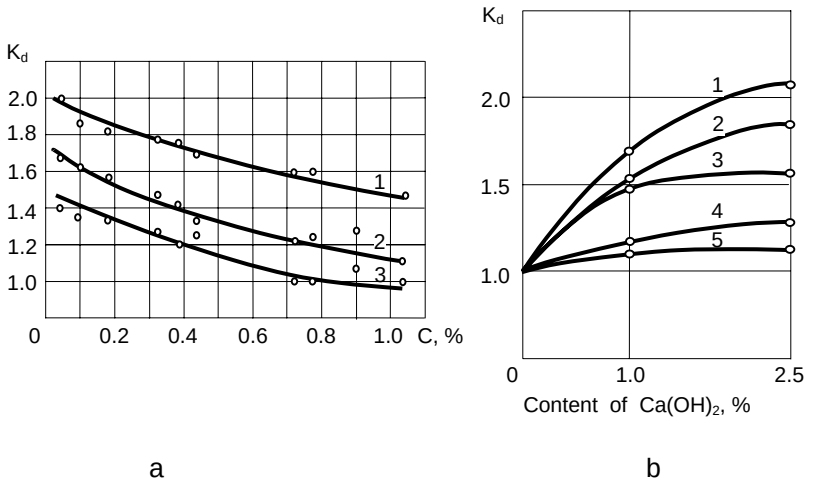

a b

Figure 1.28a,b. Effect of slaked lime as an additive on the erosion rate of steels tested on the centrifugal accelerator CAK-2: **a** – dependence of ratio K_d on the carbon content of carbon steels at tests with quartz sand 0.3–1.0 mm, v_0 = 108 m/s; 1 – α = 90°; 2 – α = 60°; 3 – α = 30°; **b** – dependence of ratio K_d on $Ca(OH)_2$ content in various abrasives; 1 – mild steel (130 HV), in a stream of corundum of 0.4–1.0 mm, α = 90°; 2 – in a stream of quartz sand 0.4–1.0 from the Männiku quarry, 3 – in a stream of cast iron pellets – 0.6–1.0 mm, - α = 90°; 4 – same as 3, α = 30°; 5 – 0.8% C steel (850 HV) in a stream of corundum, α = 90°

Balbat has investigated the effect of lime additive on the erosion of technically pure metals [32]. Their sensitivity to the additive in the abrasive is characterized in Figure 1.29. Its effect on such precious metal as platinum is especially astonishing. Table 1.8 shows the effects of some other fine-grained (d<50 μm) powdered materials on the erosion of 0.2% C steel, when added to quartz sand. Tests were carried out on the machine CAK-2 [13].

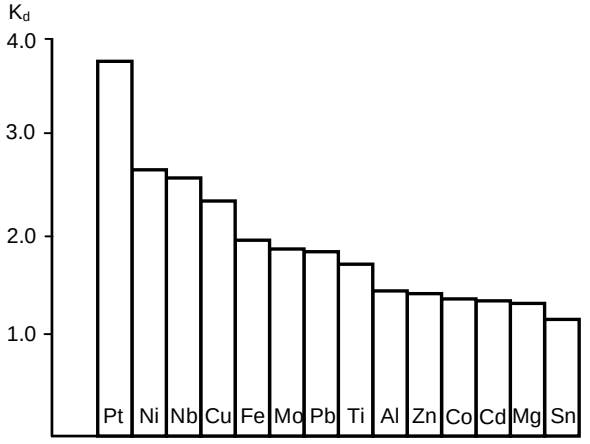

Figure 1.29. Values of K_d of various metals at erosion with the Männiku quartz sand; tests on the tester CAK-2, v_0 = 83 m/s, α = 90°, content of $Ca(OH)_2$ in the abrasive 2.5 %

Table 1.8. Influence of various solid additives on the erosion rate of mild steel (130 HV) in a stream of quartz sand from the Männiku quarry; v_0 = 125 m/s, α = 90°

Type of additive (1.5%)	I_g, mg/kg	K_d
Pure sand	660	1.0
Starch	725	1.1
NaCl	790	1.2
Chalk	790	1.2
Portland cement	795	1.2
Talc	815	1.2
Gypsum ($CaSO_4x2H_2O$)	937	1.4
Lime (CaO)	990	1.5
$MgSO_4$	1020	1.6
Ca $(OH)_2$	1320	2.0
Anhydride of gypsum ($CaCO_4$)	1350	2.0
MgO_2	1520	2.3

1.6.3 Abrasion by Industrial Dusts

The various mixtures above were composed of well studied components. In industry, dusts causing erosion are also, as a rule, mixtures, but it is far more difficult to determine their components. The latter often contain both organic and inorganic components (*e.g.* powdered fuels).

In 1970–1980, in cooperation with power engineers from St. Petersburg (former Leningrad) and metallurgy engineers from Dnepropetrovsk (the Ukraine), research on the abrasion of various industrial dusts in the conditions of exhausters and compressors used in metallurgy was conducted at TUT. Independent of the shape of their rotor vanes (straight or curved), gas-borne particles of dust entering the rotor attack the internal edges of the new vanes at *ca* α = 20°; in the course of the wearing process this angle steadily increases up to 45° [34]. Impinging a few times on the vane (see also Section 1.7), the particles are pressed by the Coriolis force on the rotor vane surface, grazing along until their exit from the rotor. Therefore, the abrasive effect of the particles was investigated – both at impacts at α = 30° and when sliding along the surface (α = 0°), at which the particles are subject to the Coriolis acceleration a_c. To perform the studies above, a centrifugal accelerator was provided with a special rotor (Figure 1.30), which enabled simultaneous determination of abrasion in both conditions. The values of sliding velocities v_1 and the Coriolis acceleration a_c, having effect on the test pieces in the rotor channels were calculated, bearing in mind their central point.

The following equations were used:

$$v_s = \omega\, r \operatorname{ctg} \beta \tag{1.11}$$

$$a_c = 2\omega\, v_s = 2\, \omega^2\, r \operatorname{ctg} \beta, \tag{1.12}$$

where ω – angular velocity,
r – distance of the midpoint from the axis of rotation,
β – fly-off angle (in the given test, the average value was considered to be 55°).

In order to prevent air whirls from changing the trajectories of the fine-grained particles, vacuum was created in the working chamber of the testing machine and the supply bunker of particles.

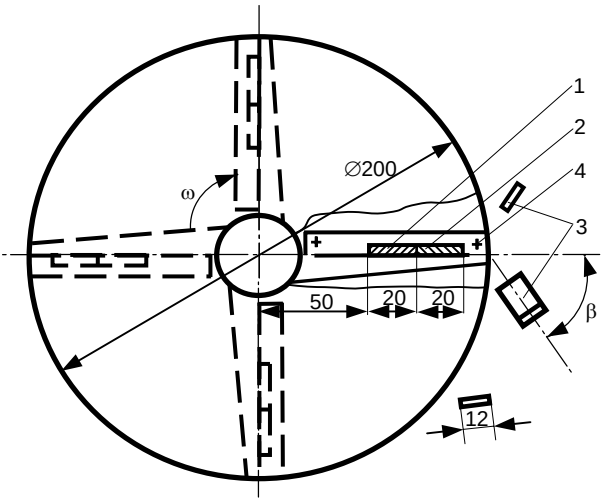

Figure 1.30. Rotor of the testing device: 1 and 2 – test pieces attached to the channels of the rotor, 3 – test pieces attached round the rotor, 4 – wedge-shaped channels

Table 1.9 shows the composition of the dusts studied. Corundum, which is stable in behaviour, has been chosen as the reference abrasive, against which the abrasion of dusts was estimated.

Table 1.9. Composition of dusts, %

No	Organic fraction	Mineral fraction	SiO_2	Fe_2O_3	Al_2O_3	CaO	MgO	K_2O	Na_2O	SO_2
1	1.9	98.1	98.1							
2	12.0	88.0	7.9	57.2	5.8	13.6	1.9	0.2	0.5	0.9
3	0.6	99.4	21.8	4.2	5.1	62.0	4.7	0.9	0.1	0.6
4	41.1	58.9	18.5	2.5	5.4	23.5	2.2	2.5	0.2	4.1
5	51.0	49.0	11.3	2.6	3.4	21.7	3.3	1.2	0.1	5.4
6	10.4	89.6	20.4	5.3	5.6	48.3	4.3	1.8	0.1	3.8
7	38.8	61.2	37.1	3.4	14.3	2.1	1.0	1.6	0.4	1.3
8	23.1	76.9	45.3	4.3	22.2	1.7	0.9	0.4	0.2	0.9
9	68.6	31.4	18.2	2.5	6.1	1.6	0.5	0.1	0.1	2.3
10	66.6	33.4	17.5	4.4	6.8	1.4	0.7	0.1	0.1	2.4
11	9.6	90.4	29.0	4.1	8.2	29.7	3.8	6.4	0.2	9.0
12	–	100			100					

1 – sand from the Privolsk quarry, 2 – dust of agglomeration, 3 – dust of cement clinker, 4 – dust of Estonian oil shale (from electric filter), 5 – the same (from cyclone), 6 – oil shale ash (from cyclone), 7 – ash of Kuznetsk coal, 8 – ash of Ekibastuz coal, 9 – dust of Irsha-Borodin coal, 10 – dust of Ekibastuz coal, 11 – ash of Estonian oil shale (from electric filter), 12 – electrocorundum 220N (GOST 3647-71).

Test results are presented in Table 1.10 and Figure 1.31. Relative abrasivity A_c was defined for erosion at $\alpha = 30°$ $A_c = I_x/I$, in which I_x is the erosion rate caused by the dust studied, and I – wear rate obtained with corundum in the same

conditions. In the case of sliding particles subject to the Coriolis force, the coefficient of abrasivity was expressed as $A_c = I_{cx}/I_c$, in which I_{cx} and I_c are, respectively, wear rates caused by the dust studied and the corundum (the measuring unit is mm³/kg·cm, *i.e*, loss of volume on a 1-cm path per 1 kg of abrasive which slides over the surface). Steel 45 (0.45% C, 175 HV) was chosen as a reference material for the tests. This stable material was used as a standard material in erosion experiments in the former Soviet Union and steel 30ChGS (0.3% C, 1% Cr, 1% Mn, 1% Si, 220 HV), the most widespread grade of steel used for manufacturing fan rotor vanes.

As can been seen from Table 1.10, the indices of relative abrasivity are quite similar because the values of I_{cx} also depend on particle size, their hardness and shape. The sequence of abrasivity, however, can change when changing the angular velocity of the rotor (Figure 1.31) because the indices of the degree of velocity in the relationships $I = a \cdot v_0^m$ and $I_c = b_c \cdot \omega^n$ vary for different types of abrasives. For corundum, $m=n=2.3$, but regarding the bulk of abrasives studied, the velocity exponent is greater, which also explains why their value of relative abrasivity increases along with the growth of rotor velocity (particularly for abrasives 1, 7 and 11). Additional research [35] has shown that by allowing the deviation of ± 15%, Equation 1.11 can be applied to the abrasives dealt with above.

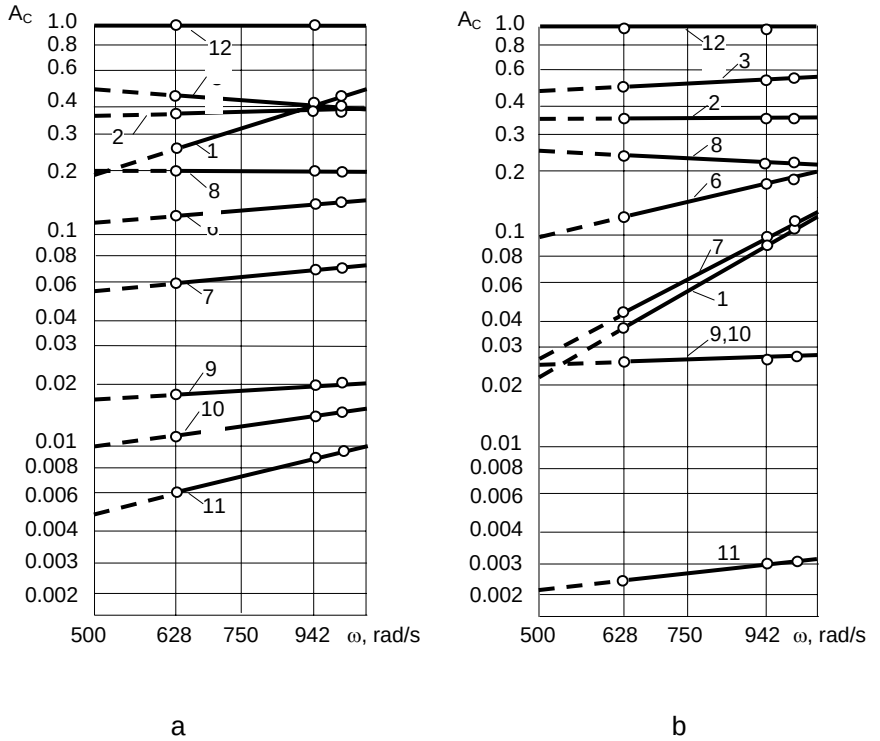

Figure 1.31a,b. Dependence of relative abrasivity of dusts on the angular velocity ω of the rotor: **a** – for erosion at $\alpha = 30°$; **b** – for slide wear, $\alpha = 0°$

Table 1.10. Comparison of erosion rates caused by industrial dusts and coefficients of abrasivity; the angular velocity of the centrifugal accelerator ω = 628 rad/s

No of abrasive	Average particle size, μm	Erosion rate, mg/kg and coefficient of abrasivity			
		Erosion at α = 30°, v_0 = 75 m/s		Erosion at α = 0°, a_c = 33,170 m/s^2, v_s = 26 m/s	
		Steel 45	Steel 30ChGS	Steel 45	Steel 30ChGS
1	600	16.5/0.24	17.3/0.26	0.16/0.04	0.16/0.04
2	285	25.0/0.36	26.6/0.40	1.50/0.38	1.69/0.44
3	450	28.9/0.42	30.4/0.46	2.12/0.53	1.96/0.51
4	26	0.18/0.0026	0.20/0.003	0.008/0.002	0.011/0.0029
5	44	0.76/0.011	1.28/0.019	0.045/0.011	0.056/0.015
6	95	8.41/0.12	8.95/0.13	0.53/0.13	0.55/0.14
7	69	3.86/0.06	3.90/0.06	0.18/0.045	0.15/0.039
8	530	13.0/0.19	12.8/0.19	1.02/0.26	0.85/0.22
9	100	1.18/0.017	1.16/0.017	0.114/0.029	0.110/0.029
10	480	0.75/0.011	0.82/0.012	0.114/0.029	0.090/0.023
11	26	0.39/0.0056	0.44/0.0066	0.010/0.0025	0.012/0.0031
12	200	69.1/1.0	66.8/1.0	3.97/1.0	3.84/1.0

Note: wear rate I_g is above the fraction line and coefficient of abrasivity A_c below it.

1.6.4 Effect of Liquid Additives

The liquid that most frequently contributes to erosion is water. For example, water content in natural sand mined from a quarry is 3–7%, depending on the season. Therefore, in our experiments with quartz sand, as a rule, water was removed by heating. The effect of liquids was studied by Balbat and Üksti at TUT [32, 36, 37]. In that study, the abrasive was first dried, then a desirable amount of water was added. Tests were performed on a centrifugal accelerator. Liquids were added only to the extent that no excess water would appear and that the type of erosion under investigation would not become hydroabrasive erosion. The effect of adding water is described below. As can been seen from the results shown in Figure 1.32, adding 1% of water abruptly increases the erosion rate of mild carbon steel. The maximum of all curves was reached in the region of *ca* 8% of moisture. The effect of the added water grows with the increase of impact angle. Table 1.11 reviews the effect of water content on the erosion of harder materials.

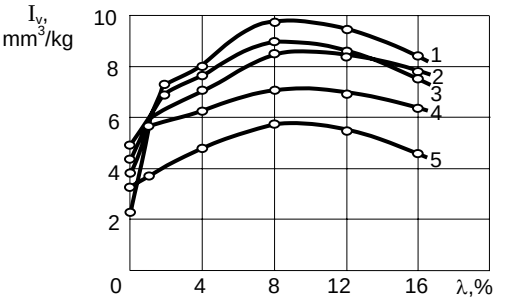

Figure 1.32. Effect of the amount of added water λ on the erosion rate of mild steel (130 HV) in a stream of sand from Privolski quarry, v_0 = 38 m/s, if 1 – α = 60°; 2 – α = 90°; 3 – α = 45°; 4 – α = 30°; 5 – α = 20° [36]

Table 1.11. Factor K_d, characterizing the dependence of erosion rate, on water content in the quartz sand from the Männiku quarry

Material	v_0 m/s	α^0	I_y mm³/kg dry sand	K_d, with water content				
				4%	8%	12%	15%	18%
0.2% C steel (130 HV)	40	45	12.2	1.4	1.4	1.3	1.1	1.1
0.45% C steel (710 HV)			8.4	1.1	1.3	1.2	1.0	1.0
White cast iron (510 HV)			8.7	1.5	1.4	1.2	1.1	1.0
Hardmetal WC-8 Co (1360 HV)			0.7	2.3	2.1	2.1	2.1	2.0
0.2% C steel (130 HV)	80	90	6.3	1.9	2.3	2.4	1.9	1.7
0.45% C steel (710 HV)			8.0	1.2	1.4	1.4	1.2	1.1
White cast iron (510 HV)			7.3	1.4	1.4	1.5	1.4	1.3
Hardmetal WC-8 Co (1380 HV)			0.8	1.4	2.2	2.4	1.8	1.6
0.2% C steel (130 HV)	40	45	63.1	1.2	1.3	1.3	1.4	1.3
0.45% C steel (710 HV)			46.6	1.1	1.2	1.2	1.2	1.1
White cast iron (510 HV)			47.1	1.2	1.2	1.3	1.3	1.2
Hardmetal WC-8 Co (1360 HV)			3.0	1.5	1.5	1.5	1.5	1.5
0.2% C steel (130 HV)	80	90	29.9	2.0	2.2	2.4	2.4	2.1
0.45% C steel (710 HV)			44.9	1.2	1.4	1.4	1.4	1.3
White cast iron (510 HV)			49.2	1.2	1.3	1.4	1.4	1.3
Hardmetal WC-8 Co (1360 HV)			2.5	1.2	1.2	1.1	1.6	1.7

Note: K_d is the ratio between wear rates caused by moistened and dry sands

Material tests shown in Table 1.11 indicate that the values of K_d change with a change of impact velocity, which is particularly obvious in testing of hardmetal. The water content corresponding to the wear maximum may vary as well.

Materials resistant to corrosion were also studied (Figure 1.33). As compared to ordinary carbon steel, a considerably lower increase in the wear effect was observed, implying the influence of corrosion on the erosion processes.

The increase in the wear rate, however, cannot be explained by the side-effect of corrosion. For instance, moistening of the abrasive with a non-corrosive liquid (*e.g.* kerosene) will considerably increase the wear rate (see Figure 1.34). Adding water to an abrasive sharply increases the wear rate of non-metallic materials as well [32], illustrated in Figure 1.35. Erosion is evidently influenced by the parallel effect of several physical and chemical processes, which require further investigation. There is no doubt that the molecular-mechanical effect, or the so-called Rehbinder effect, caused by surface active agents, such as kerosene and butyl alcohol, is one of them (Figure 1.34). The larger the impact angle, the more considerable is the effect.

As the research described above was initiated primarily to satisfy the needs of the Estonian peat briquette plants, the influence on the erosion of organic acids contained in peat was also dealt with [36,37]. The latter include acetic acid, oxalic acid and propanoic acid. In briquette manufacture, damp peat first passes through a long pipeline, which consists of drying drums, cyclones and pneumatic pipes of

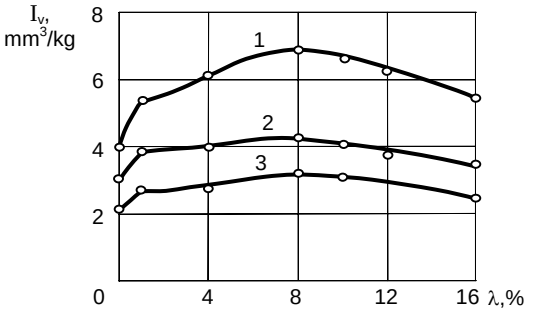

Figure 1.33. Dependence of erosion rate I_v on the amount of added water λ in the quartz sand from Privolski quarry; $\alpha = 30°$, $v_0 = 38$ m/s: 1 – steel 0.2% C (130 HV), 2 – steel 0.1% C, 17% Cr, 0.6% Ti (160 HV), 3 – steel 0.7% C, 18% Ni, 9 % Cr, 0.5% Ti (150 HV)

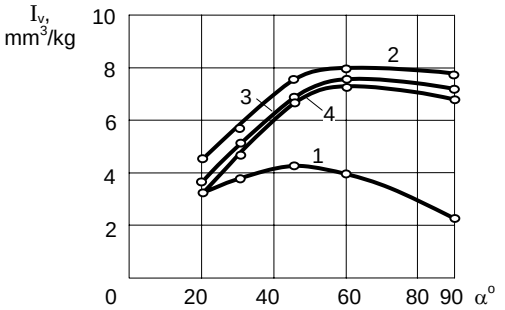

Figure 1.34. Dependence of wear rate I_v of mild steel on the impact angle α in the stream of sand from the Privolski quarry, $v_0 = 38$ m/s: 1 – dried sand, 2 – 8% water additive, 3 – 8% kerosene additive, 4 – when adding 8% of 4% water solution of C_4H_9OH to sand

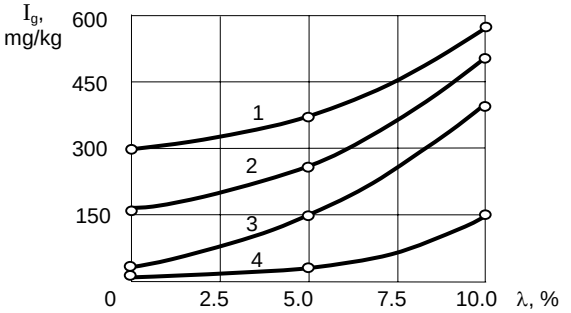

Figure 1.35. Dependence of wear rate I_g of rubber on percentage content of water λ in sand from the Männiku quarry; $v_0 = 108$ m/s. 1 – $\alpha = 15°$, 2 – $\alpha = 30°$, 3 – $\alpha = 60°$, 4 – $\alpha = 90°$

huge diameter. Although the organic part of peat is non-abrasive, depending on the deposit, it contains a mineral substance causing erosion (see also Section 5.4). The highest temperature +80 °C along that line occurs in the drier. Therefore, in the studies of relative wear resistance ε of steels resistant to corrosion in relation to mild carbon steel, Üksti also varied the temperature of the test pieces (see Table 1.12). It can be concluded from the data that relative erosion resistance and effect of application of special steels rises along with the temperature rise.

Table 1.12. Relative erosion resistance ε in the tests on moistened sand from the Privolski quarry; $v_0 = 38$ m/s, $\alpha = 30°$, $\lambda = 8\%$, 0.2% C steel as reference material

Moistening environment	*pH*	Temperature, °C	Relative wear resistance ε	
			08Ch17T	12Ch18N10T
Tap water	7	20	1.4	2.0
		60	2.3	3.1
		80	2.4	3.4
2% acetic acid	3.1	20	1.7	2.9
		60	3.2	3.9
		80	3.7	5.6
Water infusion of peat from Oru deposit	4.6	20	1.5	2.0
		60	2.0	2.7
		80	2.1	3.0

1.7 Influence of Temperature on Erosion

It was Suur who carried out thorough research into the influence of temperature on erosion by help of a special pneumatic device. A detailed description can be found in the report [6]. The design of the testing facility is shown in Figure 1.36.

The facility allows for preheating both the particles and the gas, accelerating the particles (air or argon), abrasive particles (quartz sand from the Privolski and Männiku quarries), and the test piece. A 4 mm plate-shaped test piece with a wearable surface of 20×20 mm was supplied by a transformer which produced low-voltage current (up to 1200A), passing through the whole of the test piece. There was an aperture in the test piece with a thermojunction attached to it, and the surfaces of the test piece (except for the wearable surface) were plated with chromium in order to avoid oxidization. To maintain a stable temperature, a special automatic device was inserted in the chain to supply electricity to the test piece. An electric preheating oven with heating spirals was designed. The bunker for particle preheating contained electrically heated inclined plates, providing for sand slide in a thin layer. Table 1.13 shows the chemical composition of the materials tested by Suur.

Suur's studies focused on the changes in the erosive wear at temperatures typical of power engineering and chemical plant equipment, at the same time modifying other parameters of erosion.

It should be emphasized that in the initial phase, wear rate was not constant (Figure 1.37) and the test pieces needed wearing in.

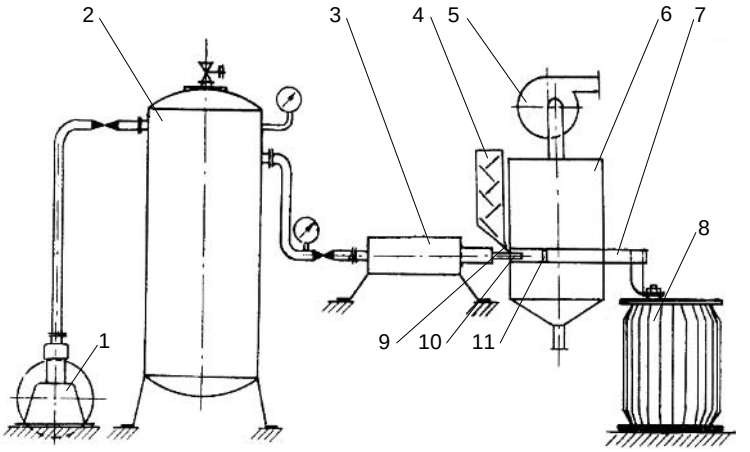

Figure 1.36. Facility for erosion testing at elevated temperatures: 1 – compressor, 2 – receiver for granting stable pressure, 3 – electrical oven for heating gas, 4 – bunker-oven for heating abrasive particles, 5 – fan; 6 – storage bunker, 7 – copper rods conducting electricity, 8 – transformer, 9 – device for supplying the nozzle with particles, 10 – nozzle, 11 – test piece

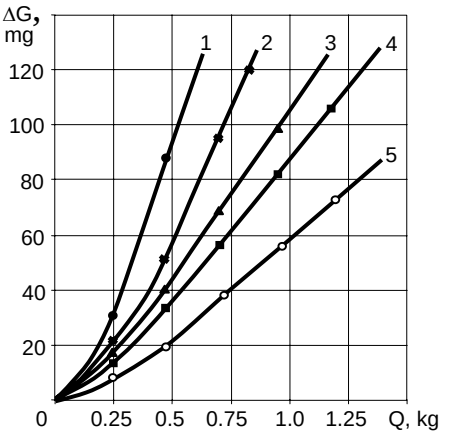

Figure 1.37. Dependence of weight loss ΔG on the amount of quartz sand attacking the test piece, $v_0 = 48$m/s, $\alpha = 90°$, particle size of sand 0.4–0.6 mm: 1 – steel St3, 2 – steel 45, 3 – U10A, 4 – R9, 5 – cast iron Ch34L

In Suur's studies of the dependence between the wear rate and temperature, five materials were used (Figure 1.38). The curves illustrate that up to 400–450 °C, the wear rate barely shows a change, or it even decreases (particularly true for carbon steel and at the attack angle of 90°). Alloy cast iron Ch34L retains stable intensity at almost up to 500 °C. Except for the latter material, a sharp rise begins from 450 °C. According to Suur, such a material behaviour is related to the influence of oxide films emerging on the surface during the wearing process. The rise in temperature is accompanied by a rapid growth of the film and, owing to the hardness of the exterior layer Fe_2O_3 (*ca* 1140 HV), the latter acts as a protective layer at temperatures up to 450 °C. Beyond 570 °C, the film consists of three

layers, out of which FeO – the only one of them combining immediately with the parent metal – is the weakest, and so is its connection with the metal. That causes a steep rise in the erosion rate, especially if all the indices of hardness of the steels themselves fall at temperatures considerably higher than 450 °C. A comparison test with argon (Figure 1.39) adequately illustrates the importance of the role of oxidizing processes: as high as 450 °C, erosion is more intensive, being accelerated by a stream of argon, and later on accelerated by a stream of air. According to the data presented in [39], the erosion rate of magnesium alloy also remains stable in the environment of argon up to 500 °C, whereas in the air it keeps growing 3.5 times as fast compared with the processes at room temperatures.

Table 1.13. Chemical composition of the materials tested

Material symbols (Russian standard)	Mean of constituent elements, wt%								
	C	Si	Mn	Cr	Ni	Ti	V	W	Mo
Steel St3	0.2	~0.2	~0.5						
Steel 45	0.45	0.25	0.6	<0.25	<0.25				
Steel U8A	0.8	0.2	0.2	<0.15					
Steel U10A	1.0	0.2	0.2	<0.15					
Steel 9Ch	0.9	1.4	0.5	1.0					
Steel 1Ch13	<0.15	<0.6	<0.6	13	<0.6				
Steel Ch17	<0.12	<0.18	<0.7	17	<0.6				
Steel R9	0.9			4			2.3	9	<0.3
Steel R18	0.75			4			1.2	18	<0.3
Steel 1Ch18N9T	<0.12	<0.3	<2.0	18	9	0.8			
Steel 5ChV2S	0.5	0.6	0.3	1.2				2.2	
Steel Ch12F1	1.3	<0.4	<0.25	12			0.8		
Cast iron Ch34L	2.0	1.5	0.7	34					

If at T = 500 °C, high speed steel R9 at low impact angles is more resistant to erosion than cast iron Ch34L, then at T = 700 °C, the resistance of erosion of cast iron substantially exceeds that of steel R9. The relative erosion resistance of steel 45, however, remains practically constant within the limits of ε = 1.1–1.2.

Suur determined the relative erosion resistance ε of all the materials in four regimes. His test results are presented in Table 1.14.

Suur studied the influence of particle velocity for three materials (Table 1.15), the velocity ranging from 48 to 70 m/s. The velocities were determined at high speed filming (see Figure 1.10). As can be seen from Table 1.15, the values of the velocity exponent are considerably higher than at room temperature. In his tests, Raask recorded 2.5 as the exponent for carbon steel at 400 °C [38]. The Czech research scientists detected an increase in m not only for steels but also for alloys based on Co, Ni and Mg [39].

The influence of the impact angle was tested on four materials, both at room temperature and in two high-temperature conditions. It was concluded that the maximum wear rate, which for steels is at approximately 30° at room temperature, shifts to *ca* 45° at high temperatures, while in the case of cast iron, it retains its position at *ca* 45°. It is easier to follow the results obtained in the axis $\varepsilon = f(\alpha)$, taking steel St3 as a reference material (Figure 1.40).

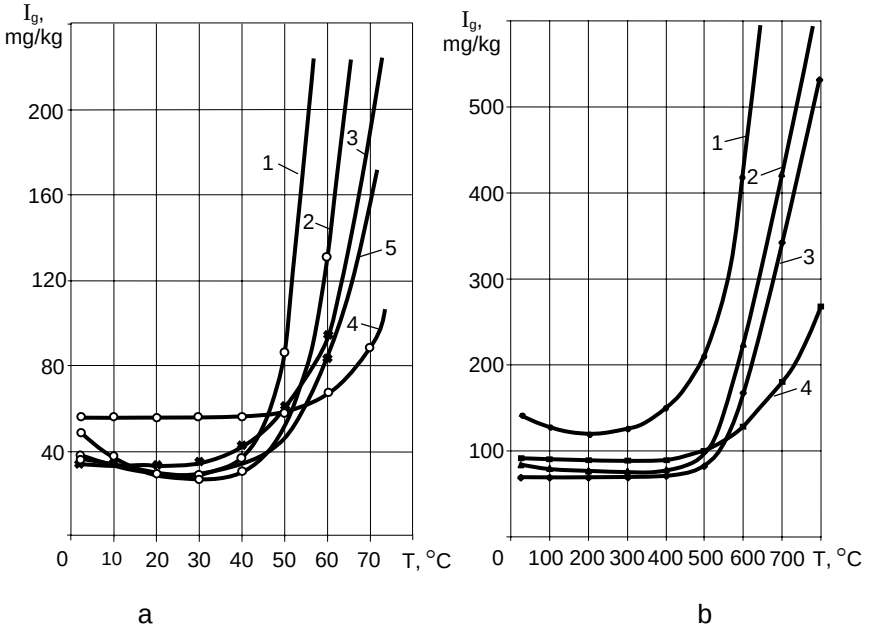

Figure. 1.38a,b. Dependence of wear rate I_g on temperature T for impact angle 45° (**a**) and for impact angle 90° (**b**), v_0 = 48 m/s, quartz sand 0.4–0.6 mm: 1 – steel St3, 2 – steel U8A, 3 – steel R9, 4 – cast iron Ch34L, 5 – steel 9ChS

Table 1.14. Relative volume erosion resistance ε of materials in a stream of 0.4–0.6 mm quartz sand in relation to reference material – steel St3 at the mean velocity of particles 56 m/s

Material	Hardness[a] HV	Relative erosion resistance ε at			
		20°C, α = 90°	600°C, α = 90°	600°C, α = 45°	700°C, α = 90°
45	185	1.1	1.2	1.3	1.4
U8A	190	1.2	2.1	1.6	2.0
U10A	197	1.2	2.5	1.8	2.4
9ChS	210	1.2	3.4	2.3	3.4
5ChV2S	230	1.3	3.6	2.1	3.1
1Ch13	160	1.1	3.6	2.1	3.1
Ch12F1	240	1.2	3.9	2.5	4.1
Ch17	160	1.1	4.2	2.4	4.6
R9	240	1.3	3.5	2.5	3.7
R18	230	1.4	3.9	2.6	4.9
1Ch18N9T	160	0.9	4.5	2.5	5.3
Ch34L	290	0.9	4.1	2.5	5.5

[a] Mean hardness at room temperature

Table 1.15. Velocity exponent m at 500 °C, fraction of sand – 0.4–0.6 mm

Material	Impact angle	
	α = 30°	α = 90°
R9	2.6	2.6
5ChF2S	3.0	3.5
Ch34L	2.5	3.2

One of the phenomena accompanying erosion is the formation of ripples on the wearing surface at angles of medium size (30–65°). In his work [40], Suur studied the mechanism of the emergence of ripples and the prerequisites of their development. It was concluded that directed plastic deformation caused by the impact of these particles plays a major role in this process. Independently of him, the same conclusions were made by Ratner and Zelensky in [41], as the latter observed erosion in boiler tubes and gas turbines working on solid fuel.

First, Suur found out that ripple formation initiates an early plastic state of the material. It is illustrated in Figure 1.41. The process starts before the impact velocity increases. In addition, the height and regular pitch of the ripples also depend on the fraction of the abrasive – these parameters keep growing as the impact velocity increases. In due course of the process, some of the ripples are destroyed, *i.e.* the ridge length and the height will increase. The ripple front is crosswise to the projection of the velocity vector, and so is the surface of the ripples in relation to the direction of the velocity vector (Figure 1.42b). The latter also accounts for the fact that the erosion rate diminishes as soon as the ripples have developed. Figure 1.42a shows a typical eroded surface with surface ripples.

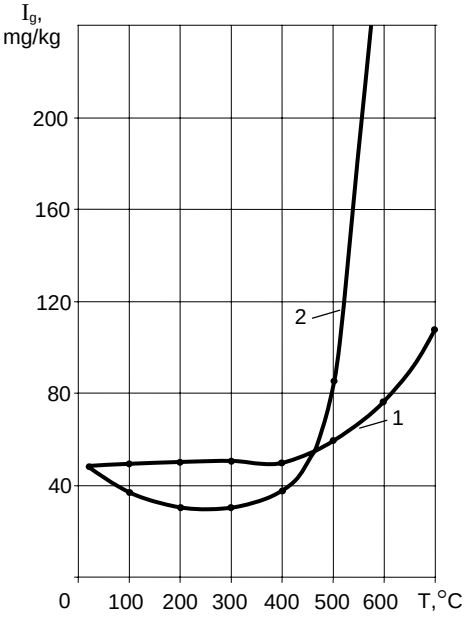

Figure 1.39. Dependence of wear rate I_g on temperature T, v_0 = 48 m/s, sand 0.4–0.8 mm: 1 – on accelerating the particles with argon, 2 – on accelerating particles with air

Further research ino the influence of low temperature on erosion dates back to 1969 [42]. A centrifugtal accelerator CAK-1 was used, fitted with special test piece holders (Figure 1.43). Liquid nitrogen poured into them enabled us to reduce the temperature of the test piece down to –160 °C. In order to make tests at minus temperatures lower than that, cardboard connective pieces of various thicknesses were used to separate the test piece from nitrogen (pos. 12).

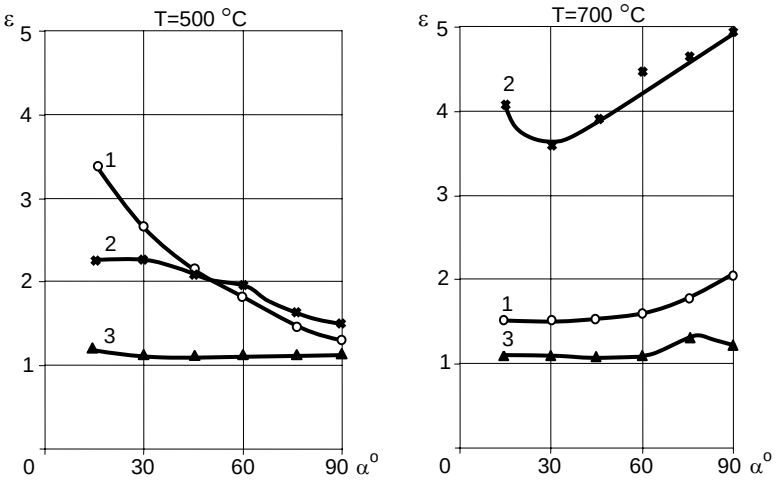

Figure 1.40. Dependence of relative wear resistance ε on impact angle α, v_0 = 48 m/s, sand 0.6–1.0 mm: 1 – steel R9, 2 – cast iron Ch34L, 3 – steel 45

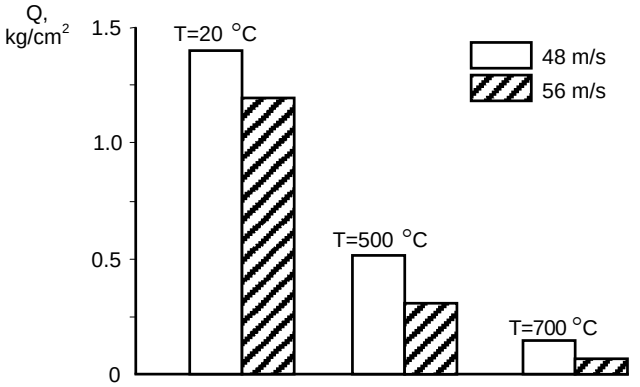

Figure 1.41. Amount of sand Q of fraction 0.6–1.0 mm necessary for emergence of wavy surface on a steel St3 test piece at various impact velocities, α = 45°

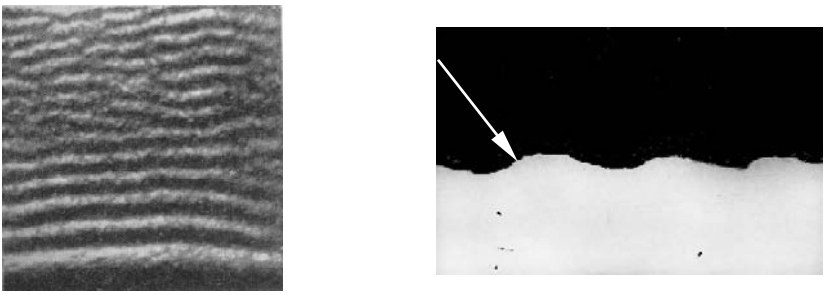

a b

Figure 1.42a,b. Surface ripples on test piece from steel St3 formed at erosion by 0.6–1.0 mm sand, T = 600 °C, v_0 = 48 m/s, α = 45°: **a** – top view x 2.5, **b** – cross-section of the test piece x12

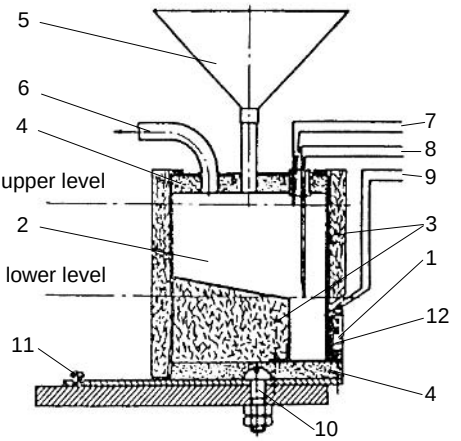

Figure 1.43. Test piece holder for tests at low temperatures: 1 – test piece, 2 – receiver for liquid nitrogen, 3 – thermal insulation, 4 – felt bottom, 5 – abradant hopper, 6 – exit pipe for nitrogen steam, 7 and 8 – thermocouples for fixing maximum and minimum levels of nitrogen, 9 – thermocouples for measuring the temperature of the test piece, 10 and 11 – fastening screws, 12 – intermediate piece from cardboard

Mild steel St3, subject to cold brittleness, copper M3, not subject to brittleness, and hypoeutectic white cast iron as a representative of a brittle material, were selected for the study. As an abrasive, fractionated quartz sand from the Privolski and Männiku quarries were used. A selection of the wear curves obtained is presented in Figures 1.44 and 1.45.

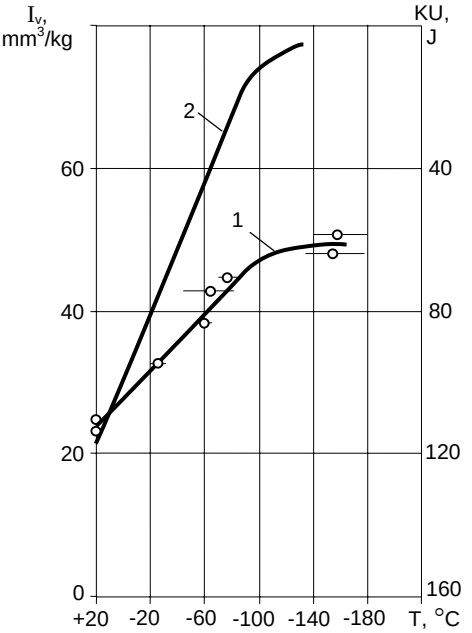

Figure 1.44. Dependence of wear rate I_v on temperature: curve 1, if α = 90°, v_0 = 82 m/s and erosive particles – quartz sand 1.0–1.2 mm; curve 2 corresponds to impact toughness *KU* of steel St3

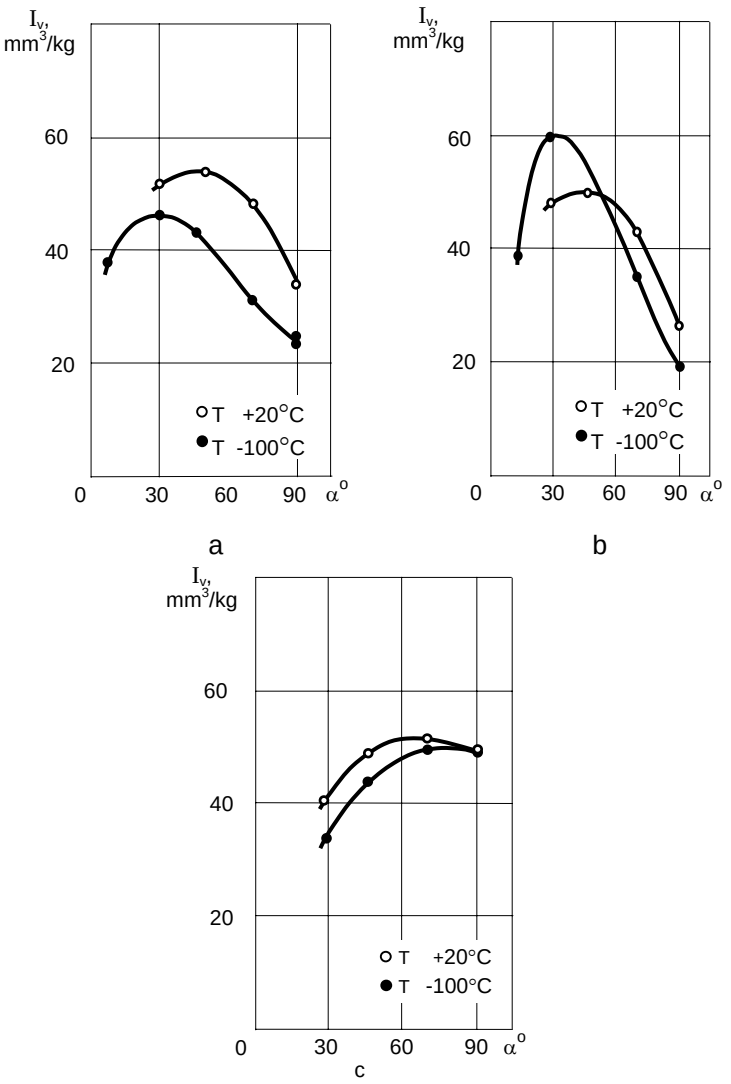

Figure 1.45a–c. Dependence of wear rate I_v on the impact angle α at velocity v_0 = 82 m/s: **a** – steel St3, sand from the Männiku quarry 1.0–1.2 mm, **b** – copper M3, sand from the Privolski quarry 0.5–0.9 mm, **c** – non-alloy hypoeutectic cast iron, sand from the Privolski quarry 0.5–0.9 mm

When the impact angle is 90°, the wear rate of steel St3 grows parallel to the curve of impact hardness linearly until the temperature drops to –100 °C; thereafter, the decline diminishes (Figure 1.44). In the axis $I_v = f(\alpha)$, the wear maximum of steel and copper shifts to ~45°. Tests in the velocity range of 28–82 m/s showed that velocity exponent m increases as the temperature falls, it is particularly true for copper (at –120 °C and if α = 30°, m =3.6). Table 1.16 reviews the behaviour of steel St3 in various test conditions.

Table 1.16. Data characterizing wear of steel St3 performed on sand from the Männiku quarry

Fraction of sand, mm	v_o, m/s	Temperature, °C	Exponent m	I_v, mm³/kg
0.3–0.4	72	+20	2.3	16.7
		–140	2.6	20.5
1.0–1.2	82	+20	2.3	23.0
		–150	2.6	47.5

1.8 Erosion of Surface by Grazing Particles

The subtype of erosion at which particles slide along the wearing surface occurs on rotor vanes of turbomachinery and fans. Although the impact angle in this case equals zero, particles are pressed against the surface by the Coriolis force. The value of the latter may prove to be rather high. For example, for a sand particle of 1 mm diameter it is 0.035 N, assuming that the rotation velocity of the rotor is 1500 rpm and the radius of the rotor 750 mm. In other words, the Coriolis force acting on the grain of sand exceeds that of gravity by 2600 times, and at n = 3000 rpm, already approximately 1000 times. The laws of such an erosion were studied on a centrifugal accelerator, using the rotor scheme [43, 44] in Figure 1.6b.

Wear rate I_c was expressed as a weight loss per 1 kg of abrasive passing through the rotor channel and per 1 cm length of channel (units mg/kg·cm). Fitting the test points into a logarithmic graph (Figure 1.46), the latter locate themselves on straight lines. Therefore, the formula describing the wear rate is expressed as follows:

$$I_c = b_c \omega^u = B_c n^u, \tag{1.13}$$

where B_c and b_c are the coefficients depending on the properties of material and abrasive,

ω – angular velocity of rotor, rad/s,
n – rotation speed of rotor, rpm,
u – for the exponent.

As can be seen in Figure 1.46, exponent u depends on both the properties of the material and the abrasive, being close to the exponent found for the so-called regular erosion. Out of these materials, the least affected by changes in the speed of rotation of the rotator, is WC-Co type hardmetal. Changing the speed of rotation at a certain point on the rotor vane (in the given case on the channel), the sliding velocity of the particle v_R changes simultaneously with the Coriolis acceleration a_c. In order to find out which parameter is more important, a series of special tests were performed, in which the angular velocity of the rotor and the distance from the rotation axis were varied. The latter allowed us to plot graphs in which at one and the same constant sliding velocity – the Coriolis acceleration alternates and so does the normal force, and in the other case, on the contrary – at constant Coriolis acceleration, the velocity of the particle changes. Typical results are represented in Figures 1.47–1.49.

It can be concluded from the data above that the wear rate is influenced by the Coriolis acceleration to a greater extent than by particle velocity. At small values of a_c, the effect of velocity is negligible. As a result of tests on hardmetal WC-3Co, it was found that the same is true for high values of a_c, which is also confirmed by the low value of exponent u in Equation 1.14. It can be concluded from the data above that the wear rate is influenced by the Coriolis acceleration to a greater extent than by particle velocity. At small values of a_c, the effect of velocity is negligible. As a result of tests on hardmetal WC-3Co, it was found that the same is true for high values of a_c, which is also confirmed by the low value of exponent u in Equation 1.14.

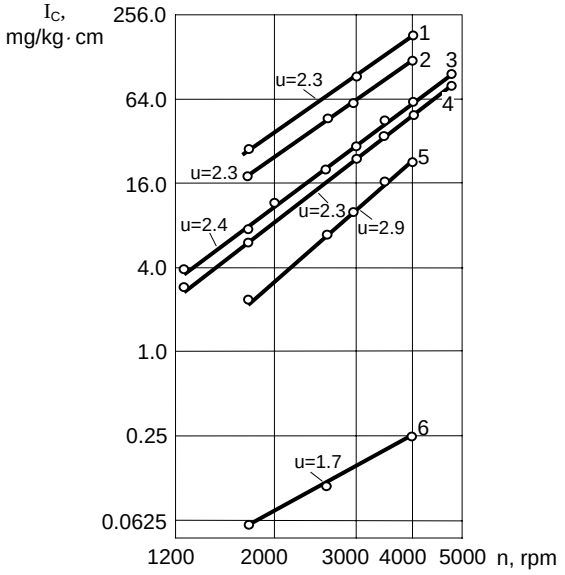

Figure 1.46. Dependence of wear rate I_c on the rotation speed of the rotor n, distance between the center of the test piece and the axis of rotation of the rotor x = 264 mm: 1 – steel St3, glass grit 0.6–1.0 mm; 2 – the same, corundum 0.6–1.0 mm; 3 – the same, cast iron pellets 0.9 mm; 4 – the same, the Männiku quartz sand 0.2–0.3 mm; 5 – hardened steel U8A (850 HV), Männiku quartz sand 0.2–0.3 mm, 850 HV, 6 – hardmetal WC-3Co, quartz sand from Männiku < 1.0 mm

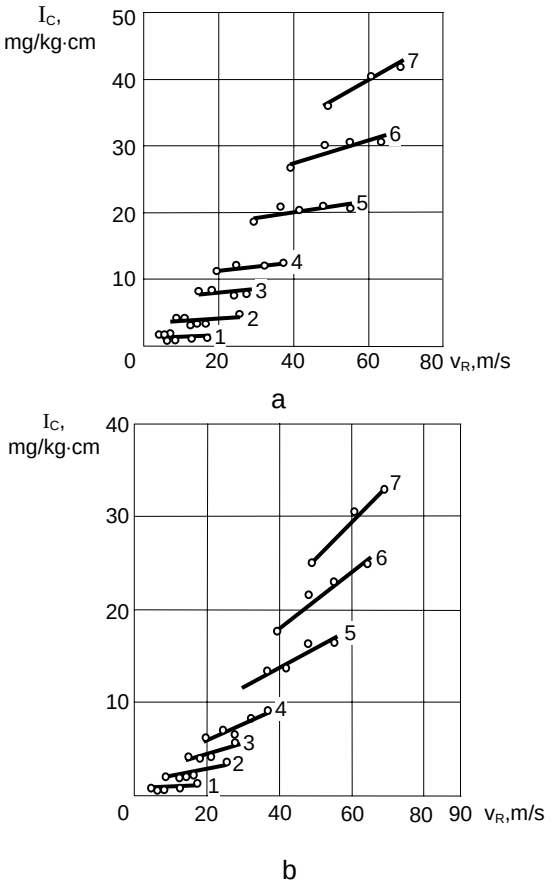

Figure 1.47a,b. Dependence of wear rate I_c on particle velocity v_R in rotor channel at varying values of Coriolis acceleration a_c (m/s²): 1 – a_c = 4500, 2 – a_c = 9000, 3 – a_c = 15000, 4 – a_c = 20000, 5 – a_c = 30000, 6 – a_c = 40000, 7 – a_c = 50000; the abrasive used – quartz sand from the Männiku quarry 0.2–0.3 mm; material of test pieces steel St3 (130 HV) (**a**), test pieces from steel U8A (850 HV) (**b**)

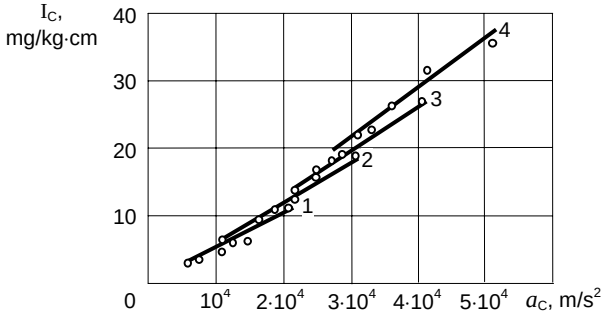

Figure 1.48. Dependence of wear rate I_c on Coriolis acceleration a_c at varying slide velocities of particles v_R (m/s) in the rotor channel; the material of test pieces – steel St3, Männiku quartz sand 0.2–0.3 mm as the abrasive: 1 – v_R = 20 m/s, 2 – v_R = 30 m/s, 3 – v_R = 40 m/s; 4 – v_R = 50 m/s

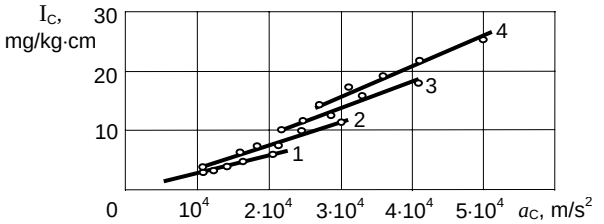

Figure 1.49. The same as Figure 1.48, if the test pieces are made from steel U8A (850 HV)

1.9 References

1. Olesevich KV. Wear of Gas Turbine Elements. Moscow: Mashgiz, 1959 (in Russian).
2. Wahl H, and Maier E. Untersuchungen über den Verschleiss von Blasversatzhrohren und -krümmern. Essen: Verlag Glückauf GmbH 1952.
3. Hint J. Disintegrator Method for Silicate and Silicalcite Product Technology. Tallinn: 1952 (in Estonian).
4. Kleis I. Analysis of the schemes of the experimental equipment used for study of erosion. Proc Techn Univ Tallinn 1965;219:17–26 (in Russian).
5. Kleis I. The device for erosion testing. Proc Techn Univ Tallinn 1958;152:1–19 (in Russian).
6. Suur U. Device for erosion study at elevated temperatures. Proc Techn Univ Tallinn 1962;192:51–67 (in Russian).
7. Wellinger K, and Uetz H. Gleitverschleiss, Spülverschleiss, Strahlverschleiss unter der Wirkungkörniger Stoffen. VDI-Forschungseft 449, Ausgabe B, Band 21, 1955.
8. Kleis I. Probleme der Bestimmung des Strahlverschleisses bei Metallen. Wear 1969; 13:199–215.
9. Tadolder J. The rules of wear of technically pure metals. Proc Techn Univ Tallinn 1966;237:3–13 (in Russian).
10. Arumäe H. Erosion of plastics. Proc Techn Univ Tallinn 1966;237:89–102 (in Russian).
11. Lepikson H, and Kleis I. Erosion of enamelled boliers. Proc Techn Univ Tallinn 1962;192:3–19 (in Russian).
12. Langeberg I. Study of Abrasive Erosion at Small Angles of Attack. PhD Thesis. Tallinn 1968 (in Russian).
13. Kleis I, and Uuemõis H. Wear Resistance of Grinding Equipment Operating on Impact. Moscow: Mashinostroenie Publishers, 1986 (in Russian).
14. Reiners E. Der Mechanismus der Peallzerkleinerung beim geraden, zentralen Stoss und die Anwendung dieser Beanspruchungsart bei der Zerkleinerung, insbesondere bei der Zerkleinerung von spröden Stoffen. Forshungsberichte Des Landes Nordrhein-Westfahlen n.1059, 1962.
15. Tiidemann T, Uuemõis H, and Kleis I. A study of erosion at higher impact velocities. Proc Techn Univ Tallinn 1973;347:29–38 (in Russian).
16. Uuemõis H. Study of Some Laws Concerning Erosion. PhD Thesis. Tallinn 1967 (in Russian).

17. Bitter JGA. A study of erosion phenomena: Part 1. Wear 1963;6:5–21.
18. Beckmann G, and Gotzmann J. Analytical model of the blast wear intensity of metals baed on a general arrangement for abrasive wear. Wear 1981;73:325–53.
19. Tadolder J. Erosion of Technically Pure Metals. PhD Thesis. Tallinn 1966 (in Estonian).
20. Uetz H. Die wichtigste Ergebnisse von Strahlverchleissuntersuchungen in der MPA Stuttgart. Proc Techn Univ Tallinn 1973;347: 3–22 (in Russian).
21. Sheldon GL, and Finnie IJ. On the ductile behavior of nominaly brittle materials during erosive cutting. Eng Ind Trans ASME 1966;88:387–92.
22. Uetz H, and Gross KJ. Strahlverschleiss in: Abrasion und Erosion. Carl Hanser Verlag 1986;236–78.
23. Uuemõis H, and Kleis I. The influence of abrasive concentration on erosion rate. Proc Inst Autoclaved Silicate Concrete. Tallinn 1967;1:92–114 (in Russian).
24. Tilly GP, and Sage W. The interaction of particle and material behavior in erosive process. Wear 1970;16:447–65.
25. Finnie I. Some observations on the erosion of ductile materials. Wear 1972;19:81–90.
26. Neilson IH, and Gilchirst N. Erosion by a stream of solid particles. Wear 1968;11:111–22.
27. Wood CD, and Espenschade PW. Mechanismus of dust erosion. Preprint N880 ASAE. Summer Meeting. New York 1964.
28. Kaschejev VN, and Glazkov VM. Wear in the stream of moving particles. Wear Testing Methods. Proc USSR Acad Sci Moscow 1962;24–31 (in Russian).
29. Antonov AA. The methods of erosion testing and results of steels and cast irons. Proc Gubkin Inst Oil and Gas Industry. Moscow 1961;34:79–95.
30. Uuemõis H, and Kleis I. A critical analysis of erosion problems which have been little studied. Wear 1975;31:359–71.
31. Mägi R. Development of Methods for Determination of Dusts Passing Rotors of Turbomachines. PhD Thesis. Tallinn 1982 (in Russian).
32. Balbat A. Methods and Results of Determination of Abrasivity of Fine-Grained Materials. PhD Thesis. Tallinn 1980 (in Russian).
33. Kleis I, and Pappel T. About the erosive wear resistance of some alloyed steels. Proc Techn Univ Tallinn 1973;347:23–28 (in Russian).
34. Kleis I, Tadolder J, and Mägi R. The abrasivity of industrial dusts at the wear of rotors of centrifugal turbomachines. Energomashinostroenie 1983;N9:32–34 (in Russian).
35. Kleis I, Tadolder J, and Mägi R. Influence of dust abrasivity to wear of centrifugal turbomachines. Proc of the I Polzunov Inst of Research and Design of Power Engineering Equipment. Leningrad 1986;227:14–20 (in Russian).
36. Üksti L. Study of the Effect of Liquid Environment on Metal Erosion. PhD Thesis. Tallinn 1983 (in Russian).
37. Üksti L, and Kleis I. An experimental investigation into erosion of metals by moistened abrasive stream. Proc Techn Univ Tallinn 1973;347:39–47 (in Russian).
38. Raask E. Tube erosion by ash impact. Wear 1969;13:301–15.

39. Hoch P, and Burda P.The erosive and corrosive wear of the details energetic equipment. Strojirenstvi 1963;2:121–29 (in Czech).
40. Suur U. Metal Erosion at Elevated Temperatures. PhD Thesis. Tallinn 1967 (in Estonian).
41. Ratner AV, and Zelensky VG. Erosion of Materials Used in Thermal Power Engineering. Moscow: Energetika Publishers, 1966 (in Russian).
42. Lepikson H, and Siimpoeg R. Method and some results of testing metals for erosive action of sand stream at low temperatures. Proc Techn Univ Tallinn 1969;271:31–39 (in Russian).
43. Kleis I, Lugus J, and Uuemõis H. The study of wear process of the rotor channels of centrifugal impact mill. Proc Inst Autoclaved Silicate Concrete. Tallinn 1974;8:139–48 (in Russian).
44. Lugus J. Study of Rules Concerning Wear of Rotors of Centrifugal Mills. PhD Thesis. Tallinn 1975 (in Russian).

2

Research into the Physical Mechanism of Erosion

Studies of processes occurring between the particles and target surface involved the following problems:

1) Macro- and microgeometry of a wearing surface;
2) Stress distribution and structural changes in the target surface layer;
3) Fragmentation of abrasive particles and adhesion of the latter to the surface.

2.1 Changes in the Macro- and Microgeometry of a Wearing Surface

In the process of erosion, changes take place both in the micro- and macrogeometry of a wearing part. From the examples given in Figure 2.1, it is obvious that these changes are also accompanied by changes in the parameters of wear (especially the impact angle). The surface is subject to gradual formation of ripples as described in Section 1.7 above.

Changes occurring in the microgeometry caused by particle impacts have been studied in relation to explaining the physical mechanism of erosion. Depending on the impact angle, properties of the material and particle shape, impact scars appearing in the surface were found to vary in shape as well. Several authors have analyzed traces of impact emerging on the previously polished – and sometimes subsequently etched – metal bodies. Those studies were carried out throughout the 1960s and 1970s [1–5].Typical impact craters brought about by normal impact (α = 90°) are shown in Figure 2.2.

Figure 2.2a,c shows the emergence of block-shaped formations around the impact crater brought about by shearing deformations of cobalt, whereas the trace of impact on the surface of brittle tungsten is surrounded by radial cracks (Figure 2.2b). At a moderate impact velocity (v_0 = 50 m/s), the trace in the surface of plastic steel – with its clear-cut outline – resembles the indentation typical for Brinell hardness test (Figure 2.2d); the impact crater obtained at high velocity (Figure 2.2e), however, is surrounded by a ridge of sparse metal which consists of the material squeezed out as a result of shear strain.

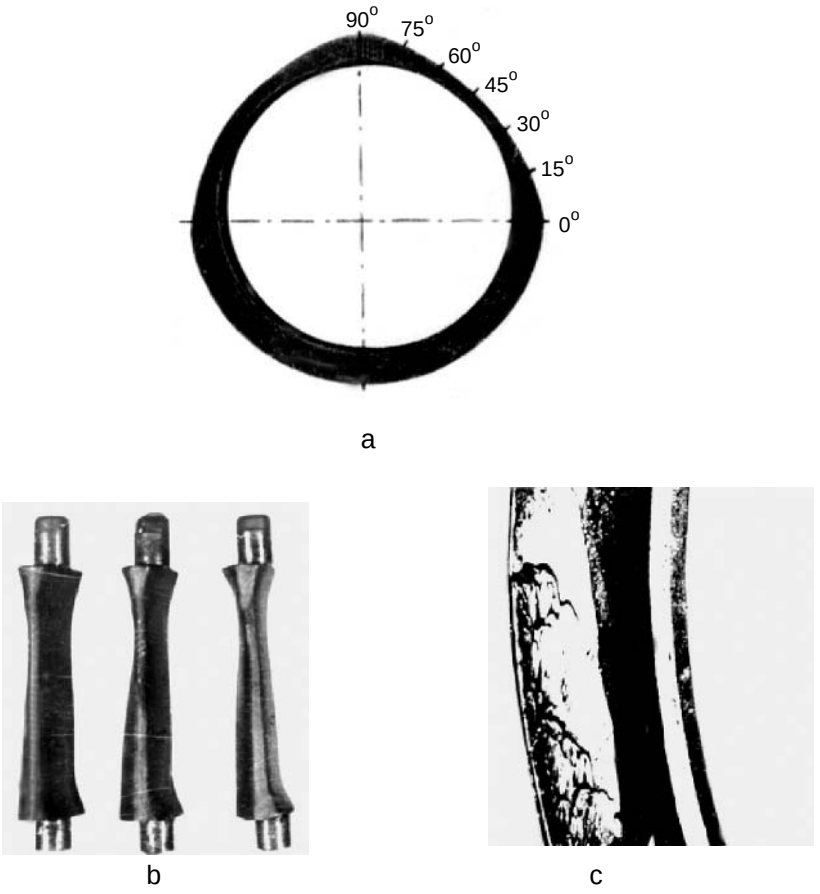

Figure 2.1a–c. Examples of changes in the macrogeometry of the component: **a** – cross-section the boiler tube, subject to fly ash erosion; **b** – gradual changes in the shape of cylindrical disintegrator pin used for grinding sand-lime mixture; **c** – surface ripples emerging in the pipe elbow used for pneumotransport (upward stream direction)

Figure 2.3 shows impact traces if $\alpha < 90°$. In this case, the material excluded from the impact trace is submitted to directed shear strain. Depending on the value of α, particle size and its position at the moment of hitting the surface, the shape of the trace can vary. Thus, the material squeezed out from the crater may become pressed to the front and the sides of the impact scar (Figure 2.3b), or form a lip the front of it (Figure 2.3d,f), without any material removal from the surface. Alternatively, the particle may remove the whole volume of material out of the crater at the first impact already (Figure 2.3a,c). Systematic research with analogous results has also been carried out by scientists from Cambridge University [6, 7].

As far as ductile materials are concerned, wear rate in the initial stage of the process is generally lower than in permanent conditions, because only a little piece of crater volume material is removed. In order to study the ratio between the

volume of impact craters and the material removed, single craters in the polished surfaces of test pieces were studied by means of a measuring microscope and profilometer [2]. Using the symbols in Figure 2.4, Table 2.1 presents the results obtained at low impact angles.

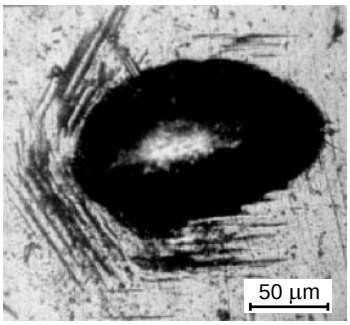

a

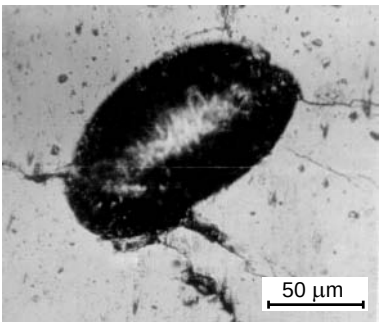

b

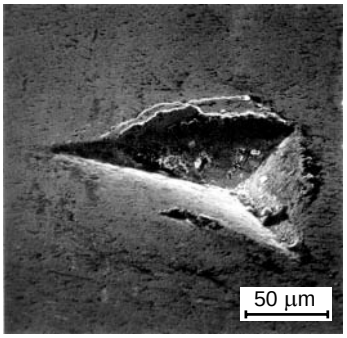

c

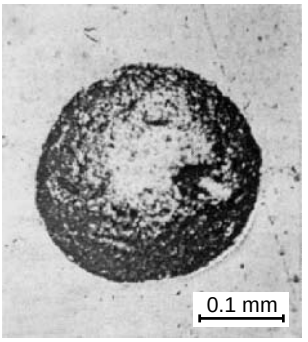

d

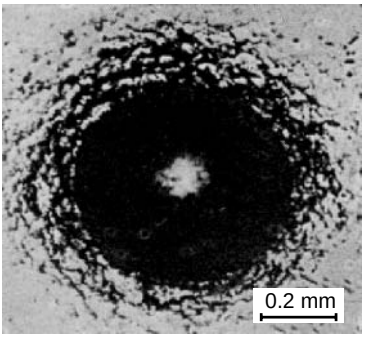

e

Figure 2.2a–e. Impact craters produced by particles hitting the metal surface at $\alpha = 90^{\circ}$: **a** – impact of particles of sand of 0.4–0.6 mm on a cobalt target, $v_0 = 80$ m/s; **b** – the same as "a" but on a tungsten surface; **c** – impact of 0.6–0.8 mm particle on a WC-6Co hardmetal surface, $v_0 = 225$ m/s; **d** – impact crater produced by a 0.9 mm spherical cast iron pellet on the 0.2% C steel target surface, $v_0 = 50$ m/s; **e** – the same as "d", $v_0 = 225$ m/s

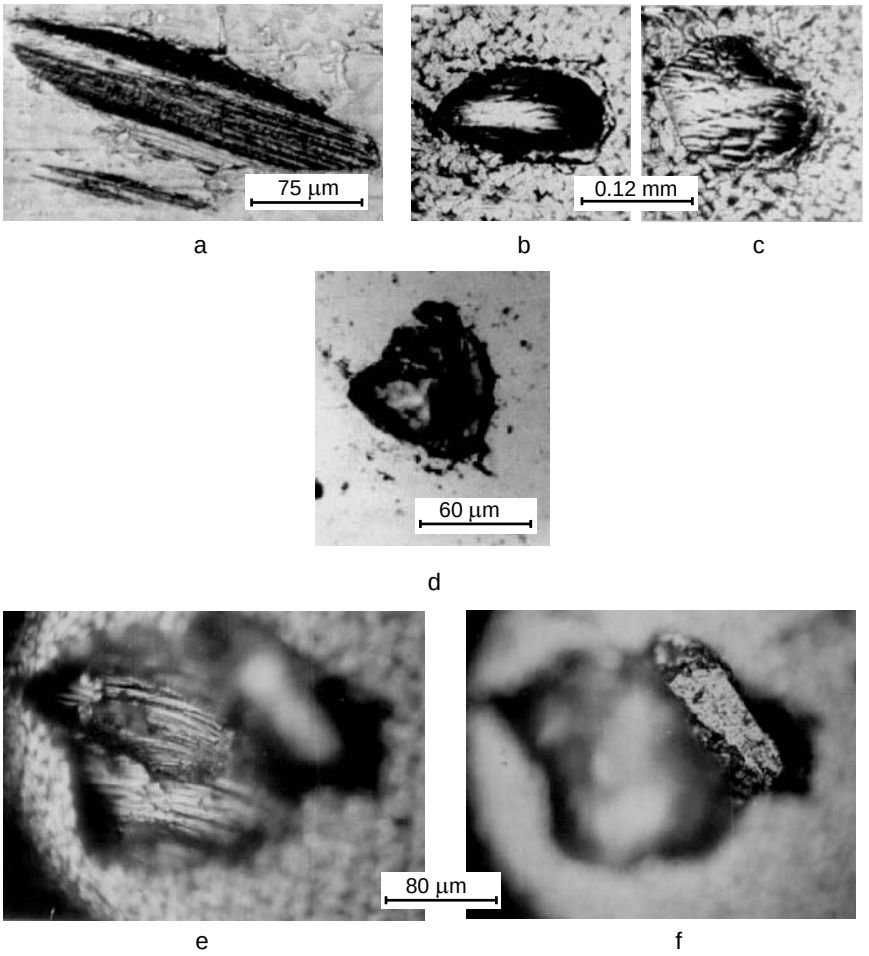

Figure 2.3a–f. Impact craters produced by particles hitting metal surface at α<90°, with the velocity vector directed from left to right: **a** – craters of 0.4–0.6 mm particles of sand from the Männiku quarry on the surface of 0.2% C steel, α = 3°, v_0 = 100 m/s; **b** – craters of 0.3–0.4 mm particles of sand from the Männiku quarry on 0.2% C steel, α = 30°, v_0 = 150 m/s; **c** – the same as "b"; **d** – impact scar left by 0.3–0.4 mm particle from the Männiku quarry on the hardened steel 710 HV, α = 45°, v_0 = 80 m/s; **e**,**f** – scars of 0.3–0.4 mm particle of sand from the Männiku quarry on the surface of 0.2% C steel, α = 40°, v_0 = 150 m/s; **e** – focused on the bottom of the crater; **f** – focused on the squeezed-out lip

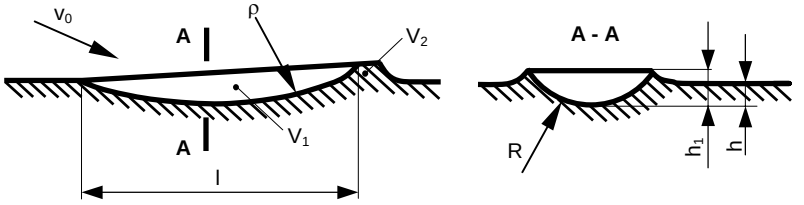

Figure 2.4. Scheme of impact crater at low impact angles: V_1 – volume of impact crater, V_2 – volume of material ousted from the surface but not separated from it

Table 2.1. Data on impact craters in 0.2% C steel target surface eroded by 0.4–0.6 mm quartz sand from the Männiku quarry, v_0 =97 m/s

α^o	l, μm	h, μm	ρ, μm	V_1, μm^{3}x10^{-3}	V_2, μm^{3}x10^{-3}	$K_g = (V_1-V_2)/V_1$	Z,%	K_g'
3	197	3	1618	6.7	3.4	0.49	100	0.49
9	136	4	580	12.2	7.9	0.35	93	0.36
15	136	7.6	308	29.8	21.4	0.28	73	0.35
30	126	10.3	192	46.4	38.7	0.17	53	0.26

Note: 1) In each regime, at least 15 craters were measured whereas the table gives mean results
2) Z shows the percentage of the impact craters from which material was removed and K'_0, in contrast to K_0, takes into account only those scars where it occurred

Analogous tests on hardened steel indicated that the values of ratio K_g were considerably higher than those of ductile steel [1]. This correlates with the test results obtained in scratching various metals [8] with a diamond bit (R = 49 μm). Curves in Figure 2.5 demonstrate the corresponding test results.

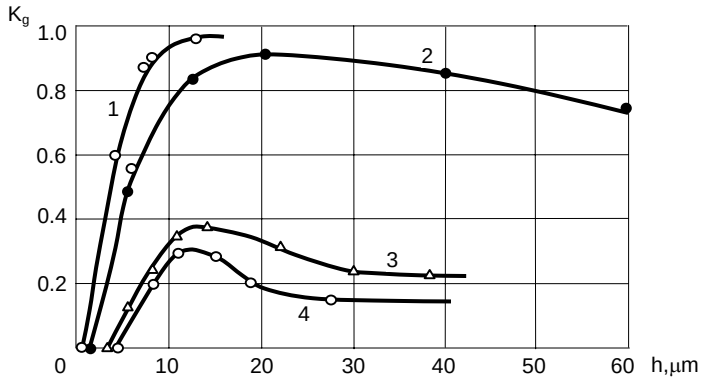

Figure 2.5. Dependence of ratio K_g on the depth of the scratch h: 1 – for hardened steel, 2 – for cast iron, 3 – for annealed steel and 4 – for copper

At single impact – as shown above – the shapes of the craters left in the surface by impacting particles vary considerably in their shape, whereas, when the craters overlap (*i.e.* in the permanent phase of the wear), the microgeometry of the surface at different angles is quite similar (Figure 2.6a,b). So are the shapes of the wear particles (except when α = 3°; see Figure 2.7a, in which the shape resembling that of a microchip prevails). In the case of hardmetals, wear-out of the binder from between the carbide grains, revealing grains of carbide, occurs quite often (Figure 2.6c) and is rather independent of the impact angle.

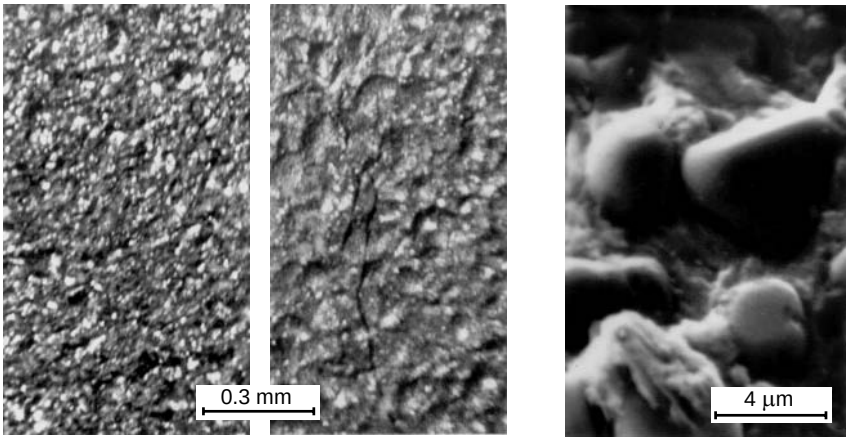

Figure 2.6a–c. Microgeometry of eroded surfaces: **a** – steel 0.2% C, v_0 = 50 m/s, α = 30°, 0.4–0.6 mm corundum; **b** – the same as "a", α = 90°; **c** – TiC-Ni-Co cermet, v_0 = 80 m/s, α = 90°, iron scale 0.1–0.3 mm

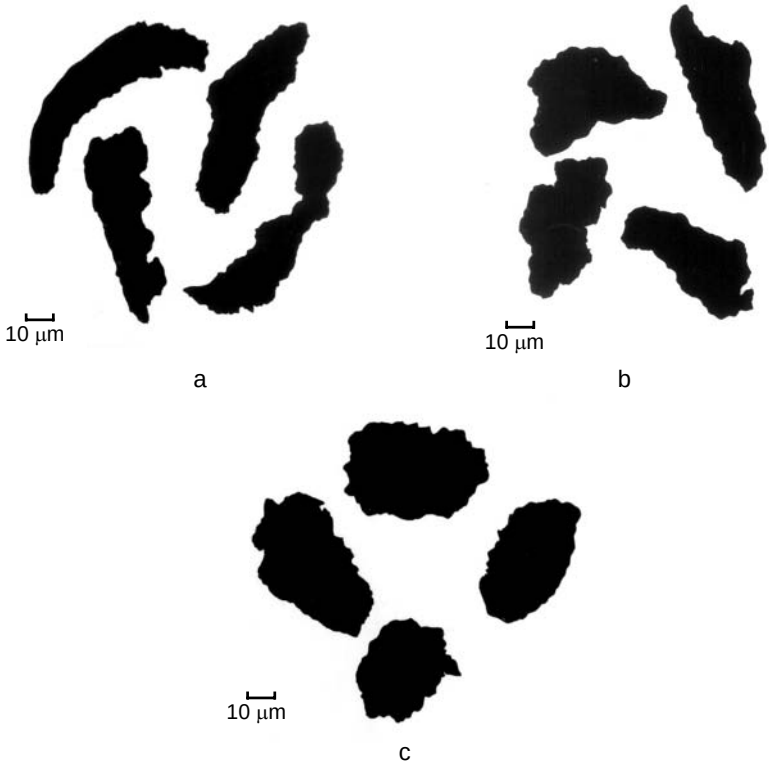

Figure 2.7a–c. Typical copper wear debris (enlarged), v_0 = 130 m/s, corundum particles 0.3–0.4 mm: **a** – at α = 3°, **b** – at α = 15°, **c** – at α = 90°

2.2 Stress Distribution and Structural Changes in Target Material Surface Layer

Ductile metals attacked by a stream of hard particles are subject to strain hardening of the surface accompanied by higher hardness and emergence of residual compressive stresses in the surface layer – an effect used in shot peening processes to increase the fatigue resistance of a metal [9]. The values of surface hardness obtained in the process of shot peening *vs* layer thickness are presented in Figure 2.8a. A picture similar to that will be obtained for the case of erosion by sand particles (Figure 2.8b).

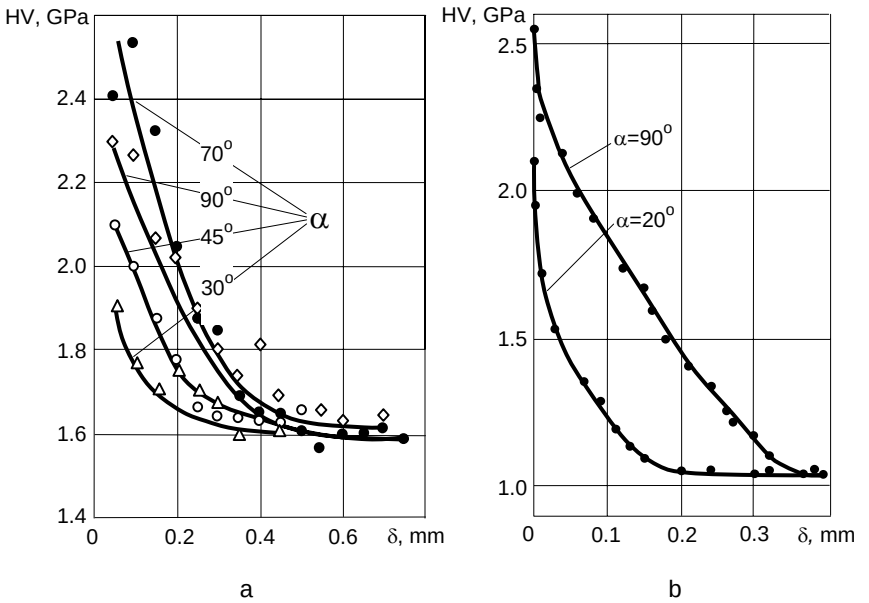

Figure 2.8a,b. Hardening – as a result of surface strain hardening – within the layer at various values of depth δ: **a** – 0.3% C steel, cast iron pellets of 1–1.5 mm are accelerated by an air stream under the pressure of 0.5 MPa [9]; **b** – Armco-iron in a stream of 0.4–0.6 mm quartz sand, v_0 = 80 m/s [4]

X-ray examination resulted in a similar picture of processes taking place in the surface layer. The first studies of this kind were carried out on specimens of 0.2% C steel subjected to stress relief annealing at 650 °C prior to the test [10]. The test specimens were eroded with 0.3–0.6 mm quartz sand from the Männiku quarry, using the CAK-1 testing facility at the velocity of v_0 = 80 m/s. Widening of interference lines on Debye-Sherrer diagrams was recorded by the X-ray defectoscope, gradually increasing the amount of sand hitting the test piece (Figure 2.9a). After that, part of the strain hardened layer was peeled off little by little by electric polishing, and relative widening of X-ray lines was determined (Figure 2.9b). It is obvious that these curves rather closely resemble those in Figure 2.8 obtained by measuring microhardness. It follows from Figure 2.9a that a permanent wear regime arrives after 1 cm^2 of the surface of the test piece has been hit by 20 g of sand because, thereafter, the X-ray lines become stable. On

the basis of Figure 2.9b it can be concluded that, in this case, the strain hardened layer is 0.25–0.3 mm thick. The same operations performed at α = 20° led to stable X-ray lines after hitting the surface by 15 g/cm² of sand and the thickness of the strain hardened layer was recorded to be 0.15–0.2 mm.

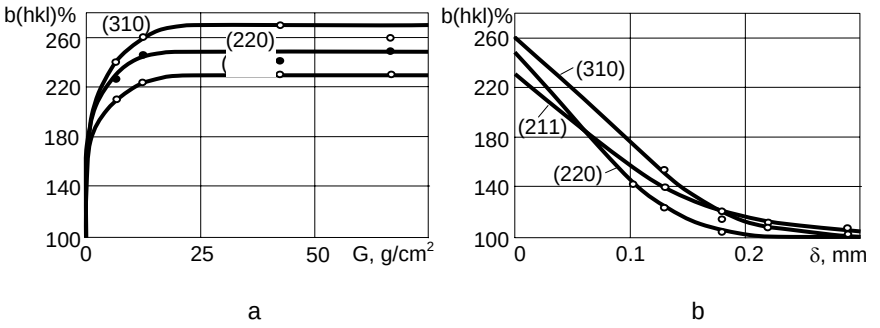

Figure 2.9a,b. X-ray studies on eroded mild steel specimens in a stream of quartz sand, v_0= 80 m/s: **a** – relative change in the width of X-ray lines b depending on the mass of abrasive hitting the test body, α = 90°; **b** – relative change in the width of X-ray lines b depending on the thickness of the strain hardened layer δ removed in the process of electrolytical polishing

Pakkas widened the range of the impact velocities at tests on mild steel as high as 195 m/s [11]. The relative widening of X-ray lines range in his work as presented in Figure 2.10.

For 0.2% C steel, analysis of the shape of X-ray lines according to Warren was carried out to determine the dependence of lattice distortion on particle velocity [5]. The range of 50–225 m/s was studied at an impact angle of 90°. Test pieces were eroded by quartz sand and cast iron pellets of 0.4–0.6 mm size. In both cases curves were obtained, with the clear-cut maximum at v_0 = 120 m/s. In view of the results of both microhardness and X-ray tests, it may be interesting to add that maximum distortion in crystallic lattice and maximum degree of strain hardening do not occur at the impact angle of 90° but in the range of 70–75°, instead.

To observe processes taking place in the surface layer, microsections of worn specimens were made transverse to the surface and examined under a microscope. Photos obtained with ductile metals, like those reported by several other researchers, show grain distortions in crystal texture and cracks running along the surface (example in Figure 2.11a).

In the microsections of hardened steel, however, white non-etchable layers of 1–2 μm thickness (Figure 2.11b) appeared, which run nearly along the equipotential lines of maximum shear strains [1]. Inasmuch as the layers are very thin, it is difficult to determine their composition – but in most cases they are treated as secondary martensite [12]. It is noteworthy, however, that at normal impact removal of the wear debris takes place along those white layers (see Figure 2.11c). A parameter closely related to the above phenomena is rise in temperature, accompanying the impact of the particles. The latter is confirmed by a number of researchers who have measured the instantaneous temperature rise both on the impact of particles and in the process of metal grinding. Similarity between thermal processes taking place on erosion (especially at low impact angles) and in the process of grinding, is also testified by the fact that in both cases flying sparks occur.

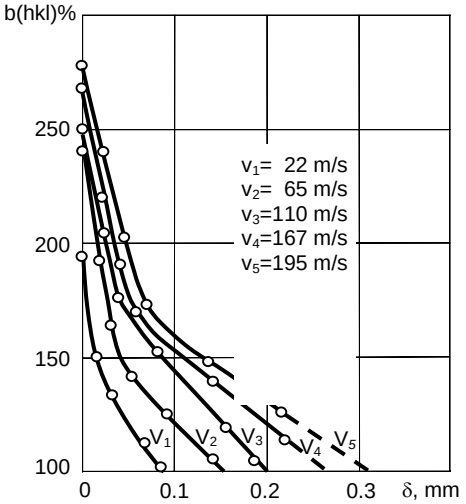

Figure 2.10. Dependence of relative widening of X-ray line (220) on the thickness of the layer removed by electrolytical polishing, $\alpha = 90°$

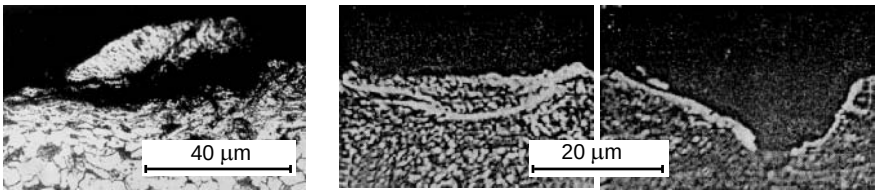

Figure 2.11a–c. Samples of microsections made perpendicularly to the worn surface: **a** – 0.2% C steel, v_0= 80 m/s, α = 45°, quartz sand 0.3–0.6 mm; **b,c** – 0.8% C hardened steel, v_0= 80 m/s, α = 90°, quartz sand 0.6-1 mm, **b** – without separation of wear debris, **c** – with separation of wear debris

Luminescence of the sample in the zone of bombardment by ash particles at velocities ranging from 200 to 300 m/s was described by Olesevich [13]. He considered that in the contact zone heating of one or both colliding bodies occurs to a temperature that corresponds to light yellow luminescence, the intensity of which depends on the impact intensity.

Uetz and Gommel [14] measured the temperature during the impact of steel pellets (790 HV) against a steel plate (190 HV). At an impact velocity of 70 m/s, the maximum temperature measured was 510 °C. The real surface temperature is assumed to be higher than that measured.

Polosatkin and Gribanov [15] used the thermocouple method in conjunction with scratching to measure the temperatures involved. Scratch velocities were in the range of 1–800 m/s. The melting temperatures on the surfaces of all metals tested were measured at scratch velocities exceeding 250 m/s.

Using a scanning electron microscope and a microanalyser, thermal processes accompanying erosion and grinding were studied in collaboration with researchers from the University of Stuttgart [16]. First, specimens of hardmetals

and steel were eroded at high impact velocities in which small spheres were detected in their surface layer (Figure 2.12). Analysis performed with a microanalyser indicated that the chemical composition of the small balls corresponds to that of the basic material. Among the products of grinding and also those flying off as sparks, analogous small balls were found both apart from and adhered to the microchips (Figure 2.13). Alternatively, combinations of molten metal may adhere to the abrasive grains of the grinding wheel (Figure 2.13e,f).The photo of broken pellets proves that they are of hollow shape (Figure 2.13b).

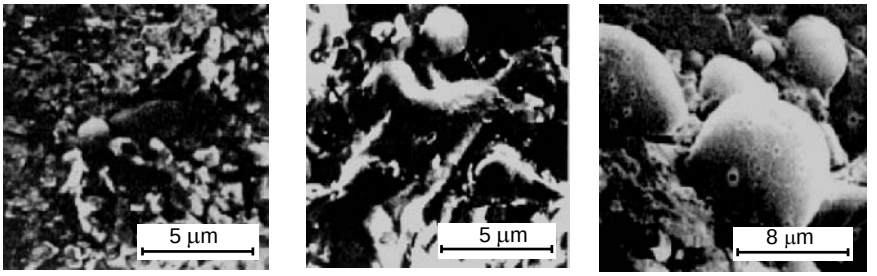

Figure 2.12a–c. Spherical particles on the surface: **a** – on the surface of WC-Co hardmetal, v_0 = 325 m/s, α = 90°, abrasive-cast iron pellets 0.4–0.6 mm; **b** – the same on the surface of chromium carbide based cermet, v_0 = 325 m/s, α = 90°, abrasive quartz sand 0.4–0.6 mm; **c** – the same on the surface of 0.45% C steel, v_0 = 108 m/s, α = 60°, abrasive quartz sand 0.4–0.6 mm

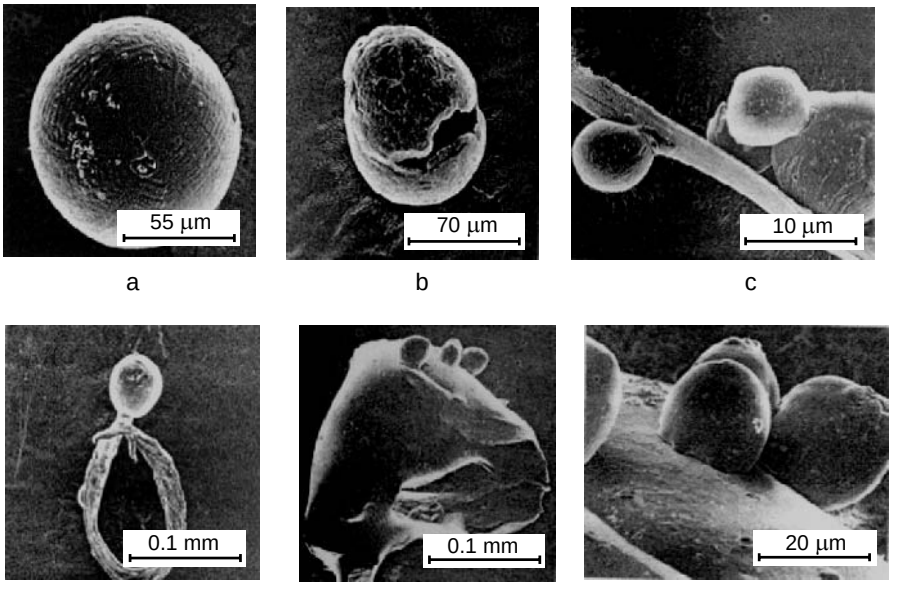

Figure 2.13a–f. Spherical particle formed in grinding: **a** – in grinding of cobalt, v_{grind} = 35 m/s; **b** – the same formed in grinding of 0.45% C steel; **c** – spherical particles of 0.45% C steel melted (agglomerated) into a group, v_{grind} = 35 m/s; **d** – the same as "b"; **e,f** – spherical particles of 0.45% C steel on the grain surface of a grinding wheel, v_{grind} = 35 m/s

From experimental evidence, melting temperatures can be attained in microvolumes during abrasive wear, *i.e.* abrasive erosion at velocities ranging from 100 to 325 m/s and grinding at a velocity of 30 m/s. Hence, during abrasive erosion, the microvolumes of a material heated to a high temperature in the impact zone may be thrown out in the shape of microdroplets. These microdroplets are shaped into spheres by the action of surface tension. The formation of spherical particles in grinding takes place in an identical manner.

When abrasive grains contact metal surfaces, depending of their orientation and pressure, a number of the microvolumes of ground material become liquid because of the local high temperatures involved and are scattered into the surrounding space. The sparks appearing in grinding, as well as in abrasive erosion, are glowing spheres.

In abrasive erosion it can be assumed that the majority of the spherical particles are scattered and lost and only a small number remain on the surface of the sample where they can be detected. The detection of spherical particles in abrasive erosion is evidence that in this wear mode thermal factors as well as mechanical factors are involved in breaking up the thin surface layers of the material. Although the quantity of spherical particles formed in the wear process is large, their specific weight in the wear product from abrasive erosion up to a velocity of 325 m/s is negligible. The preliminary evaluation of the role played by the thermal factor, *i.e.* the content of spherical particles in the total volume of the product is higher in grinding than in abrasive erosion.

2.3 Fragmentation of Abrasive Particles and Adhesion of the Latter to the Surface

One of the phenomena accompanying abrasive erosion is the fragmentation of abrasive particles. For this, depending on particle composition and initial defects, the respective critical impact velocity shall be obtained. Three different zones are distinguished in a fracturing particle at sufficiently high impact velocity [17] (Figure 1.16): the powdered lower cone, whose fragments at velocity $v_T > v_0$ are projected away along the surface; the non-destructed residual cone and the bigger orange-peel shaped splinters. The lower cone increases and the upper one decreases with an increase in the impact velocity. It is important to know all the parameters influencing the process of effective size reduction in the impact milling equipment. The milling effect is estimated quantitatively by the increase of particle specific surface ΔS (m^2/kg), using the corresponding testing equipment. The problems related to milling have been dealt with by Piel [18], and more profoundly analyzed by Kleis and Uuemõis in their monograph [19]. The main results obtained on the vacuum device VK-2 are referred to hereinafter.

Similarly to the equation $I_g = C_1 \cdot v^m$, demonstrating the relationship between the wear rate I_g and impact velocity v_0, the increase of the specific surface can be expressed through the exponential function

$$\Delta S = C_2 \, v^n . \tag{2.1}$$

An example of the experimental results is given in Figure 2.14a. Impact angle α and hardness of impact surface H are also important parameters. The maximum

fragmentation effect takes place at $\alpha = 90^o$ and the curves $\Delta S = f(\text{HV})$ are stabilized when the hardness of the impact surface exceeds that of the fractured particle (Figure 2.14b).

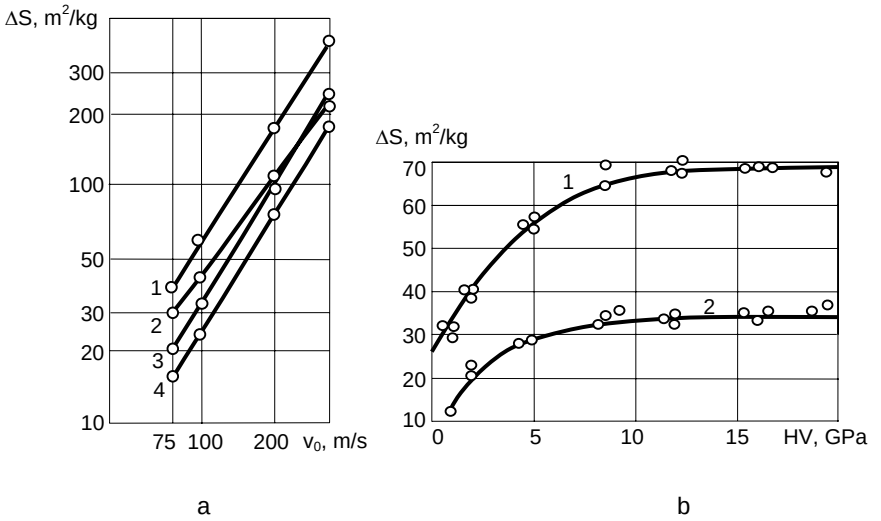

Figure. 2.14a,b. Dependence of increase in the specific surface of 0.4–0.6 mm quartz sand ΔS on impact velocity v_0: **a –** curve 1 – impact plate from WC-6Co hardmetal, α = 90°; curve 2 – the same as 1, α = 30°; curve 3 – impact plate from 0.2% C steel, α = 90°; curve 4 – the same as 3, α = 30° and dependence of the increase in the specific surface of 0.3–0.4 quartz sand ΔS, on the hardness of collision surface HV: **b** – at impact velocity v_0 = 120 m/s: curve 1 – if α = 90° and curve 2 – if α = 30°

Keeping in mind the service life (wear resistance) of mills working on the principle of collision, it is important to study what kind of materials used as impact members are most suitable for that purpose. The appropriate parameter in the analysis of the problem is the specific wear of the metal expressed as

$$K_g = I_g/\Delta S = (C_1/C_2)\, v_0^{m-n}, \tag{2.2}$$

where K_g shows the wear of the material in mg per 1 m^2 of new surface generated.

There exist two alternative modes of obtaining the desirable grinding fineness, which differ in principle – either by a single impact at high velocity (*e.g.* in a jet mill), or by subsequent impacts at moderate velocity (*e.g.* in a disintegrator). It will depend on the ratio between the value of exponents m and n: if $m>n$ (in the case of steels without heat treatment) several impacts at moderate velocity are preferable. If $m<n$, however, (in the case of hardmetals and hardened steels in milling sand and glass at v_o = 150 m/s, see Figures 1.17 and 1.18a), one impact at high velocity is preferable. It is illustrated in Table 2.2, in which the specific wear of metal when milling sand and cement clinker is shown [18].

Table 2.2. Specific wear of metal K_g, mg/m² by single impact milling, $\alpha = 90°$

V_0, m/s	Quartz sand		Cement clinker	
	0.2% C steel	WC-3Co hardmetal	0.2% C steel	WC-3Co hardmetal
75	11.5	0.15	4.7	0.13
150	15.5	0.11	6.7	0.09
325	24.7	0.09	10.5	0.05

The advantage of a hardmetal impact surface lies not only in in a restricted specific wear of metal and increased operational reliability of the mill, but also in a considerable cutdown of energy consumption for milling. Relying on the data provided in Figure 14a, if, for example, v_0 = 200 m/s, and the grinding members are from steel, to obtain 1 m² of a new surface, 200 J of energy is required, whereas with hardmetal impact members only 114 J is necessary, *i.e.* 1.75 times less.

A phenomenon accompanying breakup of the particles is their adhesion to the surface. There are materials (from among metals, especially aluminum) in the initial stage of erosion of which the particles and their debris become mechanically attached to the surface. The latter takes place at large impact angles and, instead of loss in mass of the part, the growth of it initially occurs [4]. More typical, however, is molecular adhesion of the fragments forming during the impact to the surface owing to molecular power [5], which takes place at sufficiently high velocities. Figure 2.15 shows photos of adhesion to hardmetal surface, taken by means of a scanning electron microscope.

As it can been seen from Figure 2.15a, the central part of the impact scar of a spherical cast iron particle stays clean without any adhered splinters. The latter stay positioned on a concentric circle and resemble partially molten metal sprinkles. The diameter of the circle constitutes *ca* 60% of the initial diameter of the particle. The splinters adhered to the surface of irregular particles, however, are located rather irregularly.

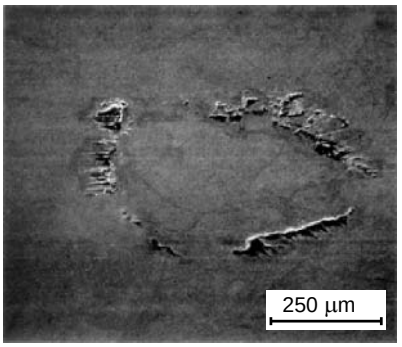

a

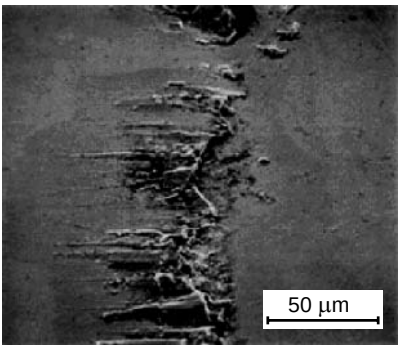

b

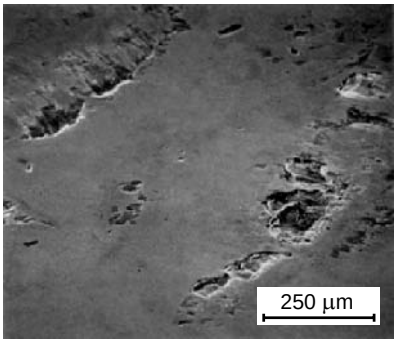

c

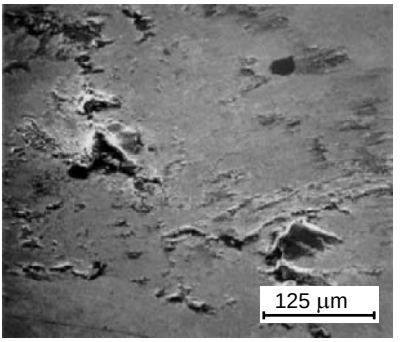

d

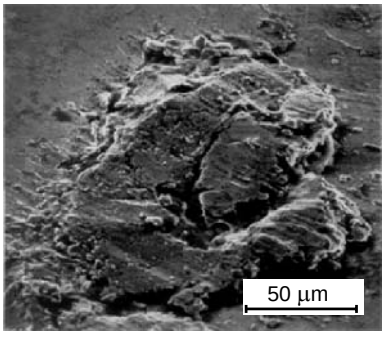

e

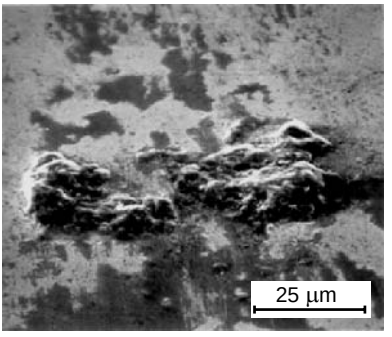

f

Figure 2.15a–f. Adhesion of 0.9 mm particle splinters to the surface of WC-6Co hardmetal in an impact at the velocity of 225 m/s, $\alpha = 90°$: **a** – impact of a spherical cast iron pellet; **b** – an enlarged fragment of photo **a, c, d** – an impact with cast iron particle of an irregular shape; **e** – an enlarged fragment of photo **c, f** – impact of a quartz sand particle

2.4 References

1. Kleis I. About the erosion of metals in the jet of solid particles. Proc Techn Univ Tallinn 1959;168:3–27.
2. Langeberg I. Research into Abrasive Erosion at Low Impact Angles. PhD Thesis. Tallinn 1968 (in Russian).
3. Uuemõis H. Study of Some of Regularities Concerning Abrasive Erosion. PhD Thesis. Tallinn 1968 (in Russian).
4. Tadolder J. Abrasive Erosion of Technically Pure Metals. PhD Thesis. Tallinn 1966 (in Estonian).
5. Kleis I, and Uuemõis H. Untersuchung des Strahlverschleissmechanismus von Metallen. Zeitschrift für Werkstofftechnik. 5. Jahrgang. Heft 7, 1974;381–89.
6. Huthings IM, and Winter RE. The erosion of ductile metals by spherical particles. J Phys D. 1975; 8:8–14.
7. Huthings IM, Winter RE. and Field JE. Solid particle erosion of metals: The removal of surface material by spherical particles. Proc Roy Soc London 1976;A348:379–92.
8. Bogomolov NI. The processes occuring in contact of abrasive and metal. Proc of Symposium “Methods of Wear Testing”. Moscow: Publications of Academy of Sciences of USSR. 1962;12–18 (in Russian).
9. Saverin MM. Shot Peening. Moscow: Mashgiz Publishers, 1955 (in Russian).
10. Mosberg R, and Kleis I. The study of the processes taking place at the surface of metal at erosion. Proc Techn Univ Tallinn 1962;192:20–28 (in Russian).
11. Pakkas LR. Research into the Changes of Crystal Lattice in the Surface Layer of a Metal Target Subjected to Abrasive Erosion. PhD Thesis. Tallinn 1968 (in Russian).
12. Rinehart JS, and Pearson J. Behaviour of Metals Under Impulsive Loads.. Cleveland: Publ by The American Society for Metals 1954.
13. Olesevich KV. Wear of Elements of Gas Turbines Operating on Solid Fuel. Moscow: Mashgiz Publishers, 1959 (in Russian).
14. Uetz H, and Gommel G. Temperaturerhöhung und elektrische Aufladung beim Stoss einer Stahlkugel gegen eine Stahlplatte. Wear 1966;9:282–96.
15. Polosatkin GD, and Gribanov SA. The measurement of temperatures on cutter surfaces at velocities of 1 to 800 m/s. Inf Bull Higher Educ Inst, Phys;3: 1965, 173–175 (in Russian).
16. Kleis I, Muiste U, Pilvre U, Uuemõis H, and Uetz H. The physical mechanism of the formation of metal microspheres in the wear process. Wear 1979;58:79–85.
17. Reiners E. Der Mechanismus der Prallzerkleinerung beim geraden zentralen Stoss und die Anwendung dieser Beanspruchungsart bei der selektiven Zerkleinerung von spröden Stoffen. – Forchungsberichte des Landes Nordrhein-Westfahlen nr. 1059, 1962.
18. Piel M. Study of the Laws Coverning Wear and Grinding Processes in Impact Mills. PhD Thesis. Tallinn 1979 (in Russian).
19. Kleis I, and Uuemõis H. Wear Resistance of the Milling Equipment Operating on the Principle of Impact. Moscow: Mashinostroenie Publishing House, 1986 (in Russian).

3

Development of Theories of Collision and Erosion

This chapter describes the kind of erosion that involves impacts of solid particles at the target surface. With metal parts, the impact is elastic-plastic. Naturally, creation and development of the theory of erosion presumes an understanding of the theory of collision. This theory, however, still needs further refinement. In the past 25 years, researchers at TUT have paid considerable attention to the studies of the theory of collision and erosion.

3.1 Hypothesis of a Constant Specific Energy; Dynamic Hardness

A comparison of data available on the quantity of energy required to produce a spherical impact crater of one unit of volume on a metal surface resulted in an amazing coincidence: independent of the mechanism, removing material from the crater (be it elastic-plastic deformation, plastic-viscous deformation, or melting of the metal at hyperspeed, or even sublimation), the numerical values of the specific energy consumed proved to be rather close for the impact directed normally to the surface. Table 3.1 shows some comparative data.

Table 3.1. Values of specific energy

Material	Static hardness HB	Impact velocity v_0, m/s	Specific energy e_0, J/mm^3	Reported by and ref. no.
Copper	41	3	0.85	Schwarz [1]
	42	111-356	0.86	Engel [2]
	45	>3600	0.88	Atkins [3]
Aluminium	24	51	0.43	Goldsmith [4]
	23	98-310	0.47	Engel [2]
	28	>5100	0.46	Kineke [3]
Low carbon steel	130	225	2.9	Kleis, Uuemõis [5]
		270	2.9	Hutchings *et.al.* [6]
	130	>5000	2.8	Atkins [3]

Coincidences in the values of the specific energy, apparently, cannot be regarded as incidental. This assumption led Kleis to the hypothesis that energy is constant, *i.e.* the specific energy can be regarded as a physical constant [7]. Similarly, the specific energy can be used to characterize the dynamic hardness of metals. However, that assumption had been proposed earlier (by Martel, a French scientist, in 1895, Unwin, a British scientist, in 1918, Wüst and Brandhauer, German scientists, in 1920 [1]). To verify the hypothesis in an elastic-plastic area, tests were performed first with a spherical indentor because it is simple to conduct such experiments, and, on the other hand, impressions obtained at hypervelocity are always spherical irrespective of the shape of the indentor [8]. Another issue to be clarified – which is crucial when defining the specific energy – was the initial energy of the indentor or the energy absorbed in the body (in fact, in the early twentieth century scientists relied on the latter [2]). At high velocities, the problem above becomes irrelevant as no rebound will occur. However, in the case of elastic-plastic collision, up to *ca* 200 m/s, with the coefficient of restitution $K>0$, it is relevant.

For tests with balls of a spherical ball bearing 850 HV, the vacuum tester VK-1 was rearranged, as shown in Figure 3.1. In order to change the velocity of the ball falling in dependence of angular velocity of the rotor, the height of diaphragm *h* in the vertical tube was made adjustable.

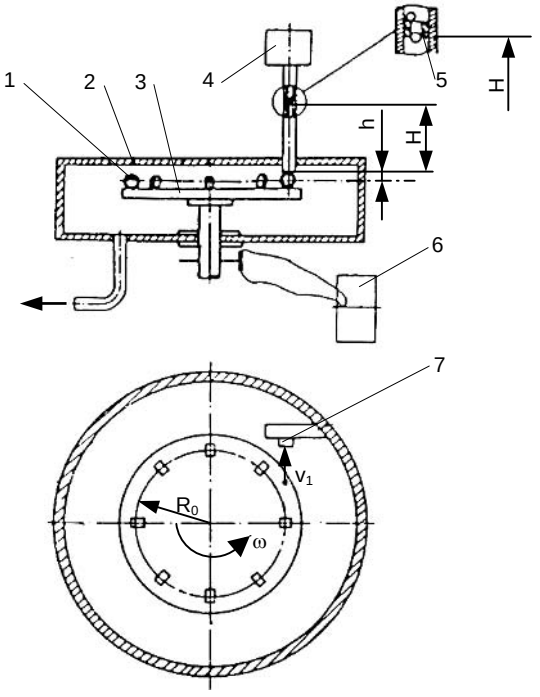

Figure 3.1. Scheme of the modified vacuum tester: 1 – specimen, 2 – hermetical body, 3 – rotor, 4 – dosing device, 5 – diaphragm, 6 – frequence meter, 7 – reference specimen

To determine the amount of energy absorbing into the specimen, the coefficient of restitution *K* has to be found. For that purpose, the velocity of the ball after

collision v_1 had to be determined. The so-called reference piece method was applied (pos. 7) to determine the desirable velocity v_1 when measuring the diameter of the impact crater on it. This method was granted the USSR Patent No 1193513:

$$v_1 = v_0 + Kv_0,$$

from which

$$K = (v_1/v_0) - 1 \tag{3.1}$$

The expressions of e_0 and e are

$$e_0 = W_0/V = m\,v^2/\,2V \tag{3.2}$$

and

$$e = W/V = mv^2(1-K^2)/\,2V, \tag{3.3}$$

where V – volume of the impact crater remaining on the surface of a polished specimen,
W_0 – initial energy of the ball on the impact,
W – energy absorbed in the impact,
$v_0=R_0\omega$ – linear velocity of the specimen,
K – coefficient of restitution.

In his thesis, Kangur studied 9 different steels and 14 technically pure metals within the impact range of 5–250 m/s [9]. First, the behaviour of duralumin, mild carbon steel and copper was thoroughly studied (see also Figures 3.2 and 3.3). It appeared that the value of specific energy of indentation e_0 remains constant, whereas the amount of absorbing specific energy necessary for producing the crater increases with the increase of impact velocity When the impact is perfectly plastic, the two specific energies will equalize with each other. The reason for $e<e_0$ is that there occurs no constant specific pressure between the indentor and specimen p_d; in contrast, it keeps growing along with the velocity (see Figure 3.18). Thus, for the rest of the materials, Kangur determined the value of e_0 only, varying both the impact velocity and the ball mass. Selected results are shown in Figure 3.4.

Further studies focused on the correlation between the static and dynamic hardness of metals. As the static hardness number (in this case, Meyer`s hardness) depends on the conditions of the test, *i.e.* the depth and speed of penetration of the indentor, researchers assumed for reference conditions $d/D = 0.4$ (d – diameter of the crater and D – diameter of the ball) and the loading time of the indentor – 15 s. Figure 3.5 shows the test results. Although at first glance the test points seem to be randomly scattered, a more detailed analysis reveals that they are grouped according to the type of the crystal lattice, so a satisfactory dispersion can be achieved by their concentration on three straight lines.

For the purpose of erosion studies, it is important to know how the depth of the impact crater h_p shall be expressed depending on the impact velocity v_0. As described in [10], a simple solution is provided by means of the dimensionless complex $\psi = \rho_1 \cdot v_0^2/e_0$, in which ρ_1 is the density of the ball. Assuming that the

radius of the impact trace R_1 and the radius of the ball R are equal (in fact, due to some elastic recovery of metal, R_1 slightly exceeds R), the crater depth in the equations regarding elastic-plastic impact will be expressed as follows:

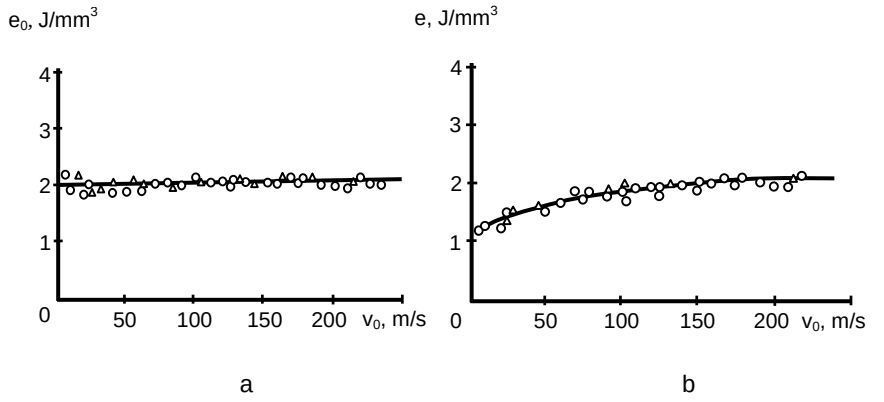

Figure 3.2a,b. Specific energy of cratering for duralumin: **a** – $e_0=f(v_0)$; **b** – $e= f(v_0)$; ○ – 1.588 mm steel balls; Δ – 2.5 mm steel balls

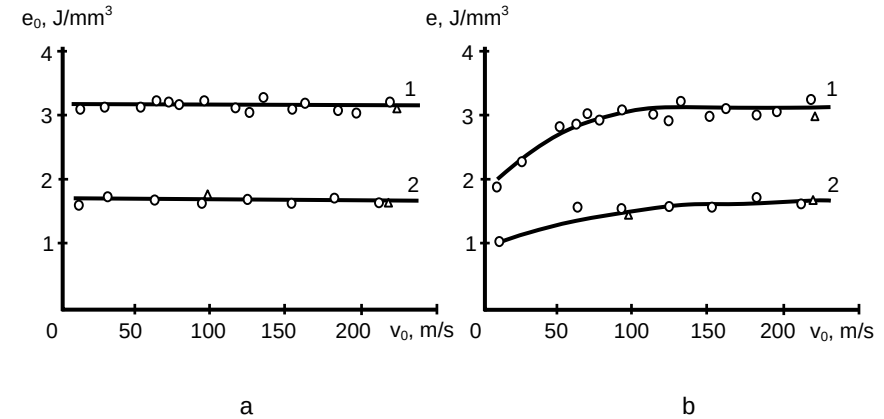

Figure 3.3a,b. The same as in Figure 3.2 for mild steel (1) and for cold rolled copper (2)

$$h_p = \{1\text{-}2\cos[(1/3)\arccos(1\text{-}\psi) + (\pi/3)]\}\, R, \tag{3.4}$$

if

$$h_p \le 0.2R,$$

then
$$h_p = (2\psi/3)^{0.5} \tag{3.5}$$

for shaft formation (if $h_p > R$)

$$h_p = R\,[\psi + (1/3)] \tag{3.6}$$

for hypervelocity impact

$$h_p = R\psi^{1/3} \tag{3.7}$$

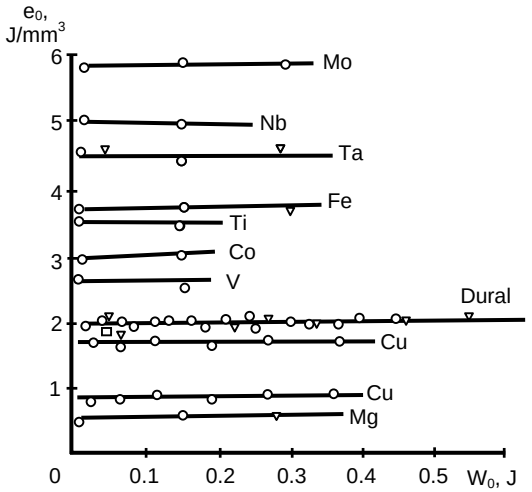

Figure 3.4. Dependence of specific energy e_0 on the initial energy of ball W_0: ○ – for a steel ball, Ø 1.6 mm; ▽ – for a steel ball, Ø 2.5 mm; □ – for a cermet ball, Ø 2.5 mm

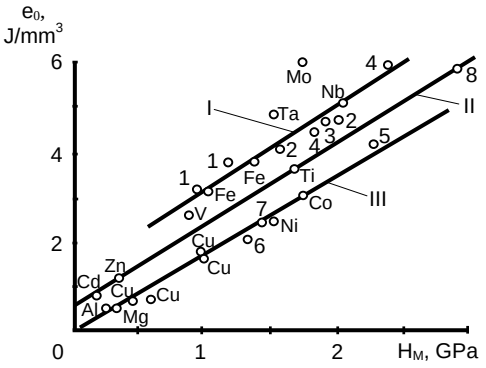

Figure 3.5. Specific energy of cratering as the function of Meyer's hardness for various target metals: I – metals with body-centered cubic lattice (BCC), II – metals with hexagonal close-packed lattice (HCP), III – metals with face-centered cubic lattice (FCC) and with hexagonal close-packed lattice (HCP); 1 – 0.2% C steel; 2 – 0.35% C steel; 3 – 0.45% steel; 4 – 0.4% C chromium steel; 5 – 0.08% C chromium-nickel steel; 6 – duralumin (4.5% Cu); 7 – brass (38% Zn); 8 – titanium alloy (6% Al, 3% Mo)

The threshold of hypervelocity is the sonic velocity in the given material. Transitions from one formation to another are illustrated by the graph in Figure 3.6. Similar curves were obtained by Goodier in [11], where in the dimensionless complex $\psi = \rho_1 \cdot v_0^2/\sigma_y$ yield point of the material was used. However, for the above reasons, these curves are of lower accuracy in application to many metals

The applicability of Equation 3.7 to calculating cosmic erosion is illustrated in Table 3.2.

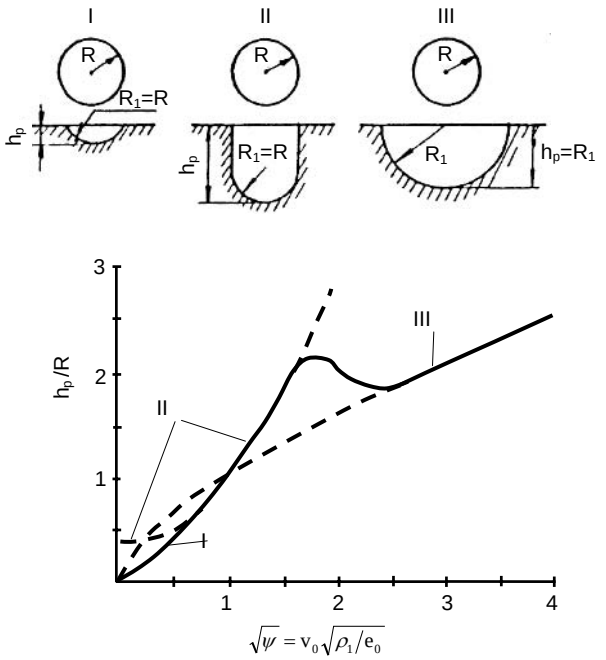

Figure 3.6. Crater in various conditions of penetration: I – elastic-plastic indentation, II – shaft formation, III – hypervelocity impact

The comparison is based on the data from Whipple, a US scientist (University of New Mexico), referred to by Singer in [12]. Allegedly, the results were employed in the development of spaceship designs both in the USA and the USSR. Since kinetic energy of meteorites W_0 was assumed for the basis of calculations, Equation 3.7 was expressed as follows: $h_p = (3W_0/2\pi e_0)^{1/3}$. According to Kangur (Figure 3.5), 0.45 J/mm³ was taken as the specific energy of aluminium. The comparative data in the table reveal a sufficiently high coincidence (differences remain within the limits of 0–4.6%).

Table 3.2. Expected damage of artificial satellites of the Earth caused by impacts of meteoroids

Mass of meteoroid, g	W_0, J	Penetration depth into aluminium h_p, mm [12]	h_p according to Equation 3.7, mm	Difference, %
1.25	10^6	109	104	4.6
0.5	4×10^5	80	77.1	3.6
0.079	6.3×10^4	43	42	2.3
0.012	10^4	23	23	0
5×10^{-3}	4×10^3	17	17	0
3.1×10^{-4}	250	6.9	6.8	1.4
2×10^{-5}	16	2.7	2.7	0
3.1×10^{-6}	2.5	1.5	1.4	0.9

It is also worth noting that all the values of h_p calculated using Equation 3.7 are lower than Whipple`s data. As referred to in [11], some scientists have obtained results indicating that the impact crater is not perfectly hemispherical but, in fact, slightly deeper. At the same time, the member characterizing the increase in crater depth is proportional to the value of $(\rho_2/\rho_1)^{0.5}$, where ρ_1 is the density of the material. In the given case, corrections cannot be introduced because of lack of data on ρ_2. If we use the same formula, replacing the value of e_0 with the yield strenght σ_y (according to [13] 0.05 GPa), as suggested by Goodier, we could obtain values of h_p more than two times higher. Equations 3.4 and 3.5 at elastic-plastic impact also provide us with more realistic results than using dynamic pressure $p_d = HM_d = C\sigma_y$, so far used by numerous authors, *e.g.* [4, 14]. For a spherical indentor, the values of C = 2.8–3 are used. It has been shown, however, that the above dependence holds true at static loading, since in the course of impact, the indentor will meet an increase in material resistance [15, 16]. The same can be concluded from our research (see Figure 3.18). Comparative data for the three materials can be found in Table 3.3, whereas data on the experiments concerning h_p were derived from [10]. Low carbon steel was used (σ_y = 290 MPa, e_0 = 3.2 J/mm³), duralumin (σ_y = 320 MPa, e_0 = 2.0 J/mm³), and copper (σ_y = 380 MPa, e_0 = 1.7 J/ mm³).

It can be concluded from the data in the Table 3.3 that Equation 3.5 suits better up to impact velocities of 100 m/s; with v_0 > 150 m/s, however, Equation 3.4 is more suitable. Operating with dynamic hardness $H_d = 3\sigma_y$ provides a more or less realistic result for copper at v_0<30 m/s. However, a major discrepancy occurs in the case of steel. The above results were obtained when testing ductile and relatively soft metals. With hard structures (hardened steels, wear resistant surfacing), effective in fighting erosion, a cone or a pyramid are the most suitable shapes for an indentor. To verify the constancy of specific energy for crater shapes other than a spherical segment, twelve different materials were studied, out of which six were various steels of 120–250 HV hardness [17]. Figures of 60° and 90° were chosen as the apex angles of the hardened steel indentors with pyramid and conic tips; the rounding radius of the indentor tips being 1–1.25 mm. The tests were performed on pendulum impact testing machines and free-falling test facilities, and impact craters (similarly to those obtained with balls) were measured with the aid of the microscope EPIQUANT. The experiments confirmed that e_0 is practically independent of the shape of the impact crater. The fact that the same results can be obtained at high impact velocities was proved through comparing results with those obtained on pure iron. Namely, Vitman and Stepanov shot a massive body of iron with cylindrical indentors with a conic 60° apex angle and a diameter of 8 mm (mass 11.1 g, impact velocity 840 m/s). The result was a cavity of 32.1 mm depth [18]. The specific energy under these conditions amounted to 2.83 J/mm^3. The result obtained is practically the same as with spherical indentors at the impact velocities of 225 and 270 m/s with mild steel (Table 3.1).

In the literature no references to experiments with spheres at which the velocity would remain within the range described by Equation 3.6 can be found. In addition to Vitman's and Stepanov's experiments, in which the impact crater takes the shape of a cylindrical shaft, Thompson from the US Navy Research Laboratory has performed similar experiments [19]. In the range of 130–2300 m/s, cylindrical indentors were shot into an aluminium target. As a result, the mean value of e_0 was found to be 0.4 J/mm^3.

Table 3.3. Penetration depth of spherical indentor Ø 1.588 mm calculated by various methods

Material	Evaluation	Penetration depth in μm at impact velocity v_0, m/s					
		10	**30**	**50**	**100**	**150**	**200**
Low-carbon steel St3, annealed	Measured value of h_p	10	29	51	102	156	207
	h_p calcul. by Equation 3.5	9.9	30	49	99	148	197
	h_p calcul. by Equation 3.4	10.1	31	51	104	158	213
	h_p calcul. by Equation 3.5 by $\psi = \rho_1 v_0^2/3\sigma_y$	19.2	58	96	192	289	385
Duralumin D16T 4% Cu, 1.5% Mg	Measured value of h_p	12	37	62	126	198	272
	h_0 calcul. by Equation 3.5	12.7	38	64	127	191	254
	h_0 calcul. by Equation 3.4	13	39	65	132	201	272
	h_0 calcul. by Equation 3.5 by $\psi = \rho_1 v_0^2/3\sigma_y$	8.3	55	92	183	276	366
Copper M1, rolled	Measured value of h_p	14	42	69	137	214	290
	h_p calcul. by Equation 3.5	13.8	41	69	138	207	276
	h_p calcul. by Equation 3.4	14.7	42	71	144	219	298
	h_p calcul. by Equation 3.5 by $\psi = \rho_1 v_0^2/3\sigma_y$	16.8	50	84	168	252	336

To determine the values of e_0 for hardened steels and hard surfacing materials, a special indentor acceleration method was created by means of air weapons [20]. Test bodies with a polished surface, which were glued to a massive steel block (Figure 3.7a), were shot at overbored (smooth) barrel air weapons with indentors of 1.95–3.15 g mass as shown in Figure 3.7b. The impact craters (see Figure 3.8) were measured under a NIKON SMZ 800 microscope, and the volume of the craters was calculated using both the rounding radius of the indentor tip r = 0.45 mm and the increase of the angle of the cone to the values of 126–128° related to the retrieval of elastic deformation.

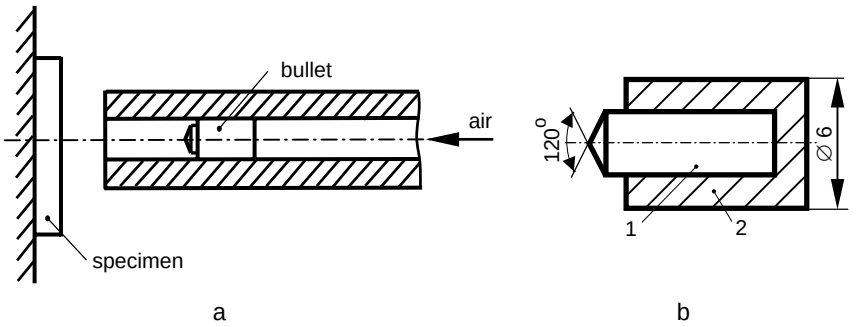

Figure 3.7a,b. Acceleration of bullets with air gun: **a** – schematic representation; **b** – bullet for acceleration: 1 – Ø 3 mm hardmetal indentor, 2 – copper shell

The ballistic pendulum method was applied, allowing for a bullet to be shot into a plasticine ball hanging from a thread, and the inclination angle φ of the pendulum was determined by means of a videocamera. The kinetic energy of the bullet was expressed as follows:

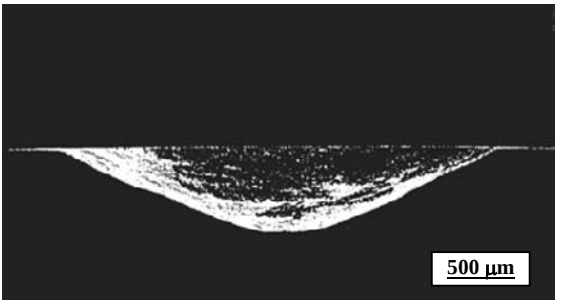

Figure 3.8. Microsection of the impact crater on the specimen surface

$$W_0 = g\,R\,(m_1 + m_2)^2\,(1 - \cos\,\varphi)\,/\,m_1, \tag{3.8}$$

where g – acceleration due to gravity,
R – distance of the centre of mass from the fixing point of the thread,
m_1 – bullet mass,
m_2 – mass of the plasticine ball.

Experiments were carried out with six different steels, which were hardened and tempered to achieve various values of hardness. Table 3.4 provides data on the steels.

Table 3.4. Data of the steels tested

Designation of steel	Chemical composition, %							HV GPa	Remarks
	C	Si	Mn	Cr	Mo	V	W		
Arne	0.95	0.3	1.1	0.6		0.1	0.6	3.6 to 6.9	Uddeholm
Calmax	0.6	0.35	0.8	4.5	0.5	0.2		3.7 to 5.2	Steelworks,
Rigor	1.0	0.3	0.8	5.3	1.1			3.8 to 4.9	Sweden
ChVG	1.0	0.2	0.9	1.0			1.5	5.5 to 8.0	Russian
U8A	0.8	0.2	0.2	0.1				5.6 to 6.3	steels
45	0.44	0.2	0.7	0.15		0.02		4.7 to 6.5	

The points shown in the axis $e_0 = f$ (HV) in Figure 3.9 (each of which is a mean of the three experiments) satisfactorily lie on the straight line, which can be described as follows:

$$e_0 = 1 + \text{HV, J/mm}^3 \text{ (or GPa)} \tag{3.9}$$

The values of e_0 calculated on the basis of Equation 3.9 were used to calculate the erosion rate of steels and surfacing. The results obtained sufficiently coincide with the test results (Section 3.4.3).

In conclusion, it may be claimed that specific energy e_0 is a constant of the material, suitable as a measure of the dynamic hardness of metals, the value of which does not depend on the shape of the indentor and impact parameters (as different from the static hardness of the material, in the calculation of which load

conditions of an indentor must be strictly defined). Thus, the present theoretical positions should be reconsidered. These concern other collision parameters, such as coefficient of restitution K, the force F applied on the indentor, and the specific pressure p, which is present when permeating into the material.

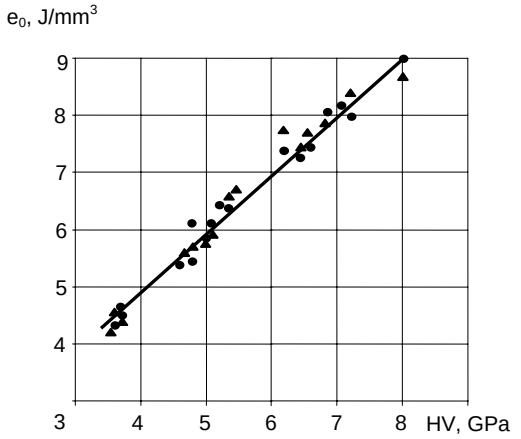

Figure 3.9. Dependence of dynamic hardness e_0 on static hardness HV: ● – test points obtained with air pistols, ▲ – test points obtained with air gun

3.2 Experimental and Theoretical Determination of the Coefficient of Restitution

The coefficient of restitution K defined by Newton has mainly been determined through experiments. The most widespread and simple method appears to be free fall:

$$K = v/v_0 = (h/h_0)^{0.5}, \tag{3.10}$$

where v_0 – impact velocity of the ball,
v – velocity of the rebounding ball immediately after impact,
h_0 – fall height of the ball,
h – rebounding height of the ball.

In such cases, impact velocity will not exceed 10 m/s. As known, with the increase of impact velocity the coefficient of restitution on elastic-plastic collision keeps on falling, approaching zero ($K = 0$ on absolutely plastic collision). Erosive processes, as a rule, take place at considerably higher velocities than 10 m/s. Thus the free fall method in these conditions appears unsuitable. The test method created by Kleis and Kangur allows testing at impact velocities of up to 225 m/s (see Section 3.1, Figure 3.1).Tests were performed using balls from ball bearing of 850 HV and Ø 1.6 mm. Table 3.5 provides data on the metals subjected to testing.

Table 3.5. Data of studied materials and dynamic hardness

Material	Brinell-hardness HB	Young's modulus E $\times 10^{-11}$, N/m^2	Poisson's ratio μ	Dynamic hardness e_0 J/mm^3
0.2% C steel	95	2.1	0.30	3.2
Duralumin 4% Cu, 1.5% Mg	130	0.7	0.33	2.1
Copper, cold hardened	98	1.2	0.35	1.7
Copper, annealed	45	1.2	0.35	0.8

When processing the test results it became evident that the coefficient of restitution K can be described by the following empirical relation:

$$K = A + B \ln v_0 , \tag{3.11}$$

whereas with duralumin $A = 0.99$ and $B = 0.151$
steel $A = 0.93$ and $B = 0.154$
rolled copper $A = 0.76$ and $B = 0.126$
annealed copper $A = 0.47$ and $B = 0.087$.

In addition, the aim was to find possibilities of expressing coefficient K in terms of theory [21, 22].Two different models of elastic-plastic behaviour of two elastic balls entering the material were analyzed (Figure 3.10).

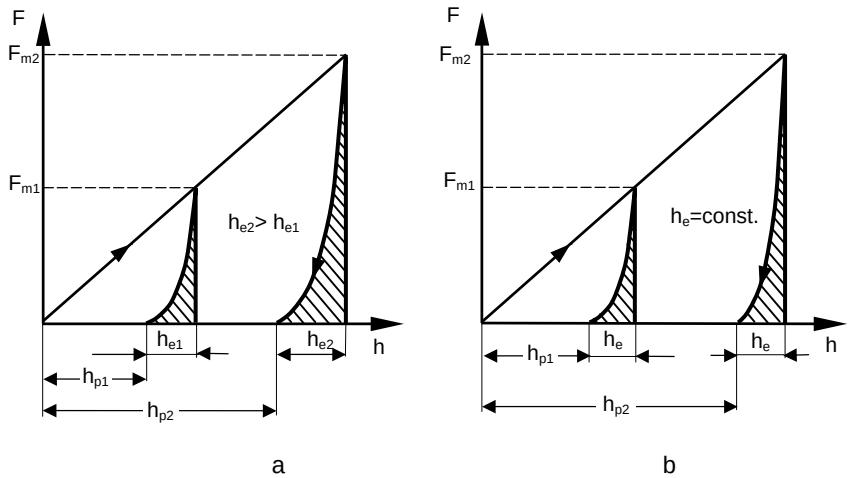

Figure 3.10a,b. Dependence of force F, exerted to the ball, on depth h of its penetration into the surface: **a** – on collision, the classical Hertz law applies, **b** – total elastic deformation h_e does not depend on the impact velocity

As with the first model, the total elastic deformation increases along with the impact velocity; in the second case, it remains constant. Figure 3.11 shows a scheme of ball penetration into the surface.

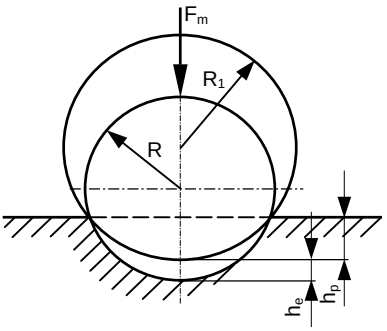

Figure 3. 11. Scheme of ball /bullet permeating into the massive board. R – radius of ball, R_1 – radius of impact crater, h_e – total elastic deformation, h_p – plastic deformation

Through the energies W_0 (initial energy of the bullet) and W_e (energy spent for elastic deformation), the coefficient of restitution can be expressed as follows:

$$K = (We/W_0)^{0.5} \tag{3.12}$$

According to Hertz, $W_e = 0.4\, F_m\, h_e$, and,

in its turn, $W_0 = 0.5\, F_m\, (h_e + h_p)$,

from which

$$K = [0.8\, h_e/(h_e + h_p)]^{0.5} \tag{3.13}$$

Theoretically, the last expression is exact; however, it is problematic whether h_e can be determined as exactly as possible. In order to determine the plastic part h_p, Equation 3.5 can be applied for metals. Applying the classical Hertz formula to the case “ball against a plane surface”, elastic deformation may be expressed as follows:

$$h_e = (0.75\, F_m J R^{-0.5})^{2/3} \tag{3.14}$$

In this equation, $J = (1-\mu^2_1)E_1 + (1-\mu^2_2)\, E_2$,

and F_m – maximum force acting on the ball,
R – radius of the ball,
E_1 and E_2 – Young’s moduli of target material and impacting body,
μ_1 and μ_2 – Poisson`s ratios.

Maximum force F_m, in its turn, depends on the coefficient of restitution K (see Equation 3.26). Thus, a new possibility for an approximated calculation had to be searched. Assuming that at low impact velocities $R(h_e+h_p) \approx R_1\, h_p$, we obtain the following relation [21]:

$$F_m = 2\pi R\, e_0\, h_p = 1.63\, \pi v_0\, R^2\, (e_0\, \rho_2)^{0.5} \tag{3.15}$$

When comparing the values of K obtained from Equations 3.13, 3.14 and 3.15 with the test results, we see that the coincidence is satisfactory with v_0 = 5 m/s. However, at v_0 > 10 m/s, with model given in Figure 3.10a, the deviations increase sharply, since the real values of K, will decrease more steeply than those found from calculations. In the case of model given in Figure 3.10b, however, the agreement is much better (see comparison in Figure 3.12). The test points of duralumin only lie higher than the theoretical curve, whereas with steel, the coincidence is excellent, the same is true for copper at v_0>20 m/s. In the calculation h_e =const was obtained, from Equation 3.14, at v_0 = 5 m/s. Model B can be justified by the curves $F = f(h)$, reported by Goldsmith [4]. However, Equation 3.15 does not provide satisfactory results for all materials. Therefore, the values of h_e obtained on the basis of Equation 3.14 prove unreliable. It seems more reasonable to determine one reference value of K (*e.g.*, by using the free fall technique), and, according to the rearranged formula, to find h_e, leaving it constant for the rest of the calculations

$$h_e = h_p / (0.8\, K^{-2} - 1) \tag{3.16}$$

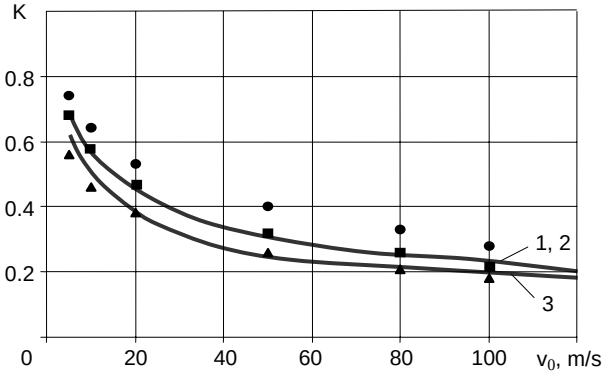

Figure 3.12. Dependence of the coefficient of restitution K on the impact velocity v_0: 1 – theoretical curve for duralumin, 2 – theoretical curve for steel (the latter practically coincide), 3 – theoretical curve for rolled copper. Test points: ● – duralumin, ■ – steel, ▲ – copper

The curves shown in Figure 3.13 were obtained in this way, using Equation 3.16 if v_0=5 m/s. The test points were added.

The values of K obtained by calculating and testing appear to have good coincidence, only with mild copper the deviation of v_0>100 m/s is considerable.

The second series of tests for determining the value of K was conducted on the Laser-Doppler Anemometer (LDA) shown in Figure 3.14. This special LDA equipment was elaborated at the Estonian Institute of Energy Research [23] to measure the velocities of impacting and rebounding particles.

To accelerate the particles, a centrifugal device was used. It allows for an operative change of the direction of the sensitivity vector, *i.e.* the direction of the measured projection of the particle velocity vector. Furthermore, the offered scheme permits the LDA to be adjusted to the particles of the defined size during the experiment. Changing the sensitivity of the receiver permits the system within a size range chosen by adjusting the optical scheme [24]. The signal from the photo receiver of the LDA is transferred to the counter which analyzes its quality and

transfers the obtained velocity of the particles crossing the measuring volume to the computer. The software is meant for the LDA measurements and consists of subroutines for data collection and analysis. The mean velocity, standard deviation and data rate are calculated. The latter is proportional to the amount of particles crossing the measuring volume and allows for the determination of particles concentration.

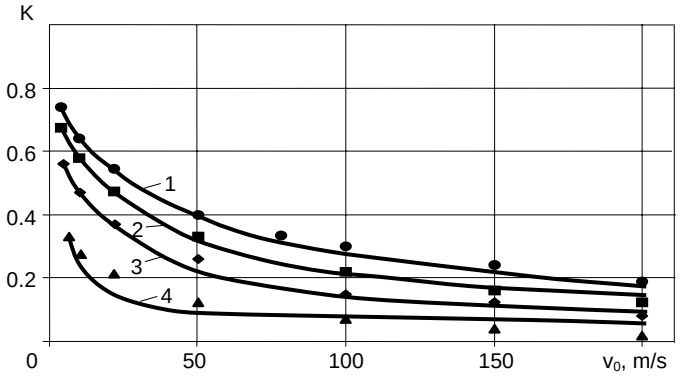

Figure 3.13. Dependence of the coefficient of restitution K on the impact velocity v_0: 1 – duralumin, 2 – steel, 3 – rolled copper, 4 – annealed copper

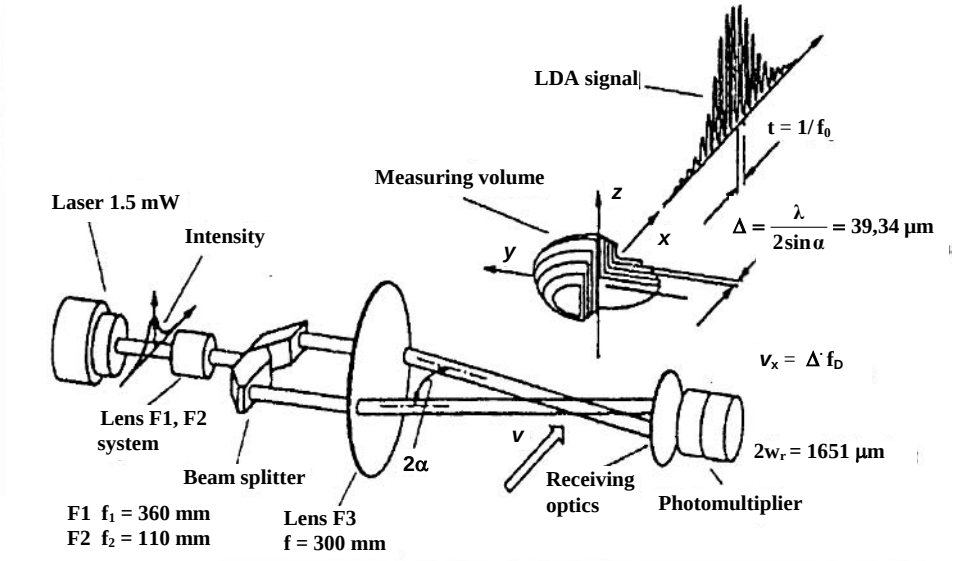

Figure 3.14. Scheme of LDA used

The rebound direction was determined as the direction of the velocity vector at the maximum particle concentration (Figure 3.15). This point was found by linear scanning along the x axis at some distance from the plate in the most probable rebound region. Then, the direction and value of the velocity vector were found at this point by the angular scanning of the LDA sensitivity vector. The concentration was determined by the number of Doppler signals registered by the system in one

time unit. This number does not only depend on the amount of particles crossing the measuring volume, but also on the measuring velocity component, adjustment of the system and the receiving conditions.

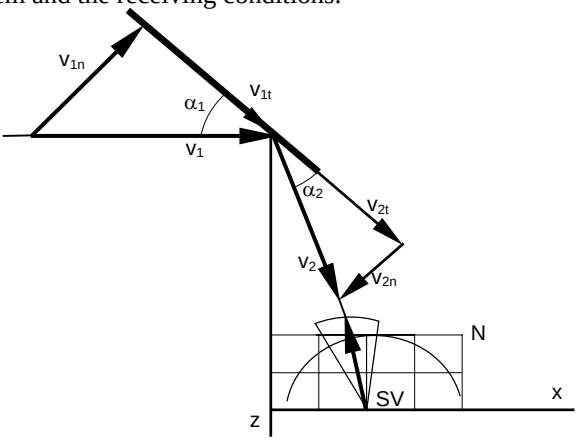

Figure 3.15. Determination of the value and direction of particle velocity; SV – sensitivity vector; *N* – the number of particles crossing measuring volume per unit of time, registered by LDA

According to the notation shown in Figure 3.15, the coefficient of restitution $K = v_{2n}/v_{1n}$ was determined. Tests were performed at impact angles ranging from $\alpha = 15°$ to 60°, using glass balls as rebounding particles with: Ø 0.7 mm, but also quartz and corundum particles of irregular shape. The results of tests with glass balls colliding against steel and ceramic plates are shown in Figure 3.16. When we calculate the theoretical curves using Equation 3.13 to determine h_e by Equation 3.16, experimental values of K at v_0 = 20 m/s serve as a basis. With steel, the divergence of test points is larger to some extent than for ceramics, when $h_p = 0$ and $K = 0.8^{0.5} = 0.89$, the coincidence of the experimental data with the theory is very good at all the velocities.

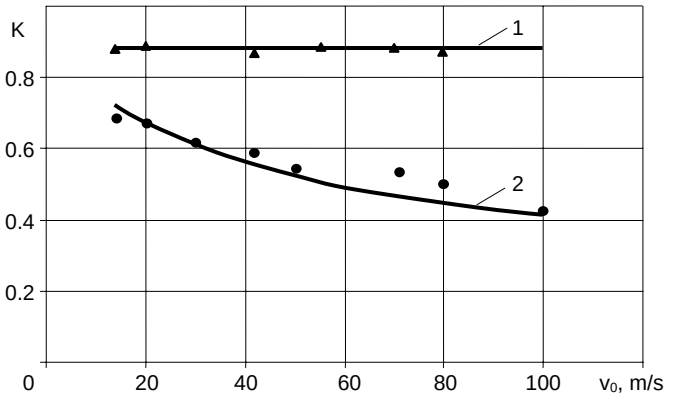

Figure. 3.16. Dependence of the coefficient of restitution on the impact velocity at impact from glass balls: 1 – against the ceramic composition CC 650 (Al_2O_3+TiN+TiC+ZrO_2, HV>1800) and 2 – against steel (0.4% C, 195 HV)

Experiments with irregular particles of corundum and quartz yielded values of K with high divergence (for steel within the range of 0.3–0.5). It can be observed here that in addition to impact velocity, the value of K is influenced by the impact angle α: as it diminishes, the value of K tends to diminish as well.

3.3 Analytical Determination of Indentation Load in Terms of Impact Energy

For the range of impact velocities from 5 to 200 m/s, characterized by elastic-plastic behaviour of metals, no reliable expressions for the calculation of impact force are available.

For the case when both colliding bodies are considered to be elastic (*e.g.* a hardened steel ball striking against a hardened steel plate), Hertzian impact theory is applicable [4, 14]. However, when plastic deformation of the plate becomes significant, neither of the theories based on Hertzian and Meyer`s equations will yield satisfactory results. In [25], therefore, we used our energetic impact theory assuming that the kinetic energy necessary to produce an indentation of unit volume at impact remains constant, independent of indentation shape. This value is a characteristic of any given material showing its dynamic hardness. This theory is outlined in [10, 25].

To determine the maximum impact force F_m occurring at the moment when the indentor penetration into the material reaches its maximum h_m, the following assumptions were made:

1. The direction of impact is normal to the plate.
2. The behaviour of the rebounding indentor is fully elastic, that of theory plate being elastic-plastic.
3. Dynamic pressure p_d between the indentor and the plate remains invariable during the impact process.

The second assumption is valid for hard mineral and glass particles, as well as for hardened steel indentors, striking against a metal target of up to 250 HB [14, 25].

The third assumption is an approximation supported by Goldsmith`s test results [4]. The studies described below were first reported in [26].

3.3.1 Mathematical Models for Force Calculation

A model for the evaluation of force F_m can be built up on the basis of Figure 3.17. With adequate difference in hardness of the two bodies, the hatched area under the curve represents the initial energy W_0 of the indentor which is absorbed by the plate during the first stage of impact. According to Gommel's tests with a ball and plate of 780/190 hardness ratio, energy consumption for plastic deformation of the ball is zero. Thus, the hatched area shown in the diagram equals that consumed for elastic deformation W_e of the ball and indentor, which makes the indentor rebound at the second stage of the process. For a spherical indentor and $h<0.2R$, the graph is a straight line, for a conical or pyramidal indentor, it takes the shape of a parabolic curve, since the projection area of the indentation crater depends on the square of its depth.

Hence, the initial energy of a spherical indentor

$$W_0 = \frac{mv_0^2}{2} = \frac{F_m h_m}{2} \quad \text{and} \quad F_m = \frac{mv_0^2}{h_m}, \tag{3.17}$$

where m – indentor mass,
v_0 – indentor velocity before impact.

For a conical indentor

$$W_0 = \frac{mv_0^2}{2} = \pi\ p_d\ tan^2(\varphi/2)\int_o^{h_m} h^2 dh = \frac{1}{3}\pi\ p_d h_m^3 \tan^2(\varphi/2)\,, \tag{3.18}$$

where φ - apex angle of the cone.

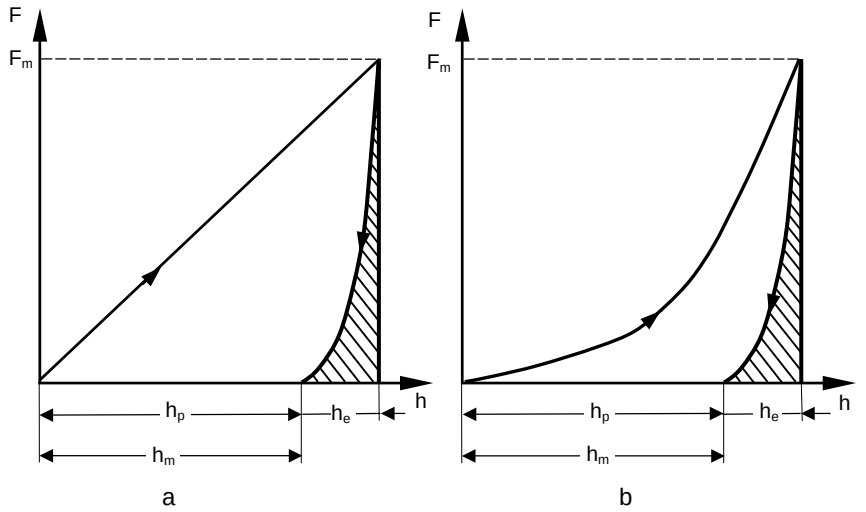

Figure 3. 17a,b. Dependence of indentor load F on impact crater depth h in the plate: **a** – for spherical indentor; **b** – for conical and pyramical indentors

For the case of a tetragonal pyramical indentor, we obtain

$$W_0 = \frac{mv_0^2}{2} = 4p_d tan^2(\varphi/2)\int_o^{h_m} h^2 dh = \frac{4}{3}\pi\ p_d h_m^3 tan^2(\varphi/2)\,, \tag{3.19}$$

where φ - apex angle of the pyramid.

For a spherical indentor, the Hertz formula is expressed as

$$W_e = \frac{2}{5} F_m h_e\,. \tag{3.20}$$

Knowing that $h_m = h_e + h_p$ (where h_p – indentation depth after impact) and taking into account Equations 3.13 and 3.16, we obtain

$$h_m = h_p(1–1.25K^2)^{-1} \tag{3.21}$$

Indentation depth h_p can be expressed by the energetic theory based on Equation 3.5 as follows:

$$h_p = Rv_0\left(\frac{2\rho}{3e_0}\right)^{0.5}, \tag{3.22}$$

where R – radius of the ball,
ρ – density of ball material,
e_0 – specific energy consumed for the formation of the impact crater or dynamic hardness of the material.

Inasmuch as $m = \frac{4}{3}\pi R^3\rho$, we obtain from Equation 3.17

$$F_m = \frac{4\pi R^3\rho v_0^2}{3h_m} = \frac{4\pi R^3\rho v_0^2(1-1.25K^2)}{3h_p} \tag{3.23}$$

If we consider the impact crater projection area $A = 2\pi h_m R$, then

$$p_d = \frac{F_m}{A} = \frac{2R^2v_0^2\rho}{3h_m^2} = e_0(1-1.25K^2) \tag{3.24}$$

$$F_m = Ap_d = 2\pi Rh_m p_d = 2\pi Rh_m e_0(1–1.25K^2)^2 \tag{3.25}$$

Equation 3.25 gives evidence of the principal difference of this theory from the commonly used one. By assuming that $p_d \approx 3\sigma_y$ (where σ_y is the yield strength of plate material), common in previous practice, the pressure is believed to be independent of impact velocity [14]; however, Equation 3.24 shows its significant dependence on impact velocity v_0 *via* the coefficient of restitution. This dependence is illustrated in Figures 3.18 and 3.19.

For practical calculations, the equation for F_m should be rearranged to eliminate h. Such a transformation of Equations 3.23 or 3.25 gives

$$F_m = 2\pi v_0R^2\left(\frac{2}{3}\rho e_0\right)^{0.5}(1-1.25K^2), \tag{3.26}$$

or, alternatively

$$F_m = (2\pi Rmp_d)^{0.5}\, v_0(1–1.25K^2) \tag{3.27}$$

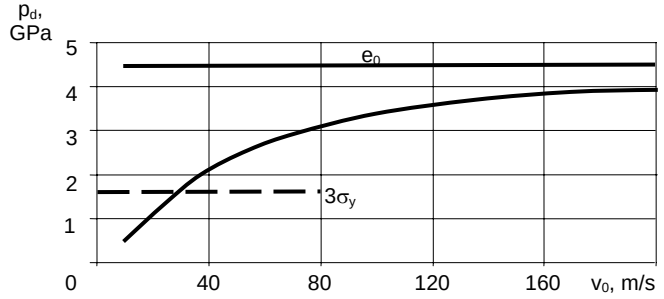

Figure 3.18. Dependence of dynamic pressure p_d on impact velocity v_0 by steel 0.15% C (190 HB); $p_d = e_0(1–1.25\ K^2)^2$, $e_0 = 1.3+1.8\times10^{-2}$ HB [25]. Values of K were obtained by Gommel [14] in tests with hardened steel ball of 1 mm diameter.

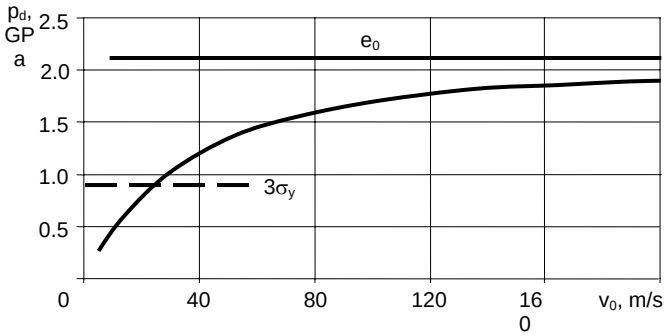

Figure 3.19. Dependence of dynamic pressure p_d on impact velocity v_0 by duralumin 2024 (130 HB); $p_d = (1–1.25\ K^2)^2$, $e_0 = 1.7+10^{-2}$ HB [25]. Values of K were obtained in tests with hardened steel ball of 1.6 mm diameter [25].

For conical and pyramidal indentors, similar expressions involving the restitution coefficient K cannot be obtained because no theory exists for the determination of W_e. However, we can assume that the values of p_d will be approximately the same as those obtained with a spherical indentor. Furthermore, should the p_d value differ from the actual value by a factor of n, the calculated F_m value will differ merely by a factor of $\sqrt[3]{n}$ (see Equations 3.30 and 3.33).

For a conical indentor

$$F_m = p_d A = \pi\ p_d h_m^2 \tan^2(\varphi/2)\,. \tag{3.28}$$

From Equation 3.18 we obtain

$$h_m = \left(\frac{3mv_0^2}{2\pi\ p_d \tan^2 \dfrac{\varphi}{2}} \right)^{1/3}, \tag{3.29}$$

consequently,

$$F_m = \left[1.5\pi^{0.5} m v_0^2 p_d^{0.5} \tan(\varphi/2)\right]^{2/3}. \tag{3.30}$$

For a pyramidal indentor

$$F_m = p_d A = 4 p_d h_m^2 \tan^2(\varphi/2). \tag{3.31}$$

It follows from Equation 3.19 that

$$h_m = \left(\frac{3mv_0^2}{8 p_d \tan^2 \frac{\varphi}{2}}\right)^{1/3} \tag{3.32}$$

thus,

$$F_m = \left[3mv_0^2 p_d^{0.5} \tan(\varphi/2)\right]^{2/3}. \tag{3.33}$$

3.3.2 Comparison of Calculated and Experimental Results

Goldsmith [4] and Gommel [14] have determined the impact load for some target materials using spherical indentors. Regrettably, tests with conical indentors were mostly conducted on target materials whose properties were similar to those of the indentors [4], *i.e.* the second condition was not fulfilled.

Figure 3.20 shows the test data obtained with steel balls at two velocities. Dashed lines represent Goldsmith's test data, and solid lines are drawn according to the above theory where the values of F_m and h_p were found by Equations 3.26 and 3.22, respectively. It can be seen that the values of h_p correlate well, whereas significant difference in Fm values is observed. Apparently, a share of the impact energy amount which was not consumed in the impact process went elsewhere, since the condition fixed in Equation 3.17 is not fulfilled, *i.e.*, the area below the curve on the graph is less than expected in terms of the initial energy $0.5\,mv_0^2$. However, it may be concluded from Goldsmith's tests that p_d will decrease with the decrease of impact velocity, since at v_0 = 46.6 m/s, the curve slope is more gentle than at v_0 = 88.3 m/s.

Graphs in Figures 3.21 and 3.22 illustrate the dependence of F_m on v_0 for three different materials. Apparently, the force measurement results reported by Goldsmith are affected by a systematic error, but the values of h_m and h_p are fully authentic. For this reason, the curves are plotted by points found from Equation 3.17 expressing F_m by means of h_m, m and v_0. It can be seen that in this case the experimental points lie quite close to the theoretical curves.

In impact force F_m measurements, Gommel [14] employed a ballistic method which is estimated to keep deviations of results within the limits of ±3%. However, these measurements were taken only at three impact velocities relatively close to each other. For comparison, the calculated and experimental values are presented in Table 3.6.

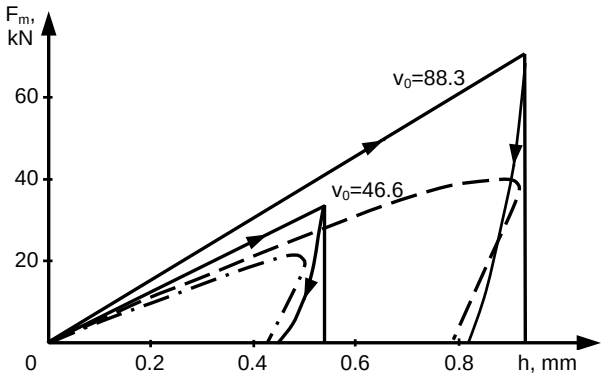

Figure 3.20. Comparison of curves plotted for results calculated by the energetic theory and (*dashline*) for Goldsmith's experimental data [4]. Plate material – duralumin 2024-T4 (140 HB), e_0= 2.3 GJ/m^{-3}, hardened steel ball 12.7 mm diameter

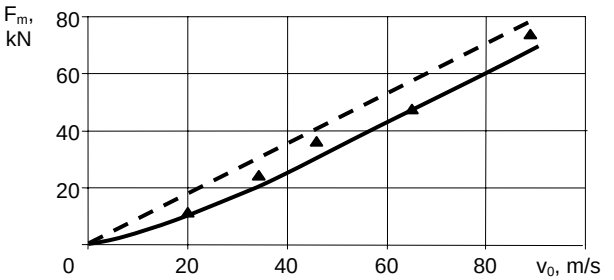

Figure 3.21. Comparison of $F_m = f(v_0)$ curve plotted from Equation 3.26 with Goldsmith's experimental data [4]. Plate material – duralumin 2024-T4, steel ball 12.7 mm diameter. *Dashed line* shows the case when $p_d = e_0$

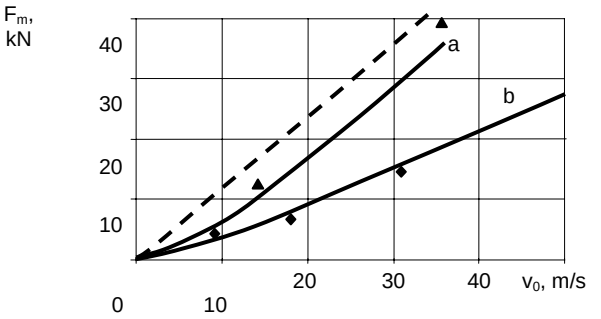

Figure 3.22. The same as Figure 3.20: a – tool steel (195 HB, e_0 = 5 GJ/m^3); b – aluminium 1100-F (64 HB, e_0 = 1.1 GJ/m^3)

Table 3.6. Indentation force F_m, N applied by a hardened steel ball of 1 mm diameter impacting against a C15 steel plate (190 HB)

	Impact velocity v_0, m/s		
	45.5	**58.3**	**70.5**
Experimentally measured	273	339	405
Calculated by Equation 3.26	244 (10.6%)	333 (1.8%)	421 (4.2%)
Calculated by Equation 3.27, assuming $p_d = 3\sigma_y = 160$ MPa	206 (25%)	264 (22%)	319 (21%)
Ratio of results found by Equations 3.26 and 3.27	1.18	1.26	1.32

Notes: 1) Deviations from the measured values are shown in brackets; 2) Values of restitution coefficient K used in Equation 3.26 were as given in Gommel's test data

The results obtained with conical indentors are illustrated in Figure 3.23. The p_d values used for plotting the theoretical curves were taken from Figure 3.18 and multiplied by a correction factor of 1.1 which takes into account the difference in hardness (and, consequently, in e_0 values) of the materials.

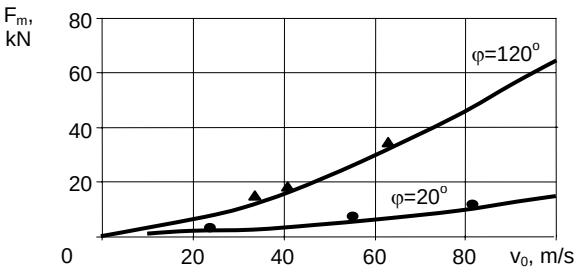

Figure 3.23. Dependence of F_m on v_0 as calculated by Equation 3.30 with Goldsmith's experimental points. Plate material – duralumin 2024-T4, conical steel indentors m = 8.33.

3.3.3 Conclusions

A comparative analysis of the results allows us to conclude that the values of impact force obtained by the presented theoretical equations coincide well with experimental data both for spherical and conical indentors. As distinct from the previously used method, this theory postulates that the coefficient of restitution K must be taken into account. In the range of high impact velocities, satisfactory results will be obtained when K is taken equal to zero, *i.e.* by taking $p_d = e_0$. With lower impact velocities (v_0<10 m/s), such a simplification would lead to an error which may exceed 100%.

Within a certain range of impact velocities (for the above metals v_0 = 20–60 m/s), the approximation $p_d = 3\sigma_y$ is applicable, yielding results quite close to those obtained with the use of the suggested theory.

With conical and pyramidal indentors, attention should be paid to the apex angle φ, which has a significant effect on the value of F_m.

3.4 Theoretical Treatment of Erosion

3.4.1 A Short Survey of Erosion Theory

Two theory-based directions have been followed: first, prediction of the service life of wearing parts and, second, estimating the relative erosion resistance of the parts. However, the latter has been more successful.

The first mathematical expression, meant to determine the working resource of a boiler tube in the conditions of erosion caused by fly ash, was reported by Russian researchers [27]. Recognized in the former Soviet Union for a long time, this approach presumed that wear rate of the boiler tubes has to be proportional to the kinetic energy of the stream of flue gases, *i.e.* to the gas stream velocity in second power:

$$I_v = A_c \varepsilon^{-1} v^2 , \tag{3.34}$$

where I_v – volume wear rate of the material, mm³/kg,
A_c – empirical coefficient, characterizing the abrasivity of fly ash,
v – velocity of flue gases,
ε – relative wear resistance of the material of the boiler tube (in reference to standard pipe of non-alloyed steel $\varepsilon = 1$).

The value of velocity exponent 2 is also present in Lebedev`s [28] and Finnie`s [29] theories, both of whom conceive erosion as microcutting. Later investigations by several other authors indicate, however, that the value of this exponent is dependent on the properties of both the material and the particles and may vary within a wide range.

Bitter was the first research scientist to consider erosion as a combination of two kinds of damage – microcutting and deformation wear [30]. His formula, therefore, consists of two addends, thus excluding the common drawback of Lebedev's and Finnie`s theories, according to which at normal impact ($\alpha = 90°$), $I_v = 0$.

Nepomnyashchy [31] assumed that erosive wear of metals is caused by low-cycle fatigue or microcutting. The erosion mechanism depends on the so-called critical impact angle. According to this theory, the velocity exponent proves to exceed two.

Abramov [32] supposed that, in the course of impact, metal deformation is governed by Hooke`s law, and its breaking occurs along the lines of maximum shear stresses.

Beckmann and Gotzmann [33] derived an analytical expression for the erosion of metals from the hypothesis that, in abrasive and erosive wear, the volume removed is proportional to the work of shear forces in the surface layer. The basic model was formulated from the study of deformation caused by a single spherical particle.

Peter [34] in his model used Beckmann and Gotzmann`s erosion theory after the replacement of the equations for computing the indentation depth of the particle and the specific shear energy density.

None of the above-mentioned theories can do without empiric parameters directly derived from erosion experiments (depending on the theory these range from 1 to 5). Based on the experimental data obtained by Tadolder [35] and Levin

[36], when testing with quartz sand on a centrifugal accelerator, Ellermaa [37] compared the two theories to establish the most suitable approach for further development. Table 3.7 provides the values of sums of the least squares calculated from different erosion theories based on the following equation:

$$S = \sum_{i=1}^{n} (I_c - I_e)^2 / I_e^2 , \tag{3.35}$$

where n – the number of tests,
I_c – calculated values of erosion rate,
I_e – the experimental values of the erosion rate.

It can be seen from Table 3.7 that it is the Beckmann's and Gotzmann's theory that provides the best possible coincidence with the experimental data; the worst, however, is obtained by means of Nepomnyashchy`s theory. Therefore, in his article Ellermaa focuses only on the first mentioned theory.

Table 3.7. Application of the method of least squares to different erosion theories

Theory	Sums of least squares, S (n = 14)				
	Al	Ti	Fe	AISI 1020 steel	
				434 HV	193 HV
Lebedev [28]	3.72	4.99	4.07	2.81	2.59
Finnie [29]	3.30	5.15	4.46	4.92	4.33
Bitter [30]	1.49	2.56	2.83	0.68	0.43
Nepomnyashchy [31]	1200	39.25	98.55	3.12	28.74
Abramov [32]	5.86	3.35	5.99	3.84	4.69
Beckmann and Gotzmann [33]	0.92	2.31	1.97	0.25	0.39
Peter [34]	1.29	7.10	4.96	3.56	0.92

3.4.2 Erosion by Plastic Contact

3.4.2.1 Energetic Erosion Theory

Beckmann's and Gotzmann`s theory of energetic wear is a collaborative effort of researchers from Tallinn and Zittau. The universal nature of the theory was essential, *i.e.* its applicability to both the erosion of solid particles and drop erosion, adhesive and abrasive wear. The results of the collaborative research were published in the monograph by Beckmann and Kleis [38]. The theory assumes that before removing the wear product from the metal surface, a certain amount of energy necessary for shear deformation on the surface must be accumulated. Micrographs [6] taken by scientists from Cambridge University provide a vivid illustration of the shear deformation on erosion. An example is shown in Figure 3.24.

As the analysis of such impact craters shows, in the initial part of the contact (zone a), no shear occurs in the surface layer of the metal; in zone b, however, the shear in the surface layer of the material caused by "dragging the material along", is clearly visible, especially in the "lip", emerging on the edge of the impact crater, not separated from the basic material as yet (zone c).

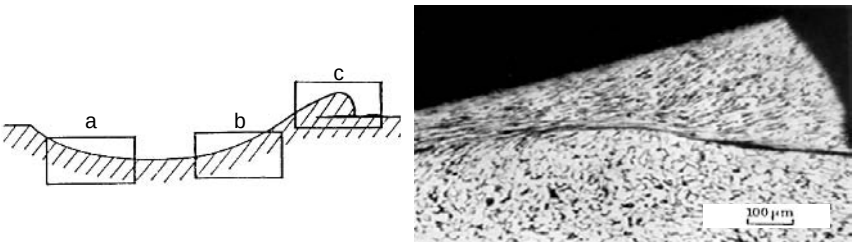

a b

Figure. 3.24a,b. Longitudinal section of the impact crater left in mild steel when hit by hardened steel ball R = 4.75 mm, α = 30°, v_0 = 141 m/s: **a** – special zones of the impact trace, **b** – microphoto of zone c

The assumptions followed in creating the erosion theory were:

1. The solid spherical particles causing erosion are homogeneous and elastically deformable, with a radius R and density ρ_2.

2. The velocity of the particles immediately before the impact v_0 is constant, whereas the angle between the velocity vector and the wearing surface is α; the particles have no rotational energy.

In addition, hardness of the particles H_2 has to exceed hardness of the material H_1 by 1.6 times as a minimum [5]. The wear rate of target material I_v can be expressed as follows:

$$I_v = \frac{3}{4\pi\rho_2} \cdot \frac{\tau_0}{e_s} \; (J_I + J_{II}), \tag{3.36}$$

where $$J_I = \left(\frac{5}{3} + \pi\right)\sqrt{2}\left(\frac{h_p}{R}\right)^{0.5} \frac{2\rho_2}{3H_1} v_0^2 \cos^2\alpha = 6.81\left(\frac{h_p}{R}\right)^{0.5} \frac{2\rho_2}{3H_1} v_0^2 \cos^2\alpha \tag{3.37}$$

and

$$J_{II} = 0.85\left(\frac{h_p}{R}\right)^2, \tag{3.38}$$

where J_I stands for the share of wear caused by tangential component of velocity,

J_{II} shows the same of the normal component,

h_p appearing in the formula is the depth of indentation produced by the eroding particle,

τ_0/e_s is a dimensionless ratio, where the numerator means shearing stress τ_0 in the target material. It can be calculated using the following relation:

$$\tau_0 = \frac{1}{3} L\rho_1 \ln\left(\frac{T_m}{T}\right), \tag{3.39}$$

where

L – material latent heat of melting,

T_m – melting temperature of the material in K,

T – ambient temperature in K,

e_s – specific shear energy density.

According to Beckmann and Gotzmann, the ratio τ_0/e_s is a universal parameter used to determine the wear resistance of metals. On the basis of statistical data, a graph (Figure 3.25) has been plotted on pure metals, carbon and alloy steels and white cast iron [38].

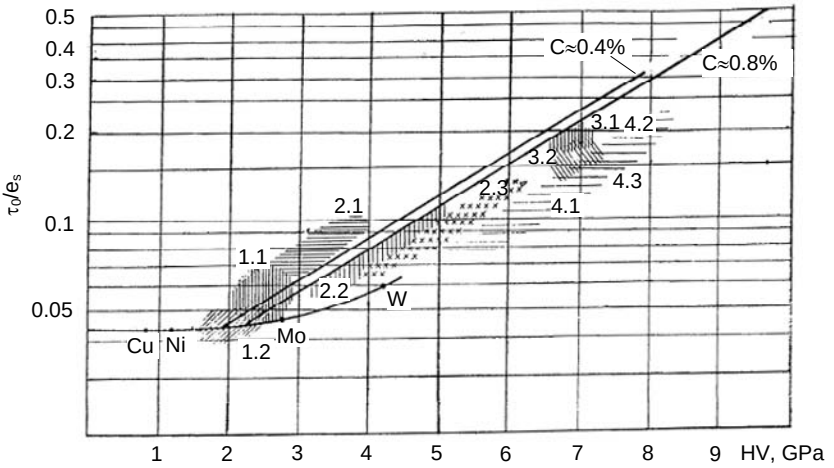

Figure. 3.25. Variation of τ_0/e_s as a function of initial hardness H_m of the target material: 1.1 – low-alloy structural steels; 1.2 – austenitic manganese steels; 2.1 – pearlitic carbon steels; 2.2 – steels alloyed with Mn, Si and Cr; 2.3 – alloyed cast steels; 3.1 – hardened tool steels; 3.2 – hardened chromium steels; 4 – carbide-base structures; 4.1 – C>1.5% special steels alloyed with Mo, W and V; 4.2 – special ledeburitic steels alloyed with W, Mo and V; 4.3 – high-alloy white cast irons containing various carbides

An essential parameter – depth of impact crater h_p – was determined by using the following relation:

$$h_p = R\sqrt{\frac{2\rho_2}{3H_1}\left[v_0^2 \sin^2\alpha - \frac{4E'}{5\pi\rho_2}\left(\frac{H_1}{E'}\right)^5\right]}, \tag{3.40}$$

where the reduced modulus of elasticity is

$$E' = \left[\left(1-\mu_1^2\right)/E_1 + \left(1-\mu_2^2\right)/E_2\right]^{-1}. \tag{3.41}$$

E_1 and E_2 are Young`s moduli of the target material and abrasive particle, $\mu_1$ and $\mu_2$ are Poisson`s ratios for the same materials.

In the early stage of the development of the theory, the corrective coefficient $k = k_R \cdot k_\varphi$, which considers real conditions, was used. It takes into account the shape

of the particles – their angularity, *i.e.* difference of the particles from a sphere. Based on Tadolder's studies [35] and his own tests, Beckmann suggested the following values of k_R:

Spherical white cast iron shot	1.0–1.1
Rounded quartz	1.05–1.3
Angular quartz	1.3–1.6
Corundum	1.6–1.9
Glass grit	1.9–2.1
White iron grit	2.3–2.7

The second coefficient of correction k_φ takes into account the effect of the amount of particles φ hitting the surface within a time unit (*i.e.* the concentration coefficient k_φ). Namely, at φ >10 g/cm²s, particles rebounding from the surface will have a considerable screening effect, hindering the motion of primary particles; at φ = 200 g/cm²s, the value of k_φ is reduced to 0.4 [38]. The values of k_φ remaining within the range φ = 10 to 200 g/cm²s can with sufficient precision be obtained from the relation

$$k_\varphi = 2 \cdot \varphi^{-3} \tag{3.42}$$

If φ < 10 g/cm²s, k_φ = 1.

A comparison of the results based on the theory and on experimental data on a limited number of materials provided satisfactory results at impact velocities 40–80 m/s, which can also be seen in Table 3.7.

3.4.2.2 Verification and Modification of Energetic Erosion Theory

Although the theory created by Beckmann and Gotzmann proved to be the most promising, a thorough check-up and refinement was required. It was Ellermaa who started modification of the theory [37]. Although in its initial form, the theory takes into consideration differences between particle shape and the sphere through the coefficient k_R, it neglects the effect of their diameter. In terms of experimental data, Ellermaa introduced another corrective coefficient k_d to the formula:

$$k_d = d/120 \text{ if } d = 0 \text{ to } 120\ \mu\text{m} \tag{3.43}$$

and $$k_d = 1 \text{ if } d > 120\ \mu\text{m}$$

In order to take into account the effect of the hardness of particles, Ellermaa added one more coefficient k_H:

$$k_H = (H_2 - H_1)/0.6H_1 \text{ if } H_1 < H_2 < 1.6H_1 \tag{3.44}$$

and $$k_H = 1 \text{ if } H_2 > 1.6H_1.$$

If Beckmann and Gotzmann offered an equal value of τ_0/e_s = 0.044 both for pure metals and mild steel (see Figure 3.25), Ellermaa recognized that it was necessary to modify that parameter, relying on Peter`s suggestion [34]

$$\tau_0/e_s = e_0/10C_M \rho_1 (T_m - T) \tag{3.45}$$

where C_M is the specific heat capacity of the material.

In that case, τ_0/e_s of iron = 0.067, which coincides best with the experimental data.

Static hardness in Equation 3.37 was replaced by dynamic hardness e_0 when finding the particle penetration depth h_p into the surface

$$h_p = v_0 R \sin\alpha (2\rho_2/3e_0)^{0.5} \tag{3.46}$$

Besides that, Ellermaa added the coefficient k_{60}, to improve the coincidence of test points with the calculated curves if $\alpha > 60^o$.

Ellermaa`s positions, however, are based on experimental results of a limited number of materials, in addition, he lacked the data on the values of e_0 for hardened steels.

Represented below are the suggestions of Kleis and Ellermaa on how to modify the energetic erosion theory, which cover only steels and fused coatings of ferrous materials as materials of practical interest. First, they compare experimental data in the conditions as close as possible to the assumptions of the theory. The most stable and reliable particle velocity is obtained when experimenting on the vacuum device VK-1 (maximum difference from the nominal velocity 1.5%). The results of experiments performed on this device with spherical white cast iron pellets are reported in [39]. The dynamic hardness of the 0.2% C carbon steel has been estimated at 3.2×10^9 J/m³ [10]. According to Ellermaa, assuming that $\tau_0/e_s = 0.067$ and operating with dynamic hardness in the equations, graph 1 in Figure 3.26a can be obtained. It is obvious that coincidence with test points is good only at low impact angles, while at large angles (especially at 90^o), the divergence is substantial.

According to the theory, at $\alpha = 90^o$ the velocity exponent is 2.0, independently of the material. However, the experiments give 2.3 as the value of the exponent. If $\alpha < 90^o$, and the member J_{II} is added to the formula, the exponent m_t is more than 2, which improves the coincidence of the data. The values of the exponents resulting from the theory are presented in Table 3.8.

Table 3.8. Dependence of exponent m_t on impact angle

Impact angle α^o	15	30	45	60	75	90
Exponent m_t	2.4	2.4	2.3	2.1	2.1	2.0

A comparison of experimental data with the theory shows that in the given case, the coincidence of the results occurs if v_0 = 25 m/s; above that, the values of I_v gained from the theory are smaller than those obtained in the experiments, below that, they are larger. For purposes of correcting, coefficient k_v must be introduced:

$$k_v = (v_0/25)^n \tag{3.47}$$

In the expression $n = m_e - m_t$, in which m_e denotes an experimental value and m_t the value of the velocity exponent derived from the theory. The graph in Figure 3.26b shows changes in the value of exponent n, depending on the angle of impact α, when tested with cast iron pellets.

Experiments with mild steel, in which round quartz sand is involved in erosive particles, are described in [39, 40]. In these experiments, sand from the Volga

quarry that has extremely stable properties and is especially additive-free (content of quartz 99.5%) was used. This sand was also used as standard sand in testing cement in Russia. In this case, if $\alpha > 60^o$, a considerable deviation between the theory and experimental results can be noticed, resulting from the differences in the velocity exponent (see Table 3.9).

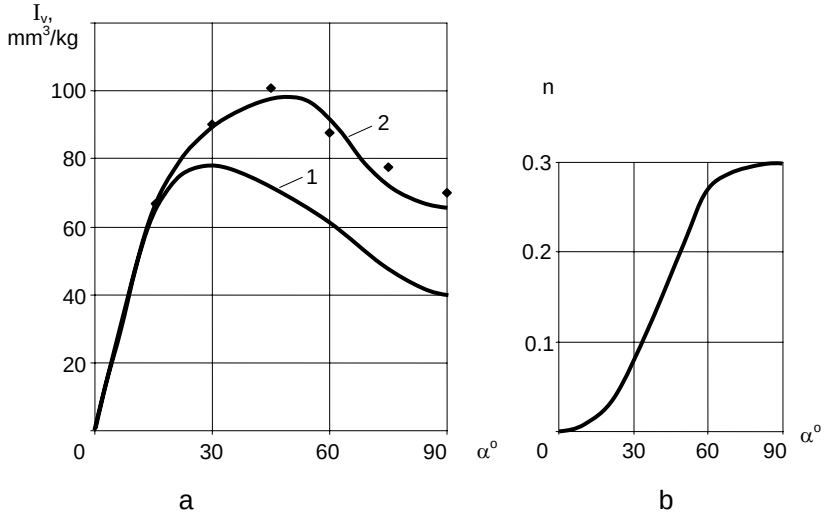

Figure 3.26a,b. Dependence of wear rate I_v of 0.2% C steel on the impact angle α: **a** – $v_0 = 120$ m/s, white iron pellets $R = 0.2$–0.3 mm: curve 1 – obtained by help of Equation 3.36, curve 2 – corrected with coefficient k_α and **b** – dependence of the exponent n on the impact angle α

Table 3.9. Dependence of velocity exponents m_e and m_t on impact angle

Impact angle α^o	20	30	45	60	75	90
Exponent m_e	2.6	2.5	2.4	2.5	2.6	2.7
Exponent m_t	2.4	2.45	2.3	2.2	2.1	2.0

Since with these particles $\alpha = 90^o$, the coincidence of experimental data and theory occurs at $v_0 = 60$ m/s, where the coefficient k_v can be expressed as $k_v = (v_0/60)^n$. The initial curves, those obtained as a result of correcting, as well as the test points are presented in Figure 3.27.

The examples above correspond to the wear conditions caused by round particles without any sharp corners or salient protuberances, and the shape coefficient is close to 1. Particles irregular in shape complicate the situation and make it difficult to determine, as it is the case with broken glass or artificial corundum, but also with quartz sand, an abrasive material frequently found in nature. Depending on the site of the deposit, sand particles vary in shape and, very importantly, in fracture resistance at impact (*i.e.*, a deficiency of internal structure). The more defects, the lower the abrasivity. The latter finds proof in Neiman`s [41] experiments on a centrifugal accelerator, in which abrasivity and grindability of 125 various sands from the Baltic and Northwestern Russia were studied. Differences varied up to 16 times, and when selecting sands of similar granularity, up to 5 times. In addition, it has been proved that the effect of the shape factor k_R

on the wear rate depends on the impact angle α. As a result, the shape factor must be corrected by means of coefficient k_α. Experimental data covering mild steel in Uuemõis [42] thesis, obtained on the vacuum device VK-1 are shown in Table 3.10.

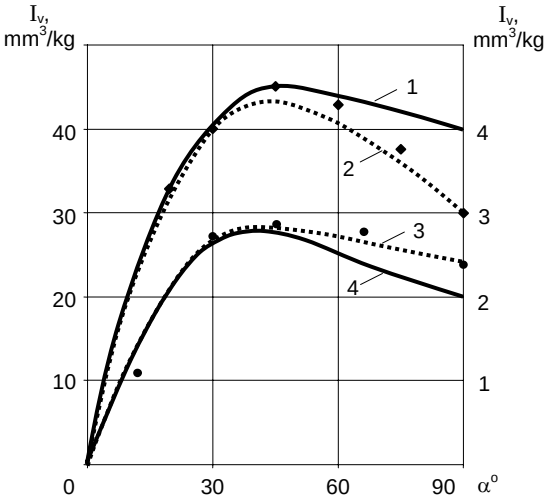

Figure 3.27. Dependence of wear rate I_v on the impact angle α, round quartz sand R = 0.3 mm, 0.2% C steel, e_0 = 3.2 GJ/m^3, τ_0/e_s = 0.067, k_R = 1.05. In the case of curves 1 and 2 – v_0 = 38 m/s and the right-hand scale is valid; curves 3 and 4 – v_0 = 82 m/s and the left-hand I_v scale. Curves 2 and 3 were corrected using exponent k_v.

Table 3.10. Values of coefficient k obtained for mild steel at v_0 = 120 m/s

Type of particle	$k = k_R \cdot k_\alpha$			
	α = 45-90° k_α = 1	α = 30° k_α = 1.3	α = 15° k_α = 1.4-1.6	k_R [38]
Corundum	1.8	2.4	2.5	1.6–1.9
Crushed glass	2.1–2.2	2.5	3.1	1.9–2.1
Crushed white cast iron	2.3–2.7	3.2	4.1	2.3–2.7

Table 3.10 shows that the values of the correction coefficient k_R remain more or less unchanged at impact angles from 45° to 90°, (which complies with data in [38], *i.e.* k_α = 1), at low impact angles, the values of k_α increase considerably. In contrast, when testing with hardened steel, Uuemõis [42] obtained the opposite result, *i.e.* the k_R of quartz sand and artificial corundum decreased with the decrease of α.

As a rule, sands of stable properties and inconsiderable defectiveness were used in laboratory experiments. As shown in Figure 3.28, with the help of various laboratory equipment highly compatible results can be obtained with various sands, which follow the theoretical curve of wear. In the given case, experiments made by Uetz and Gross [43] were performed with sand from Neckar on a pneumatic device, the rest of them with sand from the Männiku quarry in Estonia, using a centrifugal accelerator [44, 45] and the vacuum device VK-1 [42]. This means that deviations of a more serious nature can still be obtained, which is especially true for sands with particularly defective grains.

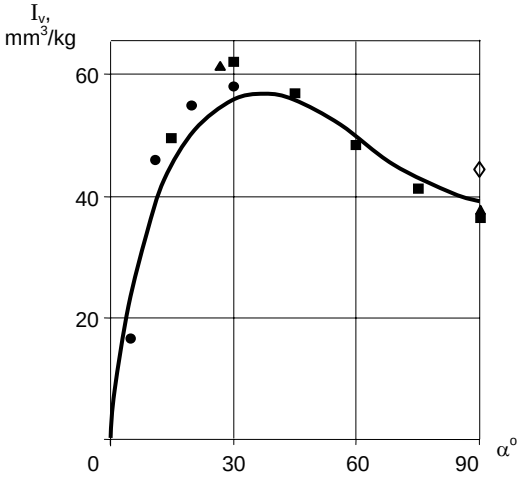

Figure 3.28. Dependence of wear rate I_v of mild steel on the impact angle α, v_0 = 100 m/s, quartz sand d = 0.4–0.8 mm; test points: ■ – Uetz/Gross, ● – Langeberg, ▲ – Kleis, ◊ – Uuemõis

In the fight against erosion, heat treated steels (hardened and tempered) as well as hard coating materials are of more interest than mild steel. In fact, no reliable data on their dynamic hardness were available until 2003. On the basis of data presented in Figure 3.9, the applicability of the theory on the above – mentioned materials was tested, whereas the values of τ_0/e_s were derived from the graph in Figure 3.25. Examples of comparison between the theory and experimental data can be found in [46]. First, the experimental data obtained with quartz sand on the vacuum device VK-1 [47] were compared with those resulting from the theory. The material to be studied was heat treated 0.8% C steel, 850 HV (Figure 3.29). In this case, $k_\varphi = k_d = 1$, but $k_H = 0.78$, derived from Equation 3.44. Applying the shape exponent k_R=1.4=const to the sand from the Männiku quarry, a theoretical curve was drawn. At impact angles α <75°, it runs much higher than the experimental data would allow for. For correction, exponent $k_\alpha = \sin^{0.4}\alpha$ will suit, which, actually, corrects the shape factor of particles k_R, and thus, according to [42], also decreases with the decrease of α.

Data obtained from testing steel on a centrifugal accelerator also coincide with theoretical curves at v_0 = 80 m/s fairly well if the same correction coefficient k_α is used (Figure 3.30a). However, with white corundum, where the effect of the impact angle is considerably higher, k_α is expressed as $k_\alpha = \sin^{0.8}\alpha$ (Figure 3.30b). The greatest deviation from experimental data in the latter occurs again at α = 90°. It is because no theory was available – the velocity exponent at this angle is 2. Thus, coefficient k_v is required, as was the case with mild steel (the real exponent in this case is 2.4). It is also noteworthy that the values of correction coefficient k_α are considerably higher for hardened steel than for mild steel [42].

In addition to hardened steel, we have at our disposal data on the erosion of fused surfacings materials, although only for a limited number of impact angles only (Table 3.11). In experiments on the centrifugal accelerator, rounded (k_R = 1.05) quartz sand was used, d = 0.5 to 0.9 mm, the velocity of particles v_0 = 54 m/s [49]. Numerical values of parameters τ_0/e_s were obtained as mean values of data in Figure 3.25, e_0 was found from Equation 3.9.

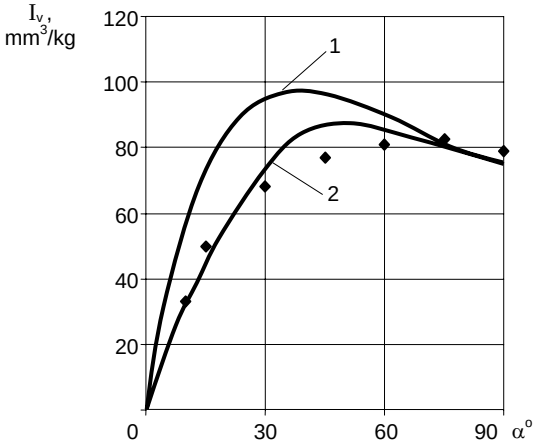

Figure 3.29. Dependence of wear rate I_v on the impact angle α: curve 1 – theoretical curve not corrected by means of coefficient $k_\alpha = \sin^{0.4}\alpha$; curve 2 – 0.8% C steel, 850 HV, $v_0 = 120$ m/s, quartz sand $d = 0.3$–0.6 mm

Table 3.11. Comparison of experimental and calculated wear rates I_v, mm³/kg of fused surfacings at erosion in a stream of quartz sand

Composition of fused surfacing on the basis of Fe	Hardness HV	Impact angle α^o		
		30	45	90
2.5% C, 25% Cr, 4% Ni, 4% Si	629	2.2/4.4	3.9/5.7	6.5/6.3
0.7% C, 20% Cr, 2% B	890	2.8/4.0	4.6/5.3	7.0/6.1
0.3% C, 2% Cr, 8% W	438	3.0/4.0	5.1/5.1	5.7/5.4
0.37% C, 10% Cr, 14% W	476	2.7/4.4	4.8/5.4	6.0/5.8

Note: The experimental data of I_v are given above the fraction line, the calculated data – below it

It can be seen in Table 3.11 that the theoretical and experimental data coincide satisfactorily at impact angles of 45° and 90°; however, at 30° it is not so *(i.e.*, experimental data are considerably lower than theoretical ones). It is difficult to explain the reasons. Test results may prove incorrect since the ratio of wear rates at α = 90° and 30° (1.9 to 2.9) is markedly greater than with hardened steels of similar hardness (1.2 to 1.5).

In conclusion, it is suggested that wear results obtained from experiments cannot always be replaced fully by the results obtained from either the initial or the modified Beckmann-Gotzmann erosion theory that still enables us to predict rather precisely the wear rate when varying parameters v_0, α, d and φ, with the properties of erosive particles experimentally predetermined (*i.e.* the correction coefficient k, including coefficients k_R, k_α and k_v, is known). In that case it is advisable to create a program package on the basis of these data, as described by Ellermaa [37].

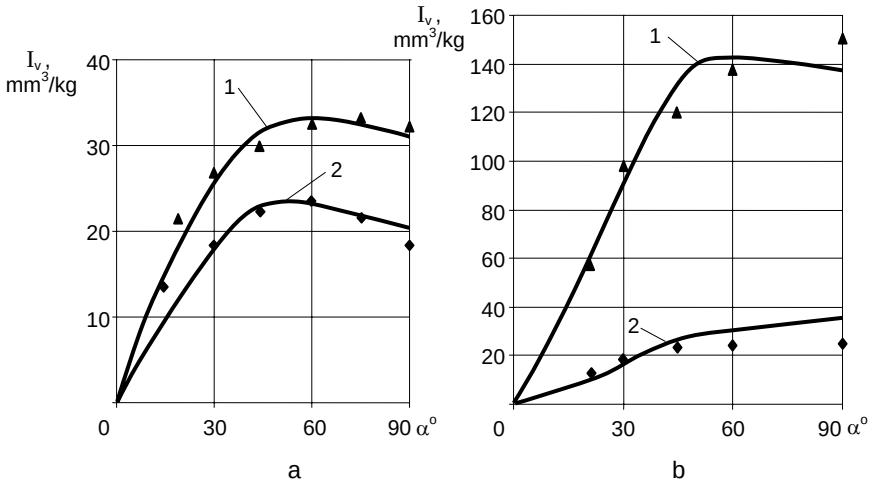

Figure 3.30a,b. Dependence of wear rate I_v on the impact angle of attack α; **a** – v_0 = 80 m/s: curve 1 – 0.8% C steel, 850 HV, quartz sand d = 0.3–0.6 mm, k_R = 1.4, k_H =0.78, test points from source [48]; curve 2 – 0.2% C steel, 434 HV, d = 0.4–0.6 mm, k_R = 1.3, test points from source [36]; **b** – 0.95% C, 820 HV, manufactured corundum particles d = 0.3–0.6 mm: curve 1 – v_0 = 80 m/s and curve 2 – v_0 = 40 m/s; k_R = 6.6, k_H = 1

3.4.3 Erosion by Brittle Behaviour

3.4.3.1 Modelling of Wear

The concept of plastic deformation is also applicable to brittle materials (ceramics); however, as proposed by Gotzmann and Beckmann, two important aspects must be added [50–52]. First, the wear particle removal mechanism caused by plastic deformation must be completed by a mechanism of brittle fracture. Second, if the existence of two mechanisms is accepted, a question arises when one or the other mechanism is predominant.

The modelling of the behaviour of brittle materials, such as ceramics, under solid particle erosion is based on:

a) The knowledge of the failure mechanisms (for brittle materials),
b) Selected parts of the theory of plastic deformation of metals

Threshold Values for Wear Mechanisms

Depending on the intensity of the impact process, the contact can lead to reversible or irreversible deformations in the surface area of the basic body. This is a principal classification, *i.e.* it is independent of material properties.

The reversible impact process generates only stresses in the target surface layer which lie below the yield strength, consequently, they are of elastic nature. However, this does not apply to an abrasive. Due to elastic deformations, material removal can be caused by fatigue. Nevertheless, this wear component is many times lower than that caused by irreversible deformations.

The process of material removal starts after a relatively small number of irreversible deformations, *i.e.* contacts between abrasive particles and the target.

Therefore, the first threshold values must be exceeded, so that generally serious wear can be established. Greenwood and Williamson [53] suggested the following analytic criteria. During an indentation process, *i.e.* pressing a hard particle into an elastic deformable basic body, the threshold value – hardness – contact hardness H_c can be determined. From hardness H_c, the elastic contact appears, while values under it lead to irreversible deformations:

$$H_c = E' \left(\frac{5\pi\rho_2 R_2 v_0^2 \sin^2 \alpha}{4E'} \right)^{0.2}, \tag{3.48}$$

where ρ_2 – density of the abrasive,
R_2 – radius of the spherical indenting body,
v_0 – velocity of the particle before impingement,
α – impact angle,
E' – reduced modulus of the elasticity of contact (see Equation 3.41).

$$E' = \frac{E_1 \cdot E_2}{\left(1-\mu_1^2\right)\cdot E_2 + \left(1-\mu_2^2\right)\cdot E_1} \tag{3.49}$$

where E_1 and E_2 are the Young's moduli,
μ_1 and μ_2 – Poisson's ratios of the material and abrasive, respectively.

Furthermore, the allocation of the respective mechanism is deterministic rather than stochastic. Cracks which reach far beyond the deformation cup are likely to occur and thus the brittle failure mechanism will be initiated. This probability p (probability of a fracture or crack initiation) is determined by the normal force F_n caused by the bulging particle in the contact. It is to be expected that besides force F_n, hardness H_1 and fracture toughness K_{1C}, the basic body material will have an influence on the probability of a crack initiation and on the transition behaviour. Thus, with the contacts that cause crack initiation and the total number of irreversible contacts, four variables exist, which influence the process. This number of variables can be reduced according to the Buckingham theorem of two dimensionless parameters, such as probability p and the value

$$\frac{const \cdot F_n \cdot H_1^3}{K_{1C}^4}.$$

In addition it is assumed that between these dimensionless parameters the Weibull distribution is valid and expressed in the form

$$p = F(F_n) = 1 - \exp\left\{ -\left(\frac{F_n \cdot H_1^3}{const \cdot K_{1C}^4} \right)^m \right\} \tag{3.50}$$

with parameters $\frac{const \cdot K_{1c}^4}{H_1^3}$ and m. According to [51], the appearing constant can obtain values from $(0.5–1.5)\times 10^3$.

According to [54], the fracture probability p can also be given in the following form:

$$p = F(F_n) = 1 - \exp\left\{-\left(\frac{0.6 \cdot F_n}{F_C}\right)^{\alpha}\right\}, \tag{3.51}$$

where F_n – the normal force,
F_C – the minimal force of crack initiation,
α – Weibull distribution shape parameter.

With ceramics, these cracks can hardly be recognized, consequently, Equation 3.51 cannot be used in practical wear problems.

Consideration of Single Mechanisms

The effect of the particle stream is substituted by a superposition of the effects of single spherical particles with radius R. Figure 3.31 shows the kinematical and geometrical dimensions of the contact process already explained, the velocity of particle v_0, impact angle α, radius of the abrasive particle R, plastic penetration depth h_p, radial crack length C_r, and the depth of the lateral crack h_l. For both wear rates I^B (for wear by brittle fracture) and I^P (for wear by plastic deformation), formulae in [51] can be used.

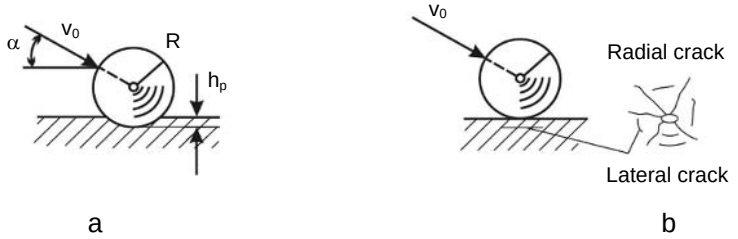

Figure 3.31a,b. Model of contact by impact with a ceramic material with: **a –** small (plastic shear deformation) and **b –** great probability of fracture (brittle fracture dominating)

The plastic penetration depth of indentation h_p in the basic body can be calculated using Equation 3.40. For large contact surfaces and homogeneous materials, macrohardness can be used as hardness H_1. With small contact surfaces or diverse materials, the local hardness of the surface must be taken into consideration. With ceramics that is always the case.

Hardness Distribution

The contact radii, as they appear with the wear caused by solid particle erosion, lie in general in the scale of grain dimensions. Therefore, hardness distribution must be considered. If one looks at hardness as a random variable, the heterogeneity of the material and available defects (microcracks, cavities, inclusions, grain size, grain distribution, *etc.*) must be taken into account. With monotonous distribution of the average hardness in the contact area, the Weibull distribution is acceptable in the following form:

$$F(H) = 1 - \exp\left\{(H/H_0)^m\right\}. \tag{3.52}$$

According to Equation 3.52, the distribution function is shown in Figure 3.32. For wear calculation, the values of *F(H)* around zero and one can be excluded, so that the distribution function is to be looked for with in the range of $\varepsilon \le F(H) \le 1-\varepsilon$. In practice, the value of ε = 0.03–0.05. Therefore, the hardness of the area H'... H'' must be taken into consideration. The limit values are

$$H' = H_0 \cdot \exp\left\{\frac{1}{m} - \ln\left[\ln(1-\varepsilon)\right]\right\} \tag{3.53}$$

$$H'' = H_0 \cdot \exp\left\{\frac{1}{m} - \ln(-\ln\varepsilon)\right\} \cdot \tag{3.54}$$

With contact hardness Equation 3.48

$H_C > 5H'$ (HV) – plastic contact is dominant
$H_C \le 5H'$ (HV) – the contact is elastic-plastic
$H_C < H'$ (HV) – the contact is elastic

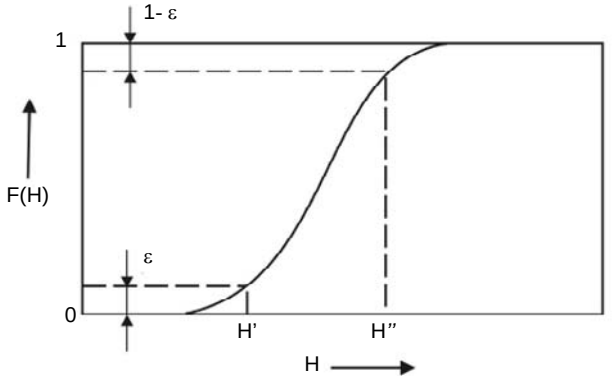

Figure 3.32. Hardness distribution function of a material

If the contact is irreversible, the process can react in two ways. It can follow one of the two alternative mechanisms: small plastic deformation or dominating brittle fracture.

If the threshold value of contact hardness, calculated according to Equation 3.48, $H_C \le H'$, the contact is reversible. For all values of $H_C > H'$, the contacts are irreversible. For the hardness values $H' < H_C < H''$, the area for the wear calculation H'... H_C will be used and for $H_C > H''$, the area H'... H'' will be taken into consideration. Therefore, the irreversible effective hardness area is either

$$\Delta H = H_C - H' \tag{3.55}$$

or

$$\Delta H = H'' - H' . \tag{3.56}$$

Wear by Brittle Fracture

As an approximated model for material removal due to impact, a cylinder shape cavity will be used. As a radius of the cylinder, the middle length C_r of a radial crack outgoing from the impact centre will be employed. Cylinder height h_l corresponds to the depth of the cavity caused by the surface-parallel lateral crack (see Figure 3.31). According to [54], the middle length of the radial crack C_r can be calculated as

$$C_r = \lambda \left(\frac{v_0^2 \cdot R_2^2 \cdot \rho_2}{K_{1C}} \right)^{2/3} . \tag{3.57}$$

Constant λ depends on the crack geometry; its value is approximately 0.5. The depth of a lateral crack h_l corresponding to the penetration depth h_p of a particle can be calculated by

$$h_l = R_2 \cdot \sqrt{3} \cdot \left(\frac{h_p}{R_2} \right)^{0.5} . \tag{3.58}$$

Wear rate at brittle fracture I^B can be calculated using Equations 3.57 and 3.58 with an assumption that every crack-propagating contact will lead to material removal:

$$I_g^B = \frac{\Delta m}{M} = \frac{\pi C_r h_l \rho_1}{(4/3)\pi R_2^3 \rho_2} = 0.75 \cdot \sqrt{3} \frac{\rho_1}{\rho_2} \left(\frac{C_r}{R_2} \right)^2 \cdot \left(\frac{h_p}{R_2} \right)^{0.5} \tag{3.59}$$

Equation 3.58 is valid only for the brittle fracture phase. If one uses the values of C_r (Equation 3.57) and h_p (Equation 3.40), the exponential dependence of the wear rate on the particle velocity becomes visible. It is also evident that an enlargement of the kinetic energy of an abrasive particle will lead to an enlargement of the indentation depth. Then the effective force as well as the portion of brittle fracture grow in the impact area. The rise of the kinetic energy can be reached by an enlargement of the speed. With the identical kinetic energy of the particles, the share of the brittle fracture grows with the impact angle at irreversible deformations.

By real brittle materials, the elastic deformation (at low velocities) and intensive brittle fracture are accompanied with plastic deformation.

The wear by plastic deformation is calculated on the basis of the wear model for ductile materials [38]. With this model, material removal is caused on the one hand, by the effects of plastic deformation on the penetration of the abrasive particles into the basic body and on the other hand, by the rebound from it. Also, this model enables us to take into account hardness distribution in the basic body surface. Material properties, such as shear energy density e_s and shear strength τ_0, appear here. We can interpret them as mechanical energy, which can accumulate in a unit material volume before it is abraded. With ductile materials, it has turned out suitable to use the relation $(e_s\, \tau_0)^{-1}$ as a specific shear energy density.

Wear rate at plastic deformation I^P can be calculated using Equation 3.36.

For the penetration depth, Equation 3.40 and for hardness H_i, the values from the distribution function at Equation 3.52 are used.

To distinguish between elastic and plastic contact, the following relation [15] will be used:

$$\frac{h_p}{R_2} \geq < \left(\frac{H_1}{E'}\right)^2 \tag{3.60}$$

≥ relation means plastic contact.
< relation means elastic contact.

To investigate hardness distribution, the area ΔH will be divided according to Equations 3.55 and 3.56 in n subranges with average hardness H_i (i=1 ... n). The total wear rate consists of the portion of brittle fracture with the weight p and a portion from the plastic deformation with weight 1–p.

$$I^{B\&P}(H_i) = \left\{ I^B(H_i) \cdot p(H_i) + I^P(H_i) \cdot [1 - p(H_i)] \right\} \times f(H_i) \cdot \frac{\Delta H}{n} \tag{3.61}$$

where

$$f(H_i) = F'(H_i) = \frac{m}{H_0} \left(\frac{H_i}{H_0}\right)^{m-1} \cdot \exp\left\{ -\left(\frac{H_i}{H_0}\right)^m \right\} \tag{3.62}$$

is the probability density function of the Weibull distribution (see Equation 3.52).

3.4.3.2 Verification of the Model

Checking of the model of erosion wear on brittle materials assumes that both of the parameters inserted to the wear calculation model and the comparative test results are obtained using the same material. As data on the composition of engineering ceramics and some properties to be introduced to the calculation formulae are incomplete, the model is difficult to check. The results obtained by modelling with sheet glass and using hardness distribution were quite correct.

Gotzmann [51] obtained the required data from the model and tests of Sheldon and Gulden [55, 56], as analogy was used for hardness distribution. Otherwise, results from the comparison are interesting, because they involve up-to-date progressive ceramic materials tested with different solid particles and at different impact velocities. The results provide insight into the expected mechanisms of wear in different intervals. Taking into consideration approaches concerning hardness distribution proposed by Beckmann and Dierich [57], the above calculation method was simplified and improved.

The application of the model on Torgan sheet glass, a brittle material, is based on experiments by Sheldon and Finnie [55]. The impact velocity was 152.5 m/s; the hardness distribution based on hardness measurements is expressed by the regression equations

$$H_0 = 3 + 4.577 \cdot r^{-0.587}$$

$$m = \frac{35.571 \cdot r}{5.191 + r},$$

where contact radius r is in mm and H_0 in GPa.

The other parameters were

F_c = 3 N; λ = 0.5

α = 4.0; τ_0/e_s = 0.2

The results are shown in Figure 3.33, where calculations are supplemented with the fracture probability.

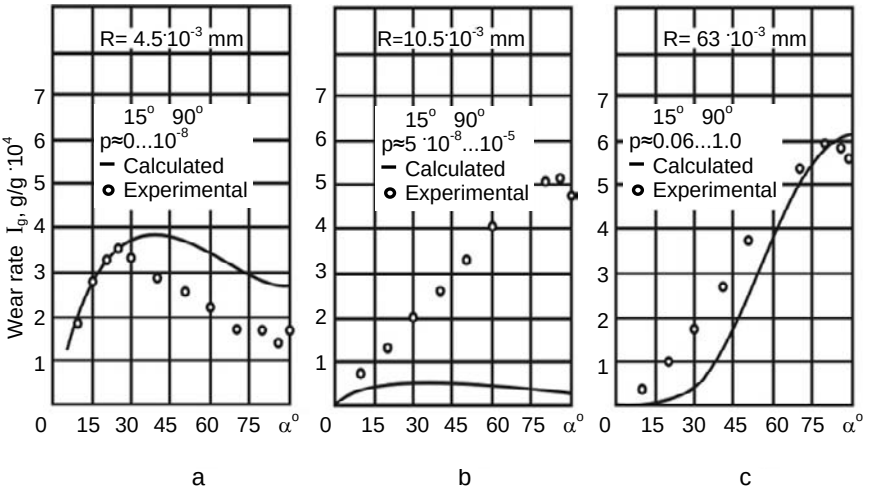

Figure 3.33a–c. Comparison of calculated and Sheldon's and Finnie's experimental [55] wear rates by sheet glass; abrasive – SiC, jet velocity – 152 m/s

Figure 3.33 clearly shows how a brittle fracture mechanism by relatively large abrasive particles is transformed to plastic deformation by small particles.

It is obviously difficult to determine the value of F_c, but it is very important in terms of prognostication of the transition area. In Figure 3.33b, with the radius of particle $R = 1.05\times10^{-2}$mm and F_c= 3 N, the calculation suggests a plastic deformation; at the same time, experimental results confirm the acceptance of a brittle fracture. Decreasing the value of F_c ten times, as compared to the value used earlier, the real wear level and tendency were obtained. The following conclusion can be drawn: US-glass has higher fracture probability.

Another example demonstrating the application of the model is based on ceramics pairs (hot pressed Si_3N_4/SiC, reactive sintered Si_3N_4/quartz, MgF_2/quartz), studied by Gulden [56]. The parameters given in Table 3.12 are complemented with K_{1c}^4/H^3.

Table 3.12. Data of materials used in the calculation of wear

Material	E GPa	K_{1c} MPa·m$^{0.5}$	H^a GPa	ρ g/cm^3	K_{1c}^4/H^3 ×10^{-3}N
Si_3N_4, hot pressed (hp)	320	5	16	3.2	0.153
Si_3N_4, reactive sintered (rs)	170	2.2	8	3.2	0.046
MgF_2, hot pressed (hp)	117	1	6	2.5	0.0046
Quartz, natural	95	0.7	6	2.5	0.0011
SiC	420	3	23	2.7	0.0067

[a]Macrohardness

Hardness distribution was estimated as with glass – by microindentation. Table 3.12 presents the values of macrohardness. The regression equations for hardness distribution are as follows:

MgF_2/quartz	$H_0 = 6 + 15 \cdot r^{-1.0}$;	$m = \dfrac{6r}{r+12}$
hp Si_3N_4/SiC	$H_0 = 16 + 60 \cdot r^{-1.0}$;	as above
rs Si_3N_4/quartz	$H_0 = 8 + 50 \cdot r^{-1.1}$;	as above

Calculation results and Gulden's [56] experimental results are given in Figure 3.34.

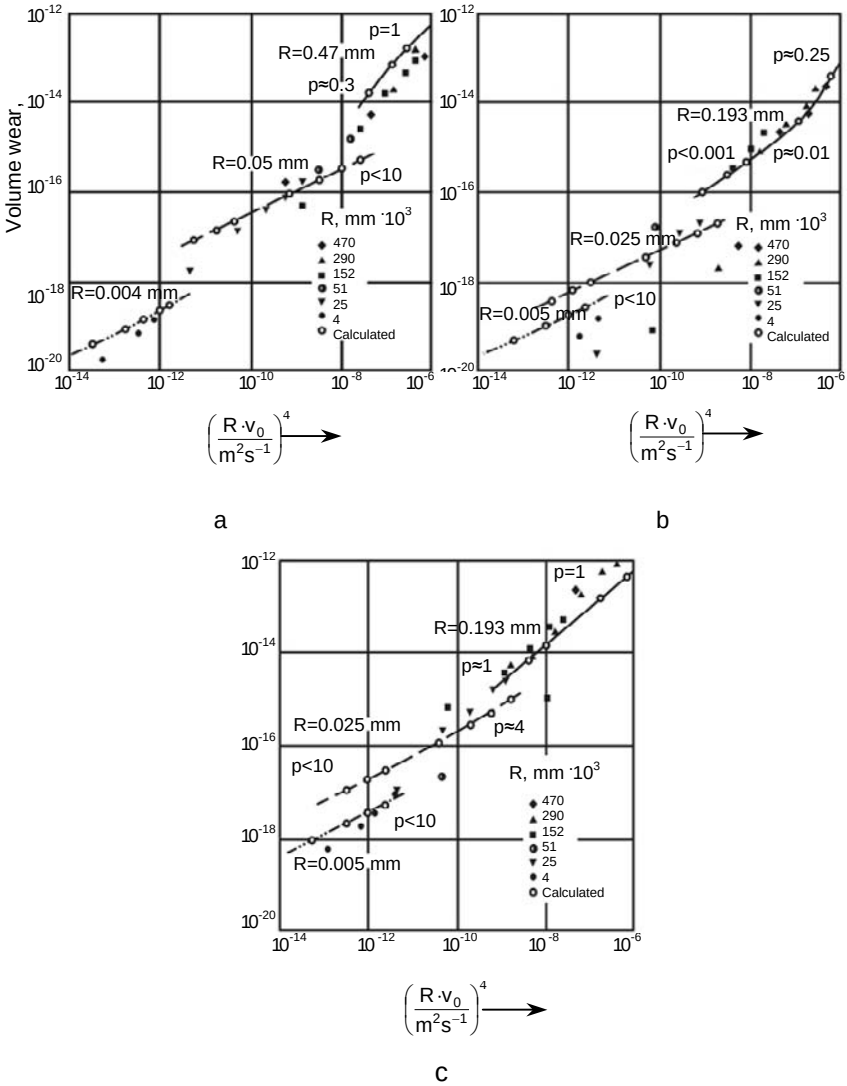

Figure 3.34a–c. Dependence of Gulden's measured [56] and calculated volume wear on parameter $(R \cdot v_0)^4$: **a** – pair hp Si_3N/SiC; **b** – pair rs Si_3N_4/quartz; **c** – pair hp MgF_2/quartz

The conclusions drawn from the comparison of the calculated and experimental results of different pairs are as follows:

1. By the pair **hp Si_3N_4/SiC**, the coincidence at all radii of particles is sufficiently good (at constant radius, the curves based on calculations are flatter, with a slope smaller than with experimental ones). At the same time, it must be kept in mind that hardness distribution was obtained through appraisal. It is possible that at smaller contacts, hardness values increase more than suggested and the wear decreases. By the small radii of particles and $\tau_0/e_s = 0.5$, good coincidence was obtained. It gives evidence that very hard materials show higher resistance to plastic deformation. The calculated values of p revealed that transition from one mechanism of wear to another takes place approximately in the middle section of the abscissa axis.

2. By the pair **rs Si_3N_4/quartz**, the coincidence of results obtained through appraisal of parameters was good. It is necessary to decrease parameter F_c following from expression K_{1c}^4/H^3, from 50 N to about 150 N to describe the sharp transition from brittle fracture mechanism to plastic with particles of large radius. Gulden [56] described the material as porous, pores being barriers for crack propagation; it is an answer to the sharp rise of the curve. The coincidence is very good at small τ_0/e_s values (about 0.1); so the plastic deformation mechanism is connected with a large area, where the wear resistance is high.

3. By the pair **MgF_2/quartz**, it was necessary to decrease the values of F_c (from 5 to 2 N), where $\tau_0/e_s = 2$, that indicates decreased wear resistance in the plastic area. It is in accordance with the above considerations. The difference in the calculated and experimental results (the calculated curves are flatter) indicates the necessity to correlate hardness distribution parameters.

As a result of verification the model by Gotzmann [51], the following parameters characterizing materials are necessary:

- Parameters of hardness distribution,
- Fracture toughness K_{1c} characterizing of the brittle fracture mechanism,
- Fracture probability parameter p, preferably on the value of F_c,
- Shear energy density τ_0/e_s, characterizing material removal by plastic deformation.

3.4.4 Calculation of Erosive Wear of Composite Materials

Tribological materials and coatings are typical of heterogeneous structure: hard particles in a relatively soft matrix. Typical representatives of wear resistant coatings are nickel and cobalt self-fluxing alloy-based and carbide-based with a metal binder. First, tungsten carbide (WC) based hardmetal type or self-fluxing alloys-based coatings containing WC, applied by spray and fusion methods, are used. The first type of coatings is dominated by plastic contact and the model of plastic deformation is applicable. With the hardmetal type coatings, where carbide content exceeds 50%, brittle fracture of carbide is dominating. With composite metal-matrix structures, both models must be taken into consideration: by a relatively soft metal matrix – the model of plastic deformation, by the hard-phase – the brittle behaviour model of wear. Wear of metal matrix may be calculated by Equation 3.36. To obtain the weight wear rate, the material density ρ_1 is introduced.

According to Equation 3.36, wear rate calculation of the metal matrix at plastic deformation takes the following form:

$$I_g^P = \frac{3}{4} \cdot \frac{\rho_1}{\rho_2} \cdot \frac{\tau_0}{e_s} \left[6.81 \sqrt{\frac{h_p}{R_2}} \cdot \frac{2\rho_2}{3H_1} v_0^2 \cdot \cos^2 \alpha + 0.85 \left(\frac{h_p}{R_2} \right)^2 \right] \tag{3.63}$$

As was mentioned above, this wear model is valid in the conditions $H_2 > 1.6\ H_1$.

The wear of the hard phase (reinforcement) consists of a brittle fracture and plastic deformation, calculated by Equation 3.61.

By both calculations (I_g^P and $I_g^{B\&P}$), the mean values of hardness intervals H_i from the distribution function at Equation 3.52 were used. The total wear rate was obtained summarizing the calculated results. First attempts to calculate of wear of composites was done in [58, 59]. The composite metal-matrix structures with large reinforcement particles and small hard phase particles in iron- and nickel-alloy based matrices were under study in [60].

In the calculations the following materials served as examples:

- FeCr-alloy based metal-matrix PM composite consisting of about 20 vol% VC micrometrical particles and WC reinforcement with particle size about 100 μm,
- Thermal spray-fused self-fluxing NiCrSiB-alloy based composite coating consisting of about 20 vol% (WC-Co) hardmetal reinforcement with particle size about 50–100 μm and dissolved small micrometrical WC particles.

Table 3.13 shows the initial data for the calculation of the erosion wear of the above mentioned composite coating and Figure 3.35 shows the microstructure of the MMC material and coating.

Table 3.13. Initial data for calculation of erosive wear of composite metal-matrix structures

Composite constituents	ρ_1 **kg/m^3**	H_1 **(HV) GPa**	E_1 **GPa**	μ_1	K_{1c} **MPa·m$^{0.5}$**	**Reduced modulus of elasticity** E'**, GPa**	**Contact hardness** H_c**, GPa**		K_{1c}^4/H_1^3 **N**
							$\alpha = 30^o$	$\alpha = 90^o$	
Commercial NiCrSiB-alloy coating	8900	4.8	217	0.21	-	-	-	-	-
Commercial tool steel WR-6	7400	3.8	220	0.28	-	-	-	-	-
Matrices									
- NiCrSiB-matrix	8900	5.6	175	0.21	75	61.5	2.8	2.4	180
- Cr- steel matrix	7400	6.8	220	0.28	15	66.8	1.8	2.1	161
Hard phases									
- WC hard phase	15800	24.5	680	0.22	5–11	82.0	3.5	3.0	8.7×10^{-5}
- WC-15Co hard phase	14500	14.0	560	0.23	12	80.1	3.4	2.96	7.6×10^{-3}
Quartz sand R_2 = 0.05–0.15 mm	2200	H_2 11.5	E_2 90	μ_2 0.17	0.7	-	-	-	15.8

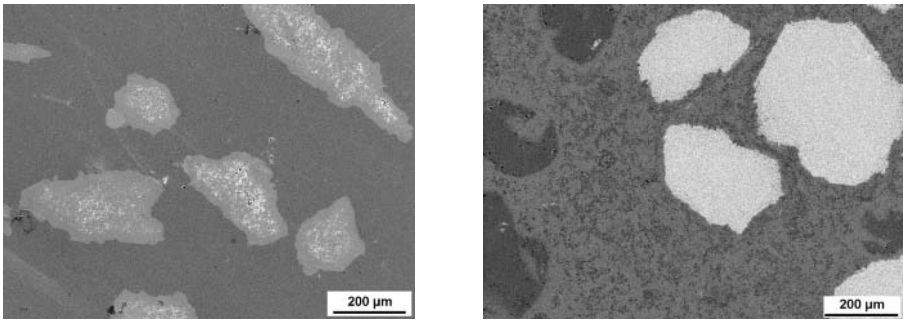

a b

Figure 3.35a,b. Micrograph of the cross-section of: **a** – (Cr-steel-VC) + WC MMC material, **b** – NiCrSiB- (WC-Co) MMC coating

Hardness and Fracture Thoughness Characterisation

Depending on the microstructure of the Cr-steel based MMC material with multimodal reinforcements (sub-micronical VC carbides and WC particle sizes of some hundreds of microns), different hardness measurements (macro-, micro- and nanoscale) for the evaluation of hardness distribution of the MMC material were carried out.

Hardness measurements in the *macrohardness* range of the MMC material with Vickers hardness tester at load 294 N were performed. Hardness values varied from 5925 to 6927 MPa. The results were divided into six groups. The parameters of the Weibull distribution function at Equation 3.52 as the most suitable mathematical function to describe the distribution of hardness values, median hardness H_0 and the shape parameter m were found to be 6.3 and 3.0 respectively. Figure 3.36 demonstrates the fit of experimental and calculated distribution functions. Following from the narrow hardness interval later in erosion rate calculations mean hardness (6426 MPa) was used.

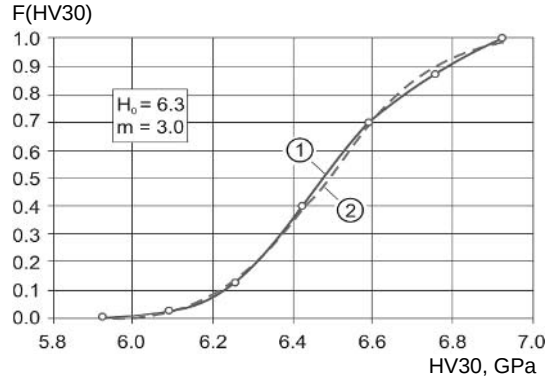

Figure 3.36. Experimental (1) and theoretical (2) hardness HV30 distribution of MMC material

Hardness measurements in the *microhardness* range of the MMC material with the universal hardnessmeter Zwick 2.5 at a load 9.8 N and microhardnessmeter

Micromet 2001 at a load of 0.98 N were performed. The hardness values taken into consideration varied from 4073 to 12,336 and from 3080 to 22,490 MPa at universal hardness HU1 and microhardness HV0.1 respectively.

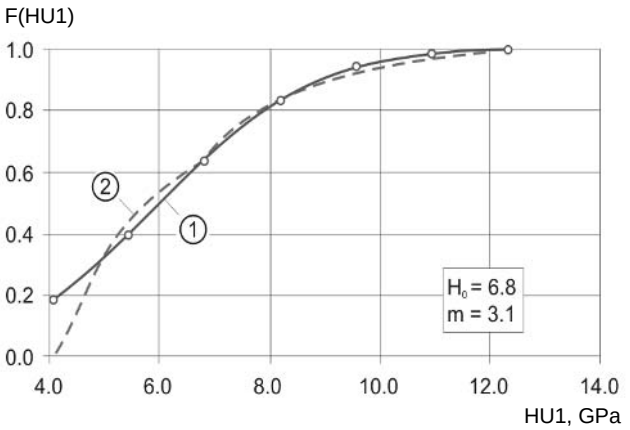

Figure 3.37. Experimental (1) and theoretical (2) universal hardness HU1 distribution of MMC material

For experimental and theoretical microhardness distribution functions, given in Figures 3.37 and 3.38, the shape parameters m, and median hardness H_0 were found.

The interval mean values of universal hardness of measured hardness values of MMC measured by depth sensing hardnessmeter Zwick Z 2.5 at load 9.8 N varied from 4762 to 11,650 MPa.

As follows from Figure 3.37 there exists a good coincidence between experimental HU1 and the theoretical values with median hardness H_0 = 6.8 and shape parameter m = 3.1.

The interval mean values of microhardness of MMC material measured by microhardnessmeter at load 0.98 N varied from 4540 to 19,040 MPa.

The best coincidence of the experimental and theoretical Weibull distribution values was observed with median hardness H_0 = 12.0 and shape parameter m = 2.0. The coincidence between theoretical and experimental microhardness HV0.1 distribution curves can be witnessed only at higher hardness values (Figure 3.38a).

Following analysis of the microhardness HV0.1 test results, the measurements were divided in to two distinctive groups: 67 measurements between 3080 and 5722 MPa (metal matrix) and 23 measurements between 8818 MPa and 20,490 MPa (hard phase). Later, the second group of hardness values was divided into six hardness intervals. The length of the interval was 1954 MPa. The hardness distribution functions of hard phase are given in Figure 3.38b. The median hardness H_0 and shape parameter m were found. The best coincidence of the experimental and theoretical two-parametrical Weibull distribution values of microhardness of hard phase was observed if H_0 = 17.0 and m = 6.0 (Figure 3.38b).

Hardness measurements in the *nanohardness* range of the MMC material were done using the MTS nanoindentation tester and Berkovich indentor. Tests were performed under load control. The limit was set on 100 nm, after achieving the required indentation depth, the load was removed.

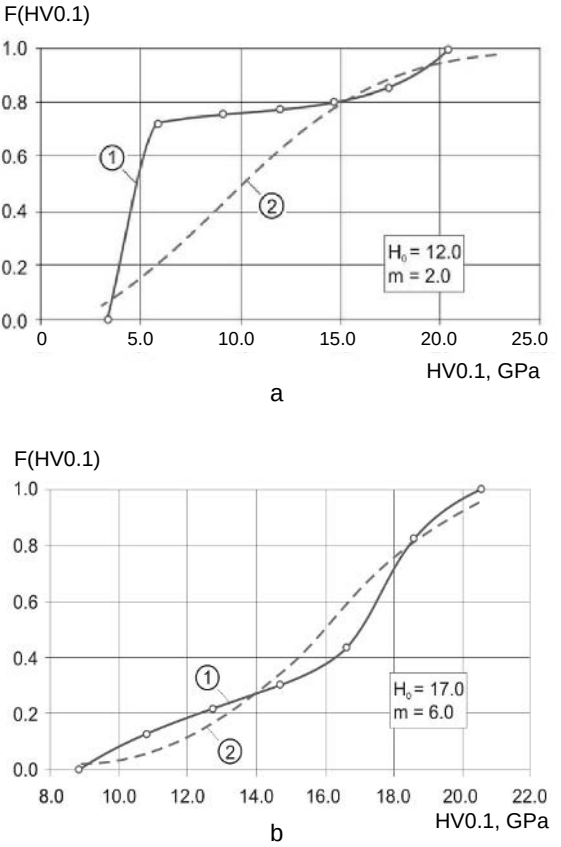

Figure 3.38a, b. Experimental (1) and theoretical (2) microhardness HV0.1 distribution of: **a** – MMC material and **b** – hard phase

The measured hardness values were in the range of 1380 to 10,010 MPa. The total hardness range was divided into $n = 6$ intervals. The median hardness H_0 and shape parameter m values of the nanohardness distribution function were calculated. Figure 3.39 illustrates the nanohardness distribution function . The best coincidence of the experimental and theoretical Weibull distribution values was observed if median hardness $H_0 = 4.5$ and shape parameter $m = 2.4$.

The indentation hardness measurements of MMC material carried out, using different load scales, differed from each other in order of magnitude, showed that the minimum and maximum hardness values measured on the same sample may differ significantly, depending on the used hardness scale. The conclusion from hardness measurements is following – indentation methods and parameters selection has based on a presumption that the wear marks caused by the erodent and the indents produced by the hardness measurement procedure must have similar geometry, *e.g.* similar depth and/or diameter.

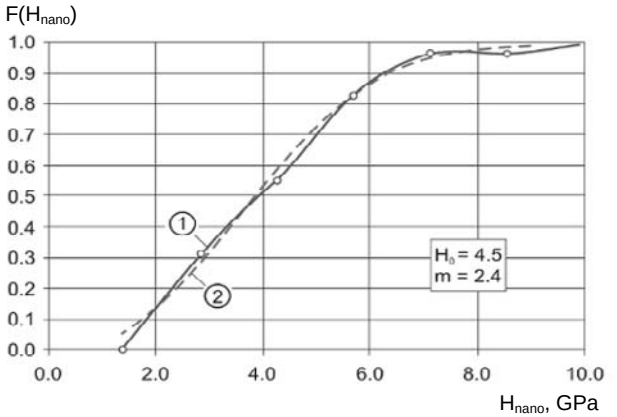

Figure 3.39. Experimental (1) and theoretical (2) nanohardness distribution of MMC material

The indentation hardness measurements of the FSF NiCrSiB-alloy based MMC coating were obtained using a depth sensing indentation equipment Zwick Z2.5. An indentation load of 9.8 N was applied. The hardness of the area from 570 to 7855 MPa was taken into consideration. Hardness ranges with cumulative frequency were calculated. The theoretical and experimental hardness distribution functions are shown in Figure 3.40.

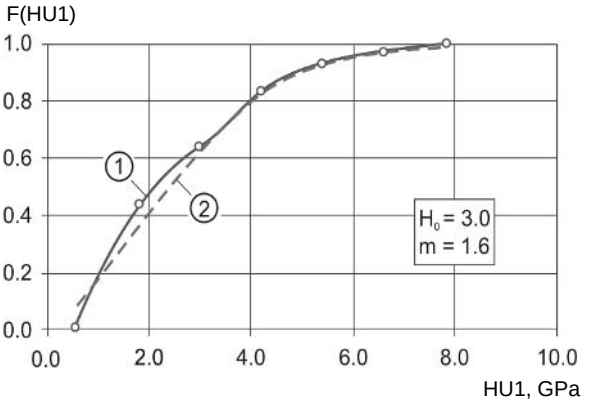

Figure 3.40. Experimental (1) and theoretical (2) hardness distribution of MMC coating

The parameters of the hardness HU1 distribution function were calculated and the values for median hardness H_0 and shape parameter m were found. The best coincidence of the experimental and theoretical Weibull distribution values of hardness was observed if median hardness $H_0 = 3.0$ and shape parameter $m = 1.6$. As follows from Figure 3.40 there exists a good coincidence of experimental and theoretical values of HU1.

The fracture toughness of single WC particles with a size of some hundreds of µm was determined using Vickers indentation method (also referred as the Palmqvist method) [61]. In the measurements of indents (Figure 3.41a) and radial cracks caused by indentations (Figure 3.41b) SEM was used.

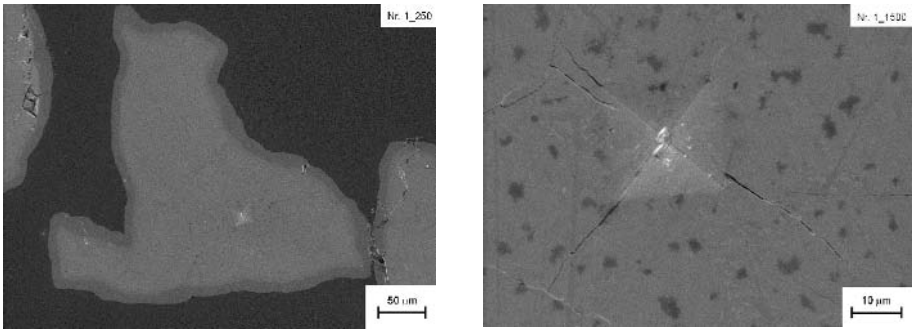

a b

Figure 3.41a,b. Vickers indents on the WC hard phase particle of MMC material at different magnifications

The fracture toughness was calculated according to Equation 3.64:

$$K_{1c} = 0.0122(E/H)^{2/5} \cdot P/a \cdot l^{1/2} \,, \tag{3.64}$$

where H is Vickers hardness HV.

Table 3.14. shows the results of the calculations of fracture toughness of the WC and probability of fracture under static indentation conditions at load 10 N. Numeric analysis of the probability p value shows, that it is highly dependent of K_{1c}.

Table 3.14. Results of fracture toughness and fracture probability calculations of hard phase in the MMC material (Cr-steel-VC)+WC

H_1, GPa	K_{1c}, MPa·m$^{0.5}$	$K_{1c}^4/H_1^3 \times 10^{-3}$, N	Probability p at HV0.1
12.5	4.4	0.1919	0.94
17.0	2.8	0.0125	0.17

Attempts were made to determine the fracture toughness K_{1c} value of the reinforcing phase – hardmetal of the MMC coating. Using different loads several Vickers indents were produced in the WC-Co hardmetal particles with size of 100–300 µm (Figure 3.42). The load varied from 0.98 N to 49 N and diagonal of the indents varied from 5 to 150 µm. Due to the relatively high toughness of the hardmetal-type reinforcement no radial cracks were produced. Higher loads were not applicable as they resulted to the fracture of the hardmetal particles. As the result, K_{1c} value from the literature (about 12 MPa·m$^{0.5}$) was used in erosive wear calculations.

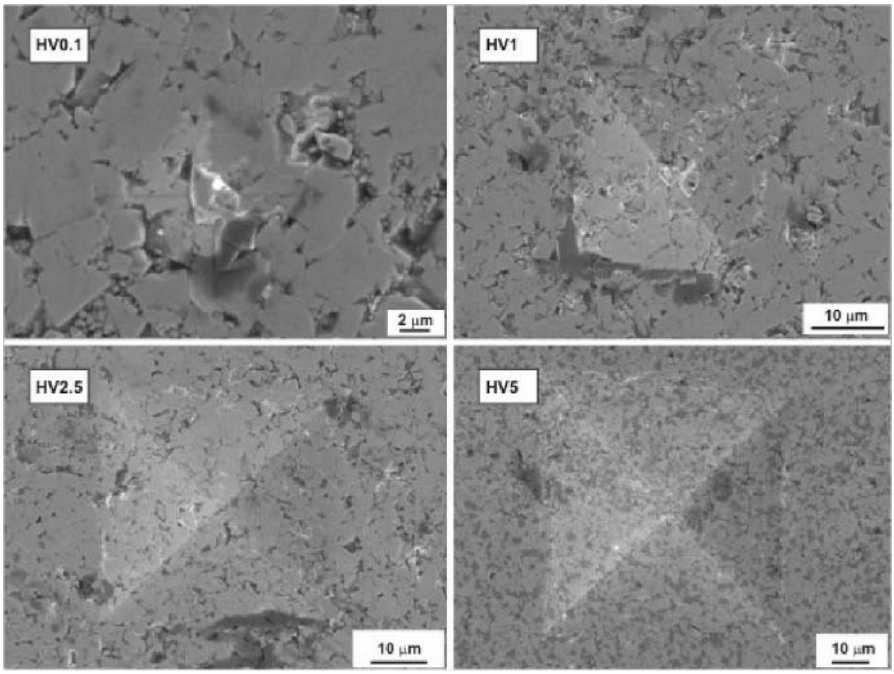

Figure 3.42. Vickers indents on the (WC-Co) hard phase particle of MMC coating at different loads

Calculation Principles

The plastic contact is dominated by the metal-matrix of MMC material and coating and the model of plastic deformation is applicable. With the hardmetal and hardmetal type coatings, where carbide content exceeds 50%, brittle fracture of carbide is dominating. With composite metal-matrix materials, both models must be taken into consideration: by the relatively soft metal matrix – the model of plastic deformation (Equation 3.63), by the hard phase – the models of plastic deformation and brittle fracture (Equation 3.61).

The wear rate of hardness of hard phase consists of the portion of brittle fracture with weight p and a portion from the plastic deformation with weight $1–p$.

As the range of mean hardness values taken into consideration was divided into n=6 intervals, for these six mean values of hardness intervals, the plastic penetration depth of indentation h_p (Equation 3.40), the corresponding radii of indentation r_n (Equation 3.65)

$$r_n = R_2\left[\left(h_p / R_2\right)_i - \left(h_p / R_2\right)_i^2\right] \tag{3.65}$$

the normal force F_n of crack initiation (Equation 3.66)

$$F_n = H_n \cdot \pi \cdot r_n^2 \tag{3.66}$$

and the probability of brittle fracture p according to Equation 3.50 were found.

The values of parameters τ_0/e_s were determined (Table 3.15) by help of Figure 3.25 according to their mean hardness: correspondingly about 4540 and 13,240 MPa for MMC material; 3000 and 6600 for MMC coating. For the metal matrix and the hard phase the values of τ_0/e_s 0.1 and 0.06 were chosen for matrices and 0.5 an 0.15 for hard phase, respectively.

Table 3.15. Values of τ_0/e_s

Type of material	Metal matrix	Hard phase
(Cr-steel –VC)+WC	0.1–0.13	0.3–1.0
NiCrSiB+(WC-Co)	0.05–0.1	0.1–0.3

Experimental Study of Erosive Wear

Modelling of erosive wear (wear rate and mechanism) was conducted in an abrasive particle jet.

Solid particle erosive tests have been performed in a conventional centrifugal-type four-channel accelerator, in which up to 15 specimens can be treated simultaneously under identical testing conditions. The abrasive – quartz sand with particles size 0.1–0.3 mm was used in these experiments.

Steady state erosion rate was studied as a function of the impact angle at abrasive particle velocities of 50 and 80 m/s. Steel of 0.45% C (200 HV) was adopted as a reference material. Parameters of the tests are given in Table 3.16.

Table 3.16. Parameters of erosive wear

Parameter	Value
Abrasive	Quartz sand,
Particle size, mm	d = 0.1–0.3
Particle hardness, HV	1100–1200
	733–880 HV0.1 (measured)
Particle velocity, m/s	
By (Cr-steel)+WC MMC material	50
By NiCrSiB+(WC-Co) MMC coating	80
Impact angles, degree	20, 30, 45, 60, 75, 90

Calculation of Erosion Rate of MMC Material

Based on the hardness distribution of HU1 and parameters H_0 and m obtained from the Weibull distribution function (Equation 3.52), applying the calculus algorithm given above (Equations 3.63 and 3.59) and taking into account the probability brittle fracture (Equation 3.61), the erosion rates were calculated for each hardness interval.

The hardness values of universal hardness HU1 taken into consideration varied from 4073 to 12,336 MPa. The portions of erosion rates from plastic and brittle wear and total wear were calculated. As it can be seen (Figure 3.43) the calculus algorithm strongly overestimates the wear caused by brittle fracture at higher impact angles.

The hardness values of microhardness HV0.1 taken into consideration varied from 3080 to 20,490 MPa. The relative weights of metal matrix and hard phase in

structure (correspondingly 0.74 and 0.26) followed from the experimental cumulative hardness distribution function, were applied. For hardness ranges with mean hardness more than 10,340 MPa (inclusive), the model of brittle fracture was applied. As it follows from Figure 3.43, curve 3, that the calculated wear rate from brittle fracture at higher impact angles is about four times higher.

In nanohardness scale the hardness taken into consideration varied from 1380 to 10,010 MPa for matrix phase only.

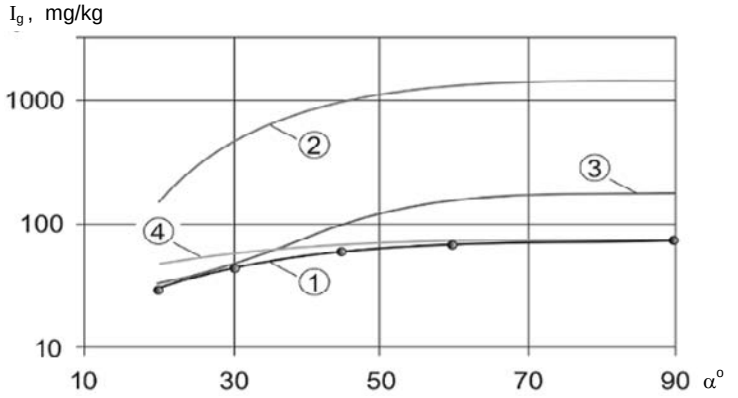

Figure 3.43. Dependence of experimental (1) and calculated wear rates on the impact angle using HU1 (2), HV0.1 (3) and H_{nano} (4) hardness of MMC material

Although the erosive wear calculations takes into account only the hardness distribution of the matrix phase reinforced with sub-micronical VC particles, the predicted wear rate coincides well with experimental erosive wear test results.

The calculated and the experimental results of the wear rates of MMC material with multimodal reinforcement and a relatively high content and wide range of particle size showed a major difference [62]. The difference between experimental and calculated wear rates using universal hardness is caused at first from the big difference in indent parameters and cavities from the abrasive particles (indent diagonals is in the range from 40 to 62.5 μm, erosion cavities from 13 to 33 μm.). If the hardness parameters determined with HV0.1 were used, the difference between experimental and calculated results is minimal at oblique impact (Figure 3.43); the predicted erosion rate at normal impact exceeds the experimental erosion rate. It can be explained by the following:

- The size of the WC reinforcing particles features, which determines the range of hardness distribution, does not correlate with input parameters for erosion wear calculation model. If the size of the indents produced by the selected hardness measurement method is in the same order of size with the indents produced by the erodent particle, the hardness distribution can be used for wear calculation.
- The nonconformity between experimental and calculated results may also indicate that the probability of the brittle fracture is overestimated and fracture toughness parameters characterizing the brittle fracture mechanism should be determined with better accuracy.

Calculation of Erosion Rate of MMC Coating

Based on the hardness distribution of HU1 and parameters H_0 and m obtained from the Weibull distribution function (Equation 3.52) the calculation of erosion rate for MMC coating NiCrSiB-20%(WC-Co) was carried out similarly as it was done for MMC material. Calculated and experimental results of the wear rates of the NiCrSiB-alloy based matrix composite coating by the observation abrasive – quartz sand (H_m<H_a) and particles velocity 80 m/s at impact angles from 30° to 75° had a very good coincidence (Figure 3.44).

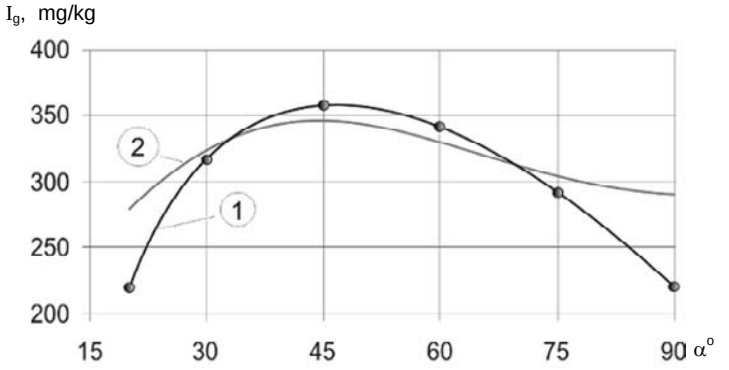

Figure 3.44. Dependence of experimental (1) and calculated (2) wear rates on the impact angle of MMC coating

The difference in the results at small impact angle (the calculated values of wear rate are higher) indicates the necessity to correlate the shear energy density; the difference at straight impact may be explained with the accuracy of K_{1c} determination.

3.5 Prediction of Relative Erosion Resistance

As mentioned above, erosion theory has also been developed to find relative erosion resistance. It is needed when the lifespan of some part is to be increased by replacing the material or coating not used yet in similar conditions. Before first studies on relative erosion resistance began, Wahl [63] and Khrushchov with Babichev [64] had reported their results on wear resistance in the abrasion process. As a result, the so-called S-curves law (Figure 3.45a) and a diagram for the evaluation of the "hardness value" were produced, depending on material type and the hardening method (Figure 3.45b).

Wahl obtained curves shown in Figure 3.45 by wearing out materials using abrasive papers, the hardness of which by Mohs' scale was between 5 and 9. Wahl also pointed out that the harder the material, the lower the curve in area III. Further research [65, 66] showed that the S-curves law also works for wear in abrasive mass and erosion, which confirms the universal value of this law.

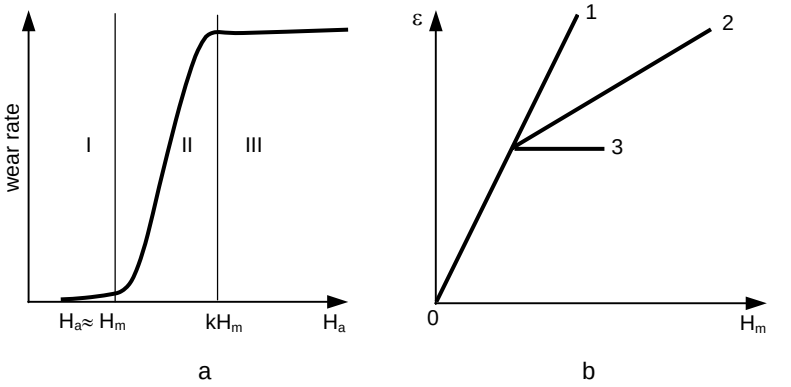

Figure 3.45a,b. Basic rules of abrasive wear of metals (schematically): **a** – dependence of wear rate on the ratio of abrasive hardness H_a and material hardness H_m: area I – wear near zero, area II – sharp transition area, and area III – maximum constant wear [50]; **b** – dependence of relative wear resistance ε on material hardness H_m: 1 – straight line for pure metals and non-hardened carbon steel; 2 – hardness increased by heat-treatment; 3 – hardness increased by strain hardening [63]

Classical research conducted by Khrushchov and Babichev, using abrasive paper, was concentrated on the process in area III of the S-curve and the evaluation of coefficient *k*. By defining relative wear resistance ε as the ratio of wear rate of a reference or standard material to the wear rate of the material under investigation, the test points fell on three different straights lines: the steepest straight line 1 goes through the test points that were obtained with technically pure materials and non-alloyed steels; straight line 2 was obtained with heat treated steels and straight line 3 by using materials in various states of strain hardening. This shows that an increase in hardness obtained by different methods increases the wear resistance to various extent.

According to Khrushchov, coefficient *k* varies between 1.3 and 1.7, after [67] between 1.6 and 1.8 during erosion. Thus, the average *k* value is 1.6. The regularity found by Khrushchov and Babichev was studied by Tadolder [68] who used quartz sand and glass grit as an abrasive. When the impact angles were 20° and 30°, the test points converged around one line, however at $\alpha > 45°$, this did not happen (Figure 3.46).

Analogous results at 90° impact angle were obtained at impact velocity of 37 m/s by researchers from Stuttgart University [69]. In [70] the relative wear resistance at the sliding wear of pure metals depending on hardness, Young's moduli of elasticity and melting temperature was studied.

The centrifugal accelerator with a rotor shown in Figure 1.6b and abrasive – corundum were used. In all the cases, the experimental points were found to be on a straight line; the minimum deviation occurred at the dependence $\varepsilon = f(T_m)$, where T_m is the melting temperature.

Tadolder also investigated the effect of strain hardening on the increase of wear rate at attack angles of 20°, 45° and 90°. Test specimens were strain hardened in two different ways: statically, by applying pressure under the press and dynamically by striking with a steam hammer. Processes of strain hardening were conducted with

different intensity to achieve different hardness. As it turned out, wear resistance was influenced by way of strain hardening and impact angle, but also by the type of crystal lattice of the material. From among metals, Ti and Co with hexagonal lattice, either strain hardened statically or dynamically, behaved in the same way as on Khrushchov's diagram, *i.e.* at all impact angles, the test points were placed on the horizontal line. Also, other statically strain hardened materials (Al, Cu, Ni, Fe, Mo and Nb) behaved in the same manner at $\alpha = 20°$, but at $\alpha = 90°$ and 45° some of them exhibited an increase in the ascent of the line (Al, Fe, Cu, Nb), *i.e.* an increase in wear resistance. However, in the case of dynamic strain hardening at the aforementioned impact angles, a slight decrease in the wear resistance was observed for most of these materials (except Co and Ti).

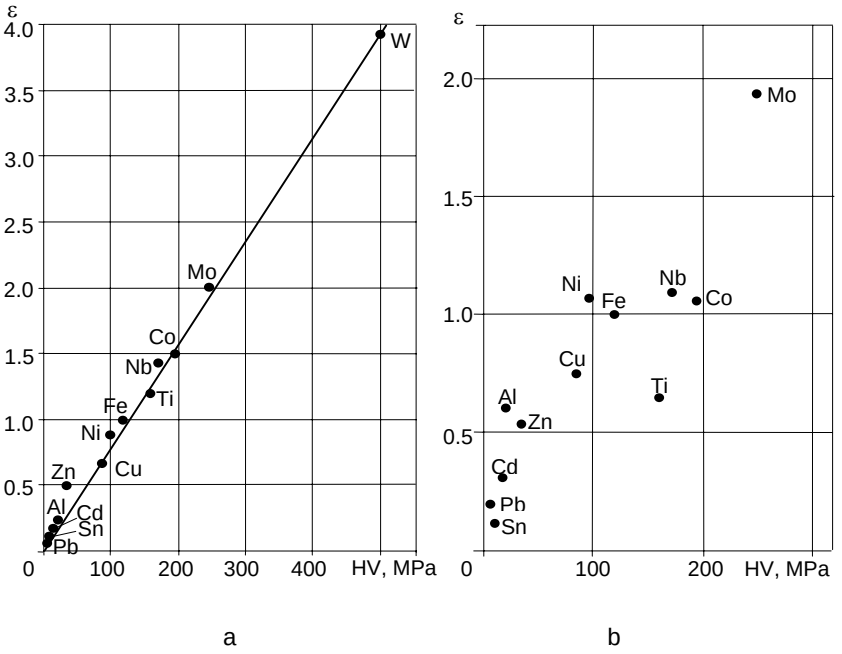

Figure 3.46a,b. Dependence of relative wear resistance ε on material hardness H_m: **a** – α = 30°, **b** – α = 90°. Abrasive – spherical quartz sand 0–6 mm, v_0 = 82 m/s, reference material – iron

Similar research of pure materials offers only theoretical interest. From a practical point of view, heat treatment of steels is of greater importance, *i.e.* the behavior of line II in erosion, reported in [71]. Changes in the wear resistance of hardened and tempered test specimens of different hardness after bombarding them with corundum and carborundum were investigated. Wear curves of steels U8 and 40Ch4 are shown in Figures 3.47 and 3.48.

From Figures 3.47 and 3.48 we can see that only at low impact angles (in this case α = 10°), when microcutting predominates in the wear mechanism, do test points fall on the ascending line, as in the tests with abrasive paper. This occurs up to α = 30°, when the velocity of the particles is low; at higher velocities the line

remains typically horizontal. At high impact angles the lines are clearly sloped down, and the higher the velocity the lower they run. Analogous results have been obtained at the University of Stuttgart at 90° impact angle, using quartz sand [69]. In addition to the difference in the behaviour of ε-H_a curves, a certain difference also exists in zone I of the abrasive and erosive wear S-curves. According to Khrushchov, if $H_a/H_m < 0.7$, the wear process on the abrasive paper practically ceases, *i.e.* $\varepsilon \to \infty$. This cannot be confirmed in the erosion process (especially at high impact angles). Differences in the flow of the curves are shown in Figure 3.49.

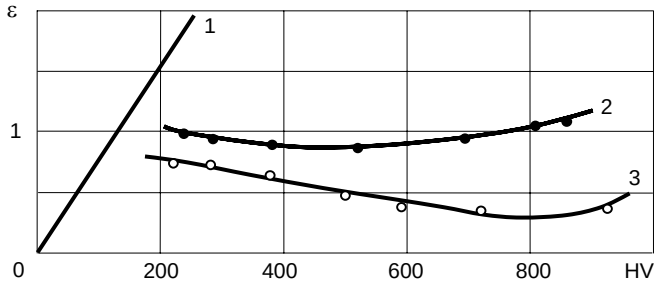

Figure 3.47. Dependence of relative wear resistance ε on target hardness HV after heat treatment: 1 – Khrushchov's line for pure metals, 2 – at $\alpha = 30°$, 3 – at $\alpha = 90°$. Abrasive – electrolytically produced corundum 0.4–1 mm. Target material – steel U8, $v_0 = 120$ m/s

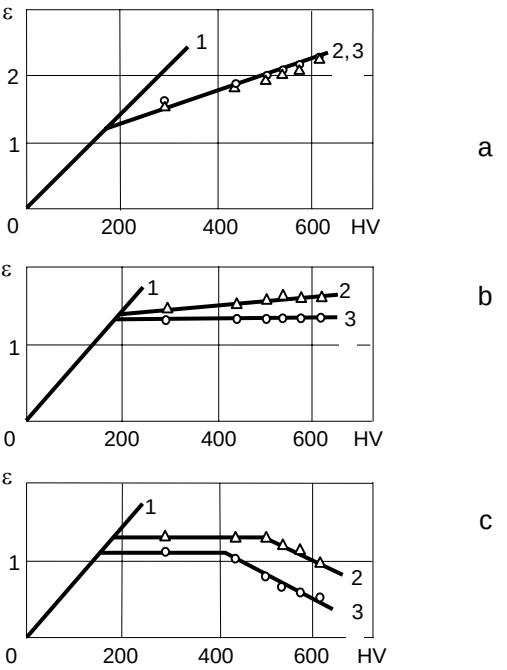

Figure 3.48a–c. Dependence of relative wear resistance ε of steel 40Ch4 on hardness after heat treatment: **a** – $\alpha = 10°$, **b** – $\alpha = 30°$, **c** – $\alpha = 90°$. Abrasive – silicon carbide 0.6–1 mm; 1 – Khrushchov's line for pure metals, 2 – at $v_0 = 13$ m/s; 3 – at $v_0 = 30$ m/s

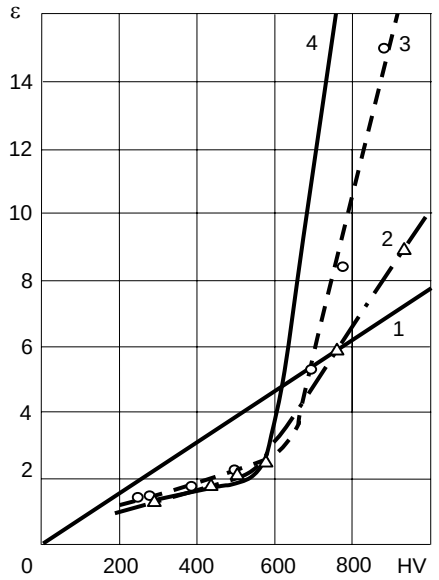

Figure 3.49. Dependence of relative wear resistance ε of steel U8 on hardness after heat treatment: 1 – Khrushchov's line for pure metals with corundum; 2 – in the flow of glass particles at $\alpha = 90°$, $v_0 = 120$ m/s; 3 – in the flow of glass particles at $\alpha = 30°$, $v_0 = 120$ m/s; 4 – rubbed against glass paper (data by M. Khrushchov)

As the graphs show, hardened martensitic steel had a relative wear resistance of only 8.4 at $\alpha = 90°$ impact angle (annealed steel 0.45% C served as reference material), while there was practically no wear on glass paper.

The test results described above allow to plot a very expressive wear curve in the coordinates of ε-H_a [69]. Reference material here was mild steel and for simplicity S-curves are shown to be made of three straight lines as in [66]. Curves have certain differences, depending on whether the impact angles are shallow (Figure 3.50a) or large (Figure 3.50b), because this determines whether the in the horizontal zone III line M_1 of the reference material is located higher or lower than line M_2 featuring the hardened material. The limiting value where transition takes place is around 45° for steels. Independent of the impact angle, the ε-curve has five clearly defined zones (Figure 3.50):

A ($H_a < H_{m1}$) – where both the wear and wear resistance are small;

B ($H_{m1} < H_a < 1.6H_{m1}$) – relative wear resistance increases rapidly to maximum value;

C ($1.6H_{m1} < H_a < H_{m2}$) – interval where the use of material M_2 is the most reasonable;

D ($H_{m2} < H_a < 1.6H_{m2}$) – zone of rapid fall of wear resistance;

E ($H_a > 1.6\ H_{m2}$) – wear resistance of material M_2 is low.

The dependence of relative wear resistance ε on the relation between H_a and H_m is supported by the test results. Table 3.17 was compiled mainly from the data obtained at TUT through different periods by help of testing facilities CAK-3m and VK-1 and supplemented with authentic data from the literature. A clear division into zones of the ε-curve is shown in Figure 3.50.

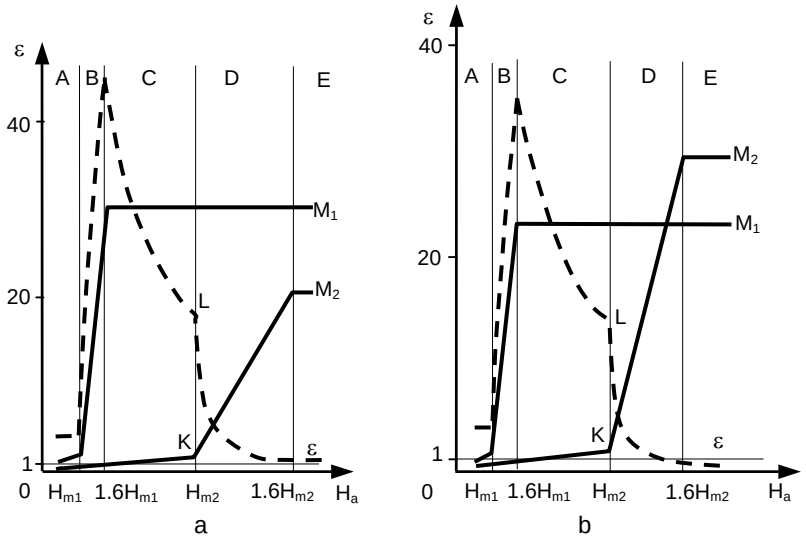

Figure 3.50a,b. Wear rate of materials M_1 and M_2 of respective hardness H_1 and H_2 *vs* abrasive hardness H_a in erosion. The *dashed line* is obtained by dividing the ordinates of curve M_1 to the respective ordinates of M_2 and shows the dependence of relative wear resistance ε on H_a: **a** – at shallow impact angles; **b** – at large impact angles.

For plotting the curves shown in the schematic drawing (Figure 3.50) for a real material at a selected velocity and impact angle, only a limited set of test data is needed. The data needed are wear rate values of the reference (standard) material (usually mild steel) against the abrasive that is softer than the reference material and the abrasive that is 1.6 times harder than it. Particles of abrasives used for tests to construct the graphs should be similar in shape and size. In particular, the position of point K is essential, because it determines the position of point L on the ε-curve as well as the course of the curve in most interesting zones C and D. The inclination of the S-curve of the material in zone I (Figure 3.45a) as well as the position of point K, for materials with equal hardness depend substantially on the structure and composition of the material.

For example, for hardmetals, compositions based on WC and Co are preferred as their K-point lies much lower than with TiC and Cr_2C_3 based cermets (see Table 3.17 about zone C). In addition, because zone B is narrow, it is difficult to find a suitable abrasive that would provide results that fall into that zone. Natural soft stones and minerals (in this case limestone) consist of particles of different hardness, whereas softer ones give results that fall into A zone and harder ones into B zone.

Plotting of ε-curves allows us to assess the prospects of a material or coating. However, it does not determine precisely the wear resistance of some concrete machine part. In addition to environmental abrasives (*e.g.*, industrial dust) that cause erosion, mixtures of particles of different hardness exist. In this case, as will be shown below, the value of ε is mainly influenced by the hardest component found in the mixture and average hardness value of particles should never be used for the estimation of ε value [71]. Assuming that particles of different hardness found in the mixture wear a surface independently of each other, the formula for the estimation of relative wear resistance can be expressed as

$$\varepsilon = (I_{e1}n_1 + I_{e2}n_2 + \ldots + I_{en}n_n) / (I_1n_1 + I_2n_2 + \ldots + I_nn_n), \qquad (3.67)$$

where I_{e1}, I_{e2}, …, I_{en} are wear rates of the reference material in mm^3/kg influenced by 1, 2 *etc.* component of abrasive;
I_1, I_2, …, I_n the same data of the investigated material,
n_1, n_2, …, n_n show the relative weight of components.

Table 3.17. Values of relative wear resistance ε with different abrasive/target material pairing (laboratory measurements)

Abrasive[a]	H_1[b] HV	Target material and hardness HV	α deg	v_0[a] m/s	ε	Range	Source
Rock salt 35 HV	130	Cast iron, 210	90	150	0.4		
	130	Cast iron, 210	30	150	0.7		
	130	0.4% C steel, 505	90	150	1.4	A	
	130	0.4% C steel, 505	30	150	1.3		
Barite 120 HV	195	14% Cr steel, 500	30	90	2.0		
	195	Weld coating, 900	30	90	3.4		
Limestone 120–190	125	Steel C60H, 830	90	70	6.4		[62]
HV	177	0.8% C steel, 864	90	100	3.0		
	177	0.8% C steel, 864	30	100	3.8	A/B	
	177	White cast iron, 620	90	100	3.8		
	177	White cast iron, 620	30	100	6.4		
Glass grit 575 HV	177	0.8% C steel, 860	90	100	8.5		
	177	0.8% C steel, 860	30	100	15.3		
	177	White cast iron, 620	90	100	14.7		
	177	White cast iron, 620	30	100	41.7		
	130	WC/Co hardmetal, 920	90	165	51		
	130	WC/Co hardmetal, 920	45	165	136		
	130	WC/Co hardmetal, 1600	90	165	204		
	130	WC/Co hardmetal, 1600	45	165	420		
	130	TiC/Mo/Co cermet, 1830	90	150	9.0	C	
Quartz sand, 1200 HV	130	TiC/Mo/Co cermet, 1830	30	150	33		
	130	Cr_3C_2/Mo/Ni cermet, 1300	90	150	3.5		
	130	Cr_3C_2/Mo/Ni cermet, 1300	30	150	4.7		
	130	WC-Co hardmetal, 1600	90	165	47		
	130	WC-Co hardmetal, 1600	45	165	78		
	130	WC-Co hardmetal, 2000	30	100	590		
	130	Weld coating, 740	90	70	11		[72]
Gas coke 610 HV	130	Weld coating, 740	15	70	35		[72]
	130	Weld coating, 1130	90	70	34		[72]
	130	Weld coating, 1130	15	70	100		[72]
Feldspar 730 HV	110	White cast iron, 554	90	70	1.2		[73]
	110	White cast iron, 554	15	70	3.0		
Glass grit 575 HV	177	White cast iron, 525	90	100	9.4		[73]
	177	White cast iron, 525	30	100	21.5		
Quartz sand 1200 HV	130	0.8% C steel, 900	90	120	0.9		
	130	0.8% C steel, 900	30	120	2.1		
	130	Weld coating, 1130	90	70	1.3		[72]
	130	Weld coating, 1130	15	70	6.1	D	[72]
	170	Weld coating, 890	75	350	1.3		[74]

Table 3.17. (continued)

Abrasive[a]	H_1[b] HV	Target material and hardness HV	α deg	v_0[a] m/s	ε	Range	Source
	170	Weld coating, 890	15	350	4.4		[74]
	130	WC-Co hardmetal, 920	90	165	4.0		
	130	WC-Co hardmetal, 920	45	165	5.8		
Corundum 2000 HV	130	WC-Co hardmetal, 1600	90	165	6.9		
	130	WC-Co hardmetal, 1600	45	165	6.6		
Quartz sand 1200 HV	110	White cast iron, 554	90	70	0.6		[73]
	110	White cast iron, 554	15	70	2.0		[73]
	175	White cast iron, 620	90	100	0.9		
	175	White cast iron, 620	30	100	1.8		
	130	Weld coating, 720	90	120	0.7		
	130	Weld coating, 720	30	120	1.4		
	130	Weld coating, 720	15	120	3.0	E	
	130	Cast iron, 210	90	165	0.5		
	130	Cast iron, 210	30	165	0.7		
	130	Cast iron, 210	15	100	1.0		
Corundum 2000 HV	130	0.8% C steel, 900	90	120	0.3		
	130	0.8% C steel, 900	30	120	1.0		
	130	WC-Co hardmetal, 920	90	165	0.8		
	130	WC-Co hardmetal, 920	45	165	1.4		

[a] The values of abrasive hardnesses and impact velocities are the mean values
[b] Reference material hardness

The validity of the formula at Equation 3.67 in the case of a two component abrasive is shown in Figure 3.51. Tests were made on a centrifugal accelerator CAK-3m [37].

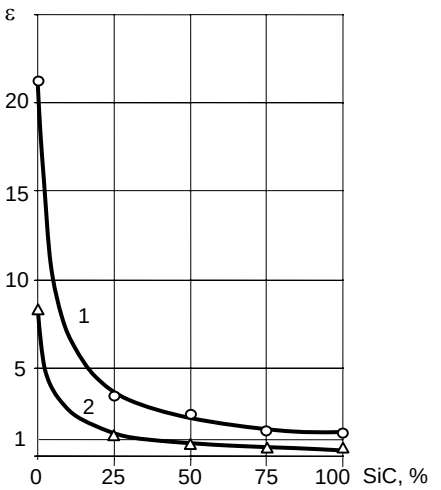

Figure 3.51. Relative wear resistance ε of steel U8, 910 HV *vs* SiC content in the mixture of glass grit and SiC. The curves are drawn as calculated by Equation 3.67, the points are based on test data; $v_0 = 76$ m/s; 1 – at $a = 15°$, 2 – at $a = 90°$.

Table 3.18. Comparison of experimental and calculated values of relative wear resistance of steel U8, 910 HV at particle velocity 76 m/s. Reference material – 0.4% C steel, 175 HV

Abrasive components %			Erosion rate I, mm³/kg				Relative wear resistance ε	
Glass grit	Quartz sand	SiC	$\alpha = 15°$		$\alpha = 90°$			
			0.4% C steel	Steel U8	0.4% C steel	Steel U8	$\alpha = 15°$	$\alpha = 90°$
100	0	0	44.9	2.3	46.5	6.1	23.9	7.2
0	100	0	10.1	8.5	15.8	20.8	1.2	0.76
0	0	100	66.2	54.9	42.5	125.4	1.2	0.34
33.3	33.3	33.3	52/44	25/22	43/35	68/51	2.1/2.0	0.63/0.69
25	50	25	37/35	19/19	35/30	54/43	1.9/1.8	0.65/0.70
10	80	10	22/20	13/13	22/22	34/30	1.7/1.5	0.65/0.73
80	10	10	47/52	7.5/8.2	44/43	20/20	6.3/6.3	2.2/2.15

Note: In the fraction numerator – experimental values; in the denominator – values calculated by Equation 3.65

The same steels were used to investigate the wear resistance of a three-component abrasive (see Table 3.18). In this case Equation 3.67 also produced real results. It should be noticed that in these tests the abrasive was mixed from the components of the same granularity (d = 0.4–0.6 mm), but small amounts of soft and very fine additives in the abrasive, like calcium sulphate (gyps), lime and magnesium peroxide can dramatically increase the wear resistance of very mild steel as was the case with the addition of water. Because the influence of these additives on the wear of hard structures is significantly smaller, the value of ε obtained with Equation 3.67 may be unrealistic. Reliable results can only be obtained by a laboratory or industrial experiment.

3.6 References

1. Davidenkov NN. Dynamic Testing of Metals. Moscow: 1929 (in Russian).
2. Engel O. Pits in metals by collision wih liquid drops and rigid steel spheres. J. of Research of the National Bureau of Standards. 1960; Vol.64A, N1:61–72.
3. Eichelberger RJ, Kineke JH. Hypervelocity Impact. In: High-Speed Physics. Vol.2, Moscow: Mir Publ, 1971;204–46 (in Russian).
4. Goldsmith W. Impact and contact phenomena at medium velocities. In: High-Speed Physics, Vol.2, Moscow: Mir Publ, 1971;153–203 (in Russian).
5. Kleis I, Uuemõis H. Untersuchung des Strahlverschleissmechanismus von Metallen. Zeitschrift für Werkstofftechnik, 1974;Heft 7:381–89.
6. Hutchings IM, Winter RE, Field JE. Solid particle erosion of metals: The removal of surface material by spherical particles. Proc Roy Soc London 1974;348A:379–92.
7. Kleis I. Hypothesis of constancy of required energy for formation of impact crashers, Proc Techn Univ Tallinn 1978;455:3–8 (in Russian).
8. Rinehart JS, Pearson J. Behaviour of Metals under Impulsive Loads. Moscow: Foreign Publishers, 1958 (in Russian).

9. Kangur HF. Dynamic Penetration of Rigid Sphere to Metallic Barrier. PhD Thesis, Tallinn 1987 (in Russian).
10. Kleis IR, Kangur HF. Resistance of metal surface to indentation by spherical projectile at impact. Proc 7th Conf on Erosion by Liquid and Solid Impact. Cambridge 1987;48-1–48-7.
11. Goodier IN. On the mechanics of indentation and cratering in solid targets of strain-hardering metal by impact of hard and soft spheres. Proc Seventh Hypervelocity Impact Symp, Tampa, Florida 1964;215–60.
12. Singer S. The influence of meteoritic particles to artifitial sattellites of Earth. Jet Propulsion, 1956;26/12:1071–75.
13. Lueger Lexikon der Technik. Band 3. Stuttgart:1961.
14. Gommel G. Stossuntersuchungen Stahlkugel – Stahlplatte im zusammenhang mit Strahlzertrümmerung und Strahlverschleiss. Techn-wiss Berichte MPA Stuttgart, 1967;Heft 67-01.
15. Tabor D. The Hardness of Metals. Oxford Univ. Press 1951.
16. Breckel H. Kenngrössen und Verschleiss metallischer Werkstoffe. Diss Univ Stuttgart 1968.
17. Kleis I, Remi T. On the geometry of impact craters produced by indentors of different shape. Proc Techn Univ Tallinn 1991;728:3–7 (in Russian).
18. Vitman FF, Stepanov AB. The influence of deformation rate to the deformation resistance of metals. Moscow: In: Some Strength Problems of Solid Body, Acad Sc USSR, 1959;207–21 (in Russian).
19. Huth G, Thompson J, and Van Valkenburg M. Some new results about the hypervelocity impacts. J of the Applied Mechanics 1957;24/1:65–68.
20. Kleis I, Remi T. Testing hardned steel targets for dynamic hardness. Proc Estonian Acad Sc Eng 2004;10/1:39–44.
21. Kangur H, Kleis I. The experimental determination and calculation of the coefficient of restitution.Proc Acad Sc USSR “Solid Mechanics” 1988;5:182–85(in Russian).
22. Kleis I. Modelle zur analytischen Bestimmung der Stossziffer bei Metallen. Acta Universitatis Ouluensis C Tehnica 1996;92:8–15.
23. Frischman F, Haljasmaa I, Pappel T, Rudi U, and Scheglov I. Investigation of particle –wall collision. Proc Estonian Acad Sc Phys Math 1994;43:263–370.
24. Kleis I, and Hussainova I. Investigation of particle – wall impact process. Wear 1999;233–235:168–73.
25. Kleis I. Dynamische Härte als eine Physicalische Konstante. Proc of OST-94 Symposium on Machine Design, Oulu: 1994;13–26.
26. Kleis I. Analytical determination of indentor load in terms of impact energy. Acta Univ Oulu, 1997;C109:25–33.
27. Kirejev AV, and Malafejev NJ. The influence of ask particles flow parameters on boiler tubes wear. Polzunov Boiler-Turbine Inst Report N5881, Lengingrad, 1938 (in Russian).
28. Lebedev IK. Erosion in the boilers. Electric Power Stations 1958;11:22–27 (in Russian).
29. Finnie IA. Erosion of surfaces by solid particles. Wear 1960;3:87–103.
30. Bitter JGA. A study of erosion phenomena:Part II.Wear 1963;6:169–90.
31. Nepomnyashchy EF. Friction and wear caused by the stream of solid particles. Interation of Solid Bodies and Calculation of Friction Forces and Wear. Moscow:1971;190 (in Russian).

32. Abramov JA. The erosion of energetic equipment. Power Engineering 1985;7: 15–21 (in Russian).
33. Beckmann G. and Gotzmann J. Analytical model of the blast wear intensity of metal based on a general arrangement for abrasive wear. Wear 1981;73:325–33.
34. Peter P. Strahlverschleiss an konventionellen Dampferzeugern-Prognose und Verschleissschutz. Wiss Berichte TH Zittau, 1004, 1989:Lecture NV/3.
35. Tadolder J. The influence of the geometry of abrasive particle on wear rate of metals. Proc Techn Univ Tallinn 1966; 237:3–13 (in Russian).
36. Levin SM. Investigation of the Erosion of Steels in Different Conditions. Dissertation, Moscow Institute of Petrochemical and Gas Industry, 1978;207 (in Russian).
37. Ellermaa RR. Erosion prediction of pure metals and carbon steels. Wear 1993;162–164:1114–22.
38. Beckmann G. and Kleis I. Abtragvershleiss von Metallen. Leipzig:1983;184. (Distributed by Springer – Verlag Wien – New York).
39. Lepikson H. and Siimpoeg R. The methodics of erosion study at low temperatures and some results. Proc Techn Univ Tallinn 1969;271:31–39 (in Russian).
40. Üksti L. Physicochemical aspects of wet sand erosion mechanism. Proc Techn Univ Tallinn 1983;560:19–27 (in Russian).
41. Neiman A. Relationship Between Abrasivity of Sands and Their Geological and Physical Indicators. Research Report, Tallinn 1968 (in Estonian).
42. Uuemõis H. An Investigation into Some Laws of Hard-Particle Erosion. PhD Thesis, Tallinn 1967;185 (in Russian).
43. Uetz H. and Gross KJ. Strahlvershleiss in Abrasion and Erosion, München Wien: Carl Hanser Verlag, 1986;326–78.
44. Langeberg I. Study of Erosion at Small Angles of Impact. PhD Thesis, Tallinn 1968;196 (in Russian).
45. Kleis I. Effect of Hardness of Abrasive Grains Metal Erosion. Research Report. Tallinn 1961;25 (in Estonian).
46. Kleis I. and Remi T. Adapting the energetic erosion theory to hardened steels. Proc Estonian Acad Sc Eng 2004;10/1:45–52.
47. Kleis I. Probleme der Bestimmung des Strahlverschleisses bei Metallen. Wear 1969;13, 199–215.
48. Kleis I. About the erosion of metals. Proc Techn Univ Tallinn 1959;168:3–25 (in Russian).
49. Kleis I, Pappel T, and Arumäe H. Strahlverschleissuntersuchungen an modernen Konstruktionswerkstoffen. Wiss. Berichte Ingenierhochschule Zittau, 1982;383:64–66.
50. Beckmann G, Dierich P, Gellrich R, Gotzmann J, and Pietschmann F. Modelling of severe wear; asurvey of the contributions of the Technical University of Zittau to tribology. J Tribology International 1996;29/3:215–20.
51. Gotzmann J. Modellierung des Strahlverschleisses an keramischen Werkstoffen. Schmierungstechnik, Fachzeitschrift für Tribotechnik, Berlin: VEB Verlag Technik 1989;20/11:324–29.
52. Beckmann G, and Gotzmann J. Modelling blast wear on ceramic materials. Proc Techn Univ Tallinn 1985;609:102–9 (in Russian).
53. Greenwood DA. and Williamson JBP. Contact of nominally flat surfaces. Proc Roy Soc Lond, 1986;A295:300–19.

54. Evans AG, Gulden ME. and Rosenblatt M. Impact damage in brittle materials in elastic-plastic regime. Proc Roy Soc Lond, 1978;A361:343–65.
55. Sheldon GL, Finnie IJ. On the ductile behaviour of nominally brittle materials during erosive cutting. J of Engineering for Industry 1966;Nov:387–92.
56. Gulden ME. Solid-particle erosion of high-technology ceramics (Si_3N_4, glassbonded Al_2O_3 and MgF_2). American Society for Testing and Materials. ASTM STP 664,1979;101–22.
57. Beckmann G, Dierich P. Tendenzdarstellungen von Mikrohärteverteilugen technischer Werkstoffe. Schmierungstechnik, Fachzeitschrift für Tribotechnik, VEB Verlag Technik Berlin 1989;20/12.
58. Kulu P. Principles of Creation of Erosion Wear Resistant Powder Materials and Coatings. Doctoral Thesis, Tallinn 1989 (in Russian).
59. Kulu P. Wear Resistance of Powder Materials and Coatings Tallinn: Valgus Publishers, 1988;119 (in Russian).
60. Kulu P, Veinthal R, and Käerdi H. Characterisation and modelling of erosion wear of powder composite materials and coatings. Int J Materials and Product Technology, 2007;28/3–4:425–447.
61. Ponton C, Rowlings R. Vickers indentation fracture toughness. Part 1; Test review of literature and formulation of standardised indendation thoughness equation. Mater Sci Tehnol 1989;5:865–72.
62. Veinthal R. Characterisation and modelling of Erosion Wear of Composite Materials and Coatings, PhD Thesis, TTU Press, 2005.
63. Wahl H. Verschleissprobleme in Braunkohlenbergbau. Braunkohle, Wärme u. Energie, 1951; 3: 75–87.
64. Khrushchov MM. and Babichev MA. Study of Metals Wear. Moscow:1960;351 (in Russian).
65. Wellinger K. and Uetz H. Gleitverschleiss, Spülverschleiss, Strahlverschleiss unter der Wirkung von körnigen Stoffen. VDI-Forshungsheft, 1955;449/B21:1–40.
66. Wellinger K, Uetz H. and Gürleyik M. Gleitverschleiss-Untersuchungen an Metallen und nichtmetallischen Harstoffen unter wirkung körnigen Stoffen. Wear, 1968;11:173–99.
67. Tereshtshenko AF. and Gavrisch VA. About the abrasive selection for testing of surfacing to erosion. Abstracts of Tribological Conference. Kiev 1970;48–51 (in Russian).
68. Tadolder J. Erosion of Pure Metals. PhD Thesis. Tallinn 1966 (in Estonian).
69. Uetz H. and Khosrawi MA. Strahlverschleiss. Aufbereitungstechnik, 1980; 21/5:253–66.
70. Stupnitsky A, Kleis I. and Rufanov Y. Wear characterictics of comercially pure metals in a grazing abrasive stream. Proc Techn Univ Tallinn 1981;381:23–32 (in Russian).
71. Kleis I. Grundlagen der Werkstoffauswahl bei der Bekämpfung des Strahlverschleisses. Werkstofftechnik, 1984;15:49–58.
72. Wellinger K. and Uetz H. Einfluss der Schweissbedingungen auf das Verschleissverhalten von Auftragschweissungen. Schweissen und Schneiden, 1960;12:465–72.
73. Katavic I. Untersuchungen über die Beeinflussung des Gefüges karbidischer Gusseisen bei abrasivet Verschleissbeanspruchung. Wear 1978;48:35–53.
74. Juzvenko J. and Paschenko M. The chromium carbide based alloys for mechanized surfacing. Automatic Welding 1969;3:24–28 (in Russian).

4

Erosion Resistance of Powder Materials and Coatings

4.1 Groups and Properties of Wear Resistant Materials and Coatings

To strengthen the surfaces of traditional materials (steels), various methods, such as hardening, thermochemical treatment and hard coating, are used. They are meant to reduce the service wear of parts and processing tools subject to abrasive wear.

High surface hardness of traditional materials does not always provide the wear resistance required for faultless operation of tools under the conditions of wear caused by contact pressure, high speed and fatigue processes. Thus, toughness parameters of materials are as important as their hardness parameters (Figure 4.1).

Due to a unique combination of properties, such as high hardness, high strength, high corrosion resistance and capability to resist high temperatures, advanced ceramic materials are increasingly being used in many technological applications, which benefit from their wear resistance potential. For example, in applications which involve impingement by solid particles, high hardness of these materials is beneficial because the rate of material removal in solid particle erosion is, in general, drastically reduced when the hardness of the eroded material supersedes that of eroding particles [1,2].

Attempts have been made to correlate the erosion rates of brittle materials with experimental and materials parameters [2,3]. In these models, hardness and fracture toughness emerge as the main material parameters that control erosion; high hardness increases resistance to plastic deformation while high fracture toughness increases resistance to fracture.

Traditional tungsten carbide-cobalt (WC-Co) based hardmetals are widely used to increase wear resistance in the conditions of sliding wear and erosion. The wide range of WC-Co-type hardmetals (content of binder metal up to 30 wt%) allows for hardmetal production with different hardness-toughness properties. At the same time, it is well-known that with an increase in Co content, wear properties decrease. Besides traditional WC-Co hardmetals, cermets based on other carbides – chromium (Cr_3C_2) and titanium (TiC) carbides – have been developed. Cr_3C_2 based

cermets are a relatively new development. Usually, Cr_3C_2-Ni cermets have lower erosion resistance than WC-Co hardmetals; however, it is higher than that of engineering ceramics. Even so, the other group, TiC-NiMo cermets developed has higher brittleness, and therefore their use for abrasive-erosion wear is limited. Most of the information available on the tribological properties of these alloys has been derived from laboratory tests rather than from engineering applications. Under abrasive erosion conditions, tungsten carbide-cobalt based systems and gas thermal coatings are highly effective [4,5]. Due to the high hardness of tungsten carbide and toughness of the binder metal – cobalt, this group of coatings has a good combination of hardness-toughness properties. They are widely used for erosion protection of machine parts and tools against abrasive wear.

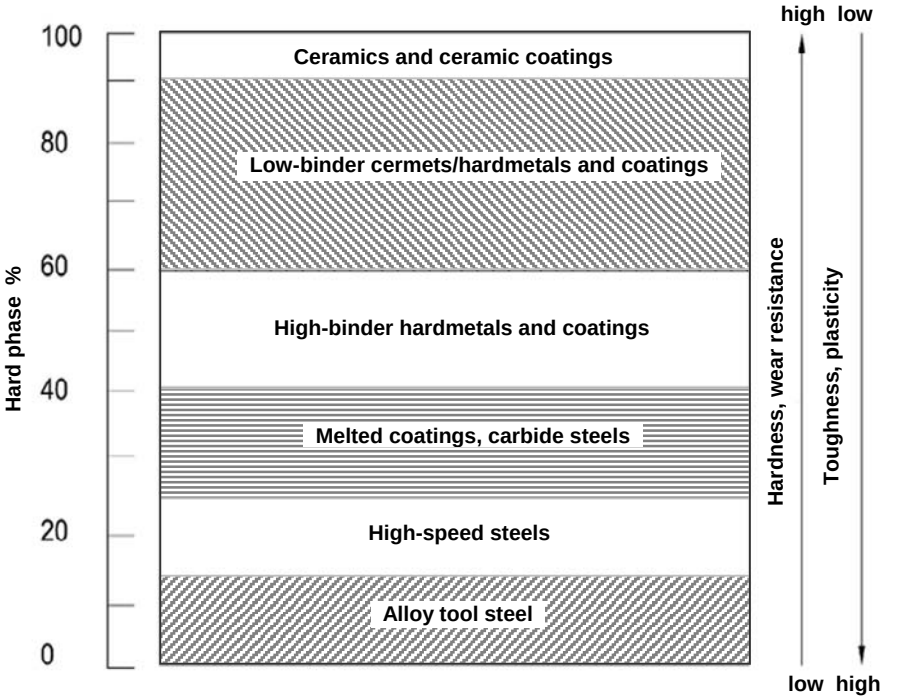

Figure. 4.1. Classification of wear resistant materials depending on the volumetric content of hard phase (ceramic phase)

Along with the methods of traditional materials and metals processing, such as coating, heat and thermochemical treatment used to implement, the properties of the "hardness-toughness" complex/system in powder technology is the most promising. The main advantage of this technology is the possibility of producing materials and surfaces with special composition and properties, *i.e.* wear resistant materials and surfaces. Hardmetals (materials on the basis of tungsten carbide and Co-binder metal) as well as high speed powder steels and cermets (ceramic and metal composites, mainly on the basis of titanium and chromium carbides and Ni-Mo binder metal) are the most widely used wear resistant materials produced by the powder metallurgy method.

During the last 15–20 years, studies of thermal spraying have focused on various high velocity spray processes (particle velocity exceeding 300 m/s). The rapid development of the high-velocity oxy-fuel (HVOF) thermal spray method has contributed to this coating technology, which can satisfy the growing needs of the market for erosion protection. Its benefits are improved bond strength with the bulk material, low porosity and oxides, combined with compressive residual stress in the coatings obtained. However, detonation spraying is another promising thermal spray technology for coating deposition with extremely good wear resistance [4,6].

A wide use of gas thermal coatings gives evidence of the cost-effectiveness of self-fusing (or self-fluxing) alloys containing tungsten carbide (WC) particles, applied by the spray and fusion methods (flame, plasma and laser fusion *etc.*). Some materials, most notably MCrBSi compositions, where M stands for either Ni, Co or Fe, can be fused by heating up to a temperature of 1050 ^{o}C. Because of their low porosity and high bond with the basic material, the above-mentioned fused composite coatings can resist significant impact loads. These coatings provide good wear and corrosion resistance. The main components of powder coatings produced by the method of powder technology are powders and powder filled materials, such as metals, alloys, carbides, oxides or their mixtures, which are sprayed on the surface of a part/workpiece or a product by the method of thermal spraying. Gas thermal and electrical spraying are the most widely used methods of thermal spraying.

It is well known that there is a dramatic difference between ductile and brittle materials when the weight loss in erosion is measured as a function of the impact angle. Cermets and ceramic coatings are considered sufficient to reduce scratching and micromachining surface damage exposed to low-angle impacting particles because of their high hardness and stiffness. At the high angle of impact, the exposed surface should be able to withstand repeated deformation. More elastic materials, such as steels, are usually preferred to ceramics and ceramic coatings in which cracks rapidly propagate and lead to material removal. With mixed erosion, there is a controversy between the hardness and fracture toughness of materials and coatings. Composite materials and particular reinforced metal-matrix composite coatings allow a partial solution of this problem.

4.2 Erosion Resistance of Advanced Ceramic Materials and Coatings

Erosion characteristics of different types of commercially available aluminas, sialons, silicon carbides and cemented carbides have been studied using silicon carbide particles as an erodent. The influence of particle size, particle velocity and angle of impact of the erodent on the erosion rate has been analyzed. Relationships between the erosion rate, material parameters and the identified erosion mechanisms of the materials investigated are discussed in [2]. SiC whiskers reinforced alumina showed the highest erosion resistance.

A range of similar [2] ceramic materials have been tested in laboratory erosion tests using gritblasting with silicon carbide abrasive [3]. Ceramics based silumina, silicon nitride and carbide and boron carbide were tested. The results of erosion tests of selected ceramics are given in Table 4.1.

According to the experiments, boron carbide shows the best erosion resistance at low impact angles (<20°), while alumina with 25 vol% silicon carbide whiskers show the best resistance at severe blast conditions of 90° impact.

Table 4.1. Erosion rates *vs* blast angle of ceramics

Grade	Material composition	HV10 (HV0.1)	Erosion rate, mm/h		
			15°	45°	90°
AZ96	Alumina+4% Zirconia	1239	0.132	0.385	0.540
AT70	Alumina+30% TiNC	1906	0.122	0.320	0.340
AX75	Alumina+25% SiC whiskers	2092	0.056	0.150	0.100
SIN100	Silicon nitride (HIP)	1666	0.065	0.365	0.420
EKA-HD	SiC (HIP)	2875 HV0.1	0.122	0.450	0.600
B_4C	Boron carbide	3255 HV0.1	0.048	0.540	0.770

Experimental studies of engineering ceramics at hard-particle erosion were conducted on a centrifugal-type test rig with quartz sand. Tests covered the range of particle velocities from 26 to 80 m/s, the impact angles ranging between 15 and 90° [7]. It was established that, unlike steels, generally, ceramics are only slightly influenced by changes in the impact velocity; hence their relative wear resistance will increase at higher impact velocities. Resistance will also increase with the decrease of the impact angle (Figure 4.2).

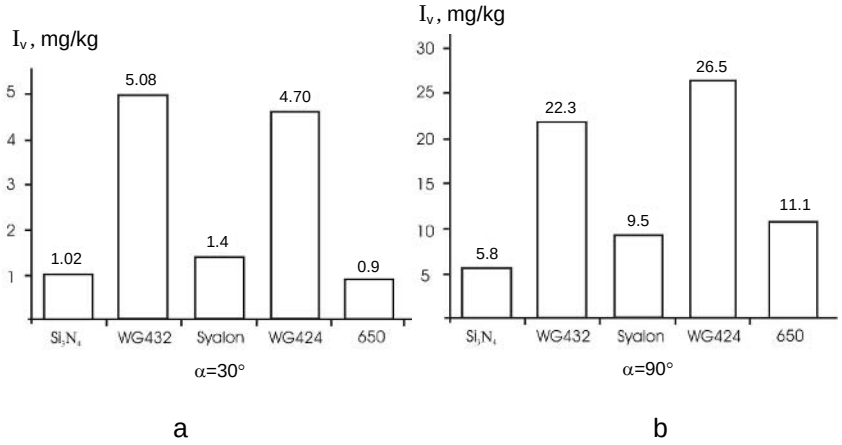

Figure 4.2a,b. Erosion rate of different ceramics: **a** – $\alpha = 30°$; **b** – $\alpha = 90°$.

According to the results obtained, the five types of ceramics under study were arranged in the following order: Si_3N_4 (most resistant), SiC, ZrO_2, Al_2O_3 and ZrO_2 (MgO) (Table 4.2).

Erosive wear resistance of different commercially available engineering ceramics at hard-particle erosion with different erodents was investigated by Jevgrafova at TUT. The following types of ceramics were under study: aluminas, silicion nitrides and sialon (Table 4.3). The properties of the erodents used are given in Table 4.4.

Erosion tests of the studied ceramics at small impact angles (30^o and 45^o) showed that higher wear resistance was demonstrated by sialon, followed by Al_2O_3+TiC and Si_3N_4. At normal impact, ceramics are characterized by erosive wear being maximal at the impact angle of 90^o. The best ceramics by erosion at 61 m/s with SiC are Si_3N_4 and sialon, by erosion with SiO_2 – Al_2O_3 and sialon.

Thermal sprayed ceramic coatings studied by Kulu [4] showed very low erosive wear resistance due to the high porosity (about 8–12%) and brittleness of coatings (Table 4.5). It is one order lower than the wear resistance of the reference material – steel 0.45% C.

Table 4.2. Relative volumetric wear resistance of different ceramic materials of different manufacturers (abrasive – quartz sand 0.1–0.3 mm; v = 76 m/s; reference material – 0.45% C, 210 HV)

Target material and hardness	Density ρ kg/m^3	Impact angle α, ^{o}		
		15	45	90
Al_2O_3[a], 1320 HV	3700	4.4	12.0	0.5
Al_2O_3[a], Rubinet, 1618 HV	3600	6.8	0.6	0.06
Al_2O_3[b] (95%), 1370 HV	3900	2.1	0.6	0.2
MgO-ZrO_2[c] (PSZ, Zn40), 800 HV	5300	1.7	0.4	0.07
ZrO_2[d], 1110 HV	5700	6.6	0.9	0.2
SiC[e], 2710 HV	3100	11.8	11.7	3.1
Si_3N_4 (85%)–Al_2O_3 (5%)–Y_2O_3 (8%), 1750 HV	3300	41.2	101	43.4

Manufacturer:
[a] Oxidkeramik GmbH, Auma
[b] Hoechst CeramTec AG
[c] Feldmühle AG
[d] unknown
[e] Elektroschmelzwerk Kempten GmbH

Table 4.3. The ceramics studied

Grade	Material composition	Hardness HV	Fracture toughness N/mm^2·m$^{0.5}$	Manufacturer
WG27432	Al_2O_3 (99.5%)	1800	4.0	VZS-SEAGOE, UK
WG27424	Al_2O_3 (88%)	2200	3.5	VZS-SEAGOE, UK
650	Al_2O_3 + TiC	3600	4.0	Sandvik, Finland
690	Si_3N_4 + ZrO_2	2500	6.0	Sandvik, Finland
WS09597	Sialon	2600	7.7	VZS-SEAGOE, UK

Table 4.4. Hardness and fraction of the erodents used

Erodent	HV	Fraction, μm
SiO_2	1200	100–300
Al_2O_3	2300	100–300
SiC	3000	700–1000
Si_3N_4	1900	500–700

Table 4.5. Relative volumetric erosive wear resistance of different thermal sprayed ceramic coatings [4]

Type of coatings (material and spraying method)	Hardness HV0.05	Relative wear resistance ε	
		$\alpha = 30^o$	$\alpha = 90^o$
Plasma sprayed			
Al_2O_3	950	0.1	0.02
TiO_2	1100	0.1	0.02
NiAl+5%Al_2O_3	420	0.3	0.1
Al_2O_3+13%TiO_2	1020	0.04	0.01
Detonation sprayed			
Cr_3C_2	930	1.6	0.4
Cr_3C_2+10%NiCr	1200	1.7	0.1

4.3 Erosion Resistance of Ceramic-Metal Composites and Coatings at Room Temperature

4.3.1 Erosion of Ceramic-Metal Composites

Wear resistance of traditional tungsten carbide-cobalt (WC-Co) based hardmetals has been extensively studied in different conditions of abrasive wear because of their wide use. Erosive wear-related studies have been conducted on WC-Co, the most common hardmetals.

Traditional WC-Co cemented carbide materials have been studied in laboratory erosion tests using grit-blasting with silicon carbide [2,3]. In the tungsten carbide category, cemented carbide with 11% Co [1] and two totally different materials have been tested: one of fine WC grain size and low Co content, and the other of high Co content and coarse grain size. The results of the erosion test [3] are given in Table 4.6.

Table 4.6. Erosion rates *vs* blast angle [3]

Grade	Material composition	HV10	Erosion rate, mm/h		
			15^o	45^o	90^o
CT85	WC+25% Co	792	0.170	0.270	0.270
CS10	WC+6% Co	1698	0.083	0.165	0.170

As follows from [3], cemented tungsten carbide displays a mixture of brittle and ductile target behaviour and gives a superior performance as compared to more brittle alumina and silicon nitride ceramics.

Cemented carbide WC-11Co [2] has a low erosion rate. Two different erosion mechanisms were distinguished. At the 45^o angle of impact, microcutting or ploughing is the dominating erosion mechanism. At 90^o, extensive plastic deformation of the target surface takes place and individual WC grains tend to crack and displace.

One of the first studies of hardmetal erosion by a centrifugal-type wear tester was conducted by Kleis [8]. WC-Co hardmetals with cobalt content from 3 up to 25 wt% and hardness of 620–1610 HV were tested in different erodents (glass,

quartz and alumina) at the abrasive particle velocity 165 m/s. Steady state erosion was studied as a function of the hardness of tested materials. The results show a direct dependence of the relative erosive wear resistance on the hardness of the target material – a hardmetal (Table 4.7).

Table 4.7. Relative erosive wear resistance of hardmetals at different wear conditions

Grade of hardmetal and composition	Glass		Quartz		Alumina	
	$\alpha = 45^o$	$\alpha = 90^o$	$\alpha = 45^o$	$\alpha = 90^o$	$\alpha = 45^o$	$\alpha = 90^o$
BK3/WC-3Co	420	204	78	47	6.6	6.9
BK6/WC-6Co	465	178	91	62	4.7	5.0
BK9/WC-9Co	238	143	51	44	3.3	2.4
BK15/WC-15Co	193	132	27	19	2.1	1.3
BK25/WC-25Co	136	51	5.8	4.0	1.4	0.8

Reference material – steel St 3

Erosive wear resistance of WC-Co hardmetals at velocities up to 330 m/s was studied by Tiidemann and others [9,10]. For that purpose, a vacuum device VK-1 was used. Traditional WC-Co hardmetals with cobalt content from 4 up to 15 wt% with the average size of tungsten carbide 2.0 μm were tested. Quartz sand of fraction 0.40-0.63 mm was used. The influence of the erosion rate on the cobalt content and the velocity of abrasive particles was established (Figures 4.3 and 4.4). Figure 4.3 shows that the erosive wear resistance of WC-Co hardmetals depends upon the Co content as well as on the grain size of tungsten carbide. At higher impact velocities of abrasive particles (up to 330 m/s), the wear rate of WC-Co hardmetals shows a tendency toward a substantial decrease (Figure 4.4).

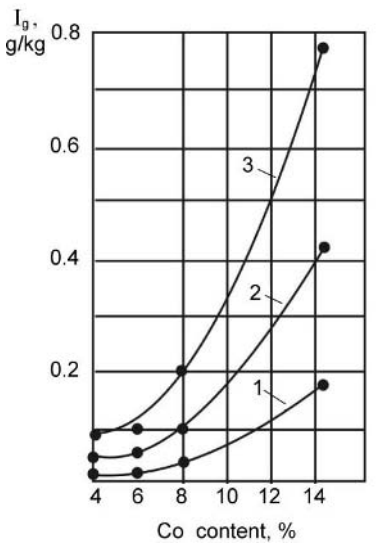

Figure. 4.3. Effect of Co content in WC-Co base hardmetal on the erosion rate at different jet velocities: 1 – 125 m/s, 2 – 225 m/s, 3 – 330 m/s

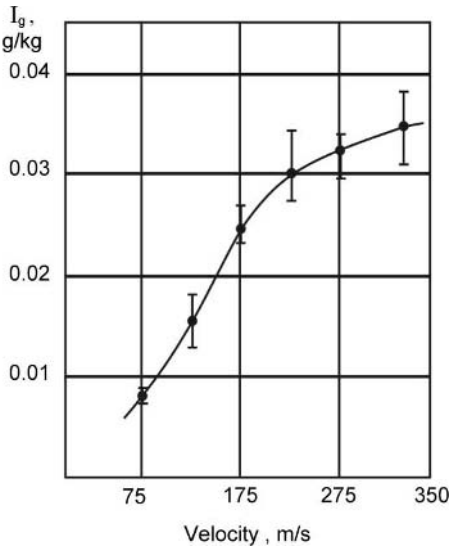

Figure. 4.4. Erosion rate of WC-3Co hardmetal *vs* abrasive particle velocity

Earlier studies devoted to erosion of ceramic-metal PM produced composites were conducted in 1970–1980 by Valdma, Pirso and Kallas from TUT [11–15]. Studies covered both Cr_3C_2- and TiC-based tungsten free cermets [11, 12, 14] and traditional WC-Co hardmetals [13]. Materials were tested in the gas-abrasive as well as in the hydroabrasive at velocities up to 80 m/s, using quartz sand and iron scale as abrasives. As a result, the mechanisms of selective wear were clarified and measures for increasing the erosion resistance of ceramic-metal composites were proposed [15]:

- To diminish the carbide grains size,
- To increase carbide content in fine-grain composites or binder content in coarse-grain composites,
- To increase the modulus of elasticity of the binder, using alloying or dispersion-strengthening.

A systematic study of the erosion resistance of different hardmetals and cermets was conducted by Kübarsepp, Pirso, Hussainova, and Reshetnyak (former Klaasen) from TUT [16–20].

The hardmetals and cermets studied can be roughly divided into three groups:

- Tungsten carbide-cobalt based hardmetals with cobalt content from 6% up to 30%,
- Chromium carbide based cermets with nickel binder content from 10% up to 30%,
- Titanium carbide based cermets with binder metal content from 30% up to 60% (Ni:Mo = 2:1).

The chemical composition and hardness of the selected hardmetals and cermets are presented in Table 4.8. Typical microstructures of the studied hardmetals and cermets (traditional and fine-grained) are shown in Figure 4.5.

Table 4.8. Composition and hardness of selected materials

Materials	Type	Composition, wt%	Hardness HV10
Hardmetals	WC-Co	6, 8, 10, 15 and 30 Co	890–1430
Cermets	Cr_3C_2-Ni	10, 20 and 30 Ni	880–1360
	TiC-NiMo	30, 40, 50 and 60 (Ni, Mo) (2:1)	920–1620

Abrasive particles used in these works were rounded silica particles. The steady state erosion rate was studied as a function of the impact angle at the abrasive particles velocity of 80 m/s. Steel of 0.45% C was adopted as a reference material.

Since differences in materials composition would lead to incorrect results because of great differences in carbide density (WC-15.6, TiC-4.9, Cr_3C_2-6.7 g/cm^3), their weight loss was measured, the volume loss and volumetric wear rate were calculated. The erosion rate was determined as the volume loss of the target sample *per* mass of abrasive particles (mm^3/kg). The relative wear resistance ε was calculated as the ratio of the volumetric wear rates of the studied and the reference materials (steel of 0.45% C with hardness 200 HV):

$$\varepsilon = I_v^{mat}/I_v^{steel}$$

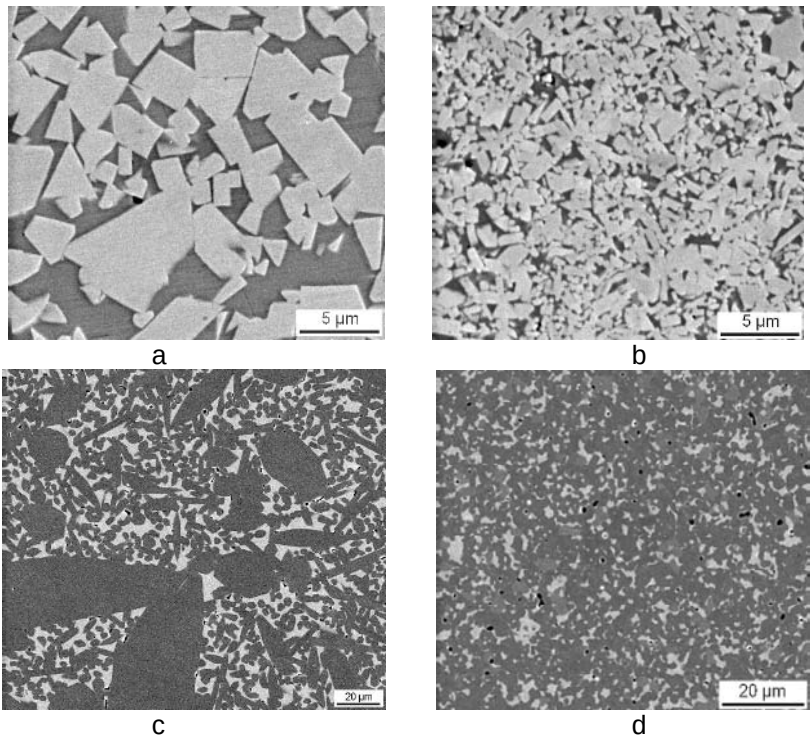

Figure 4.5a–d. Typical microstructures of cermets: **a, b** – WC-Co; **c, d** – Cr_3C_2-Ni; **a, c** – coarse-grained; **b, d** – fine-grained

The erosive wear resistance of WC and TiC-base hardmetals with different composition, structure and properties was investigated [16]. The WC-Co hardmetals studied were produced under different conditions, and therefore they varied considerably in structure and mechanical properties, even at equal content of the binder and carbide. The content of TiC in the TiC-base cermets investigated was 40–80 wt%.

As known from previous experiments, these results also confirm that the influence of hardness on the abrasive wear is insignificant and the relationship between hardness and erosion resistance of hardmetals differs substantially from the linear relationship found for metals (Figure 4.6). At the same level of hardness, the wear resistance of WC-Co hardmetals may differ by up to 50%. At the same time, an increase of hardness does not always result in an increase of wear resistance.

These results show that the hardness measurements characterized by resistance to penetration and large plastic deformation are unsatisfactory for evaluating the resistance of WC-Co hardmetals in such a complicated process as erosive wear. Hardness gives largely an incorrect pattern of material resistance to failure that accompanies the abrasive erosion process. It may be assumed therefore that the erosive wear resistance of hardmetals also depends on mechanical characteristics.

On the basis of the results obtained it can be assumed that the erosive wear resistance of WC-Co hardmetals depends both on hardness and compressive strength. In accordance with the physical model of erosive wear, this process has

two steps: (1) penetration of an abrasive particle into the material and (2) removal of the material by microcutting. Thus, resistance to erosive wear depends on both resistance to penetration and resistance to microcutting (fracture). The former is usually characterized by hardness, while resistance to cutting is expressed by means of shear strength. Owing to the similar state of stress and the correlation that exists between shear strength and compressive strength, the former can be replaced by the latter, which is much easier to determine. Consequently, it can be assumed that resistance to erosive wear depends on two properties: hardness and compressive strength ($HV \cdot R^c_m$).

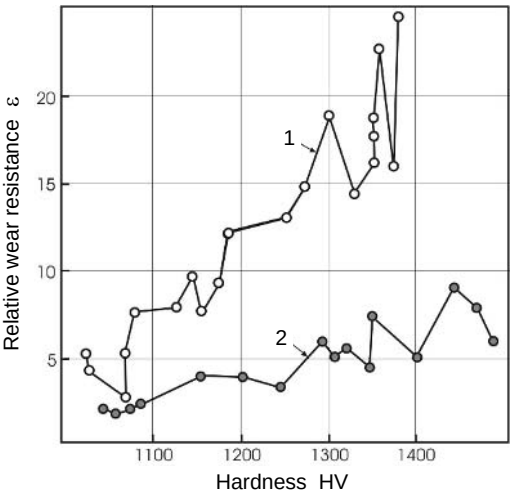

Figure 4.6. Relative erosive wear resistance ε *vs* hardness HV of hardmetals of different structure and composition: 1 – WC-base cobalt bonded; 2 – TiC-base steel bonded

The properties of steel-bonded cermets (grades TZC, TXC, THC, THX) are generally superior to those of TiC-(Ni, Mo) materials and are similar to the properties of WC-Co hardmetals. While the mechanical properties of WC-Co hardmetals are not superior to steel-bonded alloys, their erosive wear resistance exceeds that of TiC-based (for equal hardness). This is, however, true only in the case of high velocity abrasive jets. A decrease in the abrasive jet velocity results in a diminishing difference in wear resistance between WC-base hardmetals and TiC-base cermets. At the same level of hardness, the wear resistance of various steel-bonded cermets differs more (up to 80% more) than the variation found for the WC-base hardmetals (see Figure 4.6). This can be explained by the fact that composition and structure of steel-bonded cermets are characterized by greater difference than those of WC-Co hardmetals.

The binder of grades TZC and TXC has a martensitic structure while that of grades THC and TXH is austenitic (the binder of steel-bonded cermets – grade THC also carries traces of martensite). The considerable difference in structure and hardness of the binder of the steel-bonded cermets causes a difference in the gradient of the function $X = f(\mathrm{HV})$. If the hardness of cermets is less or similar to that of abrasive particles (hardness of quartz sand is *ca* 1100 HV), the wear resistance of steel-bonded cermet grades with different binder structures is not

significantly different. Neither does it differ considerably from that of WC-Co hardmetals with hardness less than that of an abrasive. If the hardness of a steel-bonded cermet is higher than that of an abrasive, then at equal hardness the wear resistance of a cermet with a martensite binder (grades TZC, TXC) and a higher binder content (therefore lower carbide content) exceeds that of a low-binder austenite binder cermet (grades THC, TXH). This fact confirms the selective nature of abrasive wear. The wear resistance of TiC-(Ni, Mo) cermets is on the same level as that of steel-bonded cermets with the austenitic structure of the binder.

The influence of the structure of cemented carbides of the two classes, tungsten carbide-base Co bonded (WC-Co) hardmetals and titanium carbide-base steel bonded cermets, in erosive wear was investigated in [17]. The study involved WC-Co hardmetals with cobalt content 10–20 wt% and an average grain size of carbide phase of 1.9–3.3 μm. The content of TiC in the TiC-base cermets was 40–80 wt% and steel bonded with chromium martensitic stainless steel (20% Cr), silicon steel (2% Si) and chrome-nickel austenitic stainless steel. The average grain size, dependent on the composition, was between 2.0–2.6 μm.

The results presented in Figure 4.6 confirm earlier results about the relation between abrasive wear resistance and hardness: an increase of cobalt content results in a decrease of hardness and wear resistance of WC-Co hardmetals.

The dependence of erosive wear resistance on the grain size of the carbide phase (the most significant parameter of the structure of WC-base hardmetals) is more noticeable than that of hardness (see Figure 4.7) and any other single mechanical property of a hardmetal. For example, an increase in the mean carbide grain size d_{wc} of the WC-Co alloy grade with 15 wt% of binder from 2.1 to 2.9 μm results in the reduction of hardness by 1.5–2 HRA units only, while the resistance to erosion decreases by 200%.

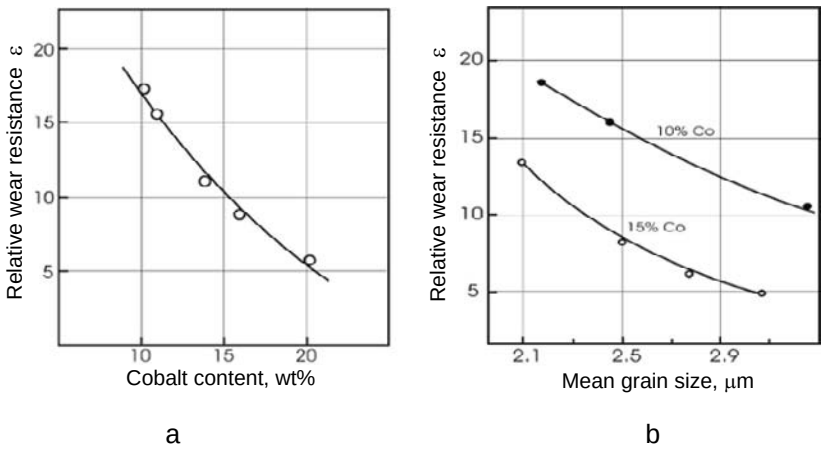

Figure 4.7a,b. Dependence of relative erosive wear resistance ε of WC-base hardmetals on: **a** – Co-binder content and **b** – mean grain size of carbides

It has been shown that the wear resistance is much more structure sensitive than any single mechanical property. The structure sensitivity of erosive wear is much lower than that of other types wear, for example, adhesive wear, which is related to differences in stress-strain states and fracture mechanisms during wear.

The steady erosion rate as a function of the impact angle and impact velocity was studied in [18,19]. Solid particle erosion tests were performed on three grades of cermets (WC-Co hardmetals, TiC-based and Cr_3C_2-Ni cermets) with silica erodent to study the effect of the impact angle on the erosion rate. The impact angles varied from 30^o to 90^o (30^o, 45^o, 60^o, 75^o, 90^o) at the impact velocity of 31 and 61 m/s [18].

Figure 4.8 illustrates the erosion rates of three cermet grades plotted against the angle of impact at the particle velocity of 61 m/s.

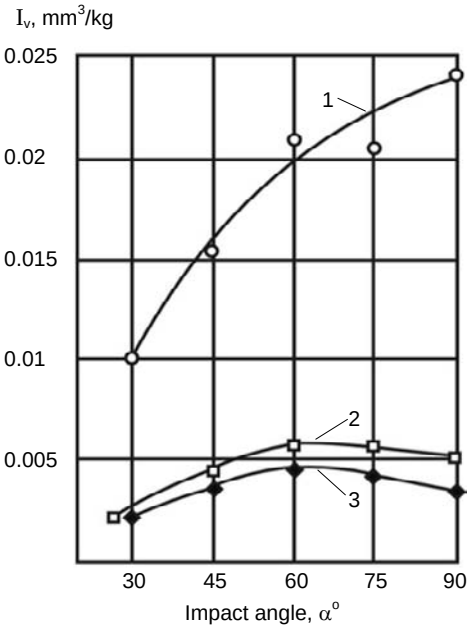

Figure 4.8. Effect of impact angle on the erosion rate of hardmetals and cermets: 1 – Cr_3C_2-30Ni; 2 – TiC-20NiMo; 3 – WC-15Co

As can be seen, some differences exist in the wear behaviour of the materials tested. TiC-based cermets exhibit the maximum erosion rate at the impact angle of 75^o, but those based on Cr_3C_2 have poorer erosion resistance at 90^o. That is closer in behaviour to brittle ceramic materials. Erosion of brittle materials occurs by the propagation and intersection of cracks caused by impacting particles. At an impact angle of 90^o, stress is markedly higher than at the impact angle of 30^o and, as a result, wear rates are higher. Tungsten carbide-cobalt hardmetals, on the other hand, exhibit a maximum erosion rate at 60^o, which is closer to the behaviour of ductile materials. There are clearly two competing mechanisms of erosion, one responsible for the loss of the softer binder phase cobalt and the other leading to the loss of brittle WC, which would explain the shift in maximum from 30^o to 60^o.

TiC-based cermets may be an alternative to WC-based ones at low impact angles and low kinetic energy of erodents. The TiC-based cermet with 20 wt% of binder may be an attractive candidate material in the erosive wear problem, provided the hardness of the erodent is greater than that of the target at impact angles lower than 75^o.

Solid particle erosion of the same three grades of cermets with the erodents (silica and silicon carbide) at the velocities of particles from 30 to 80 m/s (31, 46, 61 and 80 m/s) was analyzed in [19]. In order to clarify the details of the impact, the process of interaction of solid particles with cermet targets was studied using the LDA measuring technique, allowing for direct measurement of particle velocity without disturbing particle flow.

Erodent particles of different materials can cause different erosion rates and mechanisms. All the materials show a significantly lower wear rate when abraded with silica rather than with SiC. This may be explained by the influence of the hardness of the abrading particles, as compared to the test material. Harder silicon carbide particles (3000 HV) cause plastic indentation and lateral cracking, whereas softer silica particles cause minor chipping on a much smaller scale than that of particle contact area. The main mechanism of wear is low-cycle fatigue.

In the case of silica erodent, the erosion rate is higher for Cr_3C_2-Ni and TiC-steel bonded cermets with the lowest modulus of elasticity and hardness. For WC-Co hardmetals with the same level of hardness but the highest modulus of elasticity (WC-15Co) and transverse rupture strength, the erosion rate is the lowest. In the case of SiC erodent, the erosion rate is higher for Cr_3C_2-Ni cermet with the highest hardness and TiC-steel cermets with the lowest hardness.

The erosive wear resistance of cermets cannot be evaluated by a single mechanical property like hardness. In a study [19], the relative ranking of the materials investigated with respect to the erosion rate is probably explained by their different modulus of elasticity and fracture toughness values, while the hardness seems to be of minor importance (Figure 4.9).

The erosion resistance of WC-8Co hardmetal is much higher than that of other cermets. But with SiC abrasives, at high particle velocity, the advantage of WC-Co grade over others is diminishing. At those service conditions, TiC-NiMo cermet may be an alternative to conventional tungsten carbides for use in erosive environments. The results indicate that the solid particle erosion of ceramic-metal composites is a complicated process, controlled mainly by the properties of each individual grain and the boundaries between the adjacent grains.

In [20] the effects of microstructure on the erosive wear of multiphase materials are analyzed. The study characterizes the microstructure of materials and examines the possible modes in which the composition and microstructure influence the erosive wear behaviour. Focus is on the erosive wear resistance of TiC-NiMo and TiC-FeNi cermets in different macroscopic wear environments and on how the variations in the microstructure influence the tribological performance of cermets. The wear behaviour of TiC-based composites produced by the PM method is examined. Materials contain 50–80 wt% of hard TiC phase dispersed in various steel-based and nickel-based binder phase.

The comparison of T3, T4, TF3 and TF4 grades with an equal content of binder fraction (Table 4.9) shows the erosion resistance of TiC-based cermets to be dependent on the structure and strengthening (alloying) degree of the binder.

Figure 4.10 shows the effect of the binder content on the erosion rate. An increase in the weight fraction of the binder phase leads to a decrease in the erosion resistance of TiC-based cermets. The nature of the matrix plays an important role in determining the wear resistance of cermets, as indicated by the difference in the wear rate data for TiC-based materials. A decrease in the wear rate of TiC-NiMo cermets, as a result of an increase of the Mo content, can be explained by the gain

in binder hardness. Generally, TiC-based composites containing NiMo binder show a better erosive wear resistance than the specimens with the austenite steel binder.

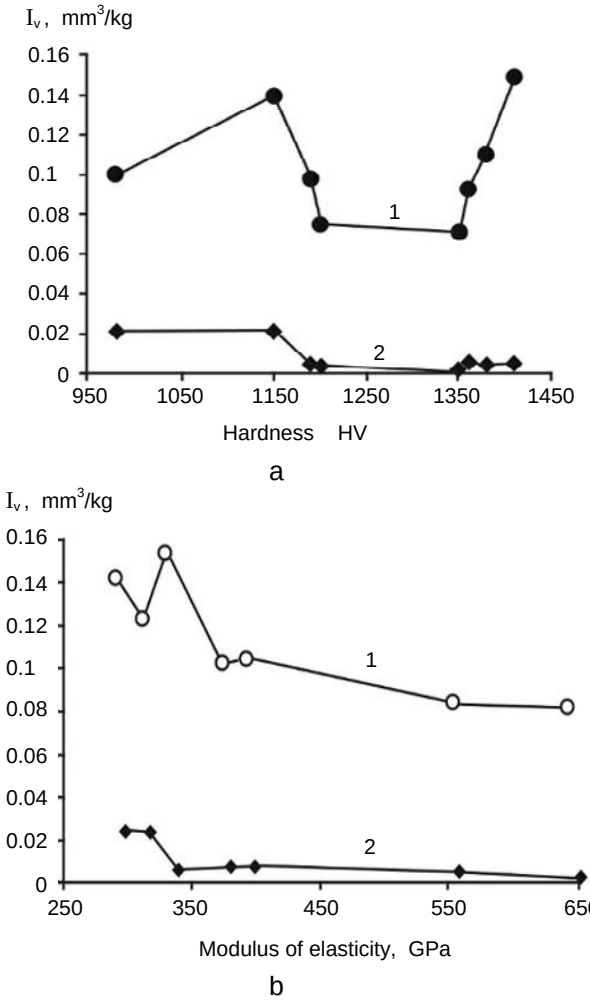

Figure 4.9a,b. Dependence of erosion rate of cermets on: **a** – hardness and **b** – modulus of elasticity; 1 – SiC; 2 –SiO_2

Table 4.9. Structure and erosion rate of cermets with 60 wt% carbide

Grade	Chemical composition and structure of binder	HV	Relative wear resistance ε	
			$\alpha = 30^o$	$\alpha = 90^o$
T3	32 wt% Ni-8 wt% Mo	990	12	32
T4	26 wt% Ni-14 wt% Mo	1190	5	18
TF3	Martensite	1280	7.1	20
TF4	Austenite	1060	11.7	27

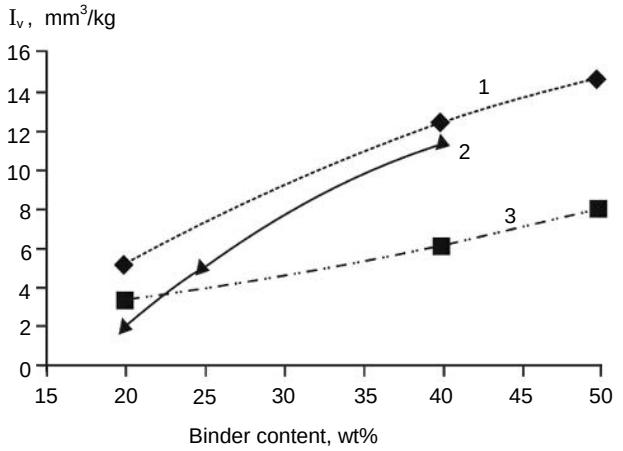

Figure. 4.10. Erosion rate of cermets *vs* binder content and structure (v = 80 m/s, $\alpha = 30^o$, erodent – SiO_2)

The results of the study suggest that microstructural variables influence the wear behaviour. Those factors include binder chemistry and grain boundary structure.

It is shown that the Ni binder contains a small percentage of Ti and a very small percentage of Mo in the solution. The majority of Mo is found within the carbide phase, forming the (Ti, Mo)C complex carbide. The hard phases present in the material consist of a core rich in titanium carbide and molybdenum carbide rich shell; core-rim structured hard grains are surrounded by a tough metallic binder phase, forming the TiC-Mo_2C-Ni material. Mo results in a decrease in the carbide phase contiguity and an increase in the interphase bond strength.

Because of the core-rim structure, no significant differences occur in the mechanical properties at the boundary interphase. Minor microstructural flaws, such a voids, interphase debonding, and binder microcracks, will occur on the TiC-NiMo surface. Both the interphase debonding and microcracks within the binder alloy are evidence that large residual tensile stresses exist within the steel binder phase. Residual stresses in TiC-Ni cermets are the result of the difference in the thermal expansion behaviour between the two phases. A carbide skeleton structure with increased rigidity, following densification, is formed (*i.e.* increased carbide contiguity). As the material cools, residual stresses will arise. This can lead to nucleation and propagation of microcracks.

The microstructure of TiC-steel cermet is developed by a continual process of dissolution and supersaturation of C in the Ti-C-Fe-Ni melt. Re-precipitation onto TiC grains results in the typical cermet core-rim microstructure (Figure 4.11). During sintering there is no complete wettability of TiC by the Fe(Ni) liquid phase and as a result, there are carbide-carbide grain boundaries forming a “skeleton” structure.

Therefore, the improvement in erosion resistance with an increase in the Mo content (Figure 4.10) is mainly due to the increase in the interphase bond strength and to the decrease in the number of microstructural flaws.

During the erosion process, the failure of cermet material starts locally and in most cases, in the binder phase [9]. Carbide grains lose their protective binder and

the eroded surface is almost entirely covered with exposed carbides. Further processes depend on the hardness ratio of the target and erodent. In all cases, the basic mechanisms of wear are plastic deformation combined with brittle fracture. The degree of fracture correlates directly with the wear resistance of the hard TiC particles.

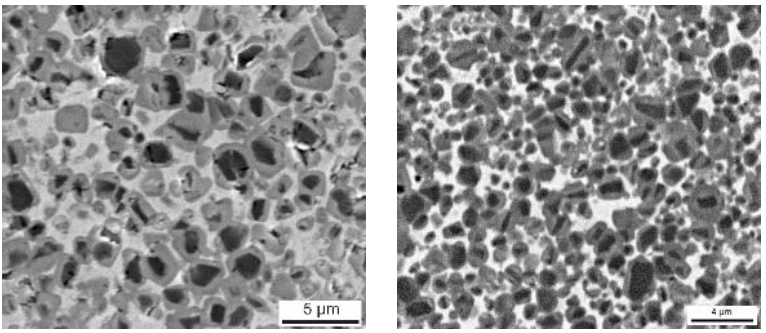

Figure 4.11a,b. SEM micrograph of core-rim structure of TiC-base cermet: **a** – coarse-grained, **b** – fine-grained structure

The boundary microstructure of the grain also plays a role in determining the wear resistance. Sintering results in the creation of Mo-rich grain rims and higher alloying materials show an increase in the wear resistance.

If target material hardness exceeds that of an abrasive, erodent particles can hardly cause a plastic flow in the hard target and the selective nature of erosion prevails. The transgranular fracture at the wear surface is minimal and does not penetrate deeply into the bulk where it occurs. The degree of elastic penetration and therefore the energy transmitted to a surface depends on the elastic modulus and, if the latter is high, less elastic penetration occurs. Therefore, as compared to abrasive hardness, the modulus of elasticity is one of the most important factors governing the wear resistance in the case of harder materials [20]. Under these conditions, continuous impact of the particles may cause a low-cycle fatigue failure of the carbide matrix and carbide grains.

If the hardness of an abrasive exceeds that of a cermet, the following processes take place: penetration of erodent particles into the material surface, microcutting or ploughing, failure of carbide grains resulting in the separation of small chips. Since the erosion of brittle grains is primarily *via* a mechanism involving the initiation and propagation of microcracks, one expects that the fracture toughness of the material will affect the erosion rate. Fracture toughness is usually assumed to be one of the indicators of the wear resistance of these types of materials in environments where brittle fracture is the predominant mode of material removal. This fact is due to the higher energy needed to initiate and propagate cracks in the target material when there is an increase in fracture toughness. However, in this study the relationship between the measured fracture toughness and the erosion rate differs substantially from the linear relationship (Figure 4.12). This result suggests that, although widely accepted, the indentation fracture toughness technique used may not be the best method for determining the toughness of heterogeneous materials intended for tribological environments.

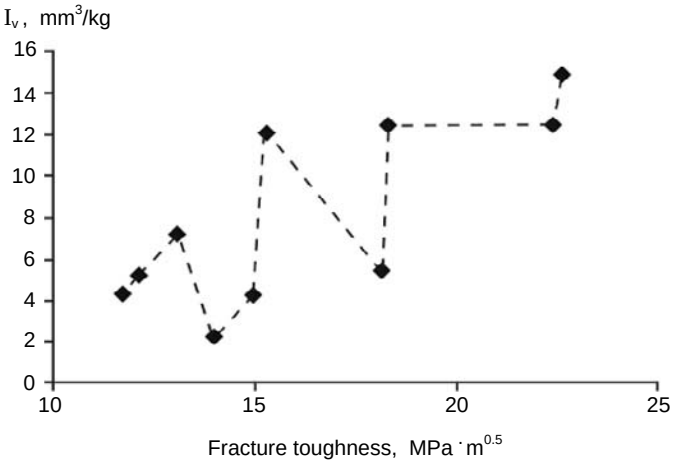

Figure 4.12. Erosion rate *vs* fracture toughness of TiC-base cermets (erodent – silica, impact velocity 46 m/s, impact angle 60°)

4.3.2 Erosion of Coatings

An early study of coating erosion by a centrifugal-type wear tester elaborated at TUT was conducted by Pappel [21]. He studied the detonation sprayed WC-8Co hardmetal coating. It was shown that the erosion resistance of detonation coating tested at 50 m/s by silica erodent of fraction 0.6–0.8 mm at impact angles 30^o and 90^o was low due to the high porosity of the coating and low cohesion between the sprayed particles of the coating. Erosion wear resistance at 30^o was on the level of the reference material rather than on that of hardened steel.

Earlier studies in the field of erosion of different coatings were conducted in 1970–1980 by Kulu from TUT. Studies focused on thermochemically treated (chromized, boronized *etc.*) porous Fe-based powder materials [22, 25] as well as on powder steels [23, 24], followed by thermal sprayed (detonation sprayed) coatings on powder steels [26, 27]. The erosion resistance was determined and the mechanism of wear was studied [28, 32]. Results of the systematic study of sprayed and fused thermal sprayed coatings are reported in [29, 30].

One of the first studies of the erosion of detonation sprayed coatings was conducted by Kulu [31]. He studied coatings from powders of eutectic alloys (Fe-B-Si and F-C-Si-Al) and WC-Co hardmetals. It was shown that erosive wear resistance of coatings from powders of eutectic systems and mixtures (WC and Co) is low; the sprayed coating from sintered hardmetal powder has the highest relative wear resistance ($\varepsilon = 3.1$ at $\alpha = 30^o$) (Table 4.10). A systematic erosion study of thermal sprayed coatings was also conducted by Kulu and others at TUT. Main results are described in [4–6, 33, 34]. The coating groups studied are described in Table 4.11.

To select coating materials and processes for abrasive-erosion wear resistant coatings, most attention was paid to producing powder coatings with minimum porosity and high adhesion strength. Based on the abrasive erosion study of thermally sprayed coatings deposited by different methods (flame and plasma spraying, detonation gun and HVOF spraying, spray fusion), it was shown that only coatings with low porosity (less than 5%) are able to work in the conditions of impact wear [4].

Table 4.10. Hardness and relative erosive wear resistance of selected coatings

Coating material	HV0.05	Relative wear resistance ε	
		$\alpha = 30^o$	$\alpha = 90^o$
Eutectic alloy powders			
Fe-B-Si	710	0.5	0.05
Fe-C-Si-Al	780	0.7	0.1
Hardmetal powders			
BK9c/WC-9Co (agglomerated and sintered)	1310	3.1	1.1
BK9m/WC-9Co (mechanical mixture)	1220	1.8	0.2
BK20m/WC-20Co (mechanical mixture)	810	1.4	0.4

Table 4.11. Composition of selected coating materials and their hardness

Method of deposition	Type of spray material	Composition, wt%	Hardness HV0.2
HVOF Spray	Amdry 927[a]	WC Co12	680/1155[e]
	Tafa 1275H[b]	NiCr16Si4Fe4B3.5	805
	Tafa 1343V	WC Co17	1300
FSF	12494[c]	NiCr11SiB2	430
	12495	NiCr13Si4B3	560
	12496	NiCr15Si4.5B3.5	700
FSF	(12494–12496)+ 15-50 wt% BK15[d]	NiCrSiB+WCCo14Fe8	675–755/1400–1465

[a] Sulzer Metco Inc.
[b] Tafa Inc.
[c] Castolin SA
[d] Recycled WC-15Co hardmetal powder +60–125 μm, TUT
[e] Hardness of metal matrix/hard phase

The materials studied were fabricated by thermal spray processes: high velocity spraying (HVS) and spray fusion (SF). For HVS processes, detonation spraying (DS) methods were applied: detonation gun spraying (DGS) and continuous detonation spraying (CDS). For DGS, Perun-S Detonation Gun Spray System (Institute of Welding, Kiev, Ukraine) was used with propane and oxygen. The HVOF Spray Machine Mounted Model Tafa JP5000 (Tafa Inc.) was applied to CDS. In the case of SF processes, the flame spray fusion (FSF) method and the corresponding flame spraying equipment (Castolin SA) were used.

The coating materials used can be roughly divided into three groups: tungsten carbide-cobalt (WC-Co) based hardmetal powders with Co content of 9–17 wt%, nickel based self-fluxing alloy (NiCrSiB) powders with 11–16% Cr, 2–4.5% Si, 2–3.5% B and composites on the basis of NiCrSiB alloy powders and WC-Co hardmetal powder. Spray materials for the coatings selected for the erosion tests and their chemical and hardness properties are listed in Table 4.11. The substrate for the coatings tested at room temperature was carbon steel with 0.45% C. Typical microstructures of sprayed and spray fused powder coatings are shown in Figure 4.13.

Erosion tests were carried out with silica of fraction 0.1–0.3 mm. The steady state erosion rate was studied as a function of the impact angle at the erodent particles velocity of 80 m/s. Steel of 0.45% was adopted as a reference material.

The erosive wear rate was determined as a volume loss of the target sample *per* mass of the erodent (mm^3/kg). The relative erosive wear resistance ε was calculated as the ratio of the volumetric wear rates of the studied and the reference materials.

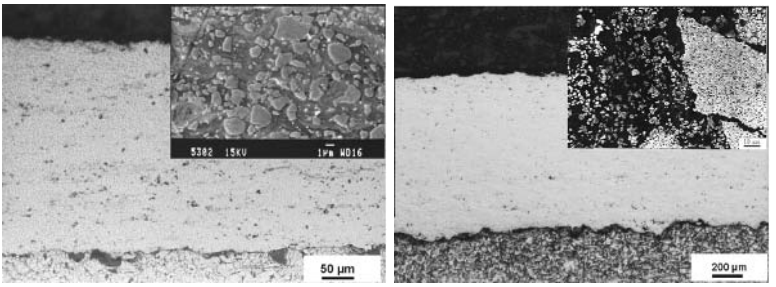

Figure 4.13a,b. Typical microstructures of thermal sprayed coatings: **a** – HVOF-sprayed WC-17Co coating; **b** – FSF NiCrSiB based reinforced with (WC-15Co) hardmetal coating

The the relative erosive wear resistance of the selected coatings are given in Tables 4.12 and 4.13.

Table 4.12. Relative erosive wear resistance of HVS coatings

Deposition technique	Composition (wt%) and type of spray powder	Porosity %	Hardness HV0.2	Relative erosive wear resistance ε	
				$\alpha = 30^o$	$\alpha = 90^o$
DGS	WC-Co12 (Amdry 927)	2.1	680/1155[b]	3.1	1.1
	WC-Co15	2.7	945	2.8	1.1
	(WC-15Co)[a] (BK15)	4.1	815	1.7	0.8
HVOFS	WC-Co17 (Tafa 1343V)	2.9	1300	11.2	2.6
	WC-Co10Cr4 (Tafa 1350VM)	0.7	1230	3.1	2.0
	NiCr16Si4Fe4B3.5 (Tafa 1275H)	1.7	805	0.6	0.4

[a] Recycled hardmetal based, fraction 32–40 µm
[b] Hardness of metal matrix/hard phase

Table 4.13. Relative erosive wear resistance of FSF coatings

Coating material	Hardness HV0.2	Relative erosive wear resistance ε	
		$\alpha = 30^o$	$\alpha = 90^o$
Self-fluxing NiCrSiB alloy based coatings			
12494	430	1.3	0.8
12495	560	1.3	0.6
12496	700	1.6	0.4
Composite coatings based on NiCrSiB and WC-15Co			
- 15 wt% (WC-Co)	675/1410[a]	1.5	0.7
- 25 wt% (WC-Co)	685/1445	1.9	0.6
- 50 wt% (WC-Co)	735/1465	2.0	0.6

[a] Hardness of metal matrix/hard phase

It follows from the experiments that hardness has a major effect on wear of materials by the mechanisms of plastic deformation, while fracture toughness is a dominant factor in wear involving a brittle fracture. Since the porosity level plays an important role in wear resistance, materials with narrow porosity, ranging from 0.7 to 3, were chosen for comparison. Topographical images of the eroded surfaces of the HVS NiCrSiB and WC-17Co coatings are shown in Figures 4.14 and 4.15, respectively. As can be seen, the wear at high impact angles results from carbide fracture or removal of sprayed microparticles due to the low-cycle fatigue processes; at low impact angle, the microcutting processes are dominating for the metal-matrix coating [33]. In the case of hardmetal coating with a low binder content, the direct fracture and low-cycle fatigue processes are dominating.

It is similar to the wear mechanism of hardmetals at erosive wear, but differs from the mechanisms observed under other abrasive wear conditions [34–37].

Similarly to normal impact erosion, direct fracture or low-cycle fatigue fracture mechanism is dominating; out of residual stresses in coatings, compressive stresses are preferable. Such compressive stress in coatings is obtained by the HVOF-spraying of hardmetal powder or by the FSF of composite coatings (Table 4.14) [38].

Table 4.14. Erosive wear resistance *vs* residual stresses in coatings

Type and coating material[a] and method of deposition	**Mean residual stress (outer layer) σ_{mean}, N/mm^2**	**Relative erosive wear resistance ε**	
		$\alpha = 30^o$	**$\alpha = 90^o$**
12495, FSF	–101.2	1.3	0.6
12496, FSF	–38.8	1.6	0.4
12495+25 wt% BK15[b], FSF	–21.1	1.9	0.6
Tafa 1343V, HVOFS	–773.0	10.8	2.6

[a] Composition of coatings – see Table 4.11
[b] Recycled WC-15Co hardmetal powder

An interesting group of thermal sprayed coatings is that from powders produced from used hardmetal [39]. The study concentrated on the WC-15Co hardmetal powder of 0.2–0.5 mm with angular and round particle shape as reinforcement in wear resistant NiCrSiB-base composite coatings. It was found in [34] that reinforcement – hardmetal powder content, particle size and shape (rounded, angular) of spray fused coatings – has an influence on the erosion rate of coatings. It was demonstrated that the effect of matrix hardness, WC-Co grain size and WC-Co content on the erosion rate is notable: the wear resistance of coatings increases with an increase in matrix hardness as well as with an increase in the hard phase content in the composite at small impact angles of abrasive particles. The influence of the above-mentioned parameters on the erosion rate at the normal impact is insignificant and the wear resistance of coatings is low.

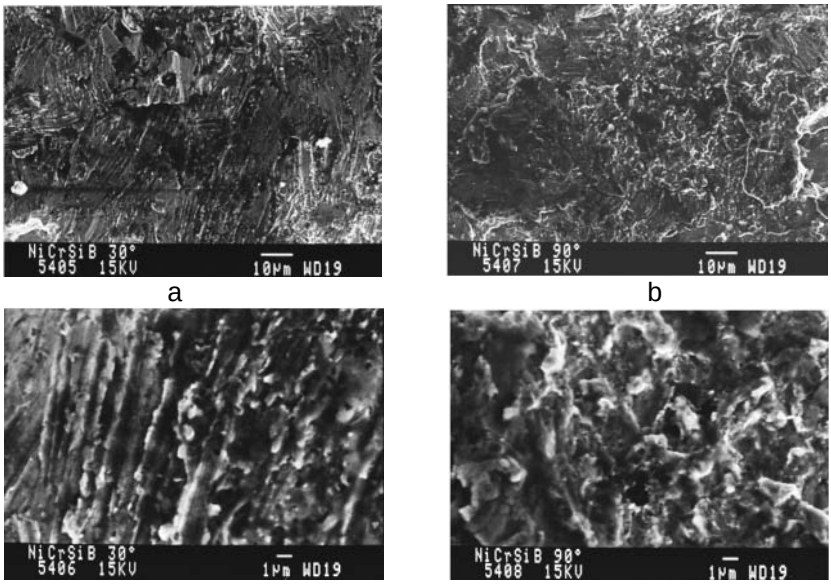

Figure 4.14a–d. Topography of eroded HVS NiCrSiB (Tafa 1275H) coating: **a, c** – $\alpha = 30^{o}$; **b, d** – $\alpha = 90^{o}$.

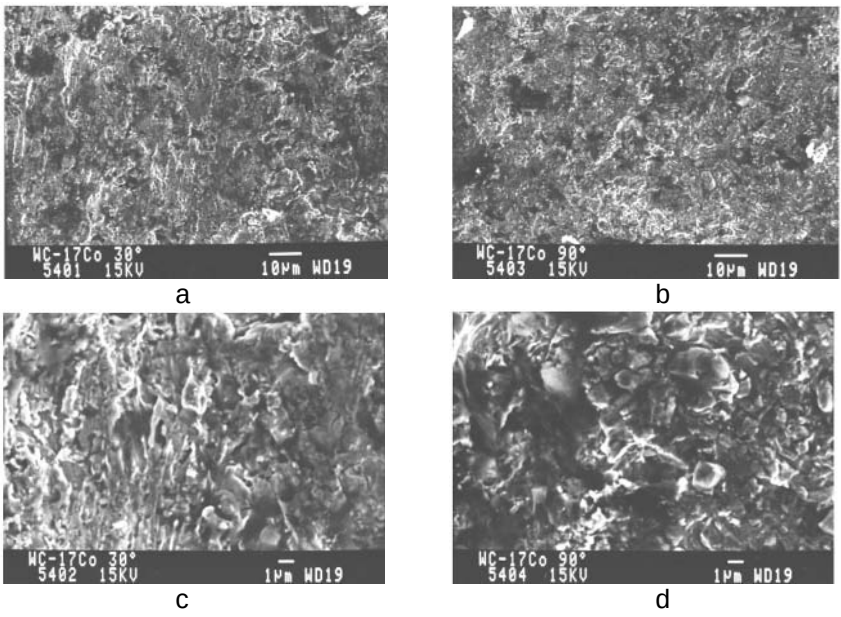

Figure 4.15a–d. Topography of eroded HVS WC-17Co (Tafa 1343V) coating surface: **a, c** – $\alpha = 30^{o}$; **b, d** – $\alpha = 90^{o}$.

4.4 Erosion Resistance of Ceramic-Metal Materials and Coatings at Elevated Temperatures

4.4.1 Erosion of Ceramic-Metal Composites

Cemented tungsten hardmetals are most effective in erosive wear conditions at normal temperature because of their excellent combination of reliability properties – high wear resistance and fair strength-toughness. Their main disadvantage is low oxidation resistance.

In an oxidizing environment, the erosion behaviour at elevated temperatures depends on the rate of oxidation and on the thickness, morphology, adherence, and toughness of the oxide layer that forms on the surface of the material during the oxidation process. For materials with a high level of oxidation, erosion behaviour is controlled by the properties of the oxide layer. These materials cannot be used when erosion processes are involved, because the oxide layer (film) readily detaches itself from the surface under abrasive impacts. In addition, repeated impacts from the erosion particles constantly expose fresh binder material to the oxidizing environment, exacerbating oxidation and material loss.

Recent efforts have concentrated on the effect of solid particle erosion of WC-Co hardmetals and ceramic-metal composites.

Alman *et al.* [40, 41] analyzed the erosion of WC-Co hardmetals. It was found that the erosive wear rate of the WC-6Co materials increases steadily with an increase in the test temperature up to 700 ^{o}C. The measured erosion rate at 700 ^{o}C was more than double the rate at room temperature. Tests were also attempted at 900 ^{o}C, but oxidation of cobalt was severe, thereby nullifying the results.

Erosive wear behaviour of titanium and chromium carbide cermets at elevated temperatures (up to 800 ^{o}C) was studied by Kübarsepp, Hussainova *et al.* at TUT [42, 43]. To analyze erosion at elevated temperatures, the centrifugal wear tester was placed into the heated test chamber. Test conditions were similar to those at room temperature. Wear conditions were as follows: erodent – silica 0.1–0.3 mm of 1100–1200 HV, particle velocity – up to 80 m/s, impact angles were from 30^{o} up to 90^{o}.

In [42] TiC-base cermets (TiC content 50–80 wt%) bonded with Ni-Mo alloys (Mo content 20 and 33 wt%), Ni-steels (Ni content 5–14 wt%) and Cr-Ni-steels (1% Cr, 1% Ni) were investigated. Tests at elevated temperatures were performed at 400, 600 and 800 ^{o}C, impact angles 70–90^{o} and jet velocity 40 m/s. To compare the erosion resistance of TiC-base cermets with that of WC-base hardmetals, WC-25Co hardmetal was used as a reference material. The results of experiments are given in Table 4.15.

As is shown, erosive wear resistance at elevated temperatures of WC-Co hardmetal and TiC-based cermets depends on the testing temperature:

- If the erosive wear resistance at moderate temperature (up to 400 ^{o}C) of WC-base hardmetals has a marked advantage over TiC-base cermets, then at elevated temperatures (above 400 ^{o}C), TiC-base cermets cemented with Ni-Mo alloys have a major advantage over steel-bonded ones and even over WC-base hardmetals;
- The results obtained confirm the selective nature of the erosive wear of cermets at elevated temperatures – surface failure starts in the binder and consequently, depends on the strength-rigidity properties of the metallic phase. At

temperatures above 600 °C, oxidation is intensified. Stable oxide films covering cermets act like protective layers. Origination of oxide films on cermets (at 600–800 °C) results in the decrease of their high-temperature erosive wear.

Table 4.15. Structural characteristics (carbide content, binder, hardness) and wear rates at elevated temperatures of TiC-base cermets

Grade	Carbide and binder content, wt%	HV30	Wear rate, mm^3/kg *per* 1 mm^2		
			400 °C	600 °C	800 °C
WA15	WC+25Co	1150	0.6	1.7	-
TH20	TiC+20Ni(Mo)2:1	1450	0.2	0.5	0.9
TH40	TiC+40Ni(Mo)2:1	1260	0.4	0.7	1.2
60TXH	TiC+40 austen. steel (14Ni, 1Cr)	1050	2.2	3.7	3.3
70TXH	TiC+30 austen. steel (14Ni, 1Cr)	1270	1.7	4.1	3.3
60TXC	TiC+40 marten. steel (1Cr, 1Si)	1350	1.1	2.6	2.8

Cr_3C_2-Ni cermets with nickel content of 10–40 wt% were studied in [41]. The chemical composition and mechanical properties of Cr_3C_2-Ni cermets studied are shown in Table 4.16.

Table 4.16. Chemical composition, hardness and wear rate at elevated temperatures of Cr_3C_2-Ni-base cermets

Grade	Carbide content, wt%	HV30	Wear rate, mm^3/kg		
			20 °C	300 °C	600 °C
C1	90	1490	2	4	8
C2	80	1368	7	13	22.5
C3	70	995	23	22.5	34.5
C4	60	900	22	18.5	32

The results of erosion tests of Cr_3C_2-Ni cermets are presented in Table 4.16 and Figure 4.16. The values of the erosion rate were determined for the impact angle of 75°. Increasing the temperature up to 300 °C, the erosion rate of cermets with a low binder content (C1 and C2) remains relatively constant. On the other hand, cermets with a high binder content show even better erosion resistance at 300 °C than at room temperature. This may be the result of the softening of the binder metallic material. For those materials, the reduction of the erosion rate to a minimum value with the temperature increasing, followed by an increase in the erosion rate with the test temperature increasing, is quite common, particularly at high impact angles. At 600 °C, all cermets tested had higher erosion rates than at room temperature.

Figure 4.17a shows the shift of maximum erosion rates to more oblique angles measured at the particle velocity of 60 m/s. At high temperatures, all the materials investigated were more ductile than at room temperature. Figure 4.17b shows the effect of particle velocity on the erosion rate of cermets.

Figure 4.17 indicates that at a high impact angle at high temperature, cermet C4 performs better than C3, even though C3 is harder and contains more carbides.

This fact can be explained by the evaluation of mechanisms which contribute to material removal from the surface during erosion.

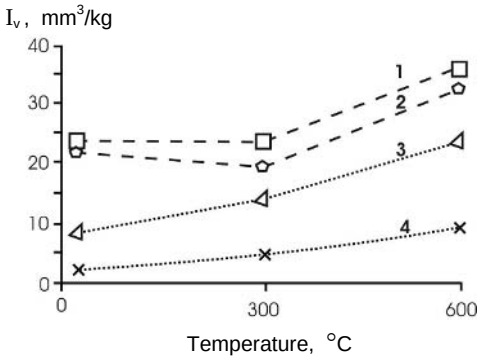

Figure 4.16. Effect of the test temperature on the erosion rate of cermets at the impact angle of 75°: 1 – 70% Cr_3C_2; 2 – 60% Cr_3C_2; 3 – 80% Cr_3C_2; 4 – 90% Cr_3C_2

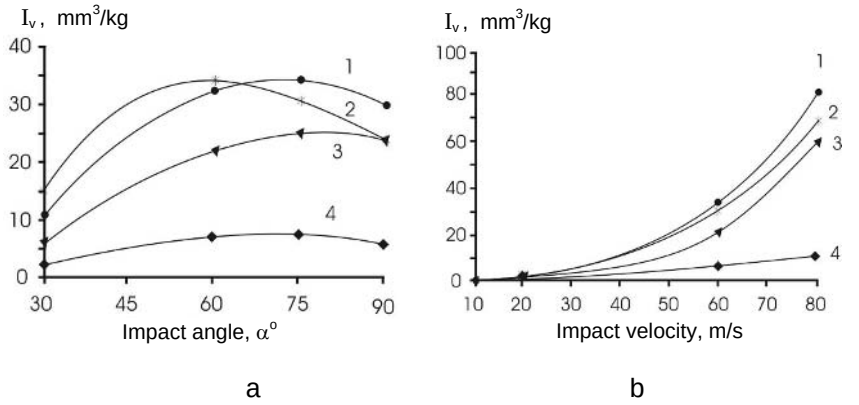

Figure 4.17a,b. Dependence of the erosion rate of cermets at the temperature of 600 °C from the: **a** – impact angle; **b** – impact velocity (designation the same as Figure 4.16)

The oxidation rate of chromium carbide-based materials is small enough at high temperatures and cannot affect the erosion rate; thus their erosion resistance at elevated temperatures depends, first of all, on the material tolerance to damage. However, an increase in the Ni content leads to the increase of the oxidation rate.

As the scanning electron micrograph of the erosion damage shows, the failure of the low binder content cermet (Figure 4.18a) is axial splitting, chipping, and cracking of the carbide particles [43]. The transgranular crack propagation mode points to the relatively strong interphase bond. In contrast, the surface of a high binder content cermet appears somewhat different (Figure 4.18b). In this case, the material is removed by the detachment of plastically deformed lips of the binder material as well as by transgranular fracture. During erosion, due to surface interaction and to the fracture of abrasive particles, debris from the erodent

accumulates and is fused by the force and generated heat; in the case of other grades, the fused erodent debris is not apparent.

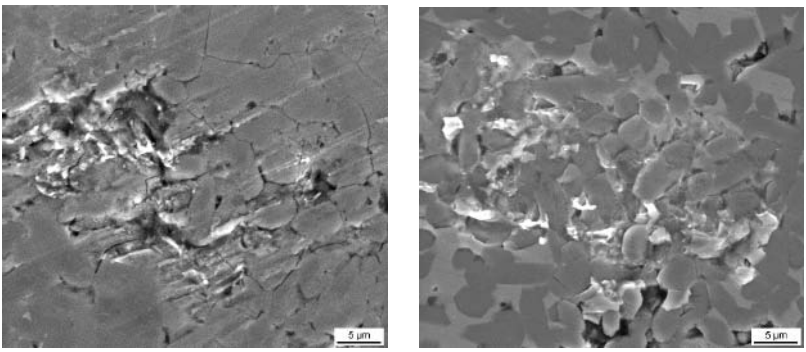

a b

Figure 4.18a,b. Erosion damage at 300° C on the surface of the Cr_3C_2–base cermets: **a** – C1 grade and **b** – C4 grade

Other mechanical factors, such as the influence of temperature on hardness, interfacial strength and fracture resistance (the ability to absorb energy of repeated impacts), may also contribute to the erosion behaviour of these materials; however, these mechanisms have not been studied in detail to date.

It was found that the erosion of ceramic-metal composites is associated with the combination of ductile and brittle modes of wear and material behaviour is influenced both by the microstructure and test conditions. A change in the maximum wear rate is observed with increasing temperature, attributed to the transition between "brittle" and "ductile" behaviour [44, 45]. The fact that an oxide can form at high temperature further complicates the analysis. The oxide layer formed on the binder phase at lower temperatures may be removed through a brittle erosion mechanism [46]. However, at higher temperatures, oxide plasticity increases, demonstrating that the erosion of cermets is a very complex phenomenon of competing tribo-corrosion processes, between erosion and oxidation of the binder materials and matrix.

4.4.2 Erosion of Coatings

Along with erosion tests of coatings at room temperature, experiments were also conducted at higher temperatures. Selected coatings, first high velocity sprayed (HVS) coatings, were tested at elevated temperatures (up to 650–700 °C) [6, 47].

Coatings from traditional self-fluxing alloys powders and WC-Co hardmetal powder based coatings included a coating with an addition of 4% Cr were studied (Table 4.17). As experimental coating materials, WC-base powders with Co- and Ni-base alloy binder powders were used; coatings from the materials studied were fabricated by the HVOF spray. Experimental materials are characterized in Table 4.18.

Erosion tests were conducted with silica of fraction 0.1–0.3 mm at the erodent particle velocity of 80 m/s. Testing temperature of coatings from commercial

powders was 650–700 °C, from experimental powders – up to 400 °C. Substrate for coatings tested at elevated temperature was austenitic stainless steel. Erosion rate was determined as a volume loss of the target sample *per* mass of the erodent (mm^3/kg).

The erosion wastage of thermal sprayed coatings is strongly affected by impact angle of the particles. However, material behaviour depends on the mechanisms of material removal, while hardness seems to be of minor importance. In its turn, microstructure influences both hardness and mechanisms of material loss.

Table 4.17. Composition, hardness and wear rates of HVOF sprayed coatings tested at the elevated temperature (700 °C)

Type of spray material	Composition, wt%	Hardness HV0.2	Wear rate, mm^3/kg			
			$\alpha = 30^o$		$\alpha = 90^o$	
			400 °C	700 °C	400 °C	700 °C
Tafa1236	NiCr11Si2B2	320	-	335	-	355
Tafa1275H	NiCr16Si4Fe4B3.5	805	56	240	163	290
Tafa1343V	WCCo17	1300	-	112	-	120
Tafa1350VM	WCCo10Cr4	1230	20	50	17	82

At the elevated temperature (700 °C) of testing and with HVS coatings (Figure 4.19b), the wear rate decreases with an increase in coating hardness both at low and high impact angles. Relative wear resistance is low for coatings of low hardness; relative wear resistance is 2–3 times higher for coatings of higher hardness. The wear mechanism of coatings at elevated temperatures differs from that at room temperature: at the elevated temperature (700 °C), the mechanism of impact wear resembles that at oblique ($\alpha = 30^o$) and normal ($\alpha = 90^o$) impact. Under both wear conditions, ploughing of the eroded surface takes place and, as a result, the worn material is removed (see Figure 4.20).

Table 4.18. Composition and erosive wear rates of coatings from experimental spray powders at room and elevated temperatures

Grade	Coating composition, wt%	Relative erosive wear resistance ε					
		$\alpha = 30^o$			$\alpha = 90^o$		
		20 °C	160 °C	400 °C	20 °C	160 °C	400 °C
M1	86WC-10Co-4Cr (com)	2.88	4.45	2.69	1.38	2.32	1.14
M2	86WC-6Co-8Cr (com)	3.60	4.28	2.11	2.26	3.91	1.48
M3	$75Cr_3C_2$-25 (80Ni-20Cr) (com)	0.84	1.59	-	0.25	0.82	-
M5	85WC-15Anval Ultimet (exp)	3.11	3.55	2.28	1.46	1.97	0.84
M6	85WC-15Alloy59 (exp2)	4.02	3.40	-	1.78	1.74	-
M12	85WC-15Hastelloy C-276 (com)	2.93	2.14	-	1.57	1.14	-
M16	85WC-15Alloy59 (exp)	2.02	3.00	3.26	1.25	1.76	1.43

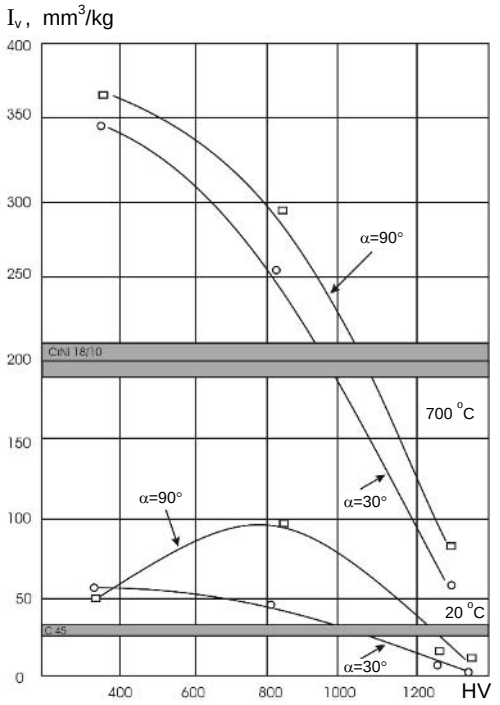

Figure 4.19. Influence of the wear rate of HVS coating on the hardness of coatings at room and elevated temperatures

For material use in an aggressive environment, coating structures have to be chosen based on definite working conditions. For all the materials tested, the erosion rate was 5–6 times higher at the elevated temperature. However, the influence of the impact angle does not have a significant effect on the erosion resistance of thermal sprayed coatings at the elevated test temperature. The erosion rate at low impact angle is only slightly higher for any material at normal impact angle.

As a result of the comparison of the erosive wear resistance of coatings from commercial WC-10Co-4Cr powder (M1) and those from experimental powder WC-15NiCr-alloy (Alloy59, M16), it was found that at room and moderate temperatures, wear resistance is the highest with coatings from commercial powder, at a higher temperature (400 ^{o}C) with the coating from experimental powder.

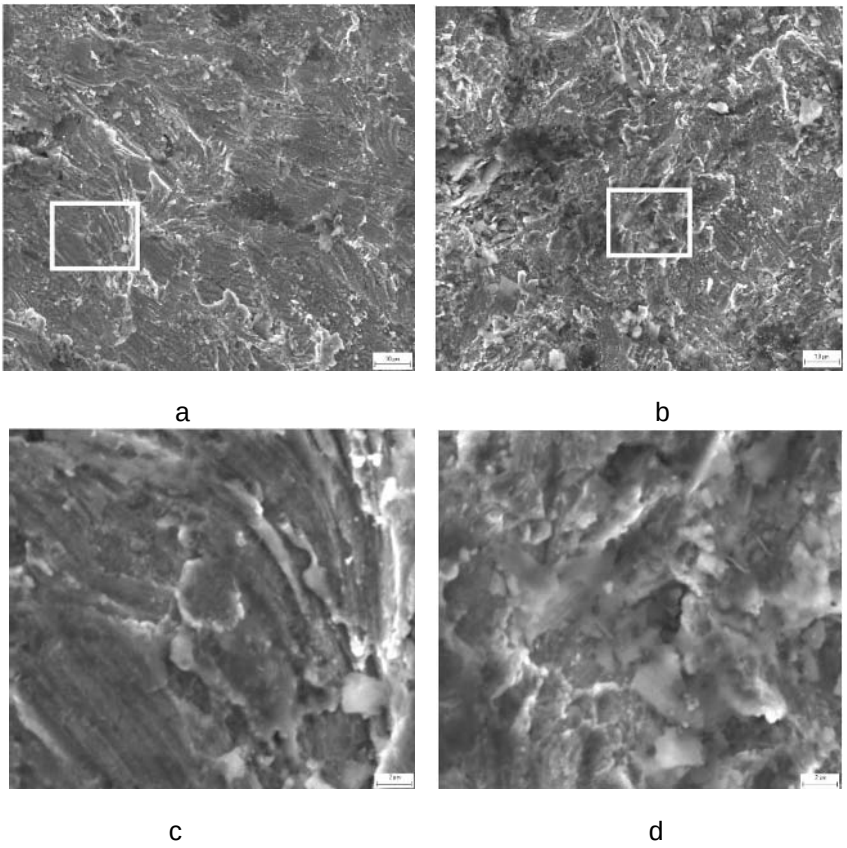

Figure 4.20a–d. Topography of eroded HVOF sprayed NiCrSiB (Tafa 1275H) coating: **a, c** – $\alpha = 30^{o}$; **b, d** – $\alpha = 90^{o}$

4.5 Criteria for Erosive Wear Resistant Material and Coating Selection

Based on the abrasive erosion studies of hardmetals, cermets and thermally sprayed coatings with different composition deposited by different methods, the main criteria for their selection can be divided as follows [47]:

- Tribological,
- Structural,
- Qualitative.

4.5.1 Tribological Criteria

Impact Angle

When selecting coatings for impact erosion, the following requirements must be taken into account:

- At oblique impact (at small and medium impact angles), with the mechanism of microcutting dominating, hardness characteristics are important,
- At normal impact, with the direct or low-cycle fracture mechanism dominating, toughness and fatigue characteristics are important.

Hardness of Erodent

The erosion rate of a material depends on its abrasive hardness, more precisely, on the material to abrasive hardness ratio (H_m/H_a) [34]. If material hardness is lower than abrasive hardness ($H_m<H_a$), microcutting or surface scratching may take place. If material hardness is higher than abrasive hardness ($H_m>H_a$), clear removal of the material usually does not take place and the entire process has the nature of fatigue. At high-energy impact of abrasive particles, brittle rupture of the material and detachment of carbide grains or their fragments take place.

Experimental studies of impact erosion with erodents of different hardness (from 120–200 up to 1900–2000 HV) showed that abrasive hardness has a major influence on the wear rate of coatings. The dependence of the wear rate at impact erosion on the hardness of the abrading material is described by the so-called S-curves. From the comparison of S-curves of different materials and coatings, the main rule of erosive wear follows – to guarantee high wear resistance of coatings at an oblique impact, their hardness must exceed the hardness of the abrasive or the material to be treated. At normal impact, the influence of abrasive hardness on the wear rate is insignificant due to effective fatigue fracture mechanisms.

The S-curves of two different coatings (sprayed hardmetal and spray fused self-fluxed Ni-alloy based) are shown as examples in Figure 4.21. From these curves it follows that WC-Co based materials (both hardmetals and coatings) with hardness about 1200–1400 HV are durable in abrasive conditions with erodent hardness up to 1000–1200 HV, high binder content cermets and coatings – with erodent hardness up to 600–800 HV.

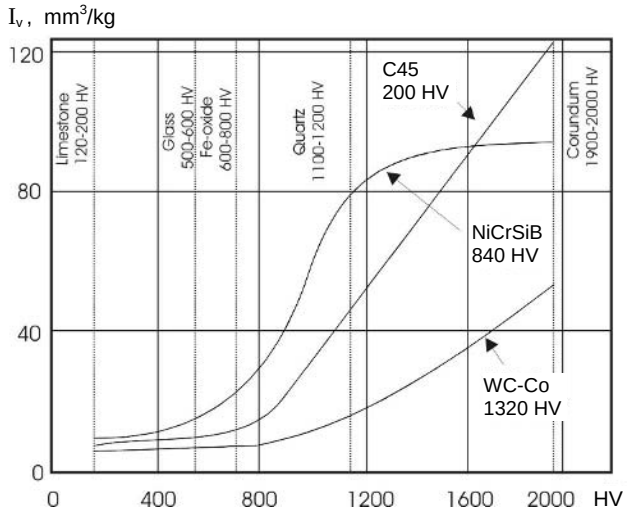

Figure 4.21. Dependence of erosion rate on the hardness of the abrasive

Shape of Abrasive Particles

As was shown by the theory of erosive wear of plastic materials, in material removal due to microcutting, erodent particle shape is of essential importance.

Based on the wear study by abrasive particles of different shape (Table 4.19) with the same hardness, direct correlation between the shape of abrasive particles and the wear rate at oblique impact was observed (Figure 4.22). The shape parameter – angularity SPQ of abrasive particles was determined by the method proposed by Stachowiak [48] used in [49].

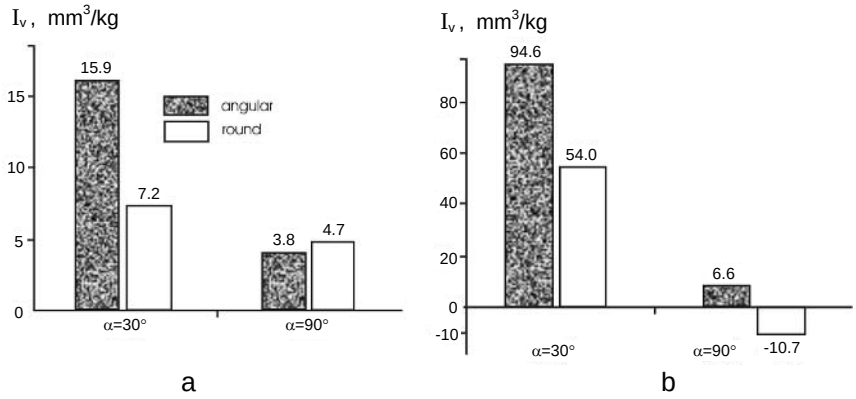

Figure 4.22a,b. Influence of abrasive particle angularity on the erosion rate: **a** – steel 0.45% C; **b** – pure Al

Table 4.19. Characterization of hardmetal powder particles with different shape

Type of abrasive	Particles size, mm	d_m, mm	SPQ
Angular	0.2–0.5	0.28	0.7
Rounded	0.2–0.5	0.32	0.5

Figure 4.22a shows the influence of the angularity of abrasive particles (angular and rounded particles) on the wear rate of steel (0.45% C) at different impact angles. At low impact angle (30°), the erosion rate is more than double in the case of angular particles. At 90°, the wear rate does not show a significant dependence on particle angularity and is slightly higher with round particles. Figure 4.22b shows the results of the same study, using pure aluminium as a target material. The difference in the wear rate with angular and round abrasive particles is practically the same as with steel. Due to low hardness and high plasticity at the small (30°) impact angle, the wear rate exceeds that of steel more than six times.

At normal impact (90°), the penetration of hardmetal particles to the Al target took place. As a result, by the angular abrasive particles, the weight of the specimen increased (the wear rate by rounded abrasive is negative – Figure 4.22b).

Figure 4.23 shows wear marks on steel C45 surfaces eroded by angular and rounded particles of the abrasive. As follows from Figure 4.23a,c at low impact angle, both by angular and rounded abrasives, plastic deformation takes place, with the microcutting mechanism dominating. When high impact angles were applied

(Figure 4.23b,d), the surface was subjected only to plastic deformation, and the wear rate was minimal.

Other Operating Parameters

The erosion-enhanced corrosion at room temperature and erosion-enhanced oxidation at high temperature increase the wear rate of coating materials substantially. As a result, more erosion-resistant coatings should be developed for reasons of corrosion and intermediate temperatures.

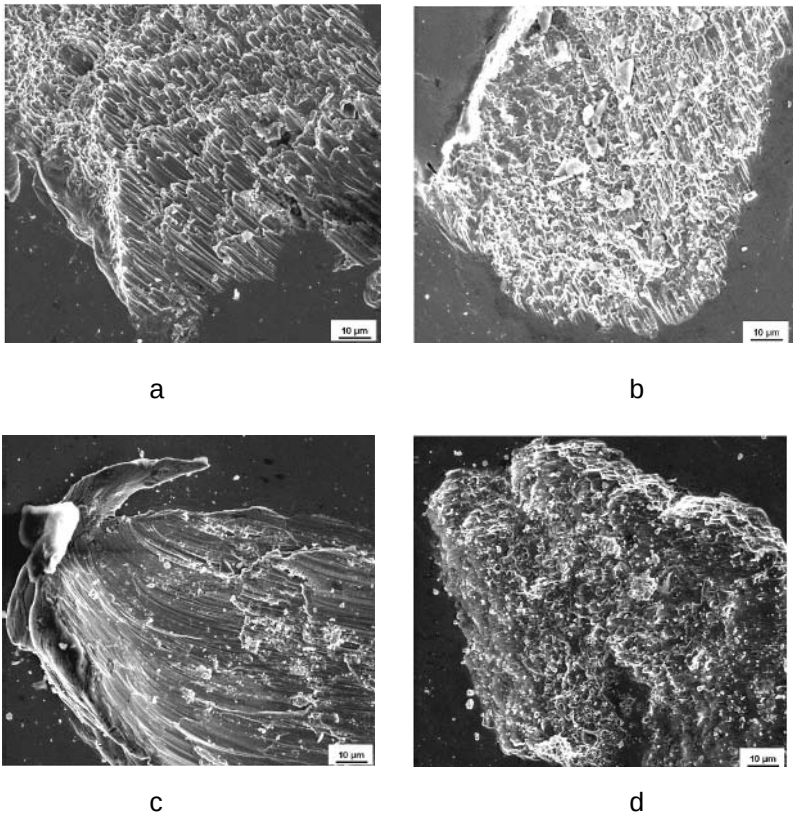

Figure 4.23a–d. SEM micrographs of wear marks on steel C45 surfaces eroded by: **a, b** – angular and **c, d** – rounded abrasive particles at **a, c** – low and **b, d** – high impact angle

4.5.2 Structural Criteria

Composition

For erosive wear, WC-Co represent an important composition both for hardmetals and thermal sprayed hardmetal-type coatings, in the conditions of simultaneous erosion and corrosion, WC-Co systems with improved corrosion resistance are required.

Based on different fracture mechanisms of wear by impact erosion under different wear conditions, the dependence of the optimal structure of materials and coatings on the conditions of wear is described in [50]. In the case of oblique impact erosion (at low and medium impact angles), where the wear rate decreases with an increase in the hardness and the mechanism of microcutting is dominating, the hardmetal type structure is preferred (Figure 4.24). The hard phase content must exceed 50%. In the case of normal impact, the metal-matrix structure with hard phase content less than 50% is preferred.

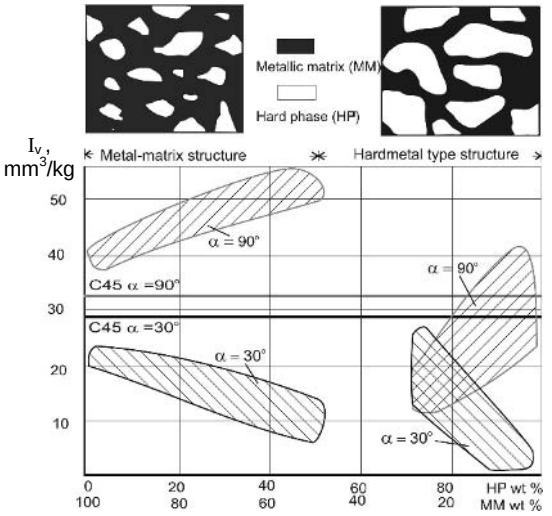

Figure 4.24. Recommended structures of materials and coating for different conditions impact erosion

Microstructure

For erosive wear conditions, materials and coatings with composite structure are preferred: very hard phases (carbides, nitrides *etc*.) in a relatively hard metal matrix.

Optimal structures, depending on the erosion conditions, are framed cermet structures for oblique impact and metal-matrix structure for normal impact; for mixed erosive wear conditions, multimodal, preferably “double cemented” WC-Co hardmetal based coating structure, instead of a simple cobalt matrix, containing particles of WC or other carbides, is a cobalt (nickel) matrix based structure containing particles of WC-Co agglomerated granules or particles of WC-Co hardmetal (Figure 4.25a). A similar structure is obtainable from hardmetal powders coated with metal (cobalt or nickel) and deposited by the HVS method. Another way to manufacture such complicated cemented structures is spray and fusion of composite powders, based, for example, on NiCrSiB self-fluxing alloy powder and WC-Co or other carbide based hardmetal powder. The resulting structure consists of WC-Co hardmetal particles in the Ni-alloy based matrix with small dissolved tungsten carbide particles (Figure 4.25b).

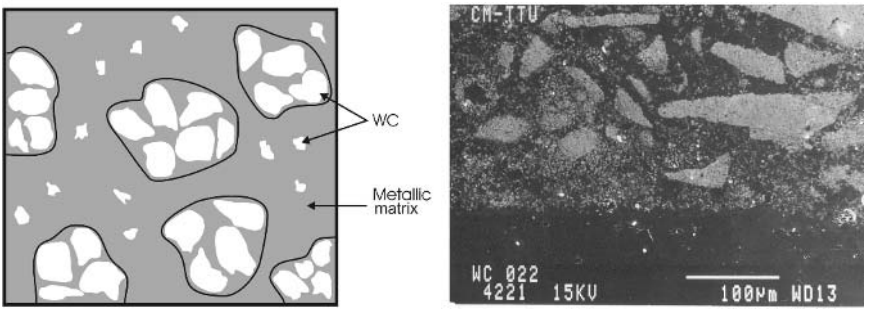

Figure 4.25a,b. Double cemented structure of coating: **a** – schematic; **b** – produced by FSF

Porosity

Minimum porosity obtainable by powder metallurgy, spray fusion or high velocity thermal spray processes guarantees high density (porosity less than 3%) and high erosive wear resistance under extreme conditions of wear (abrasive-erosive wear resistance of hardmetals exhibited up to 50 times depending on wear conditions and HVOF sprayed coatings 10 times higher wear resistance than the reference material – steel).

Medium and high porosity coatings (porosity more than 5%) of the same hardness laid by different methods (flame, plasma and detonation spraying) may differ by one order of magnitude in their wear resistance under analogous wear conditions. The relative erosive wear resistance of high porosity coatings is low (less than one). It means that high velocity spraying only or flame spray fusion guarantee low porosity (in the range of 1–3%) and high wear resistance in the conditions of impact erosion.

Thickness of Coatings

The performance and protective capacity of coatings are determined by their thickness and linear erosive wear rate. The latter depends on particle concentration and intensity of erosion (wear *per* mass unit of erodent material). From the analysis of the linear wear of different materials (ceramics, hardmetals) and coatings it follows that the linear erosion rate *per* kilogram of the erodent is in the range of 0.01–0.1 mm by hardmetals and up to 0.5–0.6 mm by ceramics at high impact angles (Table 4.20).

In practice, the linear erosion rate (wear in mm *per* erodent unit amount, mm/kg) depends on the influence of particle concentration that may be different. It differs in the machines operating in different conditions of abrasive erosion: the positive effect of high particle concentration of the material in milling equipment, for example, in disintegrators, is observed; erosion at low particle concentration takes place in ventilators, exhausters, *etc*. If in the first case, wear is in the tenth part of mm *per* hour, in the conditions of low particle concentration, it is in the hundredth or thousandth parts of mm *per* hour. As dependent on erosion conditions, thickness of coatings varies in the range of 0.2–1 mm.

Methods of thermal spray are most widely used in the production of erosive wear resistant coatings. These methods enable wear resistant surfaces to be

produced with thickness in the range from some tenth-value to some mm. The thickness of weld coating may reach 10 mm (Figure 4.26).

Table 4.20. Linear erosion rate of materials and coatings at room temperature

Type of material and composition	Author and source	Linear wear rate, mm/kg	
		At low impact angles	At high impact angles
Ceramics			
Al_2O_3, SiN, B_4C	Olsson [2]	0.05–0.06	0.1–0.4
SiC, Al_2O_3+Zr/TiNC	Olsson [2]	0.12	0.6
Al_2O_3	Kleis, Pappel [7]	0.003	0.008
Al_2O_3		0.001	-
Si_3N_4		0.0001	-
Sialon		0.0001	-
Hardmetals			
WC-(6-25) Co	Grearson [3]	0.08–0.27 (mm/h)	0.17–0.27 (mm/h)
WC-15Co	Tiidemann [9]	-	0.02–0.1
Cr_3C_2-30Ni	Hussainova [19]	-	0.02–0.24
Sprayed coatings			
HVOFS WC-Co	Kulu [34]	0.01–0.02	0.04–0.06
HVOFS NiCrSiB		0.1	0.2
FSF NiCrSiB		0.04	0.2

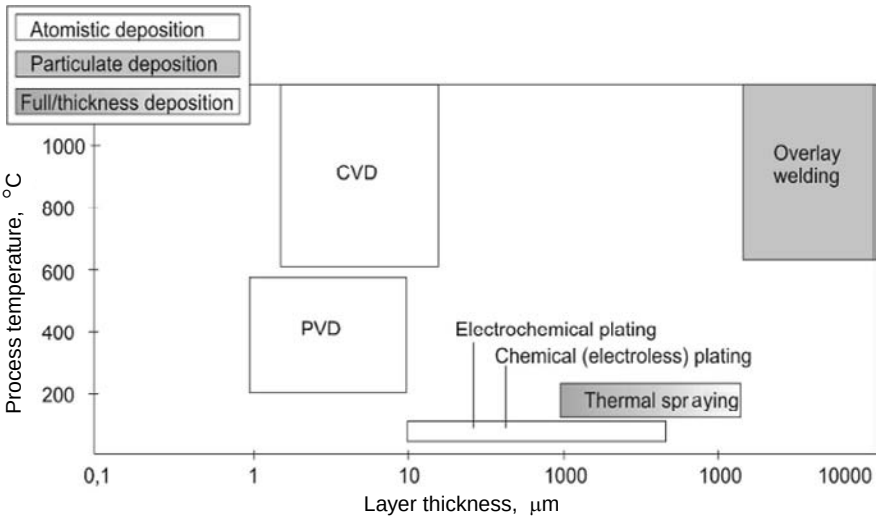

Figure 4.26. Coating thickness and process temperature of today's tribological coatings

4.5.3 Qualitative Criteria

Hardness

Hardness is one of the most important and easily measurable properties which has a major effect on target wear. By abrasive wear, material wear rate depends on material hardness – if it is lower than abrasive hardness, microcutting of the surface may take place. If material hardness is higher than abrasive hardness ($H_m > H_a$), clear removal of the material usually does not take place and the entire process has the nature of fatigue.

By erosive wear, at low impact angles as proved by numerous studies, a direct connection exists between erosion resistance and hardness of materials.

As follows from Figure 4.27 [51], a satisfactory relation between hardmetal and cermet hardness and erosive wear exists at low impact angles. This was predictable, as shown by Finnie [52] and others. The dependence between volumetric erosive wear and hardness ($V = 1/2\ mv^2\ H^{-1}\ f(\alpha)$) proposed by Finnie demonstrates that erosion volume V is directly proportional to the kinetic energy of the impact of abrasive particles ($1/2\ mv^2$), inversely proportional to the hardness (H) and function of the angle of impingement ($f(\alpha)$). Optimal hardness of coatings must be maximum and higher than that of the abrasive, depending on erosion conditions, to guarantee high abrasive-erosive wear resistance at low impact angles; at normal impact, the optimal level of hardness is recommended.

The dependence of relative erosive wear resistance on the hardness of a sprayed coating is illustrated in Figure 4.28. As shown, the main tendency of sprayed coatings is as follows: both at low and high impact angles, an increase in the hardness of HVS coatings leads to an increase in their impact erosion wear resistance. At an oblique impact angle (30^o), the wear resistance of coatings is about 10–12 times higher than that of the reference material (noncoated steel). At high erosion impact angle (90^o), the wear resistance of the best sprayed coating exhibited 2–2.5 times higher wear resistance than noncoated steel.

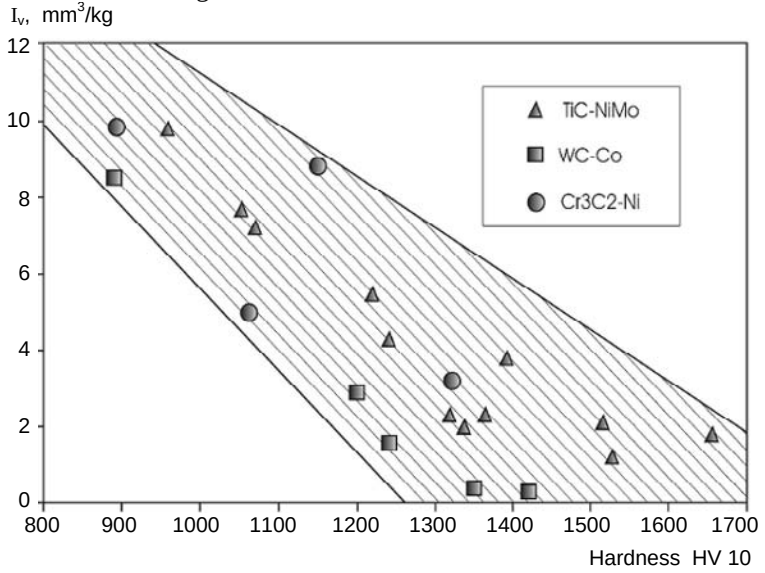

Figure 4.27. Erosive wear resistance *vs* hardmetal and coating hardness, $\alpha = 30^o$

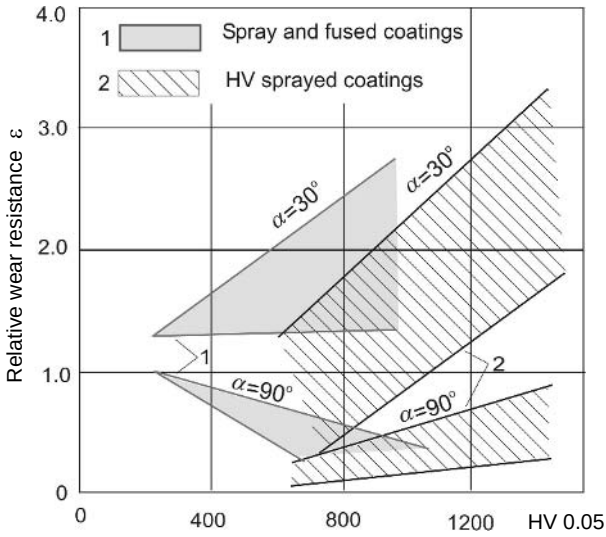

Figure 4.28. Erosive wear resistance *vs* coating hardness

The effect of the relative wear resistance on the hardness of spray and fused composite coating varies. At low and medium impact angles, the wear resistance of fused coatings increases with an increase in coating hardness (ε>1; Figure 4.28). At high impact angles, an increase in coating hardness causes a decrease in their wear resistance (ε<1).

Toughness

Toughness of a coating material is an important mechanical characteristic since fracturing determines the wear resistance to impact erosion, like at normal impact, where the direct and fatigue fracture dominate, like at oblique impact, where microcutting dominates. In the latter case, as a result of impact, crack nucleation and propagation take place; these cracks will reduce the erosion resistance as they decrease the resistance to shear force present during the impact of a particle at the oblique angle. It follows that both high fracture toughness and hardness of the coating material are obligatory at all erosive wear conditions: at high impact angles (α>60^o), high toughness and low hardness are required; at low impact angles (α<30^o), high hardness and low toughness are acceptable (Figure 4.29).

Residual Stresses

To achieve high impact erosive wear resistance, residual stresses in coatings must be compressive. Due to the higher compressive residual stresses induced during high velocity thermal spray processes, a suitable stress state and a higher resistance to fatigue for wear at normal impact are ensured.

The criteria for creation and selection of erosive wear resistant materials and coatings (tribological, structural and qualitative) are summarized in the schematic presentation shown in Figure 4.30 [47,50].

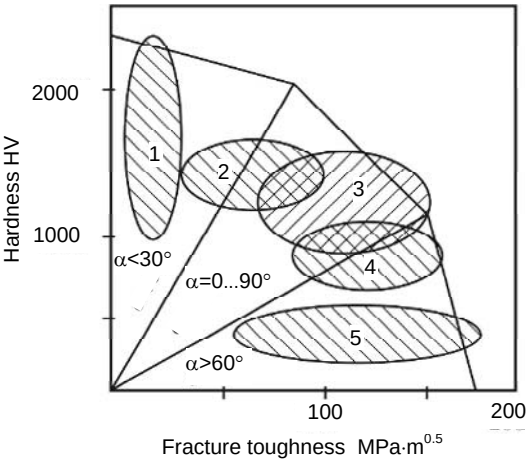

Figure 4.29. Hardness-toughness criteria of materials and coating selection: 1 – ceramics and ceramic coatings; 2 – cermets and cermet coatings; 3 – metal matrix high binder ceramics and coatings; 4 – carbide steels and hard alloy coatings; 5 – steels and metallic coatings

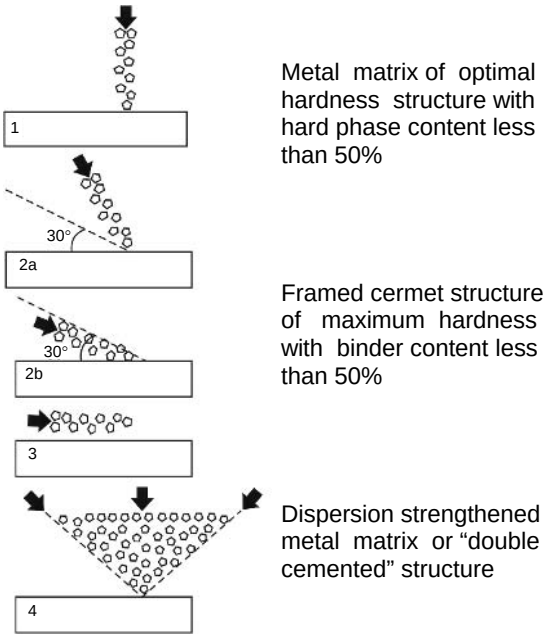

Figure 4.30. Optimal structures of wear resistant materials and coatings for different impact erosion conditions: 1 – at normal impact; 2a and 2b – at oblique impact ($0>\alpha<90^{\circ}$); 3 – tangential erosion; 4 – at mixed impact

4.6 References

1. Engel P A. Impact Wear of Materials. Amsterdam: Elsevier 1976;104.
2. Olsson M, Blomberg A, Sigur A, and Hogmark S. Solid Particle Erosion of Advanced Ceramic Materials. Proc of Intern Symposium on Metallurgy and Materials Science (Edited by Butzen JJ, Bihle Sorenson JB) 1990; 425–31.
3. Grearson AN, Aucote J, and Engström H. Wear of Ceramics in Grit Blasting. J Cr Ceram Trans 1989; 88: 213–18.
4. Kulu P. The Abrasive Erosion Resistance of Powder Coatings. J Tribologia: Finnish J Tribology 1989;8/4:12–25.
5. Kulu P, Pihl T, and Halling J. Wear-Resistant WC-Co-NiCrSiB Composite Coatings. NORDTRIB'98: Proc of the 8th Intern Conf of Tribology. Aarhus 1998; 809–17.
6. Kulu P, Veinthal R. Wear Resistance of High Velocity Thermal Sprayed Coatings. Proc. of Nordic Symposium NORDTRIB'00 (Eds.: Anderson P, Ronkainen H, Holmberg K), Technical Research Centre of Finland (VTT). 2000; 87–95.
7. Kleis I, Pappel P. Behaviour of Engineering Ceramics at Hard-Particle Erosion. Proc of the 6th Nordic Symposium on Tribology, NORDTRIB94.Uppsala, Sweden, 1994; Vol. I:215–23.
8. Kleis I. Study of impact erosion of ceramic-metal hardmetals of different hardness. Proc Tech Univ Tallinn 1965; 219:11–16 (in Russian).
9. Tiidemann T, Uuemõis H, Kleis I. A Study of Erosion at Higher Impact Velocities. Proc Techn Univ Tallinn 1973; 347:29–39 (in Russian).
10. Uuemois H, Kleis I, Tumanov V, Tiidemann T. Investigation of abrasive erosion of sintered tungsten hard alloys. J Powder Metallurgy of Ukrainian Acad Sci 1974; 3:98–101 (in Russian).
11. Valdma L, Pirso J. Character of wear of chromium carbide sintered alloys in the stream of abrasive particles. J Powder Metallurgy (Kiev) 1975; 8:83–88 (in Russian).
12. Pirso J, Valdma L. The influence of production parameters and content on properties of sintered chrome-carbide hard metal alloys. Proc Techn Univ Tallinn 1977;417:19–28 (in Russian).
13. Kallas P, Valdma L. Wearing character of sintered hard alloys in the hydroabrasive and abrasive streams. Proc Techn Univ Tallinn 1979;478:11–17 (in Russian).
14. Pirso J, Kallas P. Influence of the velocity of abrasive particles on the wearing mechanism of chromium carbide Sintered alloys. Proc Techn Univ Tallinn 1980;494:25–31(in Russian).
15. Valdma L. Selective wear of sintered hard alloys in abrasive stream. Proc Techn Univ Tallinn 1982;531:3–9 (in Russian).
16. Reshetnyak H, Kübarsepp J. Mechanical properties of hard metals and their erosive wear resistance.Wear 1994;177:185–93.
17. Reshetnyak H, Kübarsepp J. Structure Sensitivity of Wear Resistance of Hardmetals. Int J of Refractory Metals & Hard Materials 1997;15: 89–98.
18. Hussainova I, and Kübarsepp J. The Effect of Impact Angle on the Erosion of Cermets. Fundamentals of Tribology and Bridging the Gap Between the Macro- and Micro/Nanoscales (Bhushan Ed B). Kluwer Academic Publisher, 2001;537–42.

19. Hussainova I, Kübarsepp J, Pirso J. Mechanical Properties and Features of Erosion of Cermets. Wear 2001;250:818–25.
20. Hussainova I. Effect of microstructure on the erosive wear of titanium carbide-based cermets. Wear 2003;255:121–28.
21. Harlamov Y, Sokolov A, Pappel T. The Influence of Wear Resistance Due to Detonation Plating. Proc Techn Univ Tallinn 1973;347:49–54 (in Russian).
22. Kulu P, Bussel O, Pugin V. Erosion resistance of porous permeable iron. J. Powder Metallurgy (Kiev) 1974;7:56–62 (in Russian).
23. Kulu P. Effect of forging and chemicothermal treatment on properties of sintered iron and steel. J Powder Metallurgy (Kiev) 1978;12:22–26 (in Russian).
24. Kulu P, Kallas P. Abrasive erosion of forged and chemico-thermal treated sintered steels. Proc Techn Univ Tallinn 1978; 455:51–55 (in Russian).
25. Kallas P, Kulu P. Influence of porosity to abrasive erosion of porous steel. Proc Techn Univ Tallinn 1983;560:81–87 (in Russian).
26. Kulu P, Kallas P. The wear resistance of the detonation coatings on sintered steels. Proc Techn Univ Tallinn 1983;560:89–93 (in Russian).
27. Kulu P. The pecularities of creation of erosion resistant gas-thermal coatings on powder materials. Proc Techn Univ Tallinn 1984;566:35–40 (in Russian).
28. Kallas P, Kulu P, Halling J. Mechanisms of gas-abrasive wear of powder materials. Proc Techn Univ Tallinn 1985;609:37–45 (in Russian).
29. Kulu P, Halling J. Gas-thermal coatings on powder materials I.Sprayed powder coatings. J Powder Metallurgy (Kiev) 1986;8:75–80 (in Russian).
30. Kulu P, Halling J. Gas-thermal coatings on powder materials II.Fused powder coatings. J Powder Metallurgy (Kiev). 1986;9:60–64 (in Russian).
31. Halling P, Kulu P, Kallas P. Wear resistant powder hardmetal coatings. Proc Techn Univ Tallinn 1986;628:45–51 (in Russian).
32. Kulu P, Halling J. Mechanisms of abrasive erosion of powder steels. Proc Techn Univ Tallinn 1987;636:25–31 (in Russian).
33. Kulu P, and Halling J. Recycled Hard Metal-Base Wear-Resistance Composite Coatings. J Thermal Spray Technology 1998;Vol.7(2):173–78.
34. Kulu P, Zimakov S. Wear resistance of thermal sprayed coatings on the base of recycled hardmetal. J Surface and Coating Technology. 2000;130:46–51.
35. Kulu P, Veinthal R, Kõo J, and Lille H. Mechanism of Abrasion Erosion Wear of Thermal Sprayed Coatings. Advances in Mechanical Behaviour, Plasticity and Damage. EUROMAT 2000. Tours, 2000;651–56.
36. Kallas P. Indendation Energy and Abrasive Wear of Metals. Wear 1996;198:77–85.
37. Daillaire S, Legoux JG, Levert H. Abrasion Wear Resistance of Arc-Sprayed Stainless Steel and Composite Stainless Steel Coatings. J Thermal Spray Technol. 1995; 4:163–68.
38. Lille H, Kõo J, Kulu P, Pihl T. Residual Stresses in Different Thermal Spray Coatings. Proc Estonian Acad Sci Eng 2002; 8/3:162–73.
39. Zimakov S, Pihl T, Kulu P, Antonov M, and Mikli V. Application of recycled hardmetal powder. Proc Estonian Acad Sci Eng 2003; 9/4:304–16.
40. Alman DE, Tulczak JH, Hawk J, and Hebster M. Elevated temperature erosion of cermets. Mater Sci Eng 1999; A261:245–51.
41. Alman DE, Tulczak JH, and Hawk J. An assessment of the erosion resistance of iron-aluminide cermets at room and elevated temperatures. Wear 2002;329:602–09.

42. Kübarsepp J, Klaasen H, Mikli V, Viljus M. Erosive Wear of TiC-base Cermets. Proc of Kaunas Univ of Techn and Acad of Sci of Lithuania. Materials Science (Medžiagotyra) 2002;8/4:486–88.
43. Hussainova I, and Antonov M. Elevated temperature wear of chromium carbide based cermets. Proc Estonian Acad Sci Eng 2003; 9/4:261–71.
44. Stack M, and Pena D. Solid particle erosion of Ni-Cr/WC metal matrix composites at elevate temperatures. Wear 1997; 203:489–97.
45. Hussainova I. Some aspects of solid particle erosion of cermets. J Tribol Int 2001;34:89–93.
46. Sundararajan G, and Roy M. Solid particle erosion behaviour of metallic materials at room and elevated temperatures. J Tribol Int 1997; 30:339–59.
47. Kulu P. Selection of Powder Coatings for Extreme Erosion Wear Conditions. Advanced Engineering Materials 2002;4/6:392–97.
48. Stachowiak GW. Particle angularity and its relationship to abrasive and erosive wear. Wear 2000;241:214–19.
49. Kulu P, Mikli V, Käerdi H, Besterci M. Characterization of Disintegrator Milled Hardmetal Powder. J. Powder Metallurgy Progress 2003;3/1:39–48.
50. Pihl T. Powder Coatings for Abrasive Wear. PhD Thesis. TTU Press. Tallinn 2002;124.
51. Letunovitš S. Tribology of Fine-grained Cermets. PhD Thesis. TTU Press. Tallinn 2003; 127.
52. Finnie I. Wear Control Technology: Source Book American Society for Metals. 1978; 220–36.

5

Improvement of Erosion Resistance of Industrial Equipment

5.1 Fans and Exhausters

Centrifugal turbomachines include a group of machines subjected to severe erosion by dust particles borne through them by a gas stream. Such machines include exhausters used for different purposes: in metallurgy – for agglomeration, where dust from the agglomeration process passes through them; for smoke collectors – in heating plants subjected to ash – and for compressors – for natural gas transmission where erosion is caused by mineral particles found in the gas. A study was conducted at TUT in cooperation with the metallurgy industry of the Ukraine employing exhauster rotors (of 6500 m^3/min capacity) used in Dniepropetrovsk and Krivoi-Rog. These rotors are featured by the following data [1]:

1.Outer diameter – 2220 mm
2. Mass – 5500 kg
3. Number of blades – 24
4. Rotational speed – 1500 rpm
5. Temperature of gas passing through rotor – 150 ^oC
6. Motor capacity – 1700 kW.

The difference between the input and output pressure of the gas passing through the exhauster was 116 kPa. The rotor had a double-sided blade arrangement. The blades of 8 mm thickness were made of 0.3% C Cr-Mn-Si-steel (30ChGSA) (260HV) and riveted to the central disc of the rotor. The initial blade design had two zones, the wear of which determined the service life of blades (see Figure 5.1). One of those zones was at the end of the blade close to the center of the rotor. That end was subjected to impacts at 20^o impact angle from the dust particles that entered the rotor with gas. The second zone was located approximately at 2/5 of blade length from the first, where heavy wear takes place on the side that faces the disc. This is caused by the slide erosion of particles and the fact that the maximum normal force between the particles and the blade is more or less at the center of the blade. Severe wear of one side of the blade is determined by the aerodynamics of the gas stream and inertia of the rigid gas-borne particles.

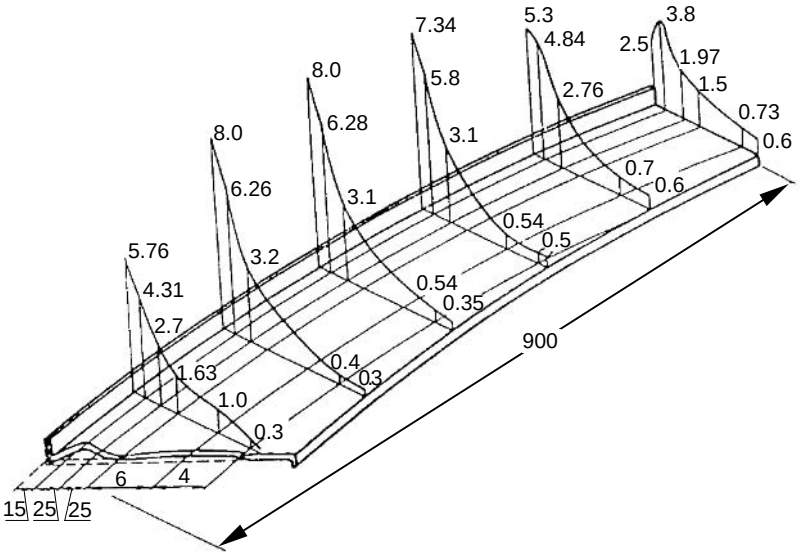

Figure 5.1. Wear graph of the exhauster blade (wear/mm)

In 1min, 7.2 kg of dust passed through the rotor; abrasivity of this dust was higher than that of quartz sand (see Table 1.10). As a result, an agglomeration factory will come to a standstill every 20–30 days and will be forced to replace the rotor. The initial solution – to use erosion resistant fused coating in zones of heavier wear – turned out to be ineffective because the wear process caused greater imbalance, followed by intensive vibration. This fact forced one to look for design solutions providing increased service life of the blades. Solutions and recommendations can also be used for smoke boxes and natural gas compressors.

5.1.1 Influence of Geometrical Parameters of the Rotor on the Erosion Rate

The most important geometrical parameters of a ventilator (compressor) with arc-shaped blades are shown in Figure 5.2.

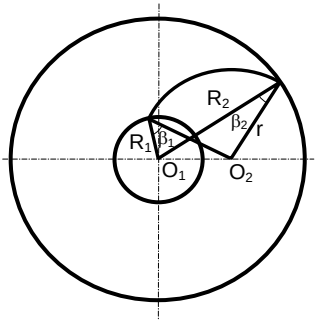

Figure 5.2. Rotor geometrical parameters: R_1 – radius of the inner ring of blade position, R_2 – outer radius of the rotor, r - radius of curvature of the blade, β_1 – entry angle, β_2 – exit angle

The relationship between the angles is expressed as follows:

$$\arccos \beta_1 = (2rR_2\cos\beta_2 + R_1^2 - R_2^2) / 2rR_1 \qquad (5.1)$$

The force system acting on a particle M was described in [1] and is shown in Figure 5.3.

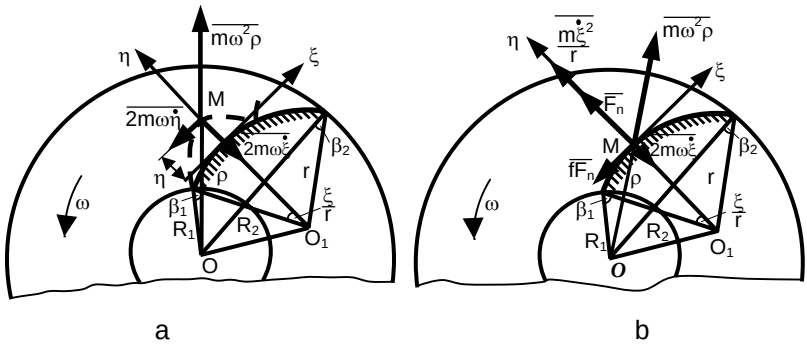

Figure 5.3a,b. Forces acting on particle M: **a** – free movement, **b** – in contact with the blade

From the forces acting on the particle, gravity and aerodynamic resistance are disregarded because particle velocity is negligible as compared to the sound velocity in the air. The movement of the particle was investigated with respect to coordinate system revolving with the rotor, where ξ is an axis along the blade, η is an axis perpendicular to the ξ, and ψ is the revolution of the particle around its mass centre is denoted by angular coordinate. Angular velocity is denoted by ω. The travel of freely moving particles is described by the following equations:

$$\ddot{\psi} = 0,$$

$$\ddot{\xi} = \omega^2(r - R_1\cos\beta_1)\sin(\xi/r) + \omega^2 R_1 \sin\beta_1 \cos(\xi/r) + 2\omega\dot{\eta},$$

$$\ddot{\eta} = \omega^2 R_1 \sin\beta_1 \sin(\dot{\xi}/r) - \omega^2(r - R_1\cos\beta_1)\cos(\dot{\xi}/r) - 2\omega\dot{\xi} + \omega^2 r + \omega\eta \quad (5.2)$$

Equations describing the case where a particle is in contact with the rotor are:

$$\ddot{\psi} = (af+b)F_n,$$

$$F_n = 2\omega\dot{\xi} - \left(\dot{\xi}^2/r\right) + \omega^2(r - R_1\cos\beta_1)\cos(\xi/r) - \omega^2 R_1\sin\beta_1\sin(\xi/r) - \omega^2 r,$$

$$\ddot{\xi} = \omega^2\left[r - R_1(\cos\beta_1 - f\sin\beta_1)\right]\sin(\xi/r) +$$

$$+\omega^2\left[R_1(\sin\beta_1 + f\cos\beta_1) - fr\right]\cos(\xi/r) - 2f\omega\dot{\xi} + \left(f\dot{\xi}^2/r\right) + \omega^2 fr \qquad (5.3)$$

where $af + b$ is the arm of the contact force in relation to particle mass center and F_n is the normal force between the particle and the blade.

Solving Equations 5.2 and 5.3 simultaneously enables us to describe the trajectory of the particle in the space between the blades [1]. To obtain an additional equation for describing the blade erosion, Reye's energetical hypothesis was used. According to that hypothesis, wear rate I is proportional to the work of external forces projected on the wear distance travelled. In this case, work is being done only against the friction force when a particle slides on the surface and the equation is written in the form that corresponds to the test results in Section 1.7:

$$I = K_1 f [F_n + (dF_n/d\xi)\xi], \tag{5.4}$$

where f – coefficient of friction,

K_1 – the coefficient that corresponds to the wear rate caused by the unit force.

A computer program was compiled for mathematical modelling of the blades based on the aforementioned equations [2]. The algorithm was employed over the whole length of the blade because after the particle enters the rotor, 2 or 3 impacts will follow occurred on a very short distance as compared to the whole length of the blade. First, the existing blade design was modified, varying the exit angle β_2. Results are shown on the graph in Figure 5.4. To verify the conclusions drawn from mathematical modelling (especially the conclusion that reducing of β_2 is favourable), a series of tests were conducted by Stupnitsky, where impact and exit angles were varied (influencing each other according to Equation 5.1. The rotor shown in Figure 5.5 had replaceable blades and was mounted on to the shaft of the centrifugal accelerator CAK-3. The abrasive was alumina 0.6–0.8 mm and blades were made of the same steel as those of the industrial rotor. Test speed in all tests was 3600 rpm. The wear rate was measured with a micrometer in previously chosen points. The results are shown in Figure 5.6.

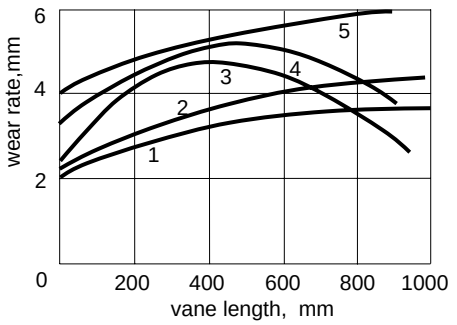

Figure 5.4. Theoretical wear rate distribution over the length of the blade, when the values of the exit angle β_2 are: 1– 22.5°, 2 – 32°, 3 – 40°, 4 – 62° and 5 – 90°

As we can see from the graphs in Figure 5.6, the wear rate decreases when exit angle β_2 and blade radius r decrease, which confirms the results of mathematical modelling. Unfortunately, these tests are not suitable for aerodynamical studies concerning changes inside a machine (pressure, capacity, performance coefficient) that take place when the shape and position of the blade are changed. Also, the

wear of the blade end cannot be adequately assessed, because, unlike from the service conditions, a relatively smooth contact occurs between abrasive particles and the blade. To account for all the parametrical changes that are brought about by changes in the rotor design, a special test facility was built equipped with a scaled down (1:5) version of the exhauster. A scheme of this test facility is shown in Figure 5.7.

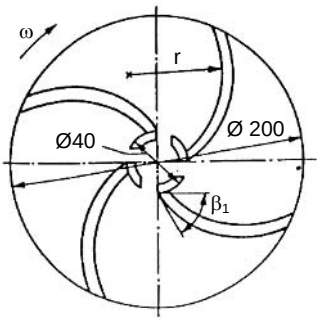

Figure 5.5. Drawing of the rotor used in laboratory experiments

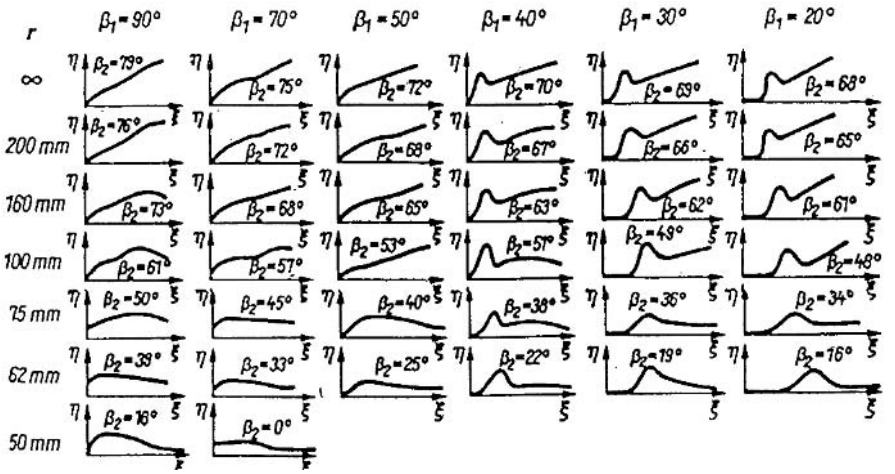

Figure 5.6. Distribution of wear rate over the length of the blade depending on different geometrical parameters in laboratory experiments

In the wear studies of blades, the system worked in a closed cycle as shown in Figure 5.7. For this, 5 kg of dust from the agglomeration process was circulated together with air at the motor speed of 7500 rpm for 20 h, maintained by 45 kW acceleration drive. Initial thickness of the blades was 3 mm. The wear rate of the blades was measured by a specially designed device with an indicator and precision of the scale of 0.01 mm. Measurements were taken through the holes in the plates placed on the blades. The number of holes was 56 and they were uniformly distributed on the surface of the blade. Test results with two rotors are shown in Figure 5.8.

To investigate the aerodynamical properties of the exhauster, the system was run in an open cycle, monitoring pressure, capacity, temperature and the performance coefficient.

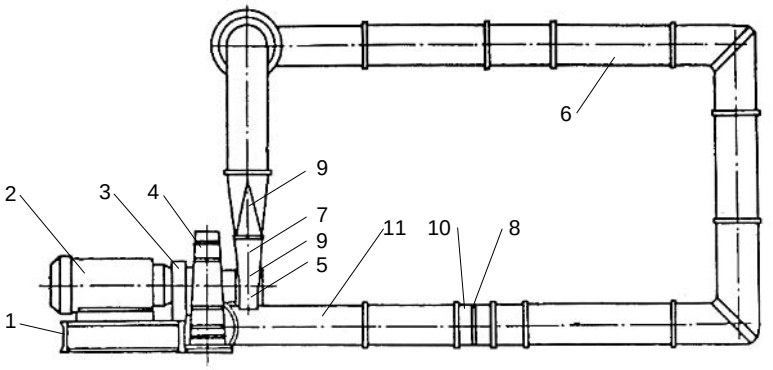

Figure 5.7. Scheme of the test facility: 1- frame, 2 – motor, 3 – acceleration drive, 4 – exhauster, 5 – suction chamber, 6 – tube, 7 – dozer, 8 – diaphragm, 9 – thermometers, 10 – placement of a differential manometer, 11 – placement of a system of manometers

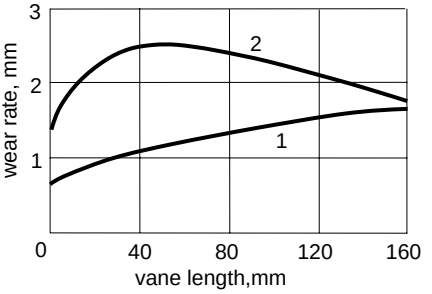

Figure 5.8. Wear trends of test rotors from the results of testing in the test facility: 1 – β_2 = 32°, r = 206 mm, R_1 = 114 mm, R_2 = 228 mm, 18 blades; 2 – β_2 = 40°, r = 250 mm, R_1 = 114 mm, R_2 = 222 mm, 24 blades

As can be seen in Figure 5.8, the curves are close to those of mathematical modelling (compare curves 2 and 3 in Figure 5.4). Also, aerodynamical parameters of the machine do not deteriorate if β_2 is 32°. As it turned out, at an equal capacity of 105 m^3 and 10 kPa, the performance coefficient of the machine even increased from 0.84 to 0.87 [3].

5.1.2 Design Methods for Reducing Erosion of Rotors

Based on the results of mathematical and physical modelling and the suggestions made by other researchers, a series of guidelines were developed to increase the service life of rotors [1]. In addition to decreasing the value of exit angle β_2, measures were suggested to enhance the aerodynamic properties of gas flow through the rotor. As Figure 5.1 shows, the concentration of particles is rather high around the end of the blades which faces the disc. This brings about undue erosion of those blade ends and the disc in the said area (see also Figure 5.9). The increase in concentration is caused mostly by heavier and more abrasive particles that

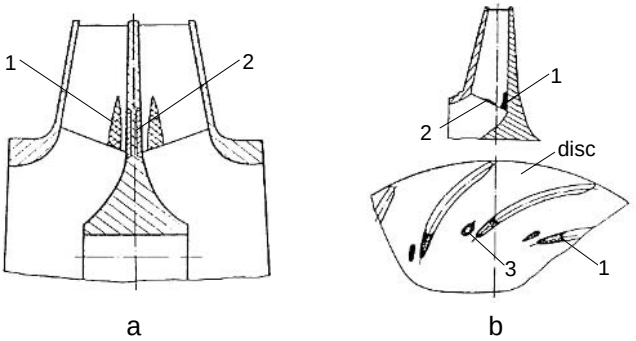

Figure 5.9a,b. Zones of intensive erosion in the area of entrance of particles into the space between blades: **a** – on an agglomeration exhauster, where 1 – blade erosion from particle impacts and 2 – zone of intensive erosion on the center disc; **b** – on a compressor with an one-sided intake, where 1 – erosion from impact of the particles resulting in a break-off, 2 – erosion taking place in the center of the blade end and 3 – zone of local erosion on the disc

deviate more from the flow because of greater inertia. The same problem occurs in compressors of natural gas [4] and fans used in lignite enrichment devices [5].

One of the simplest methods to disperse the concentration of particles is the approach suggested by Ovsjannikova – to use a cone-shaped ring (Figure 5.10a), which should guarantee a calculated increase of blade service life by 1.5 times [3]. Mathematical modelling coincides with real life results here quite well, which is seen by comparing curves 1 and 3 in Figure 5.10b. When constructing those curves, it was assumed that the maximum linear wear rate of both curves may reach 5 mm.

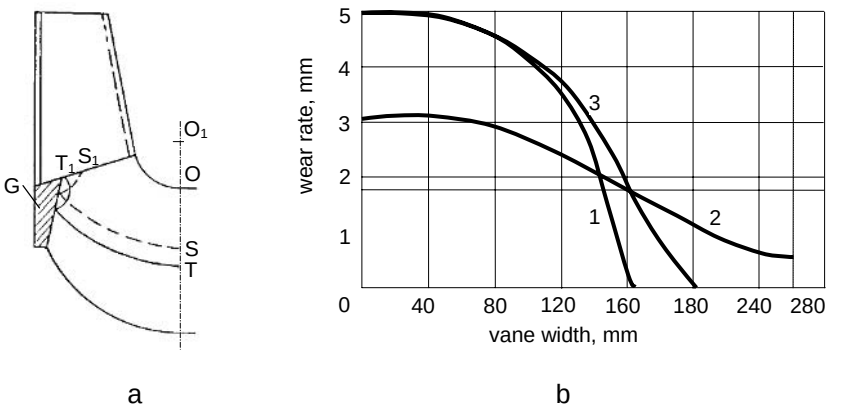

Figure 5.10a,b. The use of additional particle dispersion ring in the rotor: **a** – placement of the ring G in the rotor; S_1 and T_1 – trajectories of the particles inside the rotor; **b** – wear distribution on the edge of the blade caused by impacts from particles: 1 – obtained by mathematical modelling when there is no additional ring, 2 – obtained by mathematical modelling with an additional ring in place, 3 – actual wear curve of the rotor without an additional ring

Another method to disperse the concentration of particles used in some turbomachines is to place additional inclined blades in front of the main blades (Figure 5.11a). The report in [6] claims that an increase by 3.4 times in the operating time between failures was achieved by help of this method, provided that the rotor was assembled very accurately. The same method used in the case of a heating plant increased the rotor service life by 2–3 times [7].

However, this method can lead to a decrease of the efficiency [8]. Also, periods between service breaks may shorten because of the wear of additional blades.

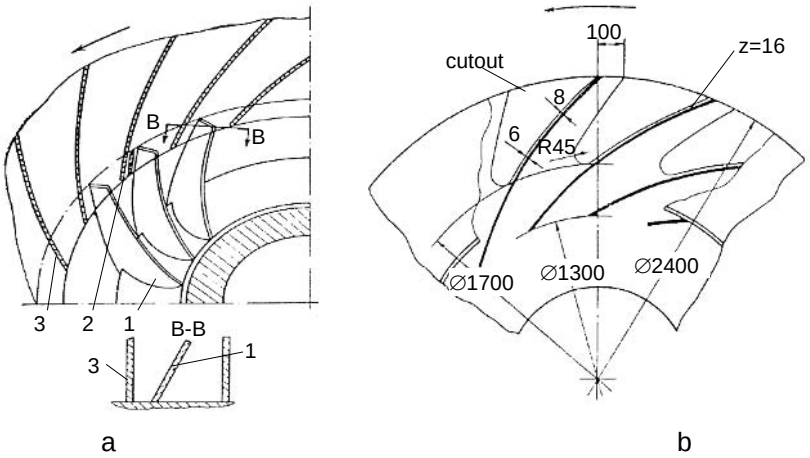

Figure 5.11a,b. Means of better dispersion of rigid particles in the space between blades inside the rotor: **a** – by use of additional blades, 1- extra blades with inclination, 2 – zone of maximum wear on the main disc, 3 – main blade; **b** – main disc with cut-outs (used only on rotors with double-sided inflow)

5.2 Disintegrators

5.2.1 Use of Disintegrators in the Building Industry

Until 1949, disintegrators (Figure 5.12, invented by Carr in 1877) were used only for grinding of rather soft and not very abrasive materials (chalk, coal *etc.*) and also as mixers, *i.e.*, for mixing the components of mold sand. The difference in disintegrator grinding is that particles of the material being ground receive many impacts in a short period of time from the grinding elements and also from other particles moving in random directions. That, in turn, causes mechanical activation of new surfaces associated with deformation of the crystal structure: the greater the deformations the more active is the surface and the stronger the product of such grinding [9].

In 1949, Hint [10] started experiments to utilize a disintegrator technology in the production of lime-sand brick, using a disintegrator with six rows of impact members – fingers to grind the mixture of sand and lime. The velocity of the outer fingers of the disintegrator was 100 m/s. According to Hint, the new technology was meant to reduce the consumption of lime in the binding material, increase the strength of bricks and simplify the production process. Simplifying

implied that there was no need for another mixer in the technological process. In fact, a disintegrator is an excellent mixer. Furthermore, another fact that served as a justification was that a disintegrator is very compact (compared to a ball mill) and efficient. Test series of bricks that were made from sand (granularity 0.3–0.6 mm) from a quarry called "Kvarts" near Tallinn confirmed that bricks made from disintegrator sand were stronger. Tests showed that bricks containing 3% lime had the following compressive strength properties: bricks from natural sand – 12 MPa, bricks from disintegrated sand – 18 MPa; increased amounts of lime enhanced their strength even further. For example, with 7% of lime, the corresponding values were 14.8 and 24 MPa [10]. Later Hint adapted disintegrator technology for use in the production of a porous thermal insulating wall material (panels and blocks made from this material were larger than bricks) [11]. The process needed gas, thus, 0.5% of aluminium powder was added into the mixture of sand, lime and water that was being disintegrated. The resultant building material is known as silicate (sand-lime) concrete, but Hint patented the material manufactured by disintegrator technology as silicalcite to distinguish it from the material made by using ball mills. To produce the new material, new plants were built in the former USSR, Austria and Japan. Before those plants were put into use, an important problem had to be solved – obtaining a significant increase in the service life of disintegrator grinding elements. In the Experimental Silicalcite Plant (in 1961, renamed as the Institute of Silicate Concrete), the durability of fingers made of non-alloyed steel was only about 8 h (see also Figure 2.1b); after that the plant had to be stopped and the rotors changed. In 1955, Hint started collaboration with TUT. The long-term cooperation programme between TUT and Experimental Silicalcite Plant was successful.

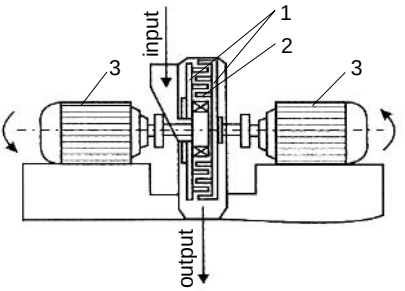

Figure 5.12. Scheme of disintegrator: 1- rotors revolving in opposite directions, 2 – grinding elements (initially cylindrical steel fingers), 3 – motors

5.2.2 Disintegrator as a Machine for Treatment of Different Materials by Collision

Impact milling is an effective method of comminution of different materials. One of the few types of impact crushing equipment for continuous processing of different materials is the disintegrator mill [12,13]. In the disintegrator, materials are crushed as a result of fracturing. By a particle colliding with a wall (target, grinding body) an intensive wave of pressure will spread from the point of contact, (Figure 5.13). The values of stresses occurring are approximately an order of magnitude higher than the material strength.

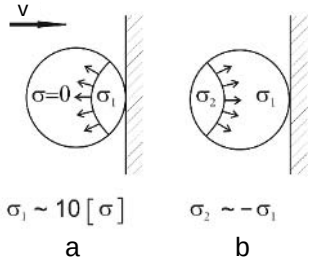

Figure 5.13a,b. Waves at collision: **a** – compression and **b** – tensile wave

After particle break-up, in each piece, the stress waves undergo multiple reflection and refraction before they transform into plastic deformation and heat. This intensive transformation influences the crystal lattice of materials, and their defects start to concentrate on the surfaces of the new small particles. As a result, the surface activity as well as the specific surface area increases and activates the material both mechanically and chemically. The parameters of disintegrator-processing differ essentially from those obtained by the traditional milling methods and equipment (jaw crusher, mortar, hand-mill, quern, vibro- and ball mill) (Table 5.1).

Table 5.1. Comparison of material treatment parameters by traditional methods and by collision

Characteristic parameter	Traditional method	Collision
Loading velocity, m/s	0.1–10	30–200
Loading time, s	10^{-2}–10^{-1}	10^{-6}–10^{-5}
Time spent in active zone, s	1–10	10^{-2}
Ratio of actual stresses to the strength of material, $\sigma/[\sigma]$	≤1	>10
Nature of stresses	Compressive+shear	Tension+shear

Multifunctional DS-series disintegrators have been developed for material treatment. The DS-series disintegrators include laboratory disintegrator systems (DSL-160, DSL-175) for the capacity of some kg/h, semi-industrial disintegrators (DSL-115 and 128, DESI) for some hundred kg/h, and industrial disintegrators (DS-158, DS-104 and DSA-600) for some t/h.

Due to the high ratio of collision stress/material strength (Table 5.1), it is possible to crush not only brittle materials but also ductile materials. In the latter case, instead of direct brittle fracture, fatigue fracture is dominating (Figure 5.14). Based on the theoretical model for size reduction of ductile materials by collision [14], the possibility of powder production from ductile metals and alloys (stainless steel, nickel and cobalt alloys) was ascertained in [15]. The developed disintegrator milling system with a combined inertial and centrifugal classifier of high separative sensitivity enables us to produce metallic micropowders with particle sizes below 5 μm [16].

Disintegrator technology is also one of the ways to produce hardmetal powder by milling from used hardmetal [17]. The technology of producing hardmetal powder is composed of preliminary thermo-cyclical treatment and mechanical size

reduction in a centrifugal-type mill by collision and final milling of pre-treated parts in the disintegrator. Due to the high hardness and abrasivity of the material to be treated, an intensive wear of working elements takes place. One way to avoid this and to protect the impact elements of the disintegrator is to use materials the hardness of which is higher than that of the material to be treated and use composite materials.

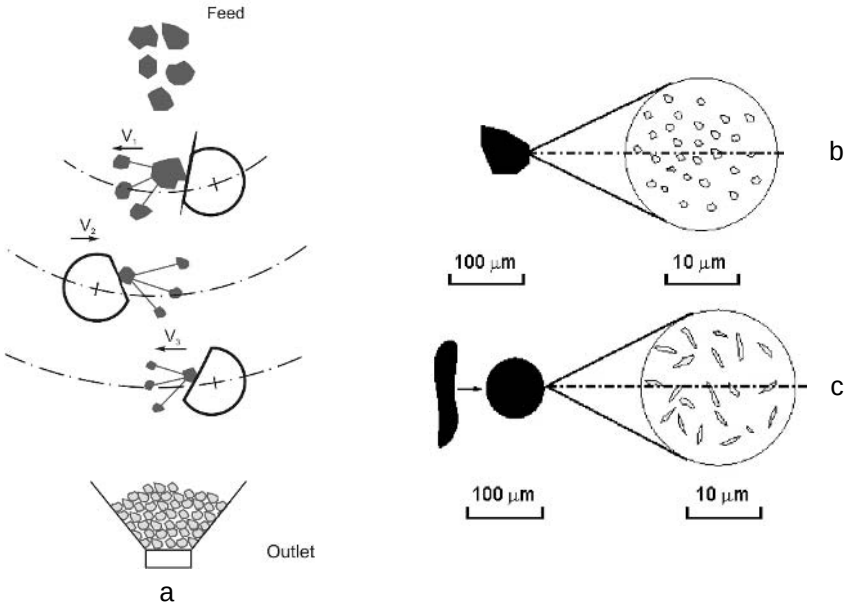

Figure 5.14a–c. Principles of disintegrator milling: **a** – schematic representation of material movement in a disintegrator and mechanisms of size reduction by: **b** – brittle and **c** – fatigue fracture

5.2.3 Application of Wear Resistant Materials and Coatings in Disintegrators

As demonstrated in Section 4, high abrasive wear resistance by erosion is guaranteed if the hardness of the material to be treated is lower than that of the material used for impact elements ($H_a<H_m$); by the hardness of the abrasive $H_a = 1.6H_m$ (Figure 3.32), high and stable wear is achieved. Experimental studies of different materials and coatings using a centrifugal accelerator CAK-3 with abradants of different hardnesses (from 120 to 200 HV up to 1900–2000 HV) showed that high hardness metal-ceramic composite materials and coatings are promising in fighting against impact wear.

For this purpose, different materials, beginning with hardmetals, were tested by Uuemõis in impact crushers [18]. It was demonstrated that only WC-Co hardmetal has significantly higher wear resistance than 0.2% C steel. A systematic study of wear resistance in disintegrators of different metal-ceramic composites (hardmetals and cermets), spray fused self-fluxing alloy based coatings and high velocity thermal sprayed (detonation and HVOF sprayed) coatings was carried out by Kulu [19, 20].

Tests were carried out using different semi-industrial disintegrators:

- Five-road disintegrator D-128 with working pins of diameter 16 mm; the maximum relative velocity of impact 210 m/s;
- Three-road disintegrator DESI with working pins of diameter 14 mm; the maximum relative velocity of impact – 95 m/s.

The principal scheme of disintegrator DESI and material movement in it is presented in Figure 5.15.

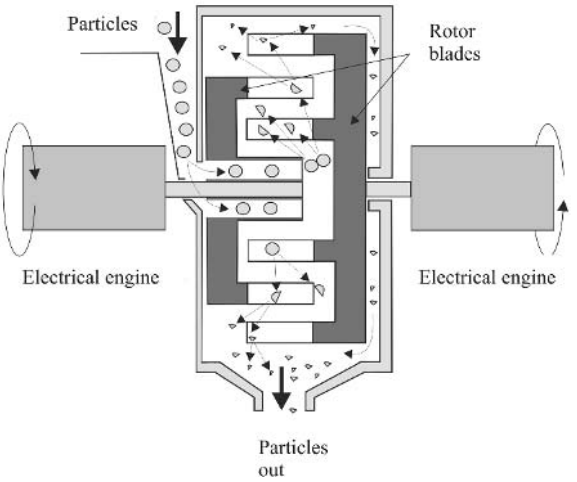

Figure 5.15. Principal scheme of disintegrator DESI

In disintegrator D-128, the following hard materials and coatings were tested [19, 20]:

- WC-20Co hardmetal (810 HV)
- Cr_3C_2-15NiCr cermet (1260 HV)
- TiC-30Ni cermet (1270 HV)
- Three types of NiCrSiB based spray fused coatings (HV from 480 to 620).

The reference material of pins was low carbon (0.2% C) steel.

The materials to be treated were:

- Quartz sand of fraction 1.6 mm, 1100–1200 HV,
- Iron oxide, 1 mm, 600–800 HV,
- Glass grit, 3 mm, 550–600 HV,
- Clay shale, 5 mm, 120–190 HV.

The abrasivity of the materials was from 0.3 to 1.0 (clay – A_c = 0.3; glass – A_c = 0.83; iron oxide – A_c = 0.7; quartz sand – A_c = 1.0).

The coefficient of abrasivity A_c was determined on steel 0.45% C:

$$A_c = I_g^{treated}/I_g^{quartz\ sand}, \tag{5.5}$$

where I_g is the wear rate by weight, mg/kg.

The results of semi-industrial tests of hardmetals/cermets and spray fused coatings in disintegrator D-128 are given in Table 5.2.

Table 5.2. Relative wear resistance of powder materials and spray fused coatings in disintegrator D-128 (rotation speed 2200 rpm, maximum diameter of road 600 mm, impact velocity 140 m/s)

Material of working pin	Materials to be treated			
	Quartz sand A_c = 1.0	**Oxide of iron A_c = 0.7**	**Glass A_c = 0.83**	**Clay shale A_c = 0.3**
Hardmetals/cermets				
WC-20Co	1.8	5.0	15.4	10.0
Cr_3C_2-15NiCr	1.7	6.0	8.1	-
TiC-30Ni	4.1	10.0	32.0	12.0
Spray fused NiCrSiB based coatings				
NiCr14Si2B2	0.92	2.3	2.0	2.1
NiCr15Si3B2	0.92	2.5	7.6	2.4
NiCr16Si3B3	0.83	2.1	12.3	3.0

To protect the working elements of disintegrators against wear, different contemporary thermal sprayed coatings – high velocity oxy-fuel (HVOF) sprayed coatings – were studied. Semi-industrial tests of thermal sprayed coatings were carried out in the disintegrator type mill DESI (Figure 5.15) by help of working pins with protective coatings based on self-fluxing alloys and WC-Co hardmetal powders [21].

The hardness of the selected coatings was from 805 HV0.2 (NiCrSiB) up to 1300 HV0.2 (WC-17Co); the hardness of the material to be treated was from 200 HV (limestone) up to 1150 HV (quartz sand).

Table 5.3 and Figure 5.16 show the results of testing coatings in a disintegrator milling system DESI by the treatment of different abrasive materials.

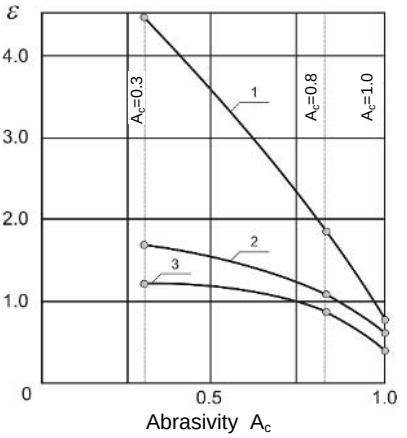

Figure 5.16. Dependence of relative wear resistance on the abrasivity of the material to be treated: 1 – WC-17Co, HVOFS; 2 – NiCrSiB, HVOFS+FF; 3 – NiCrSiB, HVOFS

It follows clearly from the results (Table 5.3 and Figure 5.16) that the wear resistance of coatings eroded by silica is lower than that of the reference material – steel 0.45% C. Erosion by glass (500–600 HV) shows an increase in the wear resistance of coatings of up to three times as compared to the reference material. It is lower than that in laboratory tests at low impact angles. However, mixed erosion occurs in a disintegrator instead of pure oblique or normal impact. In this case, the so-called "double cemented" structures – WC-Co based hardmetal particles in the metal matrix – produced by flame spray fusion (FSF) are recommended. This was confirmed by the studies of worn coated pins (Figure 5.17).

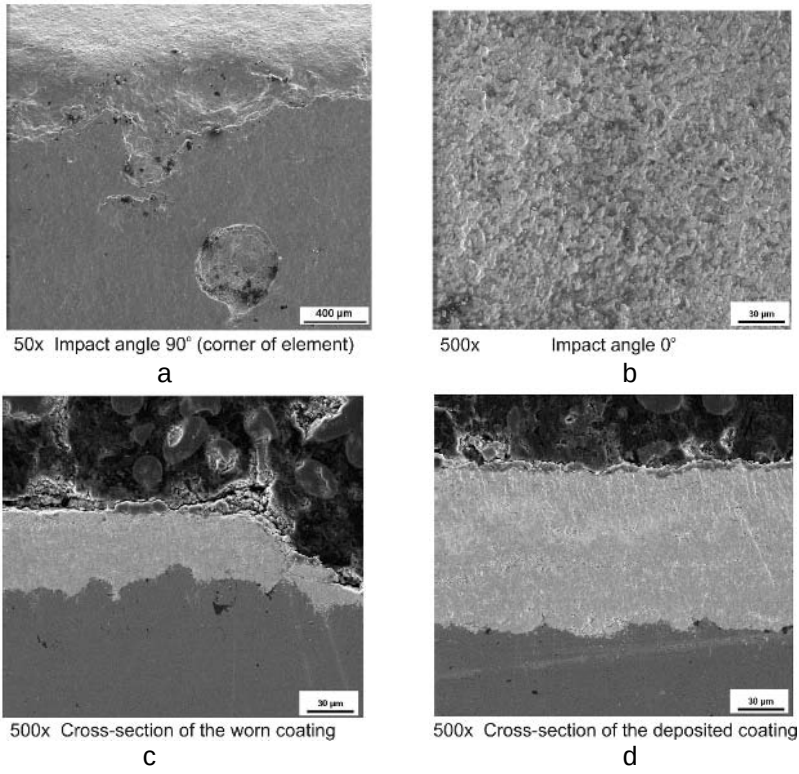

Figure 5.17a–d. Worn pins of disintegrator coated by HVOFS with WC-17Co: **a, b** – worn surfaces; **c, d** – cross-sections

Table 5.3. Results of comparative testing of pins with different coatings in the disintegrator milling system DESI

Coating material and deposition method	Abrasive particles of abrasivity A_c			
	Glass grit (550 HV) A_c = 0.83		Quartz sand (1150 HV) A_c = 1.0	
	I_g, mg/kg	ε	I_g, mg/kg	ε
Reference material steel C45 (0.45% C), normalized 200 HV	4.74	1.0	2.03	1.0
Steel 105Cr6 (hardened, 52–56 HRC)	2.74	1.7	2.43	0.8
WC-17Co (Tafa 1343V)[a], HVOFS	2.47	1.9	2.41	0.8
NiCrSiB (Tafa 1275H), HVOFS	3.66	1.1	5.31	0.4
NiCrSiB (Tafa 1275H), HVOFS+FSF	4.14	1.1	3.68	0.6
NiCrSiB (12495)[b]+15% WC-Co, FSF	3.10	1.5	4.56	0.4
NiCrFe+35% WC (12112)[b], FSF	1.44	3.3	3.34	0.6
PGSR-4[c], FSF	1.63	2.9	5.04	0.4

[a] Tafa Inc.
[b] Castolin S. A.
[c] NPO Tulachermet, Russia

5.2.4 Improvement of Disintegrator Design

Initially, the idea was to substitute carbon steel by a material more suitable for disintegrator fingers in processing materials of high hardness (more than 1000 HV) to increase their service life. However, it did not turn out to be prospective after tests conducted using a centrifugal accelerator and disintegrator at TUT [22]. Among the tested materials (hardened steels, white cast iron, coatings, hardmetals) at impact velocity 90 m/s the WC-8Co hardmetal reinforced fingers showed only increased wear resistance comparing with 0.2% C steel. Disadvantages of grinding bodies reinforced with hardmetal inserts were their high cost and brittleness.These difficulties led researchers and engineers (Toomel, Elstrok, Uuemõis, Udras) of the Institute of Silicate Concrete to look for a new solution. The purpose was to develop a protective layer that would form around the impact members under the action of centrifugal forces so as to prevent the impact members from direct contact with impact particles. For this purpose, pins and fingers were replaced with blades that could be positioned at a convenient angle in relation to a particle velocity vector, thus ensuring buildup of the protective layer. Different designs of the blades are shown in Figure 5.18, presented in the chronological order [23].

First tests were made with cast iron blades (Figure 5.18a) that were fixed with two pinions between the rotor disc and the ring and those two were, in turn, fixed together with bolts. Taking into account that iron blades are fragile and as a result of an impact from some foreign object breakages can occur, a decision was made to replace them with steel blades that were either welded (Figure 5.18b) or fixed onto the rotor, similar to cast iron blades (Figure 5.18c). The optimal angle of the blades was determined by tests. Depending on the water content in the mixture, it was between 25% and 32%. To create a more stable protective layer, the blade was then assembled from two (Figure 5.18d) or three pieces (Figure 5.18e) of steel set up at different angles. As a result, the service life of the rotors used for grinding

sand mixture for silicalcite production increased at least five times as compared to rotors with steel fingers, *i.e.* up to 40–50 h. Because erosion happened practically only on the edge of the blade that was left uncovered by protective layer, efforts were made to increase the service life of rotors by fixing ceramic plates onto blade edges (Figure 5.18f). Taking into account the erosion resistance WC-Co hardmetal type plate, the service life of rotors at v_0 = 160 m/s was expected to increase to at least 200 h. In practice, it was never achieved because even the smallest stones among sand particles were able to break hardmetal plates [23]. To prevent that from happening, sieving of the raw material would have been required. However, in view of the capacity of the machine (up to 25 tons *per* hour), product price would have been increased. This approach can be still used in small laboratory disintegrators.

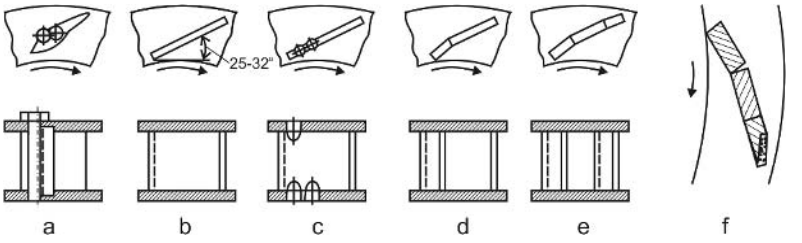

Figure 5.18a–f. Design stages of disintegrator blades for wet grinding: **a** – cast-iron blade, **b** – welded steel blade, **c** – steel blade fixed with pinions, **d** – steel blade welded from two parts, **e** – blade made of three parts, **f** – blade reinforced with ceramic plate

Grinding elements can also be protected in the buildup of the protective layer in dry grinding. The research group led by Tümanok developed such disintegrators at TUT, with researchers from other institutions involved. The type of the disintegrator (Figure 5.19) used was that for grinding of the tamping mixture in oil drilling stations, where special protective bracelets [24] are used to protect the grinding elements. According to the authors, service life increased 3–4 times as compared to rotors without protective bracelets.

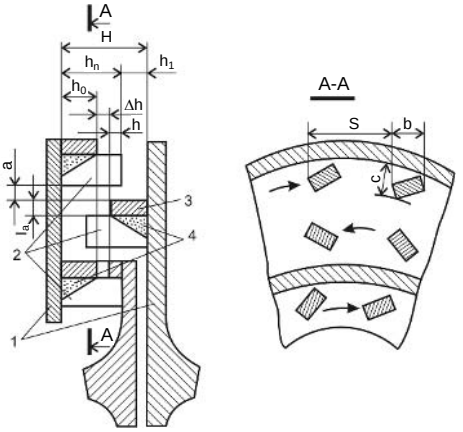

Figure 5.19. Scheme of a disintegrator used for dry grinding: 1– rotor discs, 2 – grinding elements, 3 – protective bracelets, 4 – protective layer buildup of ground material; suggested relations between geometrical parameters

From 1970 to 1975, a research and development group has been working at TUT to design a new DS type disintegrator. From the eight disintegrators designed, four were built for laboratories and another four for industrial use; their capacities are 20–40 kW and the corresponding masses 50–2500 kg. The capacity of a disintegrator depends on the raw material to be ground and on the required fineness of the end product. About 45 different materials have been ground, including abrasive stones and minerals. Blades used in rotors build up a thin protective layer. An optimum inclination angle of blades is 80^{o}. The disintegrators above can be used in three different modes – direct grinding, separative grinding and selective grinding (Figure 5.20). To produce a product of a very fine fraction, a separative grinding mode must be used, when the mass ground passes a disintegrator multiple times and the product with the desired grain is separated with the classifier. Switching from one mode of grinding to another requires only a change of the classifier. This is a simple operation. An example of separative grinding could be the final operation of metal chip utilization – pre-crushed chips are ground into 5–20 μm particles. The produced powder can be effectively used as a starting material for powder parts and spray powders.

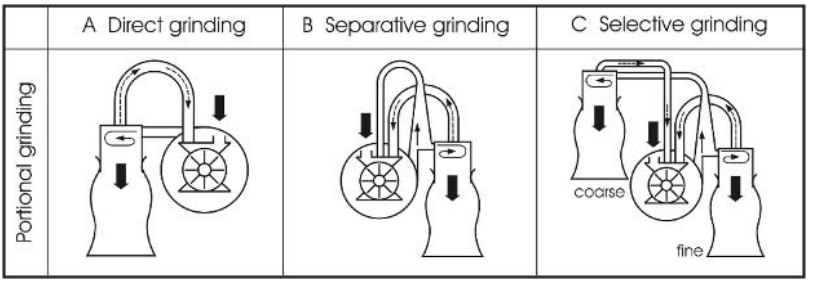

Figure 5.20. Modes of disintegator grinding

Uneven wear of the grinding elements and buildup of mass on them results in imbalance of the rotors thus generating vibrations of the disintegrator. Measures to alleviate the vibration problem have been developed at TUT since 1976 [25]. Several automatic imbalance control systems developed have been patented (*i.e.*, German Patent No. De 3509089 C2 Int. Cl. GO 1M 1/38, 23.06.1988). A scheme of a disintegrator with a balancing device is shown in Figure 5.21. Both laboratory and industrial disintegrators can be equipped with such a device. Laboratory disintegrator DSL-175 is shown in Figure 5.22 and its technical characteristics are as follows: capacity of electric motors 2+2 kW, maximum speed of rotors 11,000 rpm, maximum starting size of particles 5 mm and mass of disintegrator is 80 kg.

The balancing device (2) (Figure 5.23) consists of a circular channel (3) displayed in the rotor (1), precisely aligned with the rotor shaft (4). This channel is partially filled with oil (5) and elastic balls (6) that can easily roll on two conical surfaces (7). The surfaces are split by a groove (8), serving as a collector for sediments of oil, wear products of rolling balls and conical surfaces. As a result, the balls and conical surfaces are kept clean and the balls can roll almost friction-free in both directions. The balancing system is equipped with a robust balancing mechanism, consisting of two manually removable masses (9) fixed by a spring (10) and a screw (11). The robust balancing is carried out by a non-movable rotor

similar to balancing of a car tyre. Note that the removable masses are positioned in a symmetric equilibrium. Balancing balls with equal masses have to move so as to compensate the imbalancing force at any moment of time. Such an automatic balancing system requires elastic support of the disintegrator and overcritical velocity of revolution by normal operation of the rotor. The disintegrators produced both for laboratory and industrial use and equipped with the adaptive control device described have demonstrated excellent operation for years. A theoretical review of this system can be found in [26].

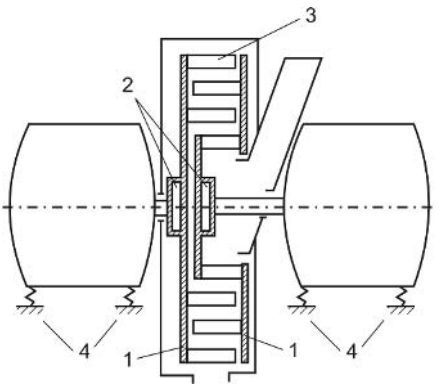

Figure 5.21. Position of the balancing device inside the disintegrator: 1 – rotors, 2 – balancing device, 3 – grinding elements, 4 – elastic supports (usually rubber elements)

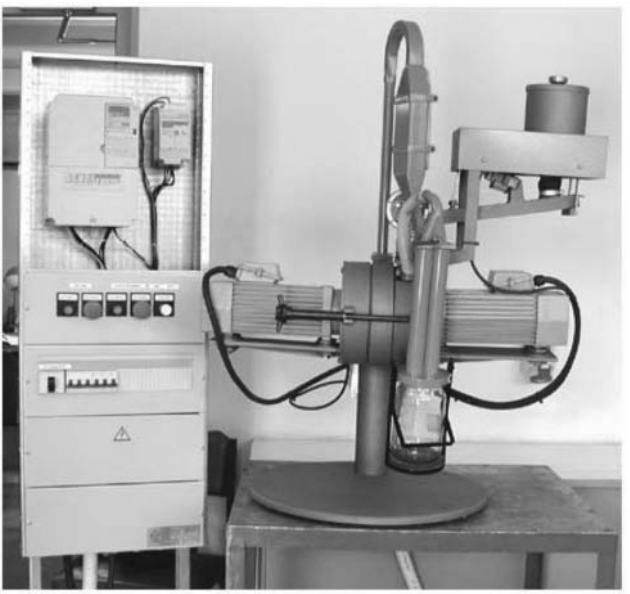

Figure 5.22. General view of disintegrator DSL-175 with inertial classifier adapted for separative grinding

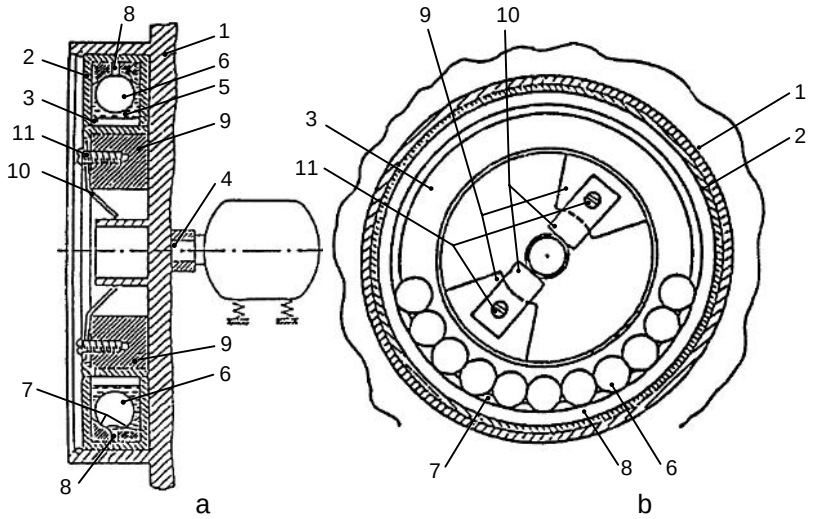

Figure 5.23a,b. Scheme of the balancing device (see explanation in the text): **a** – cross-section, **b** – view

5.3 Cyclones for Ash Separation

5.3.1 Cyclone Working Conditions

From 1956 to 1966, the Baltic Power Plant was gradually taken into use. This 1624 MW oil shale based plant is situated near Narva, in the north-east of Estonia. The plant has 26 boilers, which consume 11.7 million tons of oil shale at full capacity, supplying 8.6 billion kW of energy, and also 5975 TJ of heat energy for the city of Narva. The burning process produces fly ash of about 50% of original oil shale mass, because of high inorganic substance content in oil shale. Electrostatic filters for capturing of heavier fractions without cyclones are not effective in pollution prevention. Capturing of heavier fractions in cyclones shall precede the trapping of fine particles in the electrostatic filters. Every boiler is equipped with a battery of six cyclones. An analysis of the ash captured by cyclones showed that 70% of the particles are smaller that 30 μm, 24% of the particles fall between 30 and 60 μm, 2.5% between 60 and 90 μm and 3.5% of the particles are larger than 90 μm. Mineralogical composition of the ash was as follows: 10% $CaSO_4$, 3% $CaCO_3$, 20% CaO, 10% SiO_2 and the rest were amorphous glass-like particles [26]. Smoke that carries the ash reaches a temperature of about 140 ^oC by the time it enters a cyclone, *i.e.*, temperature has practically no role in the erosion process. To prevent the gases from cooling down in the winter to the temperature at which steam condenses into water, heat insulation is used in the cyclones. The presence of water would turn the erosion process into mechanochemical wear and thus it would be much more intensive. The first cyclones operated in these conditions for less than a year, after which perforating holes were found in the walls from erosion. To limit erosion damage of cyclones, a research contract was concluded between the Department of Machine Design of TUT and the Baltic Power Plant. The results were published in [27, 28].

5.3.2 Determination of the Impact Parameters of Erosive Particles

A series of comparative tests were performed both on cyclones and laboratory erosion tester CAK-3 to find a suitable erosion resistant material. Therefore, parameters like impact angle α, velocity of the particle v_0 and mass of particles hitting the target surface in the unit of time (concentration) were of interest. Threaded holes were drilled into the walls of cyclones where eroded zones were found (both in the cylindrical and lower conical part). First, the dominating impact angle α was determined in all locations. For this task, an original method was developed that can also be used in other similar cases. The method is based on the fact that brittle materials (glass, in our case) have their wear maximum at $\alpha = 90^o$. Test pieces of semispherical shape were fixed in a special holder and measured with a precision of 0.01 mm through an angular spacing of 5^o. The procedure was repeated again after three months inside the cyclone to determine their wear rate. The dominating direction and impact angle of the velocity vector was determined by the wear maximum on the sphere (Figure 5.24c).

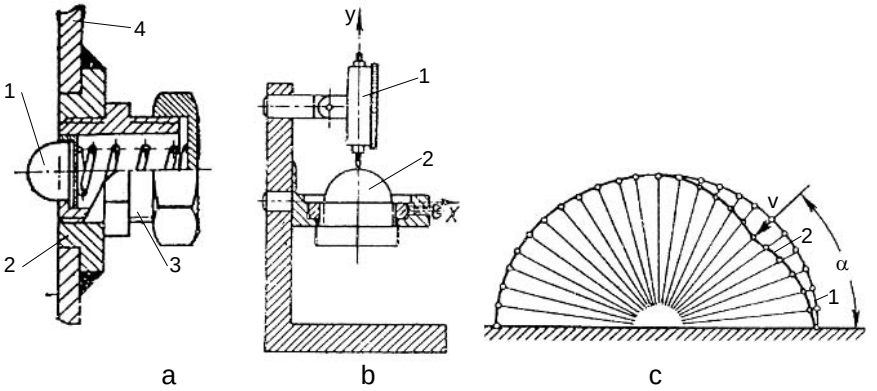

Figure 5.24a–c. Determination of the dominating impact angle in the cyclone: **a** – placement of the glass half-sphere in a fixed position inside the cyclone; 1 – half-sphere, 2 – threaded bushing, 3 – holder of the half-sphere, 4 – cyclone's wall; **b** – holder arrangement for the half-sphere: 1– indicator, 2 – sphere with the holder, *x* and *y* axles around which the sphere is turning during measurement; **c** – sphere's initial profile 1 and worn profile 2

As the measurements showed, in the cylindrical part of the cyclone, there were impact angles between 20^o and 30^o, in the conical part, the dominating impact angle was 10^o.

Afterwards, the same holes were used to determine particle velocities with the aid of Prandtl tube that was oriented inside the cyclone according to the velocity vector direction. The position of the tube was set, using the scale on the device (see Figure 5.25). Because ash particles are very small, their velocity can be taken as equal to the gas stream velocity. Depending on the position of the holes, the velocity was determined to be 11.2–16.6 m/s (in the cylindrical part) and 17–23.4 m/s (in the conical part). Concentration of the particles was determined with the Alner's tube that was also placed through the aforementioned holes. The results recalculated as a surface pressure were 0.4–0.8 kg/m^2·s.

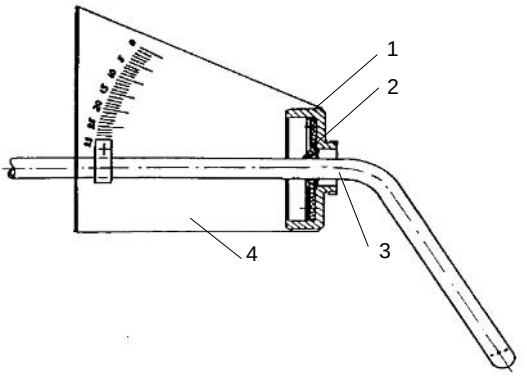

Figure 5.25. Device for measurement of gas stream's velocity: 1 – support bush with threaded end, 2 – rubber washer, 3 – Prantl's tube, 4 – plate with a scale

Tests were conducted applicable to the CAK-3 device with ash taken from the cyclone on two materials potentially applicable for cyclone protection (Table 5.4). Their relative wear resistance ε was investigated in relation to 0.2% C steel that cyclones were made of. Parallel tests were made inside the cyclones using threaded "plugs" screwed into the test holes that contained pieces of test material and reference material (Figure 5.26).

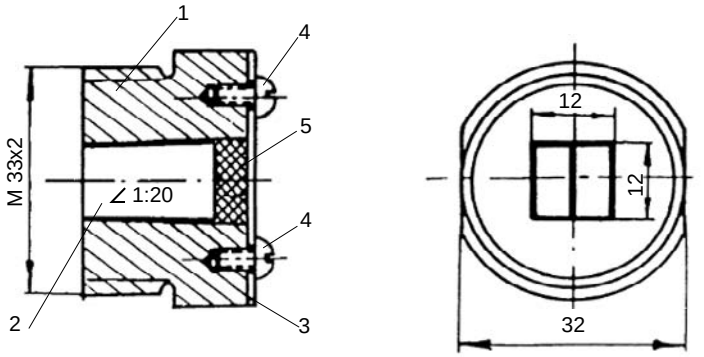

Figure 5.26. Threaded plug for determinion of the relative wear resistance in the cyclone: 1 – frame, 2 – test pieces, 3 – pressure washer, 4 – screws, 5 – asbestos

Table 5.4. Relative wear resistance obtained by different methods (reference material – 0.2% C steel)

Material	HV	CAK-3, v_0 = 23 m/s		Cyclone test		
		α^0	ε	α^0	v_0, m/s	ε
Plasma torch deposited coating	510	10	5.0	20	16.6	9.6
(3.6% C, 1% Ti, 25.5% Cr, 69.9% Fe)		30	8.0	25	14.8	6.8
Artificial basalt	730	10	6.8	10	23.0	7.0
		30	3.1	20	16.6	3.0

A comparison of the data in Table 5.4 shows that correlation between the results obtained by the two different methods is good. Based on these results, a suggestion was made that the worn out patch of a cyclone should be cut out and a wear resistant coating of 2–3 mm thick patches should be welded in as a replacement (see Figure 5.27). The result was that in critical zones wear life of the material proved to be about three times longer. It was recommended that the diameter of a cyclone should be increased from 1600 mm to 2000 mm. Thus, it would be easier to cover their inner surface with artificial basalt plates and use direct flow cyclones without a lower conical part. Basalt plates of 25 mm thickness triple the service life of the cyclone inner lining.

Figure 5.27. Cyclone battery being repaired; in the middle part of the middle cyclone there is a coated patch welded in place of the cutout

5.4 Drying Line Equipment at Peat-Briquette Works

As a country where natural resources are limited, Estonia uses peat widely for fuel, mostly in the form of pressed briquette. The production process at briquetting plants starts from crushing raw peat with the aid of hammer mills, followed by the multistage drying procedure in passing through the line equipment until the final operation of pressing peat into briquettes. Peat particles proceed through the drying line mostly in an airborne condition driven by compressed air. In 1969, a new peat-briquette enterprise was established at Oru peatland in Narva region, designed for 150,000 tons of annual production. The whole complex of peat-handling machinery was supplied by a specialized heavy engineering plant in Magdeburg (formerly DDR). However, as soon as five months after taking this equipment into use, its condition turned out to be critical due to enormous wear and appearance of perforating holes in the walls (Figure 5.28). Thereby the works hall became badly contaminated with peat dust, which might have led to serious consequences, including fire and dust explosion. That is why the works management sought technical

assistance from TUT. The respective studies were launched by Üksti who used the results obtained later in his PhD thesis [29]. All the principal units of the drying line (cyclones, vertical heat exchangers and large-size connecting pipes) were manufactured from carbon steel St37 (DIN1612). Inasmuch as soft organic matter could not be responsible for erosive wear, the main attention in this study was focused on the mineral components contained in peat. It was established that the content of mineral matter in ashed Oru probes amounted to 10%. It contained hard SiO_2, Fe_2O_3, Al_2O_3 and feldspar particles of high abrasivity, constituting 66% of the inorganic matter. However, considering the moderate velocity of peat mass flow within the system (about 10 m/s), it is obvious that mineral content cannot be the only factor responsible for the above catastrophic erosion. Consequently, the erosion process was stimulated by a physico-chemical attack of water and organic acids upon metal, changing the erosion process into mechanochemical wear. High corrosiveness of Oru probes was proved by a chemical analysis of Oru peat aqueous extract which showed a *pH* value of 4.6.

Figure 5.28. Wear damage of drying line components after five months of service – through hole in a large-size rectangular section air conduit

To verify laboratory results in industrial conditions, test plates of measured thickness made from various grades of steel were set up (tack welded) in the drying equipment at its critical points, removed after six months of service and measured again to find the extent of linear wear. Relative wear resistance for each material was found in reference to 0.2% carbon steel (see Table 5.5).

The test data obtained under real industrial service conditions proved the advantages of the Ni-based plasma-sprayed coating, which provided the highest erosion resistance (especially in the middle part of the drying line where maximum heating temperatures are applied – up to 80 ^{o}C). On the other hand, the laboratory test results also corroborated that relative erosion resistance of high-alloy steels will increase with temperature rise. The erosion rate of any material proved to reach its maximum value at the foremost (feed-in) section of the line affected by

the action of peat with maximum moisture content. As a temporary measure aimed at increasing the operating time of critical components between failures, weld-on patches of Cr-Ni austenitic steels to cover eroded areas have been used in practice.

Table 5.5. Relative wear resistance of materials from testing in service conditions

Materials tested	At the frontpart of the line		In the middle of the line	
	Wear rate mm/year	ε	Wear rate mm/year	ε
0.2% carbon steel	4.15	1.0	1.05	1.0
Steel 0.12% C, 18% Cr, 10% Ni, <0.8% Ti	1.22	3.4	0.24	4.4
Steel <0.08% C, 17% Cr, <0.8% Ti	1.32	3.1	0.31	3.4
Surfacing of Ni-based self-fluxing alloy 17% Cr, 4% B, 4% Si, 1% C	0.81	5.1	0.11	9.5

5.5 Disintegrator as a Device for Milling of Mineral Ores

One of the predominant technologies in mining, in the production of minerals, and in materials treatment is grinding. Due to the increasing scope of mining operations, large diameter ball mills are introduced. Research focused on modifying existing materials and selected variations of high manganese steel [30]. Because of its ability to withstand the severe impact conditions, such as those experienced in the large ball mills, high manganese steel became the focus of a number of the early investigations [31]. In such kinds of comminution machines as ball mills, a particle remains between the two grinding bodies (balls) and is broken by shearing. The maximum generated stresses τ that occur in the particle are locally equal or exceed the strength of the material [12].

Grinding by collision is a more effective method for refining of brittle material. One of the few machines for material grinding by collision is the disintegrator [13]. The value of the stresses generated in a material to be ground exceeds the strength of the material about ten times (see Table 5.1) and the particles are crushed into pieces.

This type of grinding implemented in twin-rotored machines is characterized by high productivity, but at the same time with the higher demands to the grinding media, the materials of grinding members and linings due to the high impact velocities and abrasivity of materials to be treated. As was shown in [17], by treatment of very hard composite material such as tungsten carbide based hardmetal, contamination of ground product, ultrafine hardmetal powder with iron from grinding media was surprisingly high (up to 15%). From this point of view, both the grindability of the materials in a disintegrator and the wear performance of grinding media are very important.

The aims of this investigation were (1) to study the grindability of different mineral materials using milling by collision in a disintegrator and (2) to predict the relative erosion wear resistance of steels as grinding media for mineral materials milling under conditions similar to those in industry.

The above-mentioned investigations were carried out at the Department of Materials Engineering of TUT, ordered by Slegten S. A., Belgium.

5.5.1 Materials to be Studied

To study the grindability of materials, different mineral materials (limestone, sandstone, basalt *etc.*) were examined.

Milling experiments to assess the grindability of different mineral materials (Table 5.6) were conducted in a semi-industrial disintegrator DSL-137 with its rotor diameter 600 mm and rotation speed 1500 rpm. The parameter of grinding – specific treatment energy – was used to estimate grindability [15].

Table 5.6. Characterization of mineral materials to be milled

No. and type of mineral material	Initial particle size, mm	Hardness HV0.2
1. Limestone (Engis)	+6.3–10 and +10–14	135–205
2. Sandstone (Trooz)	+6.3–10 and +10–14	140–205/250–280[a]
3. Porphyry (Voutre)	+6.3-10	560–880
4. Basalt (Cerf)	+6.3–10 and +10–14	560–840

[a] Dark phase in sandstone

For the abrasivity study of the above-mentioned mineral materials and different gold ores, the CAK-4 centrifugal accelerator was used. The velocity of abrasive particles was 80 m/s and impact angles – 30^o, 60^o and 90^o. Milled mineral materials with particle size less than 1 mm were used as abrasives. The types of mineral materials, gold ores and chromites as abrasives are given in Tables 5.6 and 5.7.

Table 5.7. Composition of selected mineral ores, wt%

No. and type of ore	Quartz 2000 HV	Pyrite 1530 HV	Feldpars 1290 HV	Others
Gold ores				
5. Crown Mine (South Africa)	80	2.5	1.5	16
6. Waihi (Australia)	63	2.5	27	7.5
7. South Pipeline (USA)	51	-	8	41
8. KBGM (Australia)	30	1	35	24
9. Plutonic (Australia)	15	-	25	30 (Amphibole, 946 HV); 30 – other
Chromites				
10. CMI (South Africa)	1.1	-	4	82 (Chromite, 1530 HV); 5.5 (Amphibole, 946 HV); 7.4 – other
11. Wonderkop (South Africa)	0.5	-	3	95 (Spinelle, 725 HV); 1.5 – other

Wear tests to assess the erosion behaviour of the grinding media – steels St37 and Hardox 600 – were conducted in a wear tester at the impact velocity v = 80 m/s

and impact angles 30° and 90°. The selected abrasives (sandstone, glass and quartz) with particle size 0.1–0.3 mm were used. The chemical composition and hardness of steels is given in Table 5.8. Microhardness by Micromet 2001 of mineral materials (Table 5.6) and Vickers hardness of studied steels (Table 5.8) were determined.

Table 5.8. Chemical composition and hardness of the studied steels

Type of steel	Chemical composition, wt%	Hardness
St 37-2	0.21–0.25 C; ≤0.055 P, S	140–150 HV30
Hardox 600	0.48 C; 0.70 Si; 1.00 Mn; 1.20 Cr; 2.50 Ni; 0.80 Mo	560–640 HBW[a] 580–635 HV30
Reference material C45 (normalized)	0.42–0.50 C; 0.50–0.80 Mn; ≤0.045 P and S	230–260 HV30

[a]by specification

The coefficent of abrasivity A_c of a materials used in abrasive wear tests was determined by steel St37 (normalized, 140–150 HV):

$$A_c = I_g^{mineral\ ore} / I_g^{quartz\ sand} , \tag{5.6}$$

where I_g is the weight wear rate, mg/kg.

The wear resistance of the grinding media mostly influenced by the hardest components in the mixture and calculated/reduced hardness H' values of mineral materials (gold ores and chromites) were used in the estimation of wear resistance:

$$H' = H_1 \cdot V_1 + H_2 \cdot V_2 + H_3 \cdot V_3 + \ldots H_n \cdot V_n = \sum_{i=1}^{n} H_i \cdot V_i , \tag{5.7}$$

where $H_1 \ldots H_n$ – hardness of the components of abrasive,
$V_1 \ldots V_n$ – relative weight amounts of components in the mixture.

To construct curves $\varepsilon = f(H_a)$ for steels (soft St37 and hard Hardox 600) used as the grinding media sandstone as softer abrasive (140–205 HV0.2), glass grit as medium abrasive (550–600 HV) and quartz sand as harder abrasive (1100–1200 HV) with a similar particle size (0.1–0.3 mm) were used for tests (Figure 5.29).

5.5.2 Grindability and Abrasivity of Mineral Materials and Ores

The results of grindability studies of mineral materials are given in Figure 5.30. As shown in Figure 5.30, a sandstone and porphyry showed better grindability, materials with higher hardness showed a decrease in the mean particle size after one step milling about 20%, after twin milling about 50% and more. Size reduction of limestone and basalt after first millings was less. At the same time results after multiple milling did not differ (see results limestone and porphyry after fifth milling).

Based on the abrasive wear studies, the abrasivity of materials was found. It was demonstrated that no direct correlation between hardness and abrasivity of materials to be tested exists (Table 5.9).

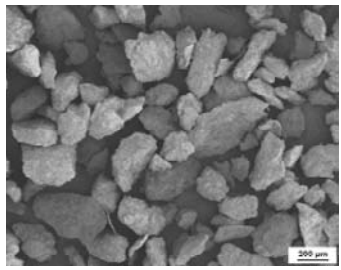

a

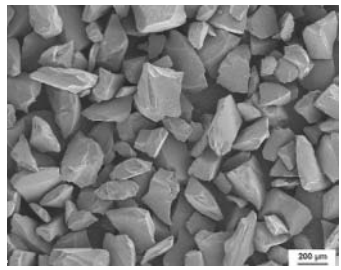

b

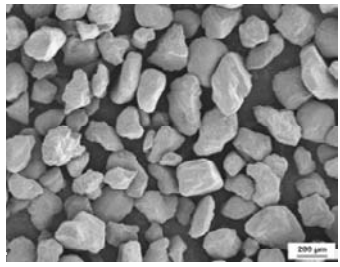

c

Figure. 5.29a–c. SEM images of abrasives: **a** – sandstone; **b** – glass grit; **c** – quartz sand

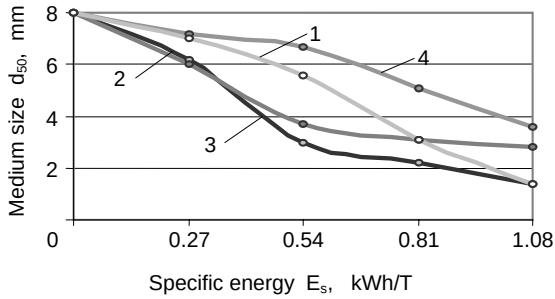

Figure 5.30. Grindability curves of minerals: 1 – limestone; 2 – sandstone; 3 – porphyry; 4 – basalt

Table 5.9. Hardness and abrasivity of the studied mineral ores

Used abrasives and their No.	Hardness HV	Coefficient of abrasivity A_C
Limestone (No. 1)	135–205[a]	0.30–0.36
Sandstone (No. 2)	140–205/250–280[a]	0.71–0.64
Porphyry (No. 3)	560–880[a]	0.59–0.48
Basalt (No. 4)	560–840[a]	0.43–0.33
Gold ore		
Crown Mine (No. 5)	1658[b]	1.0–0.94
Waihi (No. 6)	1647[b]	0.64–0.56
South Pipeline (No. 7)	1123[b]	0.51–0.41
KBGM (No. 8)	1067[b]	0.59–0.52
Plutonic (No. 9)	906[b]	0.46–0.32
Chromite		
CMI (No. 10)	1380	1.2–1.15
Wonderkop (No. 11)	775	0.85–0.75

[a] Measured with Micromet 2001 at the load 2 N (HV0.2)
[b] Calculated by Equation 5.7. The components with hardness ≥700 HV in the mixture were taken into consideration

The results of erosion tests of steel St37 with abrasives – ground mineral ore particles at impact velocity 80 m/s and impact angles 30^o, 60^o and 90^o similar to industrial conditions – are given in Figures 5.31 and 5.32. As shown in Figure 5.31, the wear rate by the studied four abrasives is not in correlation with the hardness of materials to be tested. Higher wear rate by relatively soft sandstone can be explained by the existence of a harder component in the material and by the shape of abrasives particles – the particles of sandstone were more angular as compared with porphyry or basalt. As shown in Figure 5.32, the wear rate of steel St37 in the flow of different abrasives is in good correlation with their hardness. With the increase of hardness, the wear rate decreases. The influence of the impact angle on the wear rate by all the abrasives studied was even – with the increase of the impact angle, the wear rate decreases. It is similar to steels as plastic materials. As compared with limestone, the wear resistance of steel St37 in sandstone is about 2.3 and 1.9 times higher, at 30^o and 90^o, respectively.

The wear rate and relative wear resistance of steel St37 in different mineral ores with hardness from 775 HV up to 1647 HV depends first on the composition of ores, on the amount of the hardest component – quartz (2000 HV) in mixture (see Table 5.6). The wear rate is the highest by chromites (in mixture 82% is component of hardness 1530 HV), followed by gold ore – Crown Mine (main component – 80% is quartz with hardness 2000 HV).

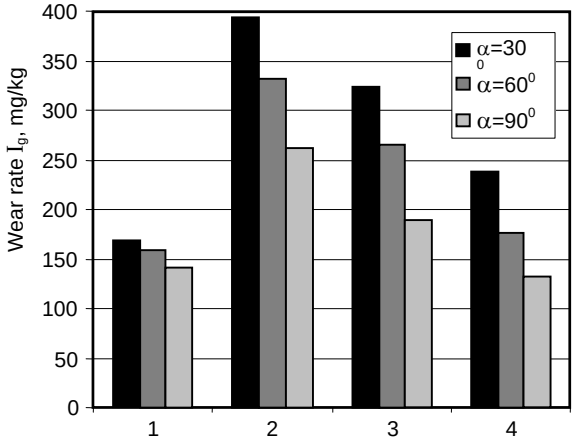

Figure 5.31. Wear rate of steel St37 at different impact angles and in abrasives: 1-limestone; 2 – sandstone; 3 – porphyry; 4 – basalt

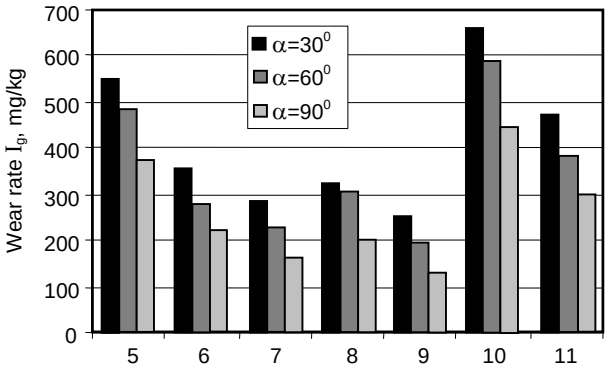

Figure. 5.32. Wear rate of steel St37 at different impact angles and in gold ore abrasives: 5 – Crown Mine; 6 – Waihi; 7 –South Pipeline; 8 – KBGM; 9 – Plutonic; 10 – CMI; 11 – Wonderkop

5.5.3 Prediction of Relative Erosion Resistance of the Grinding Media

To evaluate the suitability of hardened steels as the grinding media and to have the wear curves $\varepsilon = f(H_a)$ (see Section 3.5), the wear rates of softer reference material – steel St37 (140–150 HV30) in abrasives – in sandstone (140–205 HV) and glass grit (550–600 HV) and wear rates of harder material – steel Hardox 600 (580–635 HV30) in abrasives – in glass grit and quartz sand (1100–1200 HV) were determined. The results of experiments are given in Table 5.10.

Table 5.10. Wear rates of studied steels in soft and hard abrasives

Steel	Hardness HV30	Wear rate I_g, mg/kg					
		Sandstone, milled		Glass grit		Quartz sand	
		$\alpha = 30^o$	$\alpha = 90^o$	$\alpha = 30^o$	$\alpha = 90^o$	$\alpha = 30^o$	$\alpha = 90^o$
St37	140–150	248.4	141.9	587.2	437.7		
Hardox 600	580–635			323.4	312.8	376.9	438.4

On the basis of test results, the ε-H_a curves were constructed (Figure 5.33).
As shown in Figure 5.33, four defined zones exist:
A – wear resistance is low;
B – wear resistance increases rapidly;
C – wear resistance decreases rapidly;
D – wear resistance of Hardox is low;

In the interval B–C the use of Hardox is most preferable.

The comparative testing of soft and hardened steels as the grinding media in disintegrator type crushing devices demonstrated that hardened steels are not prospective in these applications. With the material cost increasing, the effect is low – the increase of service life of milling elements is minimal. It was confirmed by comparative testing of pins from different steels and different coatings. Relative wear resistance of steels and coatings in disintegrators by the milling of materials with hardness 1000 HV and more is low (see also Section 5.2.3).

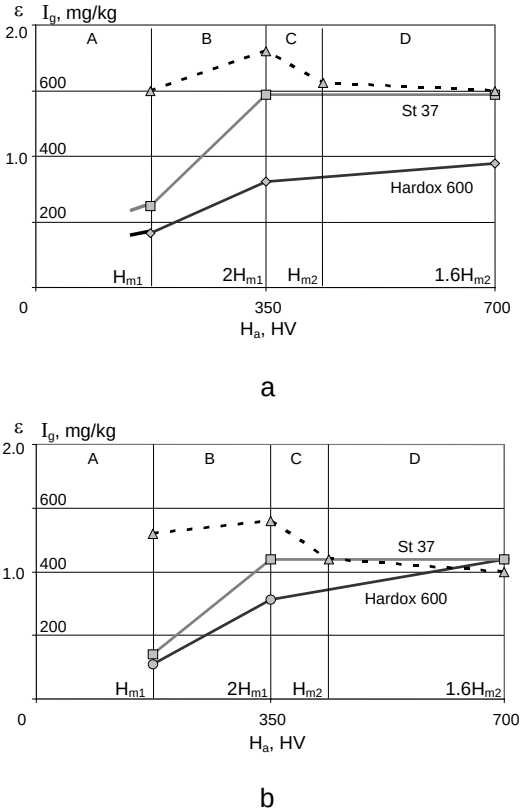

Figure 5.33a,b. Wear resistance of steel St37 (M_1) and Hardox 600 (M_2) of respective hardness H_{m1} and H_{m2} *vs* abrasive hardness H_a. The *dashed line* – dependence of relative wear resistance ε on H_a: **a** – impact angle 30°; **b** – impact angle 90°.

5.6 References

1. Stupnitsky AM. Study of Wear Resistance of Materials at Erosion. Caused by Sliding Particles. PhD Thesis. Tallinn 1976 (in Russian).
2. Kleis I, Kovalenko I, Loboda V, Ovsjannikova L, and Stupnitsky A. Study ways to increase of performance of aglomeration exhausters rotors. Proc Techn Univ Tallinn of. 1981;516:23–41 (in Russian).
3. Ovsjannikova L. Means of Increasing the Wear resistance of Centrifugal Compressor Rotors. PhD Thesis. Tallinn 1983 (in Russian).
4. Shurovsky V, Spitsyn J, Glushkov V, Surinovitch V. Erosion of Centrifugal turbomachines for earthgas. Proc Polzunov Research and Design Institute of Energetic Equipment. Leningrad 1980;181:77–82 (in Russian).
5. Wandke E, Tsherny S, and Lübke J. Massnahmen zur Verlängerung der Laufzeit von Nassentstaubunganlagen. Neue Bergbautechnik, 1964;14/6:229–33.

6. Bruk AD. The investigations of agglomeration exhausters to increase their wear resistance. Proc. Polzunov Research and Design Institute of Energetic Equipment. Leningrad 1980;181: 47–51 (in Russian).
7. Botkatchik IA, and Matveyev AS. The increase of perfomance and economy of flue-gas exhauster of heat plants. Proc Polzunov Research and Design Institute of Energetic Equipment. Leningrad 1986;227:77–81 (in Russian).
8. Ris VF, Evdokimov VE, and Semov VV. Proc Polzunov Research and Design Institute of Energetic Equipment. Leningrad 1986;181;5–13 (in Russian).
9. Bernhardt C, Gottschalk I, and Heegen H. Vergleichende Untersuchungen zur mechanischen Aktivierung von Quarz in einigen Labormühlen. Silikattechnik, 1974;25/5:183–86.
10. Hint J. Disintegration Method for Manufacturing of Silicate Products. Tallinn: Estonian State Publishing House 1952 (in Russian).
11. Hint J. The Basis of Manufacturing of Silicate Products. Leningrad-Moscow: State Publishing House of Building, Architecture and Building Materials. 1962 (in Russian).
12. Tamm B, and Tymanok A. Impact grinding and disintegrators. Proc Estonian Acad Sci Eng, 1996;2/2:209–23.
13. Tümanok A, and Kulu P. Treatment of different materials by disintegrator systems. Proc Estonian Acad Sci Eng, 1999;5/3: 222–42.
14. Tümanok A, Kulu P, Goljandin D, and Rostsin S. Theoretical model for grinding by collision of ductile metall chips into metal powder. Proc 1st Intern DAAAM Conference on Industrial Engineering – Actual Activities. Tallinn, Estonia 1997;130–32.
15. Goljandin D, Kulu P, Peetsalu P. Ultrafine metal powder produced by grinding from the Proc TMS 2002 Recycling and Waste Treatment in Mineral and Metal Processing: Technical and Economic Aspects.Vol.1.Sweden 2002;277–84.
16. Peetsalu P, Goljandin D, Kulu P, Mikli V, Käerdi H. Micrppowders produced by disintegrator milling. J Powder Metallurgy Progress 2003;Vol.3/2:99–110.
17. Kulu P, Käerdi H, Mikli V. Retreatment of used hardmetals. Proc. TMS 2002 Recycling and Waste Treatment in Mineral and Metal Processing: Technical an Economic Aspects. Vol.1. Sweden 2002;139–46.
18. Uuemõis H, Piel M. Selection and evalution of materials for impact cruchers. Proc Techn Univ Tallinn 1979;478:31–36 (in Russian).
19. Kulu P. Wear Resistance of Powder Materials and Coatings. Tallinn:Valgus Publishers 1988;119 (in Russian).
20. Kulu P. The Principles of Creation of Erosion Wear Resistant Powder Materials and Coatings. Doctoral Thesis. Tallinn 1989 (in Russian).
21. Zimakov S, Pihl T, Kulu P, Antonov M, Mikli V. Applications of recycled hardmetal powder. Proc Estonian Acad Sci Eng, 2003;9/4:304–16.
22. Kleis I, Lepikson H, and Mosberg R. The Wear of metal in Quartz Sand and Selection of Materials of Disintegrator Pins. Research Report. Tallinn 1957 (in Estonia).
23. Kleis I, and Uuemõis H. Wear Resistance of Impact Based Grinding Equipment. Moscow: Mashinostroenie Publishers, 1986 (in Russian).
24. Bytshkov RA, and Kovalev AT. Chemical and Petrochemical Machine Building 1977;42 (in Russian).

25. Tymanok A. About the energy of material to be treated in multistep rotor milling device. Proc Techn Univ Tallinn 1976;393:139–47 (in Russian).
26. Tamm B, and Tymanok A. Im balance control of disintegrator. Proc IFAC'96 Triennial World Congress. E. Nonlinear Systems I. San Fransisco 1996;173–78.
27. Kleis I, Lepikson H, and Tadolder J. Study of Wear of Boilers TR-17 Cyclons and Tubes. Research Report. Tallinn 1978 (in Estonian).
28. Kleis I, Lepikson H, and Tadolder J. Study of erosion of cyclones and gas flues. Proc Higher Education Institutions. Series Energetics.1969;11: 55–60 (in Russian).
29. Üksti L. The Influence of Liquid Additions in Abrasive to the Erosion of Metals. PhD Thesis. Tallinn 1983 (in Russian).
30. Cherje TW, Simbi DJ, Navara E. Relationship between microstructure, hardness, impact toughness and wear perfomance of selected griding media for mineral ore milling operation. J Materials and Design, 2004;25:11–18.
31. Benjamin D. Properties and selection: stainless steels, tool materials and special purpose metals. Metals Handbook, 9th edition.Vol.3, ASM,576.

Index